A computational study of the adsorption of water and carbon dioxide at oxide surfaces

Allen, Jeremy

Award date:
2009

Awarding institution:
University of Bath

A Computational Study of the Adsorption of Water and Carbon Dioxide at Oxide Surfaces

A Thesis Submitted by
Jeremy Peter Allen
for the degree of Doctor of Philosophy
University of Bath
Department of Chemistry
August 2009

Abstract

The aim of this thesis is to use computer simulation methods to consider adsorption of both water and carbon dioxide onto oxide surfaces. The materials chosen have direct relevance to current environmental concerns, alkaline earth metal oxides for carbon sequestration and uranium dioxide for the storage and stability of nuclear materials. Chapter one outlines both previous experimental and computational work relevant to these research areas.

The computational methodologies used in this thesis are described in chapters two and three. Chapter two outlines how the forces between atoms in the simulation are modelled using both potential-based and electronic structure models. Chapter three details how these are then used to find lowest energy configurations.

The main results of the alkaline earth metal oxides are discussed in chapters four and five. Chapter four uses multiconfigurational static lattice simulations of water and CO_2 surface adsorptions to identify the most probable adsorption sites and to generate surface phase diagrams as a function of surface composition. Whereas the focus of chapter five is to model interactions in liquid water with both surface and nanoparticles.

Chapters six and seven describe the results of simulations on uranium dioxide. Chapter six uses electronic structure methods to model defects and non-stoichiometry in bulk and thin film structures. Chapter seven then describes the calculations of the interactions of water with uranium dioxide surfaces, in terms of both gas phase adsorption and the mineral – water interface with results showing the favourability of surface hydroxylation on the {100} and {110} surfaces.

Finally, a summary of the main findings and achievements of this thesis are given in chapter nine, along with a discussion of possible future work.

Contents

Chapter One

Introduction

In recent times, improvements in computing power, as well as the performance and versatility of simulation codes, have allowed computational chemistry to tackle many more complex problems. Computational modelling allows researchers not only to help explain experimental observations but also to make predictions of material properties at the atomic level. The work contained in this thesis will apply computer simulation techniques to investigate materials with an environmental theme, namely those associated with carbon storage and with the stability of nuclear materials. Despite the apparent differences, the two areas require understanding of surface processes at oxide surfaces and thus the techniques deployed are common to both areas.

The central aim of the work in this thesis is to develop models of structure, stability and composition of the surfaces of oxide materials; therefore, there are three aspects we need to consider. The first is that of the surface termination, which is governed by the Miller index and, as illustrated in Figure 1.1, corresponds to the orientation of the cleavage plan. Second is the surface composition, as the position of the cleavage plane will also control the surface symmetry and the particular atoms found at the surface. Each Miller index can often give rise to a number of different surface structures, with different surface compositions. The surface termination, and hence composition, will also be governed the amount of impurities present. The focus of this work is to investigate the effect of hydration and carbonation, but other impurities or additives could play an important role. The final component is the stability, which can be calculated directly via computational methods. The stability can be inferred from the occurrence in the crystal morphology, i.e. in general, the most stable surfaces will be those expressed. Computational methods can be broadly split into two classes: atomistic modelling, using analytical potentials to describe the forces between atoms, and *ab-initio* methods, such as density functional theory (DFT). These different simulation methods will be described in detail in chapter two.

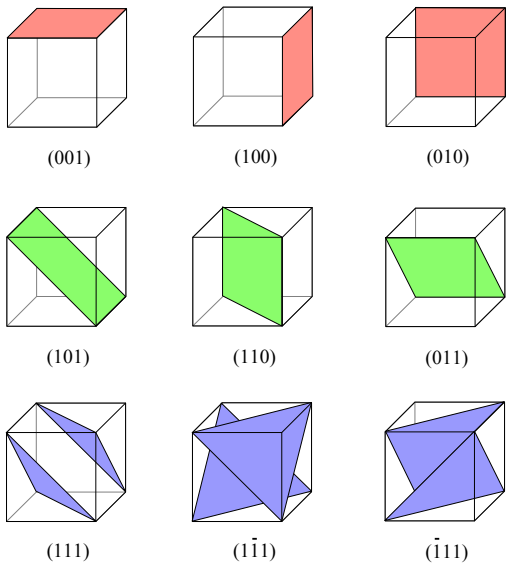

Figure 1.1: Schematic showing the relationship and orientation of different Miller indices.

There are a number of different techniques for investigating surface structure and composition, the results of which are discussed in this thesis. These consist of both computational and experimental procedures. The relevant experimental techniques used are described below, which provide a valuable comparison for computational studies.

1.1 Experimental Methods for Studying Surfaces

A large number of different experimental techniques are used to consider surfaces. These are used to probe not only the surface structure and composition, but also the reactivity of the surfaces, in terms of adsorbates and morphological changes. For a more complete overview of these techniques and alternative methods, including their operation and the interpretation of results, see Prutton [1] and Atkins and de Paula [2]. One commonly used technique is low-energy electron diffraction (LEED). LEED involves bombarding a sample under high vacuum conditions with low-energy electrons. Using low-energy electrons ensures that penetration will only occur in the first few layers, making this surface sensitive. The electrons are then diffracted and measured, giving a pattern characteristic of the surface ordering. Although often used in preparation to check surface cleanliness and ordering, it can also be utilised to give information concerning surface symmetry and reconstruction, as well as information regarding adsorbed monolayers. However, LEED has the disadvantage that it lacks elemental or chemical information and cannot easily probe depth.

Ionisation techniques can be used to gain information of the surface composition. One commonly used technique is photoelectron spectroscopy. This is based on the application of Einstein's photoelectric effect, as described by Equation 1.1.

$$E_k = h\nu - \Phi \qquad 1.1$$

where E_k is the kinetic energy, hv is the energy associated with the incident radiation and Φ is the work function, or binding energy. Practically, the sample is exposed to a beam of X-rays or UV light, giving rise to the forms of X-ray and UV photoelectron spectroscopy, or XPS and UPS, respectively. This radiation induces photoelectric ionisation, causing the emission of photoelectrons. Therefore, this method can effectively fingerprint a sample, allowing identification of surface composition, bonding characteristics and valence band features. Experimental studies of the unoccupied states in the conduction band can be studied using the related technique of Bremsstrahlung isochromat spectroscopy (BIS). This works in a complementary way to photoelectron spectroscopy, where an electron beam is directed at the sample. This then enters the conduction band, with decay leading to the emission of a photon. The technique of X-ray absorption near-edge spectroscopy (XANES) also allows surfaces to be characterised through the evaluation of unoccupied states. When X-rays pass through a sample, a certain number of them are absorbed and can cause the excitation of electrons. This electronic excitation occurs at characteristic wavelengths, where a large increase in the level of absorption is observed. This is known as an edge and the analysis of the small oscillations near the edge can give information about vacant orbitals, electronic configuration and site symmetry of the atom being measured. In addition, the excitation of electrons can occur at K, L or M edges, where the letter indicates the transition occurring between electron orbitals in terms of the change in quantum number.

Low-energy ion scattering (LEIS) also allows for the characterisation of both surface structure and composition. This works by means of directing a beam of charged particles at the surface, typically using ionised noble gases, such as He^+. As the ion only carries kinetic energy it is non-destructive and does not penetrate into the solid, resulting in high surface sensitivity. In addition, as it only interacts with surface atoms, it has the benefit that the data is not convoluted with bulk information. When the ion comes into contact with the surface, different processes can occur. As the name implies, LEIS measures the ion scattering that occurs, by measuring the

velocities and energies of these scattered ions, to gain surface information. A related technique is that of metastable-impact electron spectroscopy (MIES). This works in a similar way to LEIS, using metastable atoms, typically noble gases. When the electronically excited metastable atoms impact on the surface, most of the excitation energy is used to eject electrons from the surface. These emitted electrons are characteristic of their binding energy and therefore a spectrum can be recorded, giving information about the surface. However, as a large number of different de-excitation processes can occur using this method, it is difficult to interpret MIES spectra unambiguously.

The presence and relative binding of surface adsorbed layers can be investigated using temperature-programmed desorption (TPD). This method works by rapidly heating a sample and measuring the removal of surface adsorbed species, often with the use of a mass spectrometer. The rate of desorption can then be plotted as a function of temperature. The peaks on this plot represent the desorption of either different species or molecules in different chemical environments or bonding states and can be used to identify the different adsorption modes occurring on the surface. However, one of the obvious disadvantages is that this technique is destructive.

The visualisation of surfaces and nanoparticle morphologies can be achieved using electron microscopy. The scanning electron microscope (SEM) scans a focused electron beam across the surface of the material of study. At each scanning point some of the energy of the incident electron beam is lost, through conversion to heat, low-energy secondary electrons, X-rays and light emission. The energy of these can then be used to build up an image of the surface. SEM, like LEED, therefore gives good two dimensional resolution of the surface, with more local structure, however it also gives poor depth information. In contrast the related non-optical microscopy techniques of scanning tunnelling microscopy (STM) and atomic force microscopy (AFM), give good depth information but less accurate two dimensional resolution. These related techniques use a probe, in the form of a sharp tip, often made of platinum/iridium or gold, which can be rastered across the surface to build up a

surface topography rather than the electron beam of SEM. STM works by using the principal of quantum tunnelling, where, for a conducting surface, the measurement of the movement of electrons from the probe tip to the surface is used to build up an image of the surface topography by probing the orbitals of the surface atoms. If the electrons tunnel into the surface, information on the LUMO (lowest unoccupied molecular orbital) is gained, whereas the opposite is true for electrons tunnelling from the surface, providing information on the HOMO (highest occupied molecular orbital). Thus, STM gives both structural and electronic information at the atomic scale. AFM differs in that it does not require the surface to be conductive, instead measuring the forces acting between the surface and the tip, supported on a cantilever, to measure the topography of the surface. AFM provides very high depth contrast but is less good at precisely locating atom positions and *x*-*y* resolution. Hence, it provides a good complement to SEM, which has good *x*-*y* resolution but poor depth resolution.

The next sections of this chapter will provide an overview of recent work used as background information for the general aims of this thesis, using a combination of computational studies, as well as using the aforementioned experimental techniques. Although this discussion is by no means exhaustive, the studies described not only act as a basis for the work presented in this thesis, but also allow for the direct comparison of our results to previous work. This chapter will comprise of two sections, the first of which will consider previous work concerning the surface reactivity of calcium and magnesium oxides, with regards to water and carbon dioxide, as well as how these studies link to reducing the impact of global warming. The second section will consider previous studies which have considered the structure and stability of uranium dioxide. Previous work concerning the surface reactivity of uranium dioxide with water will also be discussed.

1.2 Global Warming and Carbon Sequestration

The first sections of this thesis will focus on the adsorption of water and carbon dioxide. The motivation for studying these processes is in relation to global warming and the enhanced greenhouse effect. In simple terms, this is caused by the increase in greenhouse gases, such as carbon dioxide, which adsorb the thermal infrared radiation emitted from the Earth's surface, thus causing an increase in the surface temperature. Many methods are being investigated in an effort to reduce this effect through either the reduction in the amount of greenhouse gas emission, including the use of alternative fuels and energy generation, or through more efficiently disposing of waste gases. One form of the latter is through carbon sequestration, which is defined as the removal of anthropogenic carbon from the atmosphere and its long-term storage.

Carbon sequestration can be considered in a number of ways, including biological, though the uptake into trees and plant life, oceanic, through reaction with water in the world's oceans, and geological, through underground storage or reaction with minerals to form the stable carbonates. This last form acts as the basis for studying the interactions of carbonate with minerals, as a thorough knowledge of the interaction of carbon dioxide and subsequent formation of carbonate phases is imperative to exploit this process fully.

Mineral sequestration, as it is termed, was suggested by Seifritz in 1990 [3] and was based on the natural weathering of alkaline silicates, due to its exothermic nature. The generalised reaction scheme for this process is highlighted by Equation 1.2.

$$(Mg, Ca)_xSi_yO_{2x-y} + xCO_2 \rightarrow x(Mg, Ca)CO_3 + ySiO_2 \qquad 1.2$$

His suggestion for this process was that pressurised carbon dioxide could be pumped into a closed container containing a suspension of pulverised silicates in water. The

resulting products could then be drained into deep ocean and the process repeated. Calcium and magnesium bearing minerals have been the main focus for mineral sequestration due to their natural abundance, reactivity with carbon dioxide and stability of carbonates. Although a number of alternatives have been considered, including hematite [4] and anthracites [5].

Although the mineral carbonation process is exothermic in nature, it is inherently slow and occurs naturally over hundreds of thousands of years. Previous research to identify and assess different feedstocks to use for this mineral sequestration process have mainly focussed on silicate minerals such as olivines and serpentines (hydroxysilicates) [6, 7], as well as CaO- and MgO-rich waste streams [8]. Olivines are known to be more reactive than the serpentines, although the abundance and wide availability of serpentines make them more attractive [9]. However, the major drawbacks of this method so far are that most studies have been based on high temperatures, partial pressures and reaction times, giving this process a high energy cost, although, chemical activation of such materials was shown to improve reactivity substantially with less energy-intensive conditions [10]. An assessment of cost, using wollastonite and steel slag as feedstock, was also carried out by Huijgen *et al*. in 2007 [11] finding that the current costs of the sequestration process is higher than other CO_2 storage methods. The cost of using steel slag was estimated as being lower than wollastonite, estimated at 77 and 102€ ton^{-1}, respectively. The major costs are associated with the feedstock and the electricity required for grinding the material and compression.

In order to help optimise the sequestration process, a number of studies have focused on understanding the carbonation process on the surfaces of the simple oxides and hydroxides of calcium and magnesium. Once the processes on these materials are more fully elucidated, the methods and techniques can be applied to more complex materials, such as the serpentines. However, due to the presence of water in the environment, an understanding of the interactions of this with these materials is also essential as it would invariably be present during the carbonation

process. Therefore, prior to discussing the work focusing on mineral carbonation, the next section will describe recent studies on the interactions with water.

1.2.1 Interactions of Alkaline Earth Metal Oxide Surfaces with Water

The simple oxides of calcium and magnesium have been extensively studied in recent times, both experimentally and computationally. For computational studies magnesium oxide is often thought of as a model system, due to its simple cubic structure and the spherical closed shell ions. Computational studies have mainly considered the low index surfaces, finding that the higher energy {110} and {111} surfaces undergo surface micro-faceting to increase the amount of {100} surface expression, hence reducing surface energy [12]. Due to the natural abundance of water, its interactions with the surfaces of calcium and magnesium oxide with water have also been studied extensively.

The adsorption of water on the (100) MgO surface has often been studied experimentally to help elucidate whether or not water dissociation occurs. For example, Xu and Goodman [13] used TPD, in conjunction with LEED and surface infrared measurements, to consider the structure and geometry of water on the MgO (100) thin film surfaces. Their results showed similar results to cleaved single crystals with a well-ordered surface structure. D_2O adsorption was studied on this surface, with no appearance of O-D stretches seen, thus indicating the presence of physisorbed water only. For the first adsorbed layer of water, desorption temperatures corresponding to binding energies of 0.56 and 0.69eV were seen, with peaks assigned to water molecules being perpendicular and angled to the surface, respectively. In addition, the coverage of the first adsorbed layer was reported as being 0.67. However, Johnson *et al*. [14], using a combination of MIES studies with computational *ab-initio* calculation, found that although hydroxylation at the mineral – vacuum interface is not energetically favourable, hydroxylation is present at the mineral – water interface. This hydroxylation was attributed to the formation of a nearest-neighbour ion pair which can then more freely adsorb. XPS and AFM

studies by Abriou and Jupille [15] also found the presence of hydroxylation on freshly cleaved MgO surfaces. However, after adsorption-desorption cycles this ability was seen to decrease, due to the hydroxyl adlayer altering the surface structure, resulting in poorer adsorption. Although surface characterisation did not extend beyond discerning that the surface which had been exposed to water vapour was visibly different under AFM than a freshly cleaved surface under nitrogen.

Computational methods have also been used extensively to consider the interactions of water with CaO and MgO surfaces, particularly from the view of dissociative adsorption. Adsorption on the {100} surfaces were reported by de Leeuw *et al*. [16] to be generally unfavourable, however at a coverage of 75% a stabilised surface was seen. This stabilisation was seen to be provided by an extensive surface rearrangement with surface cations relaxing upwards giving rise to a more rumpled surface, where the hydroxides are able to form an additional bond to the displaced cation as well as the original cation – hydroxide bond. The dissociation of water on the (001) MgO surface was further investigated using DFT by Refson *et al*. [17]. They also found the (001) surface to be unstable to hydroxylation. However, upon hydroxylation they found reconstruction to form the hydroxylated (111) surface, which they proposed was the most stable surface under ambient conditions, rather than the pure {100} surface. This hypothesis also fits with the experimental observations of why the dissociation of water is observed experimentally. The hydroxylated (111) MgO surface is identical in structure to the $Mg(OH)_2$ (0001) surface and hence explains why dissolution rates for MgO and $Mg(OH)_2$ were seen to be identical over the pH range 2-5 by Vermilyea [18]. The adsorption of water on CaO was also considered using DFT by de Leeuw *et al*. [19], showing that physisorption of water would preferentially occur on the {100} surface. Evaluation of different surface concentrations showed that at 50% coverage, water molecules orient both perpendicular and parallel to the surface, showing hydration energies of 69.9 and 56.0kJ mol^{-1}, respectively. However, when monolayer coverage is attained, repulsion between the water forces the water molecules to be positioned in a perpendicular orientation, with a hydration energy of 71.5kJ mol^{-1}. Dissociated

water adsorption was also modelled, however, it was found to be unstable, with recombination of OH groups to form molecular water.

The effect of coordination number on water adsorption has also been investigated by considering dissociative adsorption on the stepped {100} surface, using the {310} termination, and micro-faceted {110} surfaces [16]. de Leeuw *et al*. found adsorption to be energetically favourable, with adsorption preferentially occurring on low-coordinated sites. The physisorption of water on clean and hydroxylated MgO surfaces was then considered [20] and again the results suggested that associatively adsorbed water is favoured on low-coordinated sites. In addition, physisorption at five-coordinated surface ions on the {310} surface is stabilised by hydroxylation of the step edges. Larger hydration energies for molecular water adsorption were also seen on the hydroxylated surfaces. The effect of ion coordination on the dissolution of hydroxylated CaO and MgO surfaces was later studied by de Leeuw and Parker [21]. This showed that the dissolution of *M*O units from three- and four-coordinated sites is more energetically favourable than from five-coordinate {100} sites. For the planar {110} surface, dissolution was seen to be particularly favourable, with hydroxylation stabilising the resultant surface and forming a facetted, hydroxylated surface structure.

Simulations of the interaction of surfaces with liquid water have mainly been considered by studying the nature of the mineral – water interface. In 1998, de Leeuw and Parker [22] considered the structure of water above {100} and {310} MgO surfaces. They found a layered structuring of water above the surface, with the greatest density being closest to the surface. This density then reduced as distance to the surface increased, showing an oscillatory distribution. The {310} surface however showed less distinct ordering but the presence of strongly coordinated water was noted in the position inside the steps. This structuring of water above mineral surfaces has also been highlighted by Kerisit *et al*. [23] on the $\{10\,\bar{1}\,4\}$ calcite surface, showing distinct areas of high water density present at the surface, which then decreases in an oscillatory manner moving away from the surface. In

addition, further studies by Spagnoli *et al*. [24] on hematite surfaces showed variation of water orientation with the layering. The water molecules closet to the hydroxylated (0001) surface of hematite showed a perpendicular orientation, relative to the surface, with the hydrogen atoms directed away from the hydroxyl layer. The second layer then had water molecules orientated with hydrogen atoms pointed downwards towards the first layer. In addition, the diffusion coefficient and charge density in salt solutions was also seen to follow a similar oscillatory pattern to the water density. Kerisit *et al*. [25] modelled the adsorption of metal ions to the $\{10\bar{1}4\}$ calcite surface, showing that free energy adsorption profiles show an inverse relationship to water density. This was reasoned that the adsorption profile is affected by electrostatic interactions, showing energy barriers in regions of high hydrogen density but low free energies in oxygen density. Therefore, indicating that the diffusion of species to and from surfaces is clearly influenced by the structuring of water in the region above the surface.

A number of studies have also considered the interaction of water with magnesium oxide nanoparticles. Nanoparticles formed from MgO smokes characteristically give rise to cubic particles, dominated by the {100} surface [26]. The work of Hacquart and Jupille [27] considered the effect of dissolution in liquid water at neutral pH. Their studies showed that after immersion in water, following a period of seven days, the cubic MgO nanoparticles changed shape to form octahedra. This occurred via a process of (110) facets forming on the edges of the cubic crystal, followed by the appearance of (111) corner faceting, which eventually dominated to form fully hydroxylated (111) surfaces, giving the octahedral shape. However, comparisons with acidic solutions deemed that a necessary condition is a preservation of the symmetry throughout the dissolution process, as the faster dissolution rates in acidic solutions resulted in truncations parallel to the (110). Geysermans *et al*. [28] used DFT simulation to support this proposed dissolution pathway, via determination of morphology using calculated surface energies. In addition, the unexpected appearance of the (110) facets was attributed to kinetic effects, through the use of constrained Wulff constructions, where the (111) energies were discounted to mimic

its slow growth. In addition, at lower temperatures and partial pressures, hydroxylated (100) facets on the corners of the octahedral shape were predicted to occur.

An understanding of how the presence of water will affect these surfaces is clearly important, however, the interactions of carbon dioxide are crucial to the understanding of the carbon sequestration process and yet little comparable work has been done. The next section will therefore focus on relevant studies which have considered this interaction.

1.2.2 The Surface Adsorption of Carbon Dioxide

The interaction of carbon dioxide with alkaline earth metal oxides has not been as widely studied as the interactions of water; however, there have been a number of key studies in this field. The majority of modelling work has focussed on the bonding mode of carbon dioxide. Jensen *et al*. [29], for example, used cluster-based DFT calculation to determine theoretical IR frequencies following carbon dioxide adsorption on CaO and MgO surfaces. The findings of this study showed that CO_2 binds as a monodentate carbonate ion on edge sites on MgO, but bidentate on corner sites. Whereas, for CaO they found that both sites showed monodentate bonding. This work has also supported other computational and experimental work. Fukuda and Tanaka [30] reported experimental IR studies which indicated that only monodentate bonding is seen for CaO at room temperature, with bidentate bands appearing above 350°C. Bidentate bands were also reported for MgO, which were seen to decrease with increased loading. Shen *et al*. [31] provided TPD results indicating adsorption energies ranging from 80 to 170kJ mol^{-1}, depending on the surface coverage. Further TPD and IR studies by Yanagisawa *et al*. [32] also found two distinct carbonate groups on MgO surfaces, with the least stable assigned to the monodentate carbonate.

Pacchioni *et al*. [33] used *ab-initio* cluster modelling to consider the difference in reactivity of CO_2 chemisorption on the CaO and MgO (100) surfaces. Their results indicate that the carbonate species formed on the CaO surface is much more strongly bound than on the MgO surface. This difference was attributed to be a cause of the electrostatic stabilisation of the surface anion. They reasoned that the smaller Madelung potential of CaO destabilises the surface O^{2-} anion more than in MgO, resulting in a higher reactivity. Therefore, a regular CaO surface oxygen site was seen to behave similarly to a low-coordination defect site in MgO. This was further shown by the MIES study by Krischok *et al*. [34], which confirmed that CO_2 takes the form of a carbonate, through reaction with O^{2-} surface anions, with chemisorption taking place on regular oxygen sites for CaO and at low-coordinated oxygen ions only for MgO. More recent experimental studies include those of Voigts *et al*. [35] (MIES, UPS and XPS) and Kadossov and Burghaus [36] (TPD and DFT modelling) on the adsorption of CO_2 on CaO (100) surfaces. Their results again confirming that carbon dioxide adsorption occurs via carbonate formation, leading to a closed layer of $CaCO_3$. In addition, the results of Voigts *et al*. suggest that reaction stops after monolayer coverage is formed.

In addition to the reactivity and adsorption processes on the simple binary oxides, researchers have also considered the hydroxides. The study of the metal hydroxides has the appeal that they can act as model systems for the use of minerals containing hydroxide lamella, for example magnesium hydroxide itself and serpentines. In addition, the dehydroxylation process, which inherently accompanies carbonation, can also lead to surface disruption which could potentially enhance reactivity. Although the dehydroxylation processes itself has been studied in some detail [37, 38] the gas-phase carbonation has had considerably less attention. Therefore the combined dehydroxylation/carbonation reaction on magnesium hydroxide has been considered both experimentally, for example, Béarat *et al*. [39], and computationally, for example, Churakov *et al*. [40]. Béarat *et al*. used a range of experimental methods, including elemental analysis, thermogravimetric analysis and mass spectrometry, to consider this process. Their results indicated that the

dehydroxylation precedes carbonation as a distinct yet interrelated process. In addition, they reported that above the minimum CO_2 pressure required for carbonation, both the reactivity towards carbon dioxide and dehydroxylation were found to decrease. Of more practical significance was their finding that if the dehydroxylation process was conducted at low temperature (375°C), porous intermediate materials were formed, with enhanced carbonation reactivity at ambient conditions. Churakov *et al.* studied this reaction further with DFT methods. Results of the surface simulations revealed that the $(1\,\bar{1}\,00)$ surface could be dehydroxylated with the greatest ease and that the formation of vacancies between neighbouring (0001) planes may favour the diffusion of protons and hydroxide groups, facilitating further dehydroxylation. In addition, their analysis of the reaction pathway indicated that, for the dehydroxylation, the rate limiting step is the breaking of the Mg - O bond. However, for carbonation, the rate limiting step is the sp^2 hybridisation of the carbon atom. In addition, the formation of the carbonate unit itself requires the presence of an under-coordinated magnesium ion, therefore making the processes interrelated. As well as the reaction process, they also considered the compatibility of magnesite and brucite surfaces. This showed that the $(1\,\bar{1}\,00)$ surface, with channels running perpendicular to the surface to facilitate movement of OH and H ions to the surface, is compatible with the lowest energy $(10\,\bar{1}\,4)$ surface of $MgCO_3$, making the formation of a carbonation layer, with epitaxial growth, favourable on this surface.

The use of nanoparticulate CaO-based CO_2 adsorbents has also received attention in the literature. For example, Wu *et al*. [41] considered the adsorption properties of micro- and nano-sized CaO/Al_2O_3, using thermogravimetric analysis to assess the adsorption ratio. The durability of these sorbents was considered after a period of 50 cycles, with a carbonation temperature of 650°C and a calcination temperature of 800°C. Their results showed that nano-sized sorbents have both a faster decomposition rate and higher adsorption ratio to the micro-sized sorbents. For the nano-sized sorbent, durability studies showed an adsorption ratio of 68.3%, comparing with 44% for the micro-sized material. Following repeated carbonation,

X-ray diffraction and SEM studies showed that the microstructure and composition was seen to change for the nano-sized material, with pores in the material widening and the formation of $(CaO)_{12}(Al_2O_3)_7$, which acts to stabilise the compound. In addition, Lee *et al*. [42] considered MgO-based sorbents using K_2CO_3 as a promoter for CO_2 capture at low temperatures. They found that the presence of water vapour causes a reduction in the temperature needed for CO_2 sorption. Increasing relative humidity was also seen to increase the CO_2 capture capacity.

The work in this thesis, however, is not solely confined to the consideration of alkaline metal oxide materials. The interaction of water with uranium oxide surfaces is also studied. Therefore the remaining sections of this chapter will focus on the motivation and relevant work concerning this material.

1.3 The Storage and Stability of Nuclear Materials

The early actinide oxides, namely the dioxides, AnO_2, have uses in a number of nuclear technologies, particularly those of thorium, uranium and plutonium. Due to this, a complete understanding of their reactivity is imperative for both their use and long-term storage. This is particularly important in terms of their stability. Spent nuclear fuels, for example, in the United States in the 1970s were placed in water storage. Following this, they were dried and placed in storage tanks containing a zirconium-based cladding. Following studies have indicated that water will often be present on both the fuel elements and cladding material, as detailed by Hedhili *et al*. [43]. Therefore, the interaction that occurs with water is important to characterise to fully evaluate what is occurring with these materials. In addition, an understanding of their reactivity and storage capabilities can help to further elucidate any environmental impacts these materials may have.

The work detailed in this thesis will focus solely on uranium dioxide. However, due to the presence of the localised *f*-electrons, accurate simulation is not always straightforward. Therefore, prior to considering relevant studies concerning the

reactivity of uranium dioxide with water, a review of key experimental and computational studies of its electronic and magnetic structure will be conducted.

1.3.1 Understanding the Structure and Properties of Uranium Dioxide

The crystalline oxide phases of uranium can exist with a variety of oxidation states and stoichiometries, where the variability in formal valence ranges from +3 to +6. The main structure types of uranium oxide are UO_2, U_4O_9, U_3O_8 and UO_3 [44].

Uranium (IV) dioxide is known to crystallise in a face centred cubic, fluorite-like structure. One consequence of this fluorite-type structure is the presence of octahedral holes in the structure, which allows for the addition of interstitial atoms, thus allowing the formation of hyperstoichiometric UO_{2+x}. The defect structure for UO_{2+x} was shown by Willis [45] using neutron diffraction, indicating that oxygen vacancies and interstitials tend to cluster together, with no change to the uranium sublattice. This gave rise to the 2:2:2 structure, containing two oxygen vacancies, two interstitials displaced from the octahedral site along the <111> and two interstitials displaced from the octahedral site along the <110>. A number of simulation studies have modelled the defect properties of UO_2. Most notable is that of Catlow [46], using potential-based methods to consider defect formation energies, migration activation energies and defect clustering. Other significant work on defective UO_2 includes potential-based studies by Jackson *et al*. [47], as well as DFT-based simulations by Gupta *et al*. [48] and Nerikar *et al*. [49].

For the stoichiometric oxide, the band structure has been considered and elucidated using both experimental and computational studies. The valence band structure was characterised using XPS by Veal *et al.* [50], with complementary work carried out by Baer and Schoenes [51] using a combined XPS/BIS approach to consider the complete band structure of UO_2. A complete review of the photoelectron spectra can be found in Naegele *et al*. [52].

In summary, the experimental results show that the top of the valence band structure is comprised of O 2*p* and U 5*f* bands. The splitting of occupied and unoccupied 5*f* bands across the band gap gives rise to UO_2 being a Mott insulator, where conduction is caused by *f-f* transitions. To further study this region at the top of the valence band, Wu *et al*. [53] used XANES to consider the nature of the O 2*p* band by considering adsorption at the O K edge in UO_2, along with the DFT-calculated density of states. Their results showed the presence of O 2*p* hybridisation with *d*- and *f*-orbitals, with additional crystal field splitting observed.

Computational studies have also modelled the band structure, through the generation of partial density of states, using a range of techniques. The majority of studies have used DFT techniques to simulate uranium dioxide [54], however, standard DFT methods are known to fail for these materials, for example, predicting UO_2 to be metallic [55, 56]. However, despite this Kudin *et al*. did find very good agreement with the experimental lattice constant and bulk modulus, suggesting that the strong correlation effects which give rise to the band gap do not significantly affect the bonding properties of UO_2. In an effort to generate the observed band gap in these materials, a number of researchers have used alternative DFT approaches, for example, the DFT+U method [57, 58], which adds an on-site correction to the actinide elements to increase the localisation of *f*-electrons, and hybrid-DFT [56, 59, 60], which include a certain amount of Hartee-Fock exchange. Both of these techniques have been found to reproduce the band gap of UO_2. The relative positions of bands seen in the partial density of states is shown in Figure 1.2, adapted from the results of Ryzhkov and Kupryazhkin [61]. As can be seen, the band gap is due to the splitting of the uranium 5*f* bands, with hybridisation occurring with oxygen 2*p* and uranium 6*d* bands. For full details, including the relative intensities of bands, see the published total and partial density of states by Ryzhkov and Kupryazhkin. The hybridisation of orbitals also gives rise to a certain degree of covalency in these materials, as shown by Kelly *et al*. [62], through the calculation of the band structure with values of ionicity of +2 and +4 on uranium. With the reduced ionicity providing results of the band structure more in line with experimental XPS data.

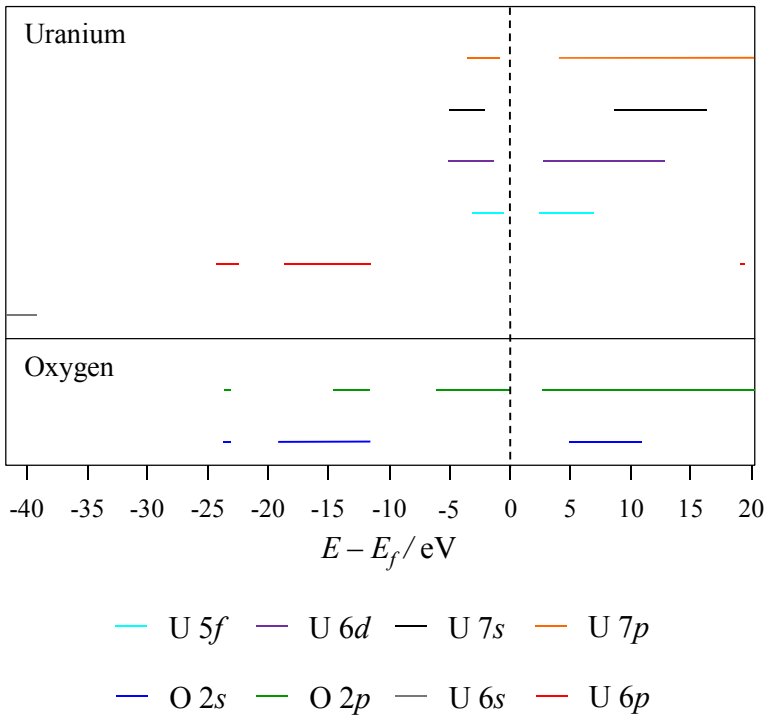

Figure 1.2: Schematic showing the relative positions of different orbital contributions seen in the calculated partial density of states for UO_2, adapted from the results of Ryzhkov and Kupryazhkin [61]. NOTE: the energy scale is adjusted so that 0eV represents the Fermi energy.

The presence of unpaired *f*-electrons in these materials also gives rise to the formation of different spin configurations and magnetic structures. The magnetic ordering of UO_2 was first established by Frazer *et al*. [63] in 1965 using neutron diffraction studies. Their results showed that at the Néel temperature of 30.8K UO_2 undergoes a transition from antiferromagnetic (AFM) to paramagnetic ordering, i.e. from an ordered structure of alternating spins to a disordered magnetic structure. Therefore, the magnetic structure consists of (001) ferromagnetic (FM) sheets stacked in an alternating fashion. Work by Faber and Lander [64] and Laskowski *et al*. [58] have also suggested a noncollinear magnetic structure from the observed oxygen displacement from the fluorite lattice positions and calculated electric field gradients, the change in the electric field at an atomic nucleus caused by the charge distribution and changes in position of other nuclei. However, a number of studies using a DFT+U [57, 59, 65] have approximated the AFM structure using a collinear

model, with spin-coupling effects neglected, and found good agreement with lattice energies, lattice parameters, band gaps and bulk physical properties indicating that this approximation is appropriate to use.

Following the work surrounding the bulk properties of the material, a number of surface studies have also been carried out using both experimental and computational approaches. These have not only assisted in characterising the low index surfaces of uranium dioxide, the central focus of this study, but also their interaction with water.

1.3.2 Uranium Dioxide Surfaces and their Interaction with Water

As the work in this thesis aims to consider the surface chemistry associated with water adsorption for the surfaces of UO_2, it is important to consider the work that has preceded it. These surfaces have been studied and characterised using both experimental and computational studies. Muggelberg *et al*. for example, used STM and LEED to study both the (100) [66] and (110) [67] UO_2 surfaces. Their results of the (100) termination indicate an oxygen-terminated surface with 50% surface vacancies, due to polar nature of this surface. The appearance of a maze-like topography was also seen, attributed to surface trenches formed from {111} facets. This surface faceting of the (100) UO_2 surface was also considered using computational methods by Tan *et al*. [68]. Their study considered the effects of different trench configurations on this surface, using atomistic modelling. The results concurred with that of Muggelberg *et al*. in that the formation of trenches on the surface indeed reduces the surface energy from that of the planar surface.

STM was also used to consider the (110) UO_{2+x} surface. The results suggest that the stoichiometric surface has a slightly defective surface, with rows of UO_2 missing in the $[1\ \bar{1}\ 0]$ direction. The addition of oxygen allowed them to consider the hyperstoichiometric surface. Oxygen insertion into a subsurface interstitial position resulted in the formation of uranium dimer structures, seen to occur in pairs on the

surface, which was believed to an electronic effect. A further type of oxygen superstructure was also seen on adsorption of molecular oxygen, with the oxygen adsorbate occupying surface interstitial positions. The formation of both of these structures appeared to be stable, as only a small amount of adsorbed oxygen was seen to move into the subsurface interstitial positions during annealing, with no observed diffusion into the bulk.

The morphology of UO_2 was studied experimentally by Castell [69]. He employed SEM to study the size and shape of microscopic voids in UO_2 single crystals. The aim of this was to consider the shape of the voids to gain information on the relative stabilities of the surfaces. This follows that the thermodynamic equilibrium shape of a crystal is directly related to the surface energies. In addition, the presence of trapped gas in the structure will form voids within the crystal, which will also exhibit the same thermodynamic morphology following extended annealing. The SEM results showed the morphology of the voids to be comprised of {111} and {100} surfaces. The {111} surface was seen to dominate giving rise to a truncated octahedron morphology, as shown in Figure 1.3.

In addition, the analysis of surface areas allowed Castell to predict a ratio for the surface energies, γ, of the two surfaces of $\gamma_{(001)} / \gamma_{(111)} = 1.42 \pm 0.05$. The benefit of this is that it allows a direct comparison to computational studies. However, many surface studies using simulation methods find a $\gamma_{(001)} / \gamma_{(111)}$ ratio greater than reported by Castell. For example, the Catlow [46] and Busker [70] potentials give ratios of 1.91 and 2.08, respectively. However, it was suggested that this discrepancy may be a result of the surface faceting observed experimentally by Muggelberg *et al*. The results of Tan *et al*. do indeed give closer agreement for the surface energy ratio to 1.67 and 1.85, for the Catlow and Busker potentials, respectively, as a result of surface faceting. However, despite this reduction, the predicted morphologies are still comprised solely of the {111}. Tan *et al*., however, did suggest that a further reduction in {100} surface energy may be a result of surface hydroxylation which would act to further stabilise this surface.

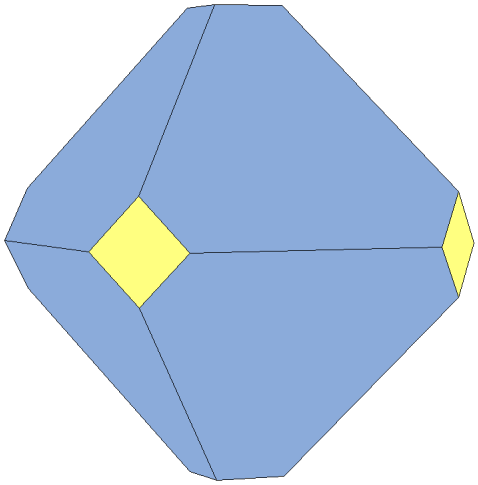

Figure 1.3: Schematic showing the truncated octahedron Wulff shape of UO_2 determined using the ratio of $\gamma_{(001)}$ / $\gamma_{(111)}$ reported by Castell [69]. {100} and {111} surfaces are coloured yellow and blue, respectively.

Experimental methods have been used to consider the interaction of water with UO_2 surfaces. The surface hydroxylation of the (001) surface of UO_2 has be studied experimentally by Hedhili *et al*. [43] using a combination of XPS and LEIS techniques with $D_2{}^{18}O$. The results of the study by Hedhili *et al*. concluded that water is completely dissociated on the (001) UO_2 surface. This is seen by incorporation of ^{18}O into the surface, with no evidence of OD formation after water exposure. The adsorption of water on this surface has also been considered using TPD by Stultz *et al*. [71] using both stoichiometric and defective surfaces. The adsorption of water on these surfaces was assessed through studying H_2 desorption, used as an indicator of complete water dissociation. Their results, however, suggested that on pristine, well-annealed (100) surface no dissociation is observed, whereas significant dissociation is seen on the oxygen deficient Ar^+ sputtered surface. A similar study was also conducted on the (111) surface by Senanayake and Idriss [72], again using stoichiometric and defective surfaces. Their results showed similar results as those of Stultz *et al*. where the clean surface showed no water dissociation but a significant amount on the reduced surface.

The interaction of water with UO_2 surfaces has also been studied using electronic structure calculation by both Hay [73] and Skomurski *et al*. [74]. The study by Hay considered the adsorption of a single water molecule, in both a hydrated and hydroxylated manner, on the {110} and {111} surfaces of UO_2 using a plane-wave DFT approach. With his results indicating that hydroxylation is favoured on the both the surfaces. The work of Skomurski *et al*. then continued this by again modelling the adsorption of a single water molecule on the {111} surface, but also by considering the monolayer coverage, as well as the electronic effects of both processes. However, for the adsorption of a single molecule of water their results differed slightly, with hydrated water being favoured over hydroxylated. This change was attributed to the difference in computational methods. Although both used similar simulation techniques, Hay used slabs with water added to one side and the bottom layers of the UO_2 slab held fixed to mimic the underlying slab, whereas Skomurski *et al*. used a model which fully relaxed, with adsorption on both sides. However, their analyses of the through-slab and between slab interactions were found to have a negligible contribution. For monolayer coverage, decreased adsorption energies were seen whilst still pertaining to the same trend. Consideration of the electronic effects found that for both hydration and hydroxylation there is no significant sharing of electron density between the UO_2 slab and water, indicating that the attractive interaction is mainly electrostatic in nature, with some further stabilisation provided by hydrogen bonding. However, the polar nature of the water and hydroxide species does caused some repulsion to the electron density causing a slight increase in the charge of the uranium atoms involved in the adsorption.

The hydroxylation of UO_2 surfaces has also been considered using potential-based methods, most notably by Abramowski *et al*. [75] and Tan *et al*. [76]. Both studies showed similar results, which indicated that the {100}, {110} and {111} surfaces are favourable to hydroxylation, with increased coverage leading to reduced surface energies. In addition, the {100} surface changes its order of stability from least stable when dry to most stable when hydroxylated. Further to the work of

Abramowski *et al*., Tan *et al*. also considered hydroxylation of a faceted {100} surface. They found that at 50% coverage, hydroxylation of the trench structure gave rise to a more stable energy than the planar {100} surface. However, at monolayer coverage, the planar surface dominates.

The next section will further summarise the previous work carried out in the subject areas concerning the work in this thesis, using them to state the aims of this work to produce results which will not only add to the current knowledge base but also be of chemical significance.

1.4 Conclusions and Aims of Thesis

In light of the previous work on these subject areas, further investigation is clearly required for a more complete understanding of these systems. The simple metal oxides show that for water adsorption, well-ordered surfaces, such as the {100} surface, will preferentially undergo adsorption of molecular adsorption rather than dissociated water. However, the dissociation of water is much more favourable on defective or rougher surfaces, in particular for the polar {111} termination. In terms of carbonation, studies have suggested that carbon dioxide is indeed favourable with the adsorption modes giving rise to monodentate adsorption on CaO (100) surfaces but a mixture of mono- and bidentate on MgO (100) surfaces. However, there has been no significant study of the effect the co-adsorption of water has on surface carbonation. The fact that brucite surfaces need a necessary dehydroxylation process prior to carbonation suggests that surface hydroxylation will indeed limit the carbonation potential. However, the interactions between these species have not been considered. Therefore the main aims of this work on these materials will include:

- Quantitative understanding of the effect of water co-adsorption on the surface carbonation, as well as variation of the partial pressures of the two adsorbates.

- Investigate the interactions of carbonate with liquid water at the mineral – water interface, with focus on the effect this plays on the structure and mobility of water.
- Examining the differences between continuous surface and nanoparticulate systems with respect to surface hydroxylation and carbonation.

In terms of the uranium dioxide, previous studies of bulk UO_2 have shown that despite the difficulties of modelling UO_2 with DFT, the band structure can be corrected predicted using a DFT+U methodology. However, there has been little work on considering the distribution of charge and spin density for this material. In addition, there has been little computational simulation on thin film structures of UO_2, with previous studies focussing on simulating the bulk and surface structures. Studies of the surfaces and their interaction with water show that the surface hydroxylation can impact both the surface energy and resulting equilibrium morphology. However, studies have mainly only considered the dissociative adsorption of gaseous water, with little consideration of either the associative adsorption, or the interaction of UO_2 with liquid water. Therefore, in this work the general aims will include the initial addressing of:

- Modelling the structure and stability of low index UO_2 thin film structures
- Estimate point defect energies and the non-stoichiometry behaviour to assess the oxygen segregation.
- Study the interactions of both associative and dissociative water adsorption on surface stability, including the effect of varying surface coverages.
- Evaluate the interactions between UO_2 surfaces and liquid water to characterise this interface, allowing the consideration of reaction sites.

Prior to the discussion of the main results of this study, the description of the computational methods used is required. This will be the focus of the next two chapters. Chapter two will discuss different methods of calculating the forces which act between atoms in a system, thus allowing the calculation of energies. Chapter

three, however, will describe the computational techniques which can then utilise this information to find lowest energy structures, as well as calculating dynamical and surface properties.

Chapter Two

The Calculation of Forces

The successful modelling of any chemical system relies upon the modelling of the forces and interactions between atoms. The correct description of these forces is crucial for accurately modelling any system. Two distinct simulation approaches can be used to model these interactions; each containing a certain number of assumptions to allow a trade off to be made between accuracy and simulation time.

The different methods can be broadly separated into two main approaches: quantum mechanical and classical methods. Classical, or potential-based, methods do not model electrons explicitly and consider only the attractive and repulsive interactions between atoms, using parameterised equations. Thus these methods can

calculate the interaction energy rapidly but suffer from not allowing for electronic redistribution. Quantum mechanical, also known as electronic structure or *ab-initio*, methods model the electron wave functions themselves, using approximations to effectively solve the many-bodied Schrödinger equation directly. However, these are still not at the stage of guaranteed accuracy because they do not yet incorporate all electronic contributions. They can also be very computationally expensive. The work in this study employs both techniques and thus the background and theory to these techniques is the main concern of this chapter.

2.1 Quantum Mechanical Techniques

Quantum mechanical methods aim to describe a chemical system accurately by solving the many-bodied Schrödinger equation at some level of approximation. The time-independent form of the Schrödinger equation is shown by Equation 2.1 below:

$$\hat{H}\Psi = E\Psi \qquad 2.1$$

where $\hat{H}$ is the Hamiltonian operator corresponding to E being the total energy of the system and Ψ is the electron wave function. The Hamiltonian itself contains the operators for the kinetic and potential energy of the system for both the nuclei and electrons and can be expressed in these terms, as described by Equation 2.2.

$$\hat{H} = \hat{T}_n + \hat{T}_e + \hat{V}_{nn} + \hat{V}_{ee} + \hat{V}_{ne} \qquad 2.2$$

where $\hat{T}_n$ and $\hat{V}_{nn}$ are the kinetic and potential nuclear operators, $\hat{T}_e$ and $\hat{V}_{ee}$ the equivalent operators for the electrons and $\hat{V}_{ne}$ is the nuclear – electron interaction. For simulation codes, the problem is that the Schrödinger equation can only be solved accurately for single-electron systems. It is not feasible to solve for a many-bodied system as the complete wave function cannot easily be decoupled into a set

of independent equations because of the $\hat{V}_{ee}$ term. Therefore, a series of approximations need to be employed to allow it to be used.

The $\hat{V}_{nn}$ term is often removed and the energy calculated, E, is simply the electronic energy of the system. Therefore, if W is defined as the total energy:

$$W = E + \hat{V}_{nn} \qquad 2.3$$

However, it is immaterial whether one solves the Schrödinger equation for E and then adds $\hat{V}_{nn}$ afterwards, or includes $\hat{V}_{nn}$ in the definition of $\hat{H}$.

The Born-Oppenheimer approximation is often used for electronic structure methods, allowing the nuclear and electronic degrees of freedom to be decoupled. Electrons are both faster and lighter than the nuclei; therefore the electronic wave functions depend upon the nuclear positions but not their velocities. This allows the nuclei to be described classically as fixed charges, becoming part of the external potential. Therefore, the Hamiltonian becomes:

$$\hat{H} = \hat{T}_e + \upsilon_{ext}\left(\{\mathbf{R}_i\}\right) + \hat{V}_{ee} \qquad 2.4$$

This considers a system of N electrons in an external potential, υ_{ext}, imposed by the nuclear positions, $\mathbf{R}_i$.

2.1.1 Density Functional Theory

Density functional theory (DFT) is one of the various electronic structure methods and allows the N-electron wave function and its associated Schrödinger equation to be replaced by the simpler electron density and its associated calculational scheme. A major innovation in modern-day DFT was by the work by Hohenberg and Kohn

[77], which legitimised both the use of electron density, $\rho(\mathbf{r})$ as a basic variable and that the ground state density minimises the total electronic energy of the system.

Their theorems state that the external potential is determined, within a trivial additive constant, by the electron density. As $\rho(\mathbf{r})$ determines the number of electrons, it follows that $\rho(\mathbf{r})$ also determines the ground state wave function and all other electronic properties of the system, for example, the kinetic energy $T[\rho]$, potential energy $V[\rho]$ and the total energy $E[\rho]$. A full proof of these theorems can be found in Parr and Yang (1994) [78]. The energy can therefore be rewritten as:

$$E[\rho] = \int \rho(\mathbf{r}) \upsilon_{ext}(\mathbf{r}) d\mathbf{r} + F_{HK}[\rho] \qquad 2.5$$

where the first term arises from the interaction between the electron density and the external potential, typically the Coulombic interaction with the nuclei, and the second term is the sum of kinetic energy of the electrons and the contribution to the energy from inter-electronic interactions. $F_{HK}[\rho]$ can be further broken down by Equation 2.6:

$$F_{HK}[\rho] = T[\rho] + J[\rho] + \text{non-classical term} \qquad 2.6$$

where $J[\rho]$ is the classical electron-electron Coulombic energy and the non-classical term becomes the part of the exchange-correlation factor.

Assuming differentiability of $E[\rho]$, the variational principle requires that the ground state density satisfies the stationary principle:

$$\frac{d}{d\rho(\mathbf{r})}\left[E[\rho(\mathbf{r})] - \mu \int \rho(\mathbf{r}) d\mathbf{r}\right] = 0 \qquad 2.7$$

This gives the Euler-Lagrange equation, shown by Equation 2.8, which can be considered as the working equation of DFT.

$$\mu = \left(\frac{dE[\rho]}{d\rho(\mathbf{r})} \right)_{\upsilon_{ext}} = \upsilon_{ext}(\mathbf{r}) + \frac{dF_{HK}[\rho]}{d\rho(\mathbf{r})} \qquad 2.8$$

where μ is the chemical potential of an electron cloud for its nuclei. It can be seen, from Equation 2.8 that if we know the exact $F_{HK}[\rho]$ then we would have an exact equation for the ground state electron density, as $F_{HK}[\rho]$ is defined independently of the external potential and is a universal functional of $\rho(\mathbf{r})$. However, $F_{HK}[\rho]$ is difficult to find in an explicit form, making accurate implementations of Equation 2.8 hard to achieve.

This problem was overcome by Kohn and Sham [79], who proposed that if orbitals were introduced, then the kinetic energy could be calculated reasonably accurately, with only a small residual correction required, which could be handled independently. The approach by Kohn and Sham represents a mapping of the interacting many-electron system onto a system of non-interacting electrons moving in an effective potential, υ_{eff}, due to all the other electrons.

The Kohn-Sham theorem states that the chemical potential, in terms of the kinetic energy of a non-interacting electron, T_{NI}, is:

$$\mu = \upsilon_{eff}(\mathbf{r}) + \frac{dT_{NI}[\rho]}{d\rho(\mathbf{r})} \qquad 2.9$$

where the Kohn-Sham effective potential is defined by:

$$\upsilon_{eff}(\mathbf{r}) = \upsilon_{ext}(\mathbf{r}) + \frac{dJ[\rho]}{d\rho(\mathbf{r})} + \frac{dE_{XC}[\rho]}{d\rho(\mathbf{r})} \qquad 2.10$$

where $E_{XC}[\rho]$ is the exchange-correlation energy. Therefore, for a given $\upsilon_{eff}(\mathbf{r})$, the $\rho(\mathbf{r})$ which satisfies Equation 2.9 can be obtained simply by solving the N one electron equations:

$$\rho(\mathbf{r}) = \sum_{i}^{N} \left|\phi_i(\mathbf{r})\right|^2 \qquad 2.11$$

where ϕ_i is the orbital of a non-interacting electron i. However, as $\upsilon_{eff}(\mathbf{r})$ is dependant on $\rho(\mathbf{r})$, this must be solved iteratively. This is done using the so-called self consistent loop, summarised in Figure 2.1.

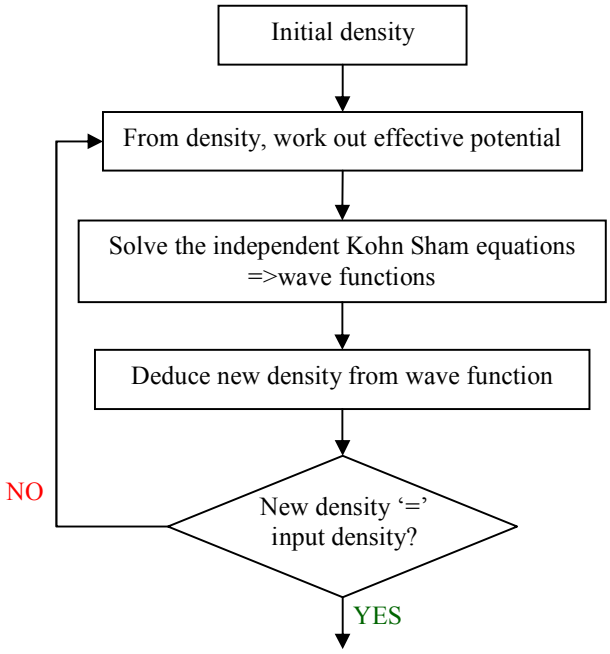

Figure 2.1: Schematic representation of the self-consistent loop, as used in DFT calculations.

Using the self-consistent loop, the energy can then be calculated directly from Equation 2.5, replacing $F_{HK}[\rho]$ with $F[\rho]$, according to:

$$F[\rho] = T_{NI}[\rho] + J[\rho] + E_{XC}[\rho] \qquad 2.12$$

2.1.2 Approximating the Exchange-Correlation Functional

The only component that is now required is the exchange-correlation functional, $E_{XC}[\rho]$. Unfortunately, exact functionals for exchange and correlation are only known for the free electron gas. However, a number of different ways to approximate this functional are used and are known to allow the calculation of reasonably accurate physical properties.

The simplest form of approximating the exchange-correlation functional is the Local Density Approximation (LDA). The LDA assumes that the exchange-correlation energy depends solely on the local electron density where the functional is evaluated:

$$E_{XC}^{LDA}[\rho] = \int \rho(\mathbf{r})\varepsilon_{XC}[\rho(\mathbf{r})]d\mathbf{r} \qquad 2.13$$

where ε_{XC} is the exchange-correlation energy for a homogeneous electron gas of density $\rho(\mathbf{r})$. The main drawback of this method is that it relies upon $\rho(\mathbf{r})$ varying slowly. For strongly correlated systems, such as semiconductors and metallic systems, however, this is not the case and therefore the LDA becomes inadequate, and is calculated to overbind.

An alternative to this method is the Generalised Gradient Approximation (GGA), which includes gradient corrections. The exchange-correlation energy in the GGA depends not only on the electron at the reference point but also on the gradient of the electron density ($\nabla\rho(\mathbf{r})$), as shown by Equation 2.14:

$$E_{XC}^{GGA}[\rho] = \int \rho(\mathbf{r})\varepsilon_{XC}^{GGA}[\rho(\mathbf{r})]d\mathbf{r} + \int F_{XC}[\rho(\mathbf{r}), \nabla\rho(\mathbf{r})]d\mathbf{r} \qquad 2.14$$

where F_{XC} is a correction chosen to satisfy one or several known limits for E_{XC}. There is no clear method by which F_{XC} can be chosen, therefore, several different

functionals have been proposed, for example, the GGA method suggested by Perdew and Wang [80] (PW91), and the simplified PBE functional suggested by Perdew, Burke and Ernzerhof [81, 82].

2.1.3 DFT+U Methodologies

One drawback with the way DFT is implemented is that it can often fail to describe systems with localised (strongly correlated) *d*- and *f*-electrons. This is an error caused by the use of a fractional number of electrons on the atoms, causing a self interaction error which artificially favours delocalised states. This causes particular problems for strongly correlated systems. One method often used to overcome this introduces a strong intra-atomic attraction in a (screened) Hartree-Fock manner as an on-site replacement to the DFT functional. This method is commonly referred to as the DFT+U method, where the U represents the on-site replacement. One method of invoking this +U correction is to use the approach suggested by Dudarev *et al.* [83]. This states that:

$$E_{DFT+U} = E_{DFT} + \frac{U-J}{2}\sum_{m\sigma}\left(n_{m\sigma} - n_{m\sigma}^2\right) \qquad 2.15$$

where $n_{m\sigma}$ gives the number of electrons occupying an orbital with magnetic quantum number m and spin σ at a particular site. The +U is determined by adjustment of two parameters: U is the effective on-site Coulomb parameter and J is the effective on-site exchange. Using the Dudarev *et al.* method, the explicit values of U and J are unimportant, it is only the difference between them that is of use. The value of the +U correction can be fitted against experimental data, such as structural data, band gap data or energy differences between defect states. Full details, including derivation, of this method can be found in the work of Dudarev *et al*.

2.1.4 The Practical Use of DFT

The use of DFT requires a number of other factors to be defined. These include the method of representing atomic orbitals and electrons in the system as well as the problem of having to calculate the wave functions for an infinite number of electrons when using periodic boundary conditions.

To further increase the realism of the calculation, periodic boundary conditions are applied, effectively reproducing the unit cell in three-dimensions by surrounding the cell with images of itself. The particles in each box move identically, thus enabling the approximate simulation of a larger system than the computational power would ordinarily permit. This is further illustrated in Figure 2.2, where the central blue box is the actual cell. The application of boundary conditions also ensures efficient convergence of the Coulombic interactions.

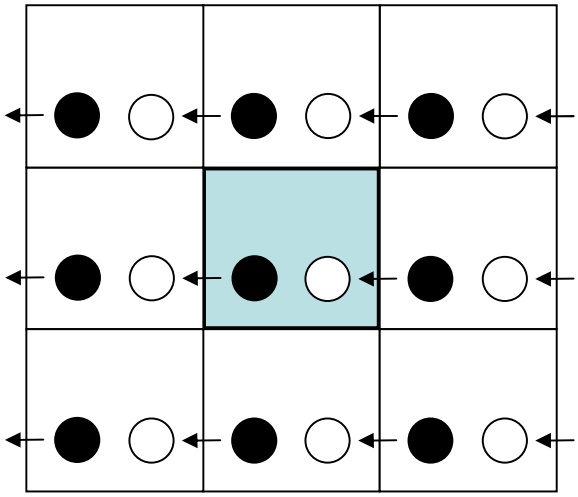

Figure 2.2: An illustration of periodic boundary conditions.

The problem that comes from using periodic boundary conditions is that a wave function must be calculated for each of the infinite number of electrons in the system. This is obviously impossible, so a combination of methods is used to overcome this problem.

The wave functions themselves are modelled using a combined plane wave basis set and pseudopotentials. A plane wave is defined as a constant-frequency wave whose wavefronts are infinite parallel planes at constant amplitude normal to the phase velocity vector. The plane waves are used in accordance with Bloch's theorem, which states that the electronic wave function at each k-point can be expanded in terms of a discrete plane wave basis set. The infinite plane wave basis set can also be truncated to include only the plane waves which have kinetic energies less than some particular energy. This energy is fixed by increasing the value until convergence is found, thus producing a finite basis set.

The main disadvantage of the plane wave basis set is in its inefficiency, in that the number of basis functions needed to describe atomic wave functions near to the nucleus would be prohibitive. However, by assuming that only the valence electrons determine the physical properties of the system; pseudopotentials can be used to represent the potentials of the ionic cores. This therefore removes the core electrons and replaces them and the strong ionic potentials by a weaker pseudopotential that acts on a set of pseudo wave functions rather than the true valence wave functions. This leads to smoother functions, and hence fewer plane waves are needed. In addition, projector augmented-wave (PAW) pseudopotentials have been used, which are known to be more accurate due to the smaller radial cutoffs used. For full details of PAW pseudopotentials see Blöchl [84] and Kresse and Joubert [85]. An important advantage of plane wave basis sets over localised basis sets is that they do not have basis set superposition error. This error occurs with localised basis sets due to the mixing of functions at short range, which are then compared to unmixed long-range energies; therefore the system can undergo unphysical electronic relaxations.

The boundary conditions effectively provide an infinite number of electrons which is accounted for by an infinite number of k points, where only a finite number of electronic states are occupied at each k point. The occupied states at each k point contribute to the electronic potential of the system so that, in principle, an infinite number of calculations are needed to compute this potential. However, the electronic

wave functions at k points which are very close together will also be identical. Therefore it is possible to represent the electronic wave functions over a region of k space by the wave functions at a single k point. In this case, the electronic states at only a finite number of k points are required to calculate the electronic potential and hence determine the total energy of the system. The computed energy will therefore converge as the density of k points increase, where the density of allowed k points is proportional to the volume of the solid.

For a periodic system, the k points which are present in the wave function belong to the first Brillouin zone, which is a uniquely defined primitive cell of the reciprocal lattice. In a system which uses Bloch, or plane, waves, it is found that the solution to all waves can be completely characterised by their behaviour in a single Brillouin zone. Therefore, all that is required is to select the grid of k points which is to be used when sampling the system. The k point scheme used in this work is that proposed by Monkhorst and Pack [86], in which the k points are distributed homogeneously in the Brillouin zone, according to Equation 2.16.

$$\mathbf{k} = x_1\mathbf{b}_1 + x_2\mathbf{b}_2 + x_3\mathbf{b}_3 \qquad 2.16$$

where $\mathbf{b}_1$, $\mathbf{b}_2$ and $\mathbf{b}_3$ are the reciprocal lattice vectors and

$$x_i = \frac{l}{n_i} \qquad l = 1,...,n_i \qquad 2.17$$

where the density of the k point grid is defined by the folding parameters, n_i. For conducting materials, such as metals and semiconductors, a finely spaced grid is required, i.e. where the folding parameters are large. However, insulating materials can be appropriately calculated with a wider spaced grid, where n_i is small. By default, the grid is centred on the centre of the reciprocal lattice, the Γ point. The grid can also be shifted according to the symmetry of the simulation cell. However, for all calculations discussed herein, the k point grid is Γ-centred, but to ensure an

accurate calculation it is important to carry out a convergence test to select the correct density of the grid, where the folding parameters are increased until convergence is achieved.

The parameters used in this study for the different DFT calculations will be given alongside the results of the simulation, along with any relevant convergence tests to determine which cut-offs and parameters to use. Although DFT has proven to be very reliable, it is very computationally expensive and thus an alternative strategy can be considered using potential models.

2.2 Potential Methods

Potential-based methods do not consider electrons explicitly but instead model the attractions and repulsions between atoms in the simulation cell by parameterised analytical functions. This therefore allows them to be considerably quicker than DFT methods, allowing for the study of much larger systems. The approach used in this thesis is based upon the Born Model of Solids (1954) [87]. This assumes that the lattice energy, *U*, can be calculated from the sum of all pair wise interactions between atoms *i* and *j*, and can be expanded to include many-body terms as shown by Equation 2.18:

$$U_{ij} = \sum_{ij} \frac{q_i q_j}{r_{ij}} + \sum_{ij} \Phi_{ij}(r_{ij}) + \sum_{ijk} \Phi_{ijk}(r_{ijk}) + \ldots \qquad 2.18$$

The first component defines the long-range electrostatic interactions, whereas the second and third terms define the short-range two-body and three-bodied interactions, respectively. The remaining sections of this chapter will be concerned with defining the equations and the parameterisation of these long- and short-range interactions, how they are fitted to ensure accuracy and, finally, the potential parameters used in this work.

2.2.1 Long-Range Interactions

The long-range Coulombic interactions account for approximately 80% of all the interactions within a simulation. When two atoms are brought together from infinity, to their lattice sites, the electrostatic contribution to U is released. The potential of the long-range interactions over an infinite lattice therefore takes the form of Equation 2.19:

$$\varphi = \frac{1}{2}\sum_{|n|=0}^{\infty}{}'\sum_{i=1}^{N}\sum_{i=j}^{N}\frac{q_i q_j}{4\pi\varepsilon_0\left|r_{ij}+n\lambda\right|} \qquad 2.19$$

where, q is the charge, ε_0 is the permittivity of a vacuum, r_{ij} is the inter-ion separation, ℓ is the set of lattice vectors representing the periodicity of the crystal lattice and n is a integer used to generate the periodic images of the simulation cell. The prime on the first summation indicates that $i=j$ is ignored for n=0. Despite the simple appearance of Equation 2.19, it convergences slowly with r, due to the $1/r$ term, and is therefore unsuitable for use in atomistic simulation. To make it useable, alternative summations by Ewald (1921) [88] and Parry (1975, 1976) [89, 90] are often applied.

2.2.1.1 Ewald Summation

The Ewald summation uses mathematical transformations to calculate the Coulombic component for a three-dimensional periodic system. Working from a periodic system of mutually interacting point ions via the Coulomb potential, this method divides the potential into three separate parts, which converge more quickly than the original expression. These comprise of a term in reciprocal space, φ_1, a real space term, φ_2, and a self-interaction term, φ_3, where:

$$\varphi = \varphi_1 + \varphi_2 + \varphi_3 \qquad 2.20$$

This method starts by effectively neutralising the long range interaction by surrounding each particle i, of charge q_i, by a spherically symmetric charge distribution of opposite sign, which cancels q_i, shown schematically in Figure 2.3(a). A Gaussian charge distribution of the following form is commonly used:

$$\rho_i(r) = \frac{q_i \alpha^3}{\pi^{3/2}} \exp\left(-\alpha^2 r^2\right) \qquad 2.21$$

where the width of the Gaussian function is controlled by the arbitrary parameter α, and r is the position relative to the centre of the distribution. These screened charges rapidly converge to zero at long-distances and are therefore short-ranged. This allows the electrostatic interactions between screened charges, φ_2, to be determined by direct summation in real space:

$$\varphi_2 = \frac{1}{2} \sum_{i=1}^{N} \sum_{i=1}^{N} \sum_{|\mathbf{n}|=0}^{\infty}{}' \frac{q_i q_j}{4\pi\varepsilon_0} \frac{erfc\left(\alpha \left|\mathbf{r}_{ij} + \mathbf{n}\right|\right)}{\left|\mathbf{r}_{ij} + \mathbf{n}\right|} \qquad 2.22$$

where *erfc* is the complementary error function, defined by:

$$erfc(x) = \frac{2}{\sqrt{\pi}} \int_x^{\infty} \exp\left(-t^2\right) dt \qquad 2.23$$

The rate of convergence of Equation 2.22 is dependent on the width of the cancelling Gaussian distributions, defined by α; the wider the Gaussians, the faster the series converges, as Equation 2.23 tends to zero with increasing x.

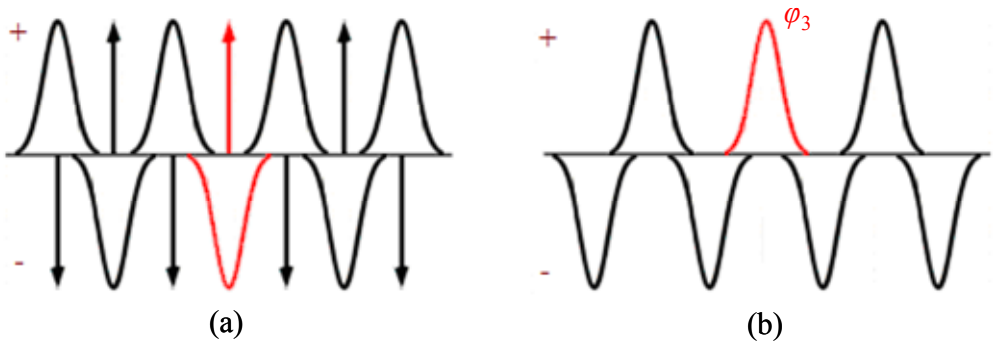

Figure 2.3: Schematic showing charge distribution as used in **(a)** the calculation of φ_2 in real space, where the charge distribution at $i = j$ is ignored, as shown in red; and **(b)** the calculation of φ_1 in reciprocal space, where the Gaussian representing the self-interaction component, φ_3 is shown in red.

However, the quantity that is required is the electrostatic interaction of the fraction of q_i which is not screened. Therefore, a second Gaussian charge distribution is added to the system, which is of the same sign as q_i, shown schematically in Figure 2.3(b). The contributions of this set of charge distributions to the electrostatic potential, φ_1, are calculated by summing their Fourier transforms in reciprocal space, full details of which can be found in Kittel (1963) [91]:

$$\varphi_1 = \frac{1}{2}\sum_{k\neq 0}\sum_{i=1}^{N}\sum_{j=1}^{N}\frac{1}{\pi\lambda^3}\frac{q_i q_j}{4\pi\varepsilon_0}\frac{4\pi^2}{k^2}\exp\left(-\frac{k^2}{4\alpha^2}\right)\cos\left(\mathbf{k}\cdot\mathbf{r}_{ij}\right) \qquad 2.24$$

where the vectors **k** are given by $\mathbf{k} = 2\pi\mathbf{n}/\ell$. It should be noted that this expression ignores the term when $k = 0$, which can be neglected provided the net charge on the unit cell is zero. Although this summation also converges more quickly than the original point charge sum, the number of terms that need to be included increases with the width of the Gaussians. Therefore, there is a trade-off between having a small α for φ_1 but a large enough value for φ_2.

The φ_1 summation includes the interaction between the continuous Gaussian charge cloud of charge q_i with itself. This self-interacting component, φ_3, therefore needs to be subtracted. This term is defined by Equation 2.25.

$$\varphi_3 = -\frac{\alpha}{\sqrt{\pi}} \sum_{k=1}^{N} \frac{q_k^2}{4\pi\varepsilon_0} \qquad 2.25$$

The three components of the electrostatic interaction can then be summed to give the overall Coulombic interaction. The usefulness of this approach is that the overall convergence can be controlled by α but as the Gaussian components cancel out; the actual interaction energy itself is independent of α.

2.2.1.2 Parry Summation

The Ewald summation method is used in systems with three-dimensional periodicity. The Parry summation, an adaption of the Ewald method, allows the calculation of the Coulombic forces for a system with two-dimensional periodicity, i.e., a surface. The Parry method considers the crystal to consist of a series of charged planes of infinite size rather than an infinite lattice. When summing the electrostatic interactions, the vectors must now be split into in-plane vectors and vectors that are perpendicular to the plane. Therefore, it can no longer be assumed that the sum of the charges on the plane equal zero, as they do in the three-dimensional cell. So, unlike the Ewald method, the term involving the reciprocal lattice vector, $k = 0$, must be evaluated. A detailed derivation of the Parry summation is given by Heyes *et al*. [92].

2.2.2 Short-Range Interactions

The short-range forces that interact between the atoms in a system are described using simple parameterised analytical functions, consisting of repulsive and attractive terms. At very short distances the proximity of electron clouds between

two species will cause the repulsive forces to dominate the interaction. However, as the species are separated, attractive van der Waals forces become more significant. When modelling covalent interactions, many-bodied interactions add a further complication in that others terms, such as bond bending and angles, as well as torsional terms, need to be considered.

There are a number of different potentials which can be used to describe these short-range forces. However, the accuracy and reliability of any model depends on the correct values of the parameters themselves, which can be fitted to experimental data or *ab-initio* calculations. The short-range potentials which have been used in this study will now be described.

2.2.2.1 The Lennard-Jones (12,6) Potential

The Lennard-Jones (12,6) approximation is often used for non-bonding interactions in covalent molecules and takes the following form:

$$U(r_{ij}) = \frac{A_{ij}}{r_{ij}^{12}} - \frac{B_{ij}}{r_{ij}^{6}} \qquad 2.26$$

The first term describes the repulsive forces, which are dependent on r^{-12} and are therefore dominant at very short range. The second term describes the attractive interactions which dominate the interaction at longer separations. The r^{-6} term describes the van der Waals dispersion forces caused by instantaneous dipole-dipole interactions. The definition of the adjustable parameters, A_{ij} and B_{ij}, are shown by Equations 2.27 and 2.28, respectively.

$$A_{ij} = \varepsilon_{ij} r_{m_{ij}}^{12} \qquad 2.27$$

$$B_{ij} = 2\varepsilon_{ij} r_{m_{ij}}^{6} \qquad 2.28$$

where ε_{ij} is the depth of the potential energy well and $r_{m_{ij}}$ is the value of r at the minimum of the energy well. The relationships between these terms for an arbitrary potential curve are shown schematically in Figure 2.4. The A_{ij} and B_{ij} parameters are species dependent and can be fitted to the physical properties of the material.

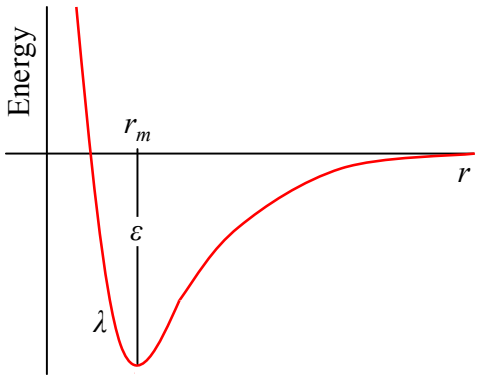

Figure 2.4: Schematic showing the relationship between the parameters used in the interatomic potentials for an arbitrary potential energy curve.

2.2.2.2 The Buckingham Potential

The Buckingham potential is closely related to the Lennard-Jones potential, except the repulsive term is replaced by a Born-Mayer expression:

$$U(r_{ij}) = A_{ij} e^{\left(-r_{ij}/\rho_{ij}\right)} - \frac{C_{ij}}{r_{ij}^6} \qquad 2.29$$

where A_{ij} and ρ_{ij} are often considered as relating to ion size and hardness, respectively. The hardness parameter defines the radial shape of the ion wave functions and hence the rate at which repulsion falls off with separation. The A_{ij} term controls the amplitude of the repulsion at a given separation and is primarily dominated by the ionic radii. The Buckingham potential can also be written in terms of the potential curve, as shown by Equation 2.30.

$$U(r_{ij}) = \varepsilon_{ij}\left[\frac{6}{\lambda_{ij}-6}e^{\lambda_{ij}\left(1-r_{ij}/r_{m_{ij}}\right)} - \frac{\lambda_{ij}}{\lambda_{ij}-6}\left(\frac{r_{m_{ij}}}{r_{ij}}\right)^6\right] \qquad 2.30$$

where λ_{ij} is related to the steepness of the exponential, shown in Figure 2.4. In this case, the adjustable parameters A_{ij}, ρ_{ij} and C_{ij} can be represented by Equations 2.31-2.33, respectively.

$$A_{ij} = \frac{6\varepsilon_{ij}}{\lambda_{ij}-6}\cdot e^{\lambda_{ij}} \qquad 2.31$$

$$\rho_{ij} = r_{m_{ij}} \Big/ \lambda_{ij} \qquad 2.32$$

$$C_{ij} = \frac{\varepsilon_{ij}\lambda_{ij}}{\lambda_{ij}-6} r_{m_{ij}}^6 \qquad 2.33$$

The Buckingham potential has a more flexible repulsive term than the Lennard-Jones potential and it is therefore more widely used in the simulation of polar solids where the repulsive terms are more significant.

2.2.2.3 The Morse Potential

The Morse potential is used to model covalently bonded interactions where separations vary significantly from the equilibrium distance, such as atoms in molecular ions:

$$U(r_{ij}) = \varepsilon_{ij}\left(1 - e^{-B_{ij}\left[r_{ij}-r_{m_{ij}}\right]}\right)^2 - \varepsilon_{ij} \qquad 2.34$$

where B_{ij} is related to the curvature of the slope of the potential energy well and is defined by Equation 2.35.

$$B_{ij} = \omega\sqrt{\mu / 2\varepsilon_{ij}} \qquad 2.35$$

where μ is the reduced mass and ω is the frequency of the bond vibration, which is related to the stretching constant of the bond, k, by $\omega = \sqrt{k / \mu}$.

It should be noted that the depth of the potential well, or bond dissociation energy, is subtracted in the Morse potential so that at infinite separation the interaction energy becomes zero. This potential can also be modified to permit a Morse function for nearest neighbour interactions with no Coulomb term, giving rise to the Coulomb subtracted Morse potential in Equation 2.36.

$$U(r_{ij}) = \varepsilon_{ij}\left(1 - e^{-B_{ij}\left[r_{ij} - r_{m_{ij}}\right]}\right)^2 - \varepsilon_{ij} - \frac{Dq_i q_j}{r_{ij}} \qquad 2.36$$

where D represents the percentage of Coulombic interaction to be subtracted. The Coulombic interactions between covalently bonded atoms are often partially or completely ignored as the Morse potential already contains the attractive component of the interaction between neighbours. The amount of Coulombic subtraction is fitted as to reproduce experimental data.

2.2.3 Many-Bodied Interactions

Covalently bonded molecules also require additional potentials to be applied to act as an energy penalty for deviations from the equilibrium values for bond and torsion angles. The three-body potential models deviations from the equilibrium bond angle as a result of bond-bending. Hence, it describes the directionality of the bonds and has a simple harmonic form:

$$U(\theta_{ijk}) = \tfrac{1}{2} k_{ijk}\left(\theta - \theta_0\right)^2 \qquad 2.37$$

where k_{ijk} is the harmonic force constant, θ is the bond angle and θ_0 is the equilibrium bond angle. The potential is dependent on the square of the deviation; therefore, the term will be zero only at the equilibrium angle.

A similar potential can also be applied to four-body bonds, to represent an energy penalty for deviations from the equilibrium torsion angle.

$$U(\phi_{ijkl}) = k_{ijkl}\left[1 - \cos(N\phi)\right] \qquad 2.38$$

where k_{ijkl} is the harmonic force constant, ϕ is the torsion angle in the crystal and N is the periodicity of the torsion. In particular, this potential is used to ensure that the carbonate ion remains planar and N is equal to 2.

2.2.4 Ionic Polarisability and the Shell Model

Ionic polarisability is defined as the induction of a dipole in an ion's electron charge cloud when brought close to an asymmetric field. This dipole can in turn affect the short-range interactions between ions. Simple rigid ion models ignore this polarisability, considering the ions as point charges. Although this approach is known to work well for a range of systems [93, 94], it does reduce the accuracy of the calculation. For this study, the ionic polarisability was modelled using the shell model.

The shell model was introduced by Dick and Overhauser in 1958 [95] and it describes the ion as being split into two components: a core of charge X, containing all the ionic mass, which represents the nucleus and core electrons, and a massless shell surrounding the core, representing the valence electrons, with a charge of Y, as shown in Figure 2.5.

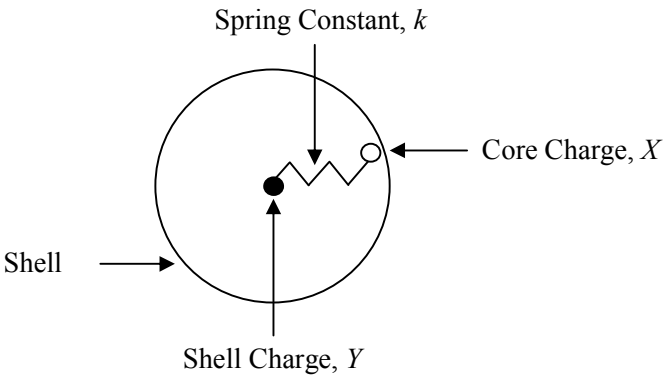

Figure 2.5: Schematic representation of the shell model [96] .

The core and shell are linked by a harmonic spring, with a spring constant k and the ionic charge is the sum of the core and shell charges. The position of the core represents the position of the ion in the crystal, with the shell position having no physical significance. The free ion polarisability, α, is related to the shell charge and spring constant, as shown by Equation 2.39:

$$\alpha \propto Y^2 / k \qquad 2.39$$

One of the disadvantages of using this approach is that it adds two further parameters for evaluation, making it more computationally expensive.

The interaction between the negatively charged electron cloud and the positively charged nucleus is modelled using a simple harmonic potential function:

$$U(r_{core-shell}) = \tfrac{1}{2} k_2 r_{core-shell}^2 + \tfrac{1}{24} k_4 r_{core-shell}^4 \qquad 2.40$$

The k_4 term is often omitted and set to zero, however, for some cases it is required to prevent unphysically large core-shell separations. This was the case for the work on uranium dioxide.

With the exception of the uranium atom, the shell model has only been used in this work to describe anion polarisability, as the cation polarisability is influenced less by its surroundings due to the electrons being more tightly bound to the nucleus. The long-range Coulombic forces act between all cores and shells except the core and shell on the same ion. The short-range forces act between shells and between cores and shells, resulting in the direct coupling of the polarisability and the short-range potentials. The cation – cation interactions are purely Coulombic, following the assumption of Lewis and Catlow [97].

2.2.5 Potential Derivation

As previously noted, the quality and accuracy of any simulation using potential-based methods relies on the correct parameters used in the parameterised equations. A large number of potentials have already been derived and are commonly used by researchers looking at similar systems. However, sometimes new potentials have to be derived to accurately describe certain properties or to simulate previously unstudied materials. Although potential derivation has not been required in this study, this section will describe the available methods to derive and fit the parameters.

Potential parameters are usually fitted using one of two approaches. The first is to adjust the parameters to reproduce *ab-initio* electronic structure data, usually by adjusting the energy with respect to atomic position. The second method is to adjust the parameters to fit experimental data. Traditionally, the latter method was the favoured as electronic structure calculations were often time consuming and beyond the scope of the computer power available. However, due to both the advancement in computer technologies and the creation of efficient *ab-initio* software, such as the VASP code [98-101], non-empirical fitting has become much more practical. Although it is noted that standard DFT codes often neglect van der Waals terms and are known to have difficulty with open shell *d*- and *f*-metals.

However, both approaches work on the same principle, to derive a model which will accurately reproduce existing data. The statistical measure of the sum of squares is commonly used to assess this accuracy. For an ideal case, the sum of squares would be zero but this is only true for trivial cases where data reproduction is guaranteed. The sum of squares, F, is defined as:

$$F = \sum_{observables} w(f_{calc} - f_{obs})^2 \qquad 2.41$$

where f_{calc} and f_{obs} are the calculated and observed quantities, respectively, and w is a weighting factor. The use of a weighting factor for each observable results in there never being a perfect fit. The choice of this term will depend on several factors, including the relative magnitude of the quantities and the reliability of the data itself.

The aim of fitting is to minimise the value of F, through the variation of potential parameters. A number of standard methods are available for solving the least squares problem. A commonly used approach is a Newton-Raphson minimisation via the simulation package GULP (General Utility Lattice Package) [102]. As with many statistical regression models; it is often advised to initially fit to a small number of parameters and then gradually increase the number of parameters in subsequent restarts. As, if all parameters are included from the start, unphysical parameters often result.

2.2.6 Potentials Used in this Study

The majority of work in this thesis uses previously derived and tested potentials. The following section will outline the original source of the potentials as well as defining the actual parameters used.

2.2.6.1 The Simple Oxide Potentials

The potential models for the simple calcium and magnesium oxides were fitted and developed by Lewis and Catlow [97], with the transferable oxygen – oxygen potential from earlier work by Catlow [103, 104]. The oxygen is modelled with a shell, whereas the cations are assumed to be unpolarisable. The parameters were empirically derived using experimental structures, lattice constants, elastic and dielectric constants. All ion pair interactions are modelled using Buckingham potentials and are given below in Table 2.1.

Table 2.1: Potential parameters for calcium and magnesium oxides.

	Core – Shell parameters		
Ion	Core charge (e)	Shell charge (e)	k_2 / eV Å^{-2}
Magnesium (Mg)	+2.00000	-	-
Calcium (Ca)	+2.00000	-	-
Mg Oxygen (O)	+0.84819	-2.84819	74.920380
Ca Oxygen (O)	+1.00000	-3.00000	47.960000
	Buckingham potential parameters		
Ion Pair	A / eV	ρ / Å	C / eV Å^6
$Mg_{core} - O_{shell}$	1428.50000	0.29453	0.00000
$Ca_{core} - O_{shell}$	1090.40000	0.34370	0.00000
$O_{shell} - O_{shell}$	22764.00000	0.14900	27.88000

2.2.6.2 The Hydroxide Potential

Using a combination of experimental data and Hartree-Fock quantum mechanical calculation Saul *et al.* [105] derived a potential for sodium hydroxide, which has be used successfully by Wright *et al.* [106] to model hydrogarnet defects in grossular. The potential was derived as a rigid ion model but later adapted by Baram and Parker [107] to model hydrogen defects at α-quartz and sodalite surfaces and in the hydroxide crystal structures of $Mg(OH)_2$ and $Al(OH)_3$, through the incorporation of a core-shell model on the oxygen. The oxygen and hydrogen are modelled using fractional charges, with the magnitude chosen to reproduce the experimental dipole moment on the OH ion. A Morse function is used to describe the intramolecular bonding, whereas intermolecular interactions are based on Buckingham potentials. The magnesium – hydroxide potential also originates from the Baram and Parker study. The hydroxide potential used in this study is taken from the work by Kerisit *et al.* [108] on iron oxide surfaces, including the oxygen – hydroxide potential. The calcium hydroxide interaction has been successfully used to model the dissociative adsorption of water on calcite surfaces [23] and has also been used to reproduce the structure and elastic constants of portlandite, $Ca(OH)_2$ [109]. The full list of hydroxide potentials is given in Table 2.2.

Table 2.2: Potential parameters for the hydroxide ion, as well as calcium and magnesium hydroxide.

Ion	Core-Shell parameters		
	Core charge (e)	Shell charge (e)	k_2 / eV Å^{-2}
Oxygen (O_H)	+0.90000	-2.30000	74.920380
Hydrogen (H)	+0.40000	-	-
	Buckingham potential parameters		
Ion Pair	A / eV	ρ / Å	C / eV Å^6
$O_{Hshell} - O_{Hshell}$	22764.00000	0.14900	6.97000
$H_{core} - O_{Hshell}$	311.97000	0.25000	0.00000
$Mg_{core} - O_{Hshell}$	941.50000	0.29453	0.00000
$Ca_{core} - O_{Hshell}$	2170.00000	0.29700	0.00000
$O_{shell} - O_{Hshell}$	22764.00000	0.14900	13.94000
$H_{core} - O_{shell}$	396.27000	0.25000	0.00000
	Morse potential parameters			
Ion Pair	A / eV	B / Å^{-1}	r_0 / Å	Coulombic Subtraction / %
$O_{Hshell} - H_{core}$	7.052500	3.174900	0.92580	100

2.2.6.3 The Water Potential

The water potential used in this work was originally derived in 1998 by de Leeuw and Parker [22] using molecular dynamics simulations of liquid water and its interaction with MgO surfaces. The potential was derived to have a polarisable oxygen atom and to be compatible with both the hydroxide potential and Catlow intermolecular oxygen potential. It was fitted to reproduce the experimental dipole moment, infrared frequencies, OH bond length and the HOH angle of the monomer, as well as the structure of the water dimer. A Morse potential was used for the intramolecular oxygen – hydrogen interaction, whereas the oxygen – oxygen

interactions were described using a Lennard-Jones (12,6) potential. A three-body harmonic potential was also included to reproduce the directionality of the covalent bonds. The Coulombic interactions inside the water molecule were also reduced to give a better representation of intramolecular vibrational frequencies.

The interactions between MgO and water also come from the water model by de Leeuw and Parker, where the Buckingham *A* parameter between the magnesium and water oxygen was modified using the approach of Schröder *et al*. [110]. This method works on the principle that the interaction energy between nearest neighbour magnesium and oxygen ions is independent of the type of oxygen, therefore the Buckingham *A* parameter can be adjusted to take into account the fractional charge on the water oxygen. This and can be illustrated using the example of deriving a magnesium – water oxygen potential from the original potential, represented by Equation 2.42.

$$\frac{q_{Mg^{2+}} q_{O^{2-}}}{r_{MgO}} + A_{MgO} e^{-r_{MgO} / \rho_{MgO}} \qquad 2.42$$

For the water model, oxygen has a charge of -0.8, and therefore the Coulombic interaction between magnesium and water oxygen is 2 x -0.8. To balance the charges we can take the square root of the product, i.e. 2 x -0.8, to give charges of $\sqrt{1.6}$ and $-\sqrt{1.6}$ for magnesium and oxygen, respectively. These can then be substituted into Equation 2.42 to give 2.43.

$$\frac{q_{Mg^{+\sqrt{1.6}}} q_{O^{-\sqrt{1.6}}}}{r_{MgO}} + A'_{MgO} e^{-r_{MgO} / \rho_{MgO}} \qquad 2.43$$

The *A'* parameter can then be adjusted so that it reproduces the original MgO data, for example, structural data and physical properties. The same method was used to fit the potential between the lattice oxygen with a water molecule.

The interaction between calcium and water was derived to study the adsorption of water onto calcite surfaces, by de Leeuw and Parker [111], and was designed to be compatible with the hydroxide and water models. The potential was then verified with structural data for calcium carbonate hexahydrate, ikaite.

The origin of the Buckingham potential between hydroxide oxygen and water oxygen comes from using the London formula to adjust the attractive C parameter. This is shown by Equation 2.44 for using this example:

$$C_{OW-OH} = \sqrt{C_{OW-OW} C_{OH-OH}} \qquad 2.44$$

The potential parameters of the water model and associated interactions with other species are listed below in Table 2.3.

Table 2.3: Potential parameters for the water molecule and its interaction with calcium and magnesium oxides and hydroxides.

Ion	Core-Shell parameters		
	Core charge (e)	Shell charge (e)	k_2 / eV Å^{-2}
Oxygen (Ow)	+1.25000	-2.05000	209.449602
Hydrogen (Hw)	+0.40000	-	-
	Buckingham potential parameters		
Ion Pair	A / eV	ρ / Å	C / eV Å^6
Ow_{shell} – Hw_{core}	396.27000	0.25000	10.00000
Mg_{core} – Ow_{shell}	490.00000	0.29453	0.00000
Ca_{core} – Ow_{shell}	1186.60000	0.29700	0.00000
O_{shell} – Ow_{shell}	22764.00000	0.14900	28.92000
O_{shell} – Hw_{core}	396.27000	0.25000	0.00000
Ow_{shell} – OH_{shell}	22764.00000	0.14900	17.14000
Ow_{shell} – H_{core}	396.27000	0.25000	10.00000
OH_{shell} – Hw_{core}	311.97000	0.25000	0.00000
	Lennard-Jones (12,6) potential parameters		
Ion Pair	A / eV Å^{12}	B / eV Å^6	
Ow_{shell} – Ow_{shell}	39344.98	42.15	
	Morse potential parameters		
Ion Pair	A / eV	B / Å^{-1}	r_0 / Å	Coulombic Subtraction / %
Ow_{shell} – Hw_{core}	6.203713	2.220030	0.92367	50
Hw_{core} – Hw_{core}	0.000000	2.840499	1.50000	50
	Three-body potential parameters		
Ion Group	k_{ijk} / eV rad^{-2}	θ_0 / °	
Hw-Ow-Hw	4.199780	108.693195	

2.2.6.4 The Carbonate Potential

The original carbonate potential was developed in 1992 by Pavese *et al.* [112], derived from structural properties, elastic constants and vibrational frequencies for calcite. The potential model consisted of Buckingham potentials to describe the intermolecular bonding, whilst containing three- and four-body terms for the carbonate. Additionally, a shell model was used to model the polarisability. However, as the potential was fitted at 0K, the effect of temperature on the crystal structure was neglected. As a result, an improved calcite model was published by Pavese *et al.* [113] in 1996. The improved model used a Morse potential to describe the carbon – oxygen interaction. Using lattice dynamics techniques, they found good agreement with cell dimensions and thermal expansion coefficients at several temperatures as well as with the thermal behaviour of the elastic constants and bulk modulus. The interaction of calcium with the carbonate group is also from this study.

The interaction between the magnesium with a carbonate oxygen comes from work by de Leeuw and Parker [114] looking at the adsorption and segregation of magnesium ions to calcite surfaces. The potential was derived as a working model for modelling magnesite ($MgCO_3$) which was also compatible with the calcite model of Pavese *et al.* and the water model of de Leeuw and Parker. It was fitted to structural and thermodynamic data of magnesite.

The intermolecular interactions of carbonate and hydroxide are from work by Kerisit *et al*. [23] and were derived to be both compatible with the Pavese *et al.* calcite model whilst reproducing the structure and elastic constants of Portlandite, $Ca(OH)_2$ [109].

The interactions between carbonate and water were introduced in 1997 by de Leeuw and Parker [111] to model the molecular adsorption of water on calcite surfaces, along with the calcium – water interactions, which were verified by simulating the structure and energy of ikaite.

As there were no current parameters for the intermolecular interaction between an oxygen atom of the carbonate group with a metal oxide oxygen, the Buckingham *A* parameter was modified using the simplified Schröder *et al.* method. The potential was derived from the oxygen – oxygen potential using Equations 2.45 and 2.46 to adjust the *A* and *C* Buckingham parameters, respectively:

$$A_{O-Oc} = A_{Oc-Oc} \times \frac{q_{Oc}}{q_O} \qquad 2.45$$

$$C_{Oc-O} = \sqrt{C_{Oc-Oc} C_{O-O}} \qquad 2.46$$

Table 2.4 below details the potential parameters used to model a carbonate ion and its interactions with different species.

Table 2.4: Potential parameters for the carbonate group and its interaction with water as well as calcium and magnesium oxides and hydroxides.

Ion	Core-Shell parameters		
	Core charge (e)	Shell charge (e)	k_2 / eV Å^{-2}
Carbon (C)	+1.13500	-	-
Oxygen (O_C)	+0.58700	-1.63200	507.400000
	Buckingham potential parameters		
Ion Pair	A / eV	ρ / Å	C / eV Å^6
$O_{C_{shell}} - O_{C_{shell}}$	16372.00000	0.21300	3.47000
$O_{C_{shell}} - Mg_{core}$	1092.20000	0.27926	0.00000
$O_{C_{shell}} - Ca_{core}$	1550.00000	0.29700	0.00000
$O_{C_{shell}} - O_{shell}$	8186.00000	0.21300	9.83000
$O_{C_{shell}} - O_{H_{shell}}$	16372.00000	0.21300	3.47000
$O_{C_{shell}} - H_{core}$	396.270000	0.23000	0.00000
$O_{C_{shell}} - O_{W_{shell}}$	12533.60000	0.21300	12.09000
$O_{C_{shell}} - H_{W_{core}}$	396.270000	0.23000	0.00000
	Morse potential parameters		
Ion Pair	A / eV	B / Å^{-1}	r_0 / Å	Coulombic Subtraction / %
$O_{C_{shell}} - C_{core}$	4.710000	3.800000	1.18000	0
	Three-body potential parameters		
Ion Group	k_{ijk} / eV rad^{-2}	θ_0 / °	
O_C-C-O_C	1.690000	120.000000	
	Four-body potential parameters		
Ion Group	k_{ijkl} / eV	ϕ / °	
Oc – C – O_C - O_C	0.112900	180.000000	

2.2.6.5 The UO_2 Potential

The uranium dioxide potential differs from those of alkaline metal oxides in that the uranium ion is modelled with a shell. The justification of applying a shell to uranium is due to the nature of the *f*-electrons. They are further away from the nucleus causing them to be less tightly bound, and therefore more polarisable. The potential model used is based upon the Busker potential, reported by Abramowski *et al*. [70]. The model was derived by fitting to bulk lattice properties, including lattice constant, defect energies, elastic and dielectric constants. The core – shell parameters are taken directly from this model, as is the uranium – oxygen Buckingham parameters. However, to ensure transferability of the previously mentioned hydroxide and water potentials, a Catlow oxygen – oxygen potential has been used. To ensure the accuracy and quality is maintained, bulk properties and surface energies have been compared to both experimental data and results of other commonly used UO_2 potentials. Details of these comparisons will be given in chapter seven. The uranium – water/hydroxide parameters have been derived from the Busker uranium – oxygen potential using DFT cluster calculations. The details and discussion of which will also be given in chapter seven. Table 2.5 tabulates the list of parameters for the UO_2 potential as used in this study.

Table 2.5: Potential parameters for the UO_2 system and the interactions with water and hydroxide ions.

Ion	Core-Shell parameters		
	Core charge (e)	Shell charge (e)	k_2 / eV Å^{-2} k_4 / eV Å^{-4}
Uranium (U)	+4.10000	-0.10000	160.000000 143990.000000
Oxygen (O)	+0.08000	-2.08000	6.300000 143990.000000
	Buckingham potential parameters		
Ion Pair	A / eV	ρ / Å	C / eV Å^6
$U_{shell} - O_{shell}$	1761.77500	0.35642	0.00000
$O_{shell} - O_{shell}$	22764.00000	0.14900	27.88000
$U_{shell} - O_{Hshell}$	1553.24250	0.35642	0.00000
$U_{shell} - O_{Wshell}$	900.71000	0.35642	0.00000

2.3 Conclusions

This chapter has described the different ways the forces between species in a chemical system can be described, either through quantum mechanical calculation, where the electrons are included explicitly, or through the use of potentials. Once the forces have been successfully calculated between different species the next step is to use them to calculate the desired properties of the study using simulation methods. The general simulation methods which can use both quantum mechanical and potential-based techniques will be described in detail in the next chapter.

Chapter Three

Computational Methodologies

A central requirement for atomistic simulation codes is that the total energy of interaction and the forces between atoms is calculated. Two of the most commonly used simulation techniques that exploit the forces and energies are energy minimisation and molecular dynamics. Energy minimisation simulations use the forces between atoms to obtain the lowest energy structure. In this thesis, we use the energy minimisation code METADISE [12] which uses potential-based models, while for electronic structure calculations using DFT, the VASP code [98-101] is used. The alternative use of the forces is via Newton's laws of motion giving rise to molecular dynamics simulations which are conducted with the DL_POLY 2.0 code

[115] using interatomic potentials. This chapter will detail these techniques along with the generation of surfaces and the calculation of their energies.

3.1 Static Lattice Energy Minimisation

The aim of the energy minimisation technique is to determine the lowest energy configuration of the structure. The approach is to start with an initial or trial structure and then adjust atom positions to move the system 'downhill' to its nearest potential energy minimum. However, there are three main drawbacks to this technique:

(i) An initial structure is required.

(ii) The minimisation technique finds the nearest energy minimum. If more than one minimum is present in the system then the minimisation may only move to a local minimum rather than the global minimum of the system.

(iii) The vibrational properties of the crystal are neglected, thereby simulating the system at 0K, with even the zero point energy ignored.

Despite these drawbacks, simulations undertaken using these methods do give good agreement with experimental crystal structures [116].

At constant volume, the minimisation process works to decrease the lattice energy, U_L, with respect to the atom positions, **r**, to effectively reduce the stress, or force, on each atom coordinate to zero, as shown by Equation 3.1.

$$\frac{\partial U_L}{\partial \mathbf{r}} = 0 \qquad 3.1$$

The minimisation of energy is an iterative procedure, with each step reducing the energy until the minimum is found. The basis of the approach is to express the energy by a Taylor expansion in terms of the basis strain, $\delta\mathbf{r}$, using Equation 3.2.

$$U_L(\mathbf{r}+\delta\mathbf{r}) = U_L(\mathbf{r}) + \frac{\partial U_L(\mathbf{r})}{\partial \mathbf{r}}\delta\mathbf{r} + \frac{1}{2!}\frac{\partial^2 U_L(\mathbf{r})}{\partial \mathbf{r}^2}\delta\mathbf{r}^2 + \mathrm{K} \qquad 3.2$$

As the position **r** is composed of three components, this gives rise to a 3*N* matrix. From the Taylor expansion it is clear that with more terms included, the minimisation procedure will be more accurate. The most commonly used minimisation techniques in solid state computational chemistry are either first or second derivative methods, with both methods having advantages and disadvantages. In general, as the accuracy of the minimisation procedure increases with increasing complexity, hence requiring fewer minimisation steps, the simulation time required for each step also increases.

3.1.1 Conjugate Gradients

Conjugate gradient [117] minimisation is an example of a first derivative energy minimisation technique. It is a modification of the steepest descent method, which is a simpler, more approximate form. According to the steepest, or gradient, descent method, the new positions of the atoms at iteration n+1, $\mathbf{r}_{n+1}$, can be calculated using Equation 3.3.

$$\mathbf{r}_{n+1} = \mathbf{r}_n + \lambda_n \mathbf{s}_n \qquad 3.3$$

where $\mathbf{r}_n$ is the position at iteration n. The value of λ_n is a numerical constant chosen for each iteration to optimise the efficiency of the minimisation and is related to the step size along the chosen direction in configurational space. It is usually determined using a line search procedure, where the energy is monitored in the chosen direction and the step size is chosen so that the new position coincides with the minimum energy. The direction itself is given by the 3*N*-dimensional displacement vector, $\mathbf{s}_n$, and is defined by Equation 3.4.

$$\mathbf{s}_n = -\mathbf{g}_n \tag{3.4}$$

where

$$\mathbf{g}_n = \frac{\partial U_L}{\partial \mathbf{r}_n} \tag{3.5}$$

As the direction of the gradient is determined by the largest interatomic forces, the steepest descent methods are often good enough for relieving the highest energy features in an initial starting configuration. However, the major downfall of this technique is that, as the direction of displacement is orthogonal to the gradient, narrow valleys are only minimised by a large number of small successive steps, and hence may not be the most efficient route to the minimum. Although the conjugate gradient method uses the steepest descent method for the first iteration, the following iterations use information from the previous gradients to calculate the new displacement vector according to Equation 3.6.

$$\mathbf{s}_n = -\mathbf{g}_n + \gamma_n \mathbf{s}_{n-1} \tag{3.6}$$

where

$$\gamma_n = \frac{\mathbf{g}_n \cdot \mathbf{g}_n}{\mathbf{g}_{n-1} \cdot \mathbf{g}_{n-1}} \tag{3.7}$$

This method has the advantage that the minimisation is more efficient than the steepest descent methods, particularly in long narrow valleys, whilst remaining a first derivative method and hence still rapid to calculate.

3.1.2 Newton-Raphson

The Newton-Raphson minimisation method [118] is a second derivative method and hence is more efficient than the conjugate gradient method as it requires less iteration steps to find the energy minimum. The approach is to take the Taylor expansion, shown by Equation 3.2, to the second derivative. The gradient at the n+1 iteration, $\mathbf{g}_{n+1}$ is as shown by Equation 3.8.

$$\mathbf{g}_{n+1} = \frac{\partial U_L}{\partial \mathbf{r}_n} + \frac{\partial^2 U_L}{\partial \mathbf{r}_n^2}\delta\mathbf{r} = \mathbf{g}_n + \mathbf{W}_n \cdot \delta\mathbf{r} \qquad 3.8$$

where $\mathbf{W}_n$ is a Hessian matrix and $\delta\mathbf{r}$ is the displacement of ions between iterations n and n+1. At the minimum in energy, where $\mathbf{g}_{n+1}$ is equal to zero, the atom displacement is described by Equation 3.9.

$$\delta\mathbf{r} = -\mathbf{g}_n \cdot \mathbf{H}_n \qquad 3.9$$

where $\mathbf{H}_n$ is the inverse Hessian matrix or $\mathbf{W}_n^{-1}$. This therefore gives Equation 3.10 as the working equation for calculating the new atomic positions using the Newton-Raphson minimisation method.

$$\mathbf{r}_{n+1} = \mathbf{r}_n - \mathbf{g}_n \cdot \mathbf{H}_n \qquad 3.10$$

It is clear that for a harmonic system this method would be able to determine the minimum in a single step. However, as this is not the case, the process again follows an iterative procedure of reducing the energy per iteration. One consequence of using the harmonic assumption is that this method can become unstable far from the minimum. Therefore, the standard approach is to use a more robust method, such as conjugate gradient, initially, to move the system close to the minimum, and then to apply the Newton-Raphson method.

3.1.3 Quasi-Newton Methods

The calculation and inversion of the Hessian matrix is the main reason that the Newton-Raphson minimisation method is so time consuming, despite its increased efficiency. Indeed, the high computational cost is the reason that the electronic structure energy minimisation codes, such as VASP, use the conjugate gradient approach. One way of speeding up the minimisation is to use quasi-Newton methods. The working equation of the Newton-Raphson method still applies but rather than explicitly calculating the inverse Hessian at each step, the approximated form is used. The inverse Hessian is approximated and only recalculated after a fixed number of iterations or when the changes in the energy are too large for the approximation to be valid. There are a number of different ways of approximating the inverse Hessian, including the Davidon-Fletcher-Powell (DFP) [119] and the Broyden-Fletcher-Goldfarb-Shanno (BFGS) [120-123] methods.

The DFP method approximates the inverse Hessian matrix using Equation 3.11.

$$\mathbf{H}_{n+1} \approx \mathbf{H}_n + \frac{\delta\mathbf{r} \times \delta\mathbf{r}}{\delta\mathbf{r} \cdot \delta\mathbf{g}} - \frac{\left(\mathbf{H}_n \cdot \delta\mathbf{g}\right) \times \left(\mathbf{H}_n \cdot \delta\mathbf{g}\right)}{\delta\mathbf{g} \cdot \mathbf{H}_n \cdot \delta\mathbf{g}} \qquad 3.11$$

where $\delta\mathbf{r} = (\mathbf{r}_{n+1} - \mathbf{r}_n)$ and $\delta\mathbf{g} = (\mathbf{g}_{n+1} - \mathbf{g}_n)$. An alternative, and more efficient approach, is the BFGS method. This is identical to that of the DFP equation with the inclusion of an additional term, shown by Equation 3.12.

$$\mathbf{H}_{n+1} \approx \mathbf{H}_n + \frac{\delta\mathbf{r} \times \delta\mathbf{r}}{\delta\mathbf{r} \cdot \delta\mathbf{g}} - \frac{\left(\mathbf{H}_n \cdot \delta\mathbf{g}\right) \times \left(\mathbf{H}_n \cdot \delta\mathbf{g}\right)}{\delta\mathbf{g} \cdot \mathbf{H}_n \cdot \delta\mathbf{g}} + \left(\delta\mathbf{g} \cdot \mathbf{H}_n \cdot \delta\mathbf{g}\right)\mathbf{u} \times \mathbf{u} \qquad 3.12$$

where the vector **u** is defined as:

$$\mathbf{u} = \frac{\delta\mathbf{r}}{\delta\mathbf{r} \cdot \delta\mathbf{g}} - \frac{\mathbf{H}_n \cdot \delta\mathbf{g}}{\delta\mathbf{g} \cdot \mathbf{H}_n \cdot \delta\mathbf{g}} \qquad 3.13$$

For a full derivation of these methods please see Polak (1971) [124], but as can be seen from these expressions, they depend only on the change in forces, strains and the previous inverse Hessian matrix. Assuming the approximation holds, with increasing iteration, the estimate of the inverse Hessian becomes closer to the true inverse Hessian matrix, and on approaching the minimum has a similar accuracy to the Newton-Raphson method.

3.1.4 Constant Pressure Minimisation

Constant pressure minimisations are conducted using a similar method, except there is also a need for the cell geometry to be optimised. One approach is to first minimise the energy of the system, using the method for constant volume, and then apply Hooke's law so that the lattice vectors are adjusted according to the bulk lattice strain, $\boldsymbol{\varepsilon}$.

$$\boldsymbol{\varepsilon} = \mathbf{C}^{-1}\boldsymbol{\sigma} \qquad 3.14$$

where the stress, $\boldsymbol{\sigma}$, is the sum of applied and static pressures ($\mathbf{P}_{static} + \mathbf{P}_{applied}$), where the static pressure is defined as $\mathbf{P}_{static} = (1/V)(\partial U_L/\partial\boldsymbol{\varepsilon})$, and $\mathbf{C}^{-1}$ is the compliance matrix, or the second order derivatives of lattice energy with respect to strain. As with the minimisation of the structure at constant volume, this is an iterative procedure. A full description of constant pressure minimisation can be found in Leach (2001) [125].

Despite the accuracy and speed of the energy minimisation method used, they do not overcome the problem of the minimisation becoming trapped in a local minimum. There are a range of techniques that can be used to overcome this limitation. One approach is simply to repeat the energy minimisation using different initial structures. A second is molecular dynamics, which gives atoms velocities to allow the system to overcome energy barriers to find the global minimum.

3.2 Molecular Dynamics

Molecular dynamics works to solve Newton's laws of motion numerically by assigning velocities to atoms and molecules, and hence allows the system to evolve over time, allowing atoms and molecules to overcome energy barriers in the system to find the global minimum. However, as the amount of real time modelled is very short, this is only applicable to small energy barriers, typically of the order of a few k_BT.

Newton's second law of motion states that the force is equal to the rate of change in momentum. Therefore, by knowing the force, $\mathbf{f}_i$, acting on an atom i of mass m_i, we can determine its acceleration, $\mathbf{a}_i$, or the second derivative of the change in position, $\mathbf{r}_i$, with time, t, by Equation 3.15.

$$\mathbf{f}_i = m \cdot \frac{\partial^2 \mathbf{r}_i}{\partial t^2} = m \cdot \mathbf{a}_i \qquad 3.15$$

Therefore, if there is no force acting on a system, the positions, after a change in time, Δt, simply change by $\mathbf{v}_i(t)\Delta t$, where $\mathbf{v}_i$ is the velocity. However, if the force is not zero but remains constant, the new velocities and positions after a change in time can be calculated from Equations 3.16 and 3.17, respectively.

$$\mathbf{v}_i(t+\Delta t) = \mathbf{v}_i(t) + \mathbf{a}_i(t)\Delta t \qquad 3.16$$

$$\mathbf{r}_i(t+\Delta t) = \mathbf{r}_i(t) + \mathbf{v}_i(t)\Delta t + \mathbf{a}_i \frac{\Delta t^2}{2} \qquad 3.17$$

In real systems, however, the forces acting on an atom will vary depending on their distance from other atoms. This causes Equations 3.16 and 3.17 to only be true when the change in time is infinitesimal. As the practical use of this approach requires the time step to have a finite size, integration algorithms are employed.

After the calculation of the forces, these algorithms allow the positions and forces after a finite time step to be determined by integrating Newton's laws of motion.

3.2.1 Integration Algorithms

All integration algorithms for molecular dynamics assume that both the atomic positions and dynamic properties can be approximated by a Taylor expansion, Equations 3.18 – 3.21, where $\mathbf{b}_i$ is the third derivative of the position with respect to time.

$$\mathbf{r}_i(t+\Delta t) = \mathbf{r}_i(t) + \mathbf{v}_i(t)\Delta t + \tfrac{1}{2}\mathbf{a}_i(t)\Delta t^2 + \tfrac{1}{6}\mathbf{b}_i(t)\Delta t^3 + \Lambda \qquad 3.18$$

$$\mathbf{v}_i(t+\Delta t) = \mathbf{v}_i(t) + \mathbf{a}_i(t)\Delta t + \tfrac{1}{2}\mathbf{b}_i(t)\Delta t^2 + \Lambda \qquad 3.19$$

$$\mathbf{a}_i(t+\Delta t) = \mathbf{a}_i(t) + \mathbf{b}_i(t)\Delta t + \Lambda \qquad 3.20$$

$$\mathbf{b}_i(t+\Delta t) = \mathbf{b}_i(t) + \Lambda \qquad 3.21$$

The simplest integration algorithm which is employed is the Verlet algorithm [126]. This approach uses information regarding the positions and accelerations at time t and the positions of the previous step, $t - \Delta t$, to calculate the new positions at $t + \Delta t$. The relationships between these quantities are shown by Equations 3.22 and 3.23 by third-order Taylor expansions for the positions at $t + \Delta t$ and $t - \Delta t$, respectively.

$$\mathbf{r}_i(t+\Delta t) = \mathbf{r}_i(t) + \mathbf{v}_i(t)\Delta t + \tfrac{1}{2}\mathbf{a}_i(t)\Delta t^2 + \tfrac{1}{6}\mathbf{b}_i(t)\Delta t^3 + \vartheta\Delta t^4 \qquad 3.22$$

$$\mathbf{r}_i(t-\Delta t) = \mathbf{r}_i(t) - \mathbf{v}_i(t)\Delta t + \tfrac{1}{2}\mathbf{a}_i(t)\Delta t^2 - \tfrac{1}{6}\mathbf{b}_i(t)\Delta t^3 + \vartheta\Delta t^4 \qquad 3.23$$

where ϑ is an accuracy parameter. These equations can then be summed to determine the position at time $t + \Delta t$, Equation 3.24.

$$\mathbf{r}_i(t+\Delta t) = 2\mathbf{r}_i(t) - \mathbf{r}_i(t-\Delta t) + \mathbf{a}_i(t)\Delta t^2 + \vartheta\Delta t^4 \qquad 3.24$$

where the accuracy is of the order Δt^4. The Verlet algorithm does not explicitly calculate the velocity, although it can be derived from the knowledge of the trajectory, using Equations 3.25 and 3.26.

$$\mathbf{r}_i(t+\Delta t) - \mathbf{r}(t-\Delta t) = 2\mathbf{v}_i(t)\Delta t + \vartheta\Delta t^3 \qquad 3.25$$

$$\mathbf{v}_i(t) = \frac{\mathbf{r}_i(t+\Delta t) - \mathbf{r}_i(t-\Delta t)}{2\Delta t} + \vartheta\Delta t^2 \qquad 3.26$$

This expression for the velocity is only accurate to the order of Δt^2. The drawback of this algorithm is that it is difficult to obtain the velocities, as they cannot be computed until the positions at t are known. Additionally as the new positions are obtained from the addition of a small term, $\mathbf{a}_i(t)\Delta t^2$, to the difference between two large terms, a lack of precision may result.

An alternative form of this algorithm is known as the Verlet leapfrog algorithm [127], as is implemented in the DL_POLY 2.0 code. This algorithm effectively evaluates the velocities at the half-integer time step, Equations 3.27 and 3.28 and uses these to determine the new positions.

$$\mathbf{v}_i\left(t - \tfrac{1}{2}\Delta t\right) = \frac{\mathbf{r}(t) - \mathbf{r}(t-\Delta t)}{\Delta t} \qquad 3.27$$

$$\mathbf{v}_i\left(t + \tfrac{1}{2}\Delta t\right) = \frac{\mathbf{r}(t+\Delta t) - \mathbf{r}(t)}{\Delta t} \qquad 3.28$$

From this, an expression for the calculation of the new positions can be given from the old positions and velocities at the half-integer time step, Equation 3.29.

$$\mathbf{r}(t+\Delta t) = \mathbf{v}_i\left(t + \tfrac{1}{2}\Delta t\right)\Delta t + \mathbf{r}(t) + \vartheta\Delta t^4 \qquad 3.29$$

Additionally, from the Verlet algorithm an expression for the update of velocities at the half-integer time step can be derived, Equation 3.30.

$$\mathbf{v}_i\left(t+\tfrac{1}{2}\Delta t\right)=\mathbf{v}_i\left(t-\tfrac{1}{2}\Delta t\right)+\mathbf{a}_i\left(t\right)\Delta t+\vartheta\Delta t^3 \qquad 3.30$$

Therefore, the velocities 'leap-frog' over the positions at time *t*, giving their values at the half-integer time step. The main advantage of this is that numerical precision is improved with the accuracy of the velocities being of the order of Δt^3 and it removes the problem of the positions being calculated through the differences in large numbers. The disadvantage, however, is that the positions and velocities are not calculated at the same time. This means that it is not possible to calculate the kinetic and potential energy contributions to the total energy at the same time. To calculate properties which require the simultaneous knowledge of the velocity and position Equation 3.31 can be used. This method can be improved by using the Verlet velocity algorithm [128], although this is not used in this study.

$$\mathbf{v}_i\left(t\right)=\tfrac{1}{2}\left[\mathbf{v}_i\left(t+\tfrac{1}{2}\Delta t\right)+\mathbf{v}_i\left(t-\tfrac{1}{2}\Delta t\right)\right] \qquad 3.31$$

A further disadvantage of these algorithms is that they are not self-starting as they require information from the previous step. Therefore, initial velocities need to be assigned to the atoms. In practice, these are assigned randomly such that the system starts at the required temperature and the simulation cell has no translational momentum, shown by Equations 3.32 and 3.33.

$$\sum_{i=1}^{N} m_i \cdot \mathbf{v}_i^2 = 3Nk_BT \qquad 3.32$$

$$\sum_{i=1}^{N} m_i \cdot \mathbf{v}_i = 0 \qquad 3.33$$

where N is the number of particles, k_B is the Boltzmann constant and T is the temperature.

3.2.2 Time Step and Equilibration

Obviously the choice of the actual time step used will have large implications on the accuracy of the molecular dynamics simulation. A very small time step will require large amounts of simulation time to calculate, whereas a value which is too large will result in the atoms moving an unphysical distance, thus failing to produce accurate results. An additional complication arises from the use of massless shells, as described in the previous chapter, in molecular dynamics simulations. Two approaches can be used to ensure that there is no exchange between the core-shell vibrations and the rest of the system. The first method is to perform an energy minimisation on the shells at each time step [129], although this can be computationally expensive. The second approach is to assign the shells with a small mass [130, 131]. This second approach is used in this work, where the mass assigned to each is shell equates to 0.2a.u. This small mass results in the shell vibrational frequencies being well separated from those of the cores and hence there is no exchange of energy. This is illustrated in Figure 3.1 which shows the calculated vibrational density of states for bulk MgO using an oxygen shell mass of 0.2 and 0.8a.u. As can be seen the core and shell vibrations are well separated at 0.2a.u. and as the highest frequency vibration expected in this study is that of a hydroxide ion, approximately at 3500cm^{-1} [132], a shell mass of 0.2a.u. is clearly suitable. This use of small mass shells puts an additional constraint on the time step, requiring it to be suitable small. For the purposes of this work, a time step of 0.2fs has been used throughout.

The initial stages of a molecular dynamics simulation comprises of an equilibration period. This process allows the system to come to equilibrium from the initial positions and velocities prior to data collection at a given temperature and pressure. The aim of this process is to allow a thermalised distribution of velocities to be attained over a fixed number of steps, typically a few tens of thousands. Data can then be collected over a length of time which is long enough to allow convergence of the properties of interest. The convergence is normally measured in

the configurational energy, temperature and pressure of the system, where convergence of a property is considered to have a rate of change with time of ~10^{-8}.

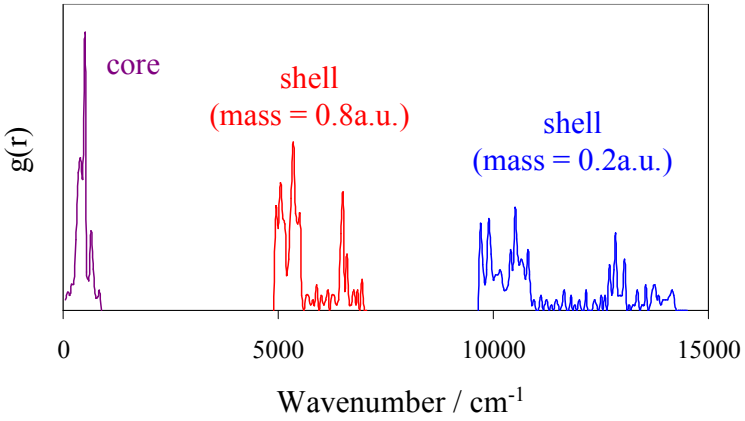

Figure 3.1: Calculated vibrational density of states for bulk MgO, using an oxygen shell mass of 0.2 (blue line) and 0.8a.u. (red line). NOTE: for clarity the core and shell states are plotted on different scales.

3.2.3 Ensembles

The conditions of the molecular dynamics simulations describing the constraints are given by the ensemble used. The most common is the microcanonical ensemble, or NVE, in which the number of particles, volume and total energy of the system are held fixed are hence remain constant. In this ensemble the conserved quantity, derived from the Hamiltonian, H, is:

$$H_{NVE} = U + K.E. \qquad 3.34$$

where U is the potential energy and $K.E.$ is the kinetic energy.

In addition, one of the other ensembles which has been used with molecular dynamics in this work is the canonical, or NVT, ensemble which fixes the number of particles, volume and temperature. The temperature is kept constant through the

coupling to a heat bath, of which a number of different methods exist, although this work uses the Nosé-Hoover thermostat [133] throughout. The temperature of the system at time t, $T(t)$, can be calculated from Equation 3.35.

$$T(t) = \frac{\sum_{i=1}^{N} m_i \mathbf{v}_i^2(t)}{k_B f} \qquad 3.35$$

where f is the number of degrees of freedom in the system, $3N$-3 for a periodic system. Therefore, to modify the temperature to a specified value, T_{ext}, the velocities in the system can be adjusted by modifying Newton's equation of motion, Equation 3.36.

$$\frac{d\mathbf{v}(t)}{dt} = \mathbf{a}(t) - \chi(t)\mathbf{v}(t) \qquad 3.36$$

where χ is the friction coefficient and is controlled by the first order differential equation:

$$\frac{d\chi(t)}{dt} = \frac{fk_B}{Q}\left(T(t) - T_{ext}\right) \qquad 3.37$$

where the effective 'mass' of the thermostat, Q, is defined by Equation 3.38.

$$Q = fk_B T_{ext} \tau_T^2 \qquad 3.38$$

where τ_T is a specified time constant, often termed the relaxation constant.

For the Verlet-leapfrog algorithm, the calculation of the velocity at the half-integer time step, Equation 3.30, is modified to form Equation 3.39.

$$\mathbf{v}_i\left(t+\tfrac{1}{2}\Delta t\right)=\mathbf{v}_i\left(t-\tfrac{1}{2}\Delta t\right)+\left[\mathbf{a}_i(t)-\chi(t)\mathbf{v}_i(t)\right]\Delta t+\vartheta\Delta t^3 \qquad 3.39$$

where the friction coefficient at both the half-integer time step and at time t can be represented as Equations 3.40 and 3.41, respectively.

$$\chi\left(t+\tfrac{1}{2}\Delta t\right)=\chi\left(t-\tfrac{1}{2}\Delta t\right)+\left[\frac{fk_B}{Q}\left(T(t)-T_{ext}\right)\right]\Delta t \qquad 3.40$$

$$\chi(t)=\tfrac{1}{2}\left[\chi\left(t-\tfrac{1}{2}\Delta t\right)+\chi\left(t+\tfrac{1}{2}\Delta t\right)\right] \qquad 3.41$$

However, as $\mathbf{v}(t)$ is required to calculate $T(t)$, and therefore itself, a number of iterations are performed using the standard Verlet algorithm, normally three, to ensure self consistency. The conserved quantity, derived from the Hamiltonian, of the NVT ensemble is the Helmholtz free energy, as defined by Equation 3.42.

$$H_{NVT}=U+K.E.+\frac{1}{2}Q\chi(t)^2+\frac{Q}{\tau_T^2}\int_0^t\chi(s)ds \qquad 3.42$$

For the purposes of this work, the NVE ensemble has been used to help stabilise systems prior to simulation with constant temperature. Thus allowing a redistribution of kinetic and potential energy in the system, with total energy held fixed. The effect of the temperature bath on the configurational energy can be assessed through a simple example of simulating bulk magnesium oxide at a temperature of 300K, using the potentials given in the previous chapter. The simulation cell contained a total of 216 atoms. This was then run for 200ps in the NVE ensemble, following an initial equilibration period of 20ps. The ensemble was then changed to NVT and run for three successive periods of 100ps, increasing the relaxation constant from 0.1 to 1.0 to 2.0 ps. The variation of configurational energy and temperature as a function of simulation time is shown in Figure 3.2.

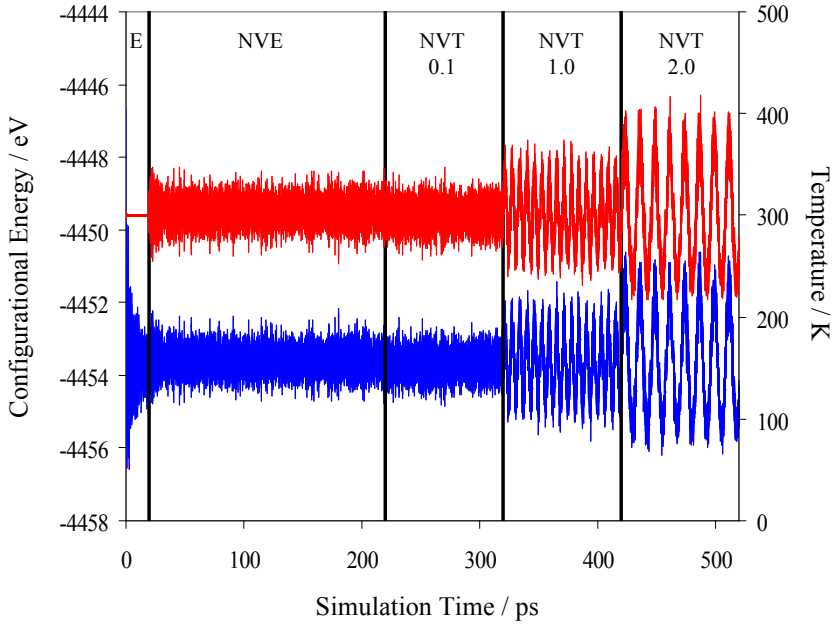

Figure 3.2: Graph showing the variation of configurational energy (blue) and temperature (red) with simulation time for bulk MgO with different ensembles. Changing simulation conditions are highlighted on the graph by E (equilibration period), NVE and NVT. The relaxation constant used with the NVT ensemble also varies from 0.1 to 1.0 to 2.0ps.

The plot shows that as the relaxation constant changes, both the temperature and configurational energy begin to oscillate, with the average value remaining constant with the value from the NVE ensemble. This allows a larger sampling of energy states and hence gives rise to more thermodynamically reasonable values which will be closer to experimental observations. Additionally, the effect of increasing the relaxation constant allows not only the amplitude of the variation to increase but also the wavelength of the oscillation. Although not as important for stoichiometric bulk materials, for more fluxional and dynamic systems this will be more significant, particularly if the system becomes trapped in a local minimum.

Other frequently used ensembles include the isobaric-isothermal, or NPT, grand canonical, μVT, and NST ensembles, where the P, μ and S refer to the pressure, chemical potential and stress, respectively. The major difference between the NPT and NST ensembles is that while the NPT allows the cell dimensions to change

during simulation, the NST also allows the shape of the cell to alter. The pressure is controlled using a barostat, in this study a Hoover barostat, which acts in much the same way as the thermostat, where the specification of a relaxation constant is required. For a full description of the Hoover barostat see Leach (2001) [125]. However, despite the ensemble used in the simulation, the bulk, surface or nanoparticle system first needs to be generated, which is the focus of the remaining part of this chapter.

3.3 Simulating Surfaces and Nanoparticles

The generation of surfaces and nanoparticles in the work, for both potential-based and electronic structure calculations, exclusively utilises the METADISE code. This is done through the previously described method of energy minimisation. For this purpose, a description of how the METADISE code generates both surfaces and isolated nanoparticles is important.

3.3.1 Types of Surface

A surface can be generated from cleavage of the bulk crystal, which is made up of charged layers of ions. Surfaces can be characterised firstly by the crystallographic direction in which the crystal is cut, as defined by its Miller index. In addition to the direction, the location is also important, as cleavage along certain planes, giving rise to different surface terminations, will lead to different surface stabilities. It was shown by Bertaut [134] that when a dipole moment perpendicular to the surface exists, the energy of the surface will diverge and become infinite. Following on from this, Tasker [135] described three possible surface types which can be generated by different cleavage locations.

- Type I surfaces, Figure 3.3(a), consist of stacked planes which each have an overall charge of zero. They contain a stoichiometric ratio of cations and anions and have no net dipole moment.

- Type II surfaces, Figure 3.3(b), comprise of charged sheets, where the stacking sequence is symmetric and thus produces no net surface dipole moment.

- Type III surfaces, Figure 3.3(c), also contain stacked charged sheets but using an alternating sequence which gives rise to a net dipole moment at the surface. These surfaces are also termed as dipolar.

Type I and II surfaces will both give rise to stable surfaces. However, the net surface dipole moment of Type III surfaces makes them unstable and hence will only form either due to surface roughening or the adsorption of foreign atoms which can stabilise these unstable surfaces. These Type III surfaces can be modified readily, for example, Oliver *et al.* [136] found that this could be achieved by removing half the surface ions and displacing them to the bottom of the cell, as shown in Figure 3.3(d). For larger surfaces, this displacement of ions can obviously give rise to a range of different surface configurations which will each need to be modelled to find the lowest in energy. This displacement can be considered as micro-faceting, which occurs in nature. Surface faceting allows for the reconstruction of polar surfaces to form neutral surfaces, where stable surfaces are used in its formation. This process is shown schematically in Figure 3.4.

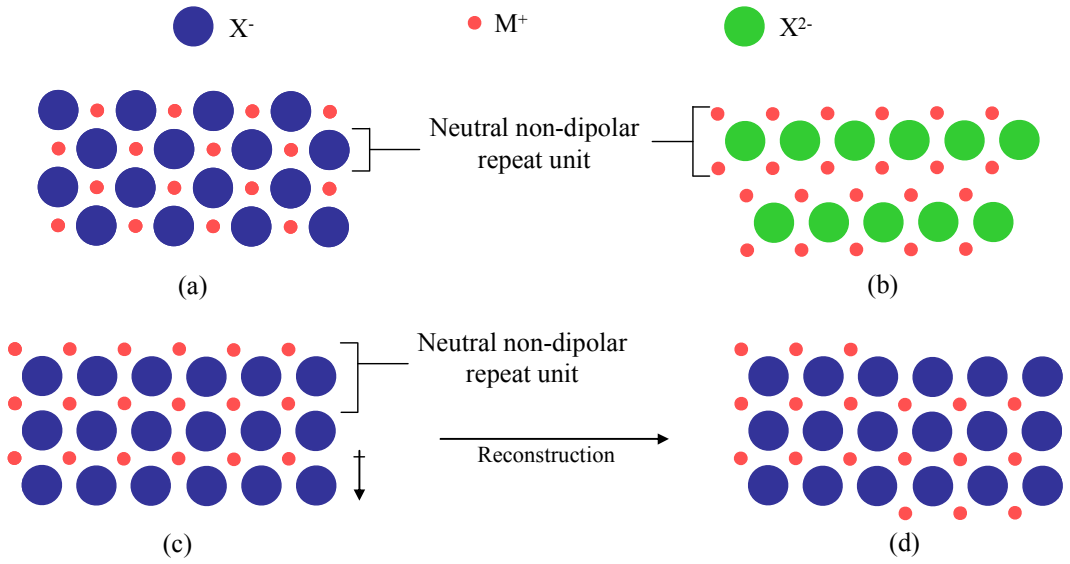

Figure 3.3: Schematic representation of the different forms of surfaces generated by cleaving a crystal. These consist of **(a)** Type I, **(b)** Type II and **(c)** Type III surfaces. Due to the net dipole moment formed for Type III surfaces, reconstruction occurs to remove this, giving rise to **(d)** a reconstructed Type III surface. [96]

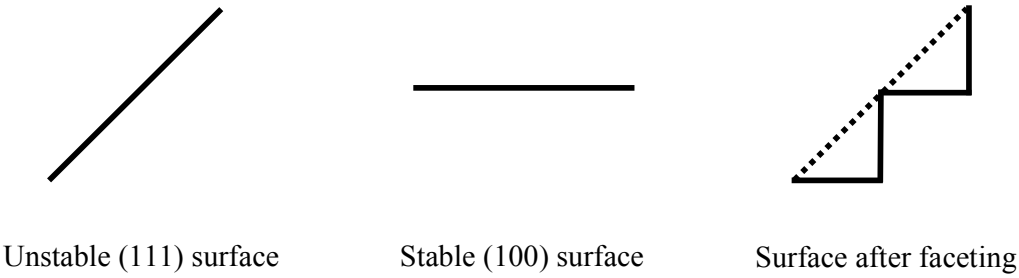

Figure 3.4: Schematic representation of the surface faceting, illustrated using hypothetical surfaces where a stable (100) surface is used to stabilise a polar (111) surface [109].

3.3.2 Surface Generation

The approach for modelling surfaces follows the method of Tasker [135], where the surfaces consist of a series of two-dimensional periodic charged planes parallel to the surface. The difficultly that this produces is that the complete crystal is comprised of many charged planes, which when modelled explicitly is

computationally expensive. To overcome this, Tasker developed the two-region approach, which is implemented in the METADISE code. This method considers a system as comprising of two blocks, which in turn contain two distinct regions, all of which are periodic in two-dimensions. The atoms in Region I are treated explicitly and allowed to relax to their mechanical equilibrium. Region II atoms, however, represent the rest of the crystal, and therefore are held fixed at their bulk equilibrium positions. A bulk simulation is conducted using two blocks with the Region I atoms adjacent. A surface, however, is modelled using just one block; with the surface present at the top of Region I. Figure 3.5 shows a schematic representation of the setup of both bulk and surface simulations using this two-region approach.

The energies of these blocks can then be determined by summing the energies of interaction between the different regions. This allows for the calculation of the energy of the bulk, U_B, and surface, U_S, simulations through Equations 3.43 and 3.44, respectively.

$$U_B = (E^B_{I-I} + E^B_{I-II}) + (E^B_{II-I} + E^B_{II-II}) \qquad 3.43$$

$$U_S = (E^S_{I-I} + E^S_{I-II}) + (E^S_{II-I} + E^S_{II-II}) \qquad 3.44$$

where the superscript *B* and *S* refer to bulk and surface components, respectively. $E_{I\text{-}I}$ is the energy of Region I ions interacting with Region I ions, $E_{I\text{-}II}$ for Region I ions and Region II, etc. The energies E^B_{II-II} and E^S_{II-II} will increase with Region II size.

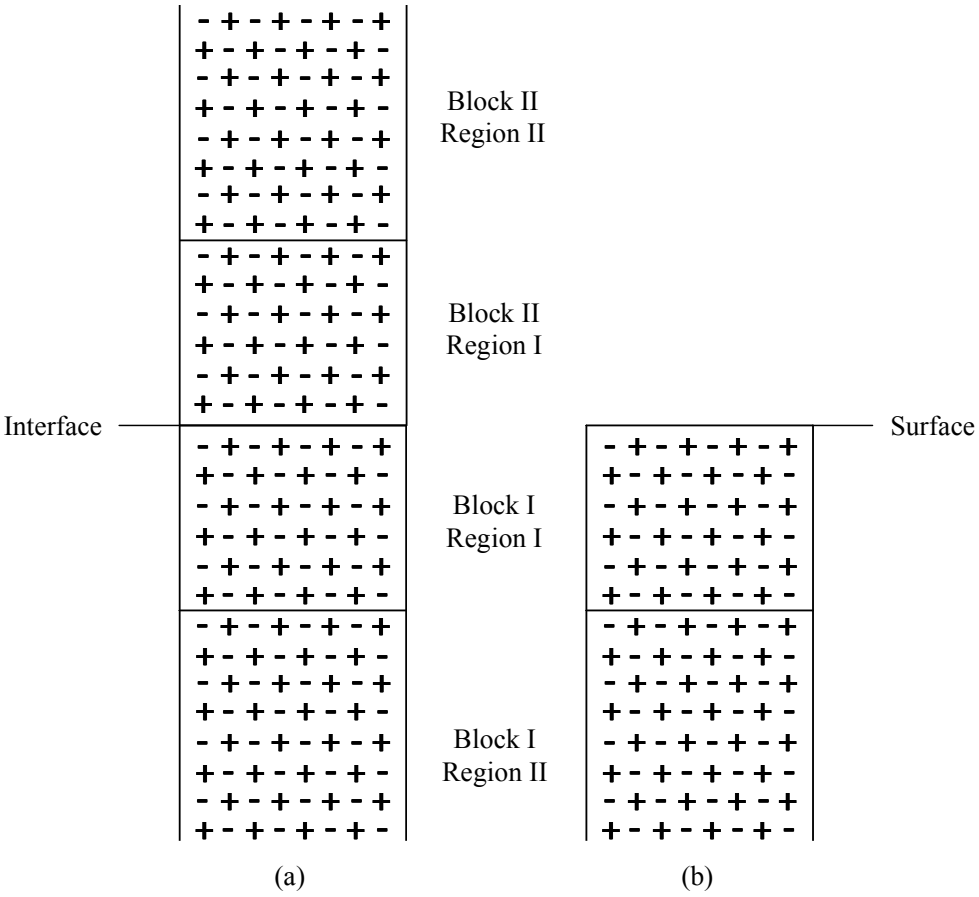

Figure 3.5: Schematic representation of the two-region approach when used to simulate **(a)** bulk and **(b)** surface conditions [96].

The surface energy of a crystal face is defined as the excess in energy of a surface simulation over the bulk system containing the same number of atoms per unit area, as expressed by Equation 3.45.

$$\gamma = \frac{U_S - U_B}{S} \qquad 3.45$$

where S is the surface area. Thus $E^B_{II-II} = E^S_{II-II}$ and hence will cancel.

3.3.3 Modelling Materials in Three-Dimensions

Both the VASP and DL_POLY codes employ three-dimensional periodic boundary conditions, exploiting the rapid convergence of electrostatic interactions. The use of these periodic boundary conditions makes the above method of surface generation unable to be used directly. Therefore, to do this, a slab of material is generated, with both sides of the slab consisting of the same surface on either side. The generation of this slab can also be done using the two-region approach in that the slab can be generated from Region I of Block I. All that is then required is that the slab is made sufficiently thick so that the surfaces are non-interacting. To model this slab a gap between the surfaces also needs to be introduced of sufficient thickness so that surfaces do not interact with their mirror in the adjacent periodic image.

3.3.4 Crystal Morphology

The accurate calculation of surface energies, using the above methods, allows METADISE to generate predicted equilibrium morphologies. This technique is based on work by Gibbs [137] which proposed that for a crystal of a given volume, the equilibrium form will be that which possess the minimal surface energy. Or that Equation 3.46 is a minimum at constant volume.

$$\gamma S = \sum_i \gamma_i S_i \qquad 3.46$$

where γ_i and S_i are the surface energy and the surface area of the i^{th} crystallographic face.

Following from this proposal, Wulff [138] suggested the crystal morphology formed would be a result of $\mathbf{h}_i$, the normal vector to the face from a point within a crystal, being proportional to the surface energy of that face, γ_i:

$$\mathbf{h}_i = \lambda \gamma_i \qquad 3.47$$

where λ is a constant that depends on the absolute size of the crystal resulting in the crystal morphology, as shown in Figure 3.6. It thus follows that high energy surfaces will not be present in the final construction.

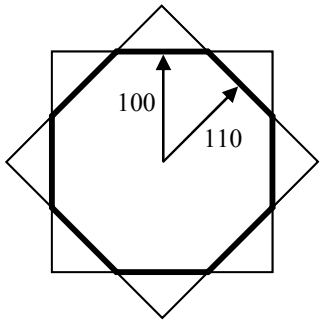

Figure 3.6: Schematic representation of the calculation of crystal morphology [139].

This approach, however, is only true for crystals grown with all surfaces in equilibrium, neglecting kinetic factors such as the growth rate. An additional problem is that it can often be unclear as to when the crystal exhibits its equilibrium morphology. However, we might expect morphologies close to the equilibrium form for small crystals as, at each stage of the growth process, rearrangement is possible, either due to the small distances over which material has to travel or if the material is formed over geological time scales.

An alternate method for considering nanoparticle morphology is to cut a portion of the bulk material, for example, a sphere, and then to anneal the surfaces to form the equilibrium morphology, similar to the approach to Sayle *et al*. [140]. This is done by raising the temperature of a molecular dynamics simulation to melt the surface regions and then to slowly cool the simulation to allow the surfaces to recrystallise. This work will consider both forms of nanoparticle generation thus allowing both the

equilibrium shape to be considered as well as allowing the stability of nanoparticles which are dominated by a particular surface to be considered.

3.4 Chapter Conclusions

The aim of this chapter has been to identify and describe the computational methodologies employed in this work. When coupled with the description of the calculation of forces in chapter two, this gives an overview of how the calculations described herein have been both setup and simulated. The remaining chapters of this thesis will discuss the applications of these methods to both surfaces and nanoparticles. This will begin with studying the adsorption process on the surfaces of calcium and magnesium oxide.

Chapter Four

Oxide Surfaces & the Adsorption of H and C

Central to our understanding of surface processes, such as adsorption, is the evaluation of reliable data on the energetics and mechanisms at the atomic level. Once such data is obtained it is then possible to predict conditions which will improve the surface behaviour as required. As mentioned in chapter one, this is of particular interest for optimising the adsorption of anthropogenic carbon in the process of mineral carbon sequestration in both dry and wet conditions. Thus, the focus of this chapter will be to investigate the surface adsorption of both H, in the

form of water, and C, in the form of carbon dioxide. The effect these have on the surface stability of the simple oxides of calcium and magnesium will be assessed and utilised to construct surface phase diagrams which will both provide prediction, for these materials, and establish a protocol for modelling different materials. We have elected to study the simple oxides which are well characterised model systems, thus allowing our predictions to be tested more easily. This study uses static lattice simulation techniques exclusively, with the forces calculated using a potential model, as outlined in the previous chapters. In addition, the energy minimisation of a large number of different surface configurations allows us to evaluate the surface free energies. The total number of individual static lattice minimisations used for the calculations detailed in this chapter exceed 180 000.

4.1 Bulk Minerals

Calcium and magnesium oxides, or periclase and lime, respectively, both have equivalent face-centred cubic crystal structures, modelled in the $Fm\bar{3}m$ space group. Perfect cleavage is observed in the symmetrically equivalent [100], [010] and [001] directions. Despite the use of previously tested potentials, it is essential to validate the potential models used in order to ensure bulk lattice parameters and physical properties can be accurately reproduced. Table 4.1 below details the comparison of the physical properties of the simple oxides with experimental data. The results of these comparisons suggest that, as expected for previously derived potentials, good reproduction of the crystal structure and the related structural properties is achieved. Larger discrepancies are seen in the comparison between elastic constants due to the neglect of the known covalency in these oxide minerals. However, previous studies [141] have shown that this neglect is satisfactory and the simulation of these materials yields accurate results.

Table 4.1: Comparison of the physical properties of bulk calcium and magnesium oxides to reference data [132, 142].

Property	CaO		MgO	
	Calculated	Experimental	Calculated	Experimental
Lattice Constant / Å	4.81	4.81	4.20	4.20
Lattice Energy / eV	-36.0	-36.2	-41.3	-39.3
Static Dielectric Constant, ε_0	10.3	11.8±0.3	8.4	9.7
High-Frequency Dielectric Constant, ε_∞	2.4	3.4	2.2	3.0
Shear Modulus, C_S / 10^{11} dyn cm^{-2}	11.3	16.4	22.9	20.1
Shear Modulus, C_{44} / 10^{11} dyn cm^{-2}	9.9	8.1	16.4	15.5

4.2 Surface Structures

The correct modelling of oxide surface structures and the subsequent calculation of surface energies is also important. However, it is not feasible to study every possible surface termination and hence, a range of surfaces have been simulated, enabling representative surfaces to be selected for studying the adsorption processes. These include the lowest index, and most stable, {100} surface along with the stepped {*n*10} and {*n*11} surfaces, with a range of *n* between 1 and 5. Table 4.2 below details the surface energies of these modelled surfaces. The low index surfaces are primarily considered as they are often the lowest in energy because they have the largest stacking vector and hence less bonds to be cut perpendicular to the surface.

Table 4.2: Table detailing the relaxed surface energies for the {100}, {*n*10} and {*n*11} surfaces of calcium and magnesium oxide, where *n* ranges from 1 to 5.

Surface Termination	CaO surface energy / J m^{-2}	MgO surface energy / J m^{-2}
{100}	0.78	1.29
{110}	1.31	2.18
{210}	1.34	2.22
{310}	1.15	1.91
{410}	1.05	1.75
{510}	0.99	1.65
{111}	2.47	4.16
{211}	1.71	2.95
{311}	2.18	3.68
{411}	1.97	3.35
{511}	1.79	3.06

The primary difference between the two materials is that the calcium surfaces are lower in energy than their magnesium equivalents, although they have the same trend in stability. This is simply a cause of the difference in bond strength. As the bonds are shorter, and hence stronger, for MgO, the energy required to break these bonds to form the surface is greater, resulting in higher surface energies.

The {100} surface possesses a structure of a 'perfect', flat surface and as expected has the lowest energy, shown in Figure 4.1. The surface structure and stability also concurs with previous simulation studies [12]. The {100} is the most stable, and the {110} surface is in turn more stable than the {111} surface. The exception to this is the {111} MgO surface which has a previously reported surface energy of 3.86J m^{-2}. This discrepancy is due to the actual model used. The model used by de Watson *et al.* has a weaker spring constant for the oxygen ions, therefore making them more polarisable. For the majority of the modelled surfaces this causes little discrepancy. However, as the {111} surface is polar, this has a larger impact, making the surface energy reported by Watson *et al.* lower in energy.

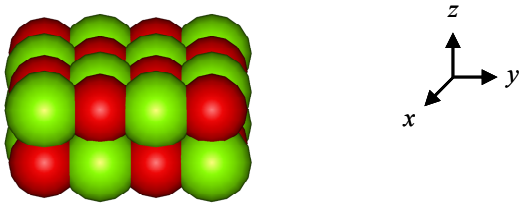

Figure 4.1: Surface structure of the {100} surface of calcium/magnesium oxide. Atoms coloured green indicate the metal atom, whereas oxygen atoms are labelled red.

The {*n*10} surfaces, as seen in Figure 4.2, are stepped, with the steps separated by terraces of {100} surfaces. The lowest energy {110} surface, Figure 4.2(a), undergoes a rearrangement giving rise to a micro-faceted surface, as previously reported by de Leeuw *et al*. [16]. The facet has a depth of 2.87Å and the sides of the facets are comprised of exposed {100} surfaces. The remaining {*n*10} surfaces, however, all have the same basic stepped structure, with the length of the terraces separating the steps increasing with the value of *n*. This is a result of the stability of the {100} surface, causing a subsequent decrease in energy with increased expression. Interestingly, all the surfaces have evenly spaced steps across the surface with the exception of the {310} which alternates between two lengths. This is most likely due to the interaction energy between the steps. As it reaches a certain limit the surface can stabilise itself more by having one weak and one strong interaction, leading to the alternate terraces. For longer terraces the distance between the steps is sufficiently large that the interaction is minimal and the surface appears regular.

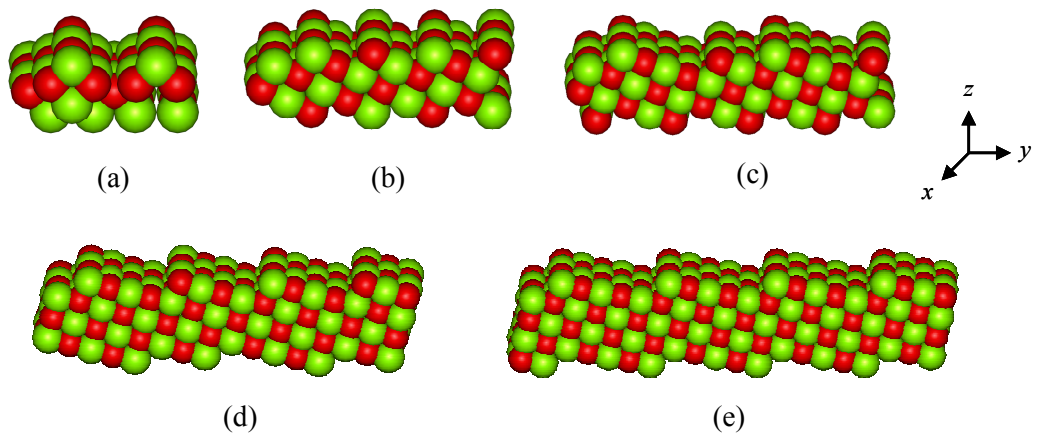

Figure 4.2: Surface structures of the {*n*10} surfaces of calcium/magnesium oxide for **(a)** {110}, **(b)** {210}, **(c)** {310}, **(d)** {410} and **(e)** {510} cuts.

The structures of the {*n*11} surfaces are shown in Figure 4.3. The high energy of the {111} surface, particularly for magnesium oxide, is a result of it being a dipolar surface. To remove this dipole, 50% of the surface oxygen atoms are shifted to the bottom of the cell, producing trench-like structures along the rows of missing oxygen atoms on the surface. Increasing *n* leads to the formation of stepped surfaces, with {110} terraces separating the steps. The low energy of the {211} surface is related to the apparent flatness of the surface, where there are no steps present. As the steps are introduced, surface energy increases. However, increasing terrace length causes a decrease in surface energy with increasing *n*, as the energy converges towards the {110} energy. The {311} surface has a similar pattern of alternating steps to the {310}, again related to the interaction between the steps, as does the {511} surface.

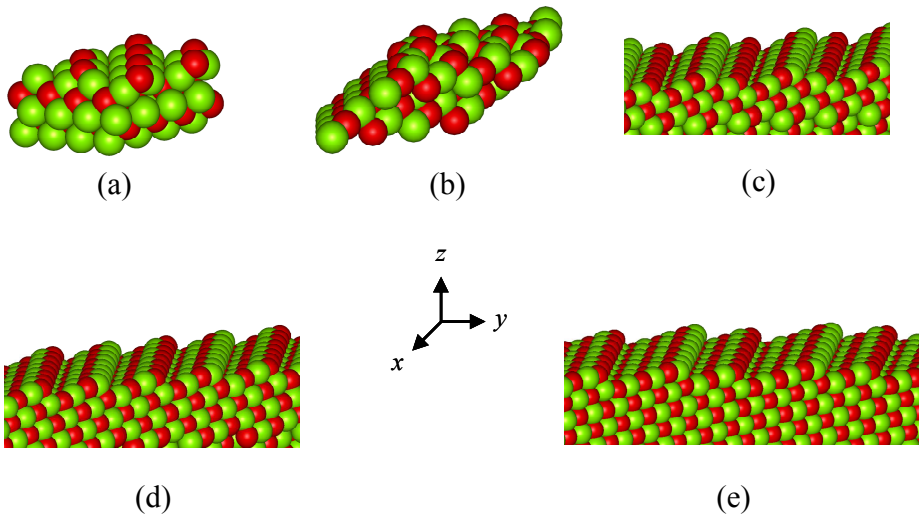

Figure 4.3: Surface structures of the {*n*11} surfaces of calcium/magnesium oxide for **(a)** {111}, **(b)** {211}, **(c)** {311}, **(d)** {411} and **(e)** {511} cuts.

The order of stability of the three low index surfaces can be rationalised through consideration of the surface metal coordination. From the {100} through to the {111} surface, the coordination number decreases from 5 to 3, with the rearranged {110} surface showing a mixture of coordination numbers of 4-6, depending on the ion's position in the surface trench. More detailed analysis of the MgO {110} surface reveals that the surface energy can be reduced further by enlargement and the deepening of the trench on the surface, as can be seen in Figure 4.4. The trench was increased in depth from 2.87 to 8.37Å which gave a subsequent reduction in the relaxed surface energy from 2.18 to 1.92J m^{-2}. This suggests that surface micro-faceting along the trenches can lead to increased surface stabilisation of the {110} surface.

Micro-faceting is also seen on the {111} surface, as shown computationally by de Leeuw *et al.* [20] and by experimental LEED patterns [143, 144]. In this case the surface comprises of pyramids, with {100} faces. Despite this reduction in surface energy, the modelling of a large number of surface adsorptions on the modified {110}

and {111} surfaces was not feasible due to the large increase in computational time needed to evaluate a considerably larger number of different surface configurations.

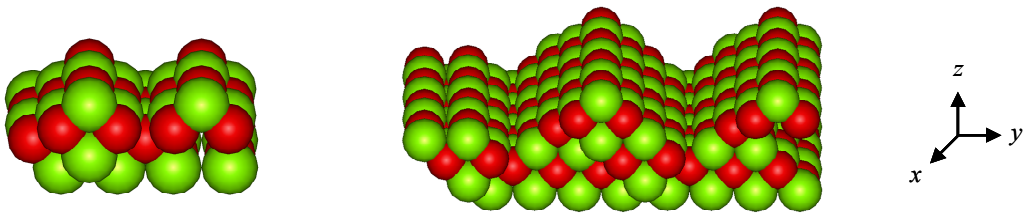

(a) (b)

Figure 4.4: Surface structures of the **(a)** original {110} and **(b)** modified {110} surface of magnesium oxide.

Thus we elected to consider a representative group of surfaces. These were the {100}, {110}, {111} and {310} surfaces. This allows us to investigate the differences between adsorption on flat, micro-faceted, polar and stepped surfaces, respectively.

4.3 Calculation of Surface and Adsorption Energies

The surface adsorption energies can be calculated from the total interaction energy of the surface, E_S, and the equivalent energy of bulk atoms, E_B, with an energy correction, E_{corr} (adsorbate), related to the self-interaction of the species, as shown by Equation 4.1:

$$\gamma = \frac{1}{S}\left[E_S - E_B\right] - \frac{1}{S} n_{\text{adsorbate}} E_{corr}\,(\text{adsorbate}) \qquad 4.1$$

where S is the surface area and $n_{\text{adsorbate}}$ is the number of surface adsorbates in the simulation cell. The energy of adsorption, E_{ads} (adsorbate) is calculated in a similar way by considering the energy difference of the 'pure' and 'modified' surfaces and is again corrected for the number of adsorbates, as shown by Equation 4.2. A 'pure'

surface is considered to be the clean surface, with no surface adsorbates present. Once a surface adsorbate is present, the surface is considered to be 'modified'.

$$E_{ads}\,(\text{adsorbate}) = \frac{E_S\,(\text{modified}) - E_S\,(\text{pure})}{n_{\text{adsorbate}}} + E_{corr}\,(\text{adsorbate}) \qquad 4.2$$

The free energies, A_S, can be estimated through the calculation of the energies of a large number of different surface configurations and is expressed relative to the minimum energy found at each level of surface coverage, $E_{S_{\min}}$. Equation 4.3 represents the calculation of free energy.

$$A_S = E_{S_{\min}} - RT\ln(Q) \qquad 4.3$$

where Q is the total partition function, summed over all surfaces at a particular coverage, as given by Equation 4.4.

$$Q = \sum_S e^{(-E_S - E_{S_{\min}})/RT} \qquad 4.4$$

The energies in Equations 4.1 and 4.2 can then be substituted for free energies, allowing the calculation of the surface free energy and free adsorption energy, respectively, assuming the entropic contribution for the bulk free energy is negligible. Additionally, this technique also allows for the evaluation of the average surface free energies, using the statistical mechanical expression shown by Equation 4.5.

$$<\gamma>= \frac{\sum_S \gamma_S e^{(-E_S - E_{S_{\min}})/RT}}{Q} \qquad 4.5$$

This requires only that we sample sufficient numbers of different configurations, which is possible using simple interatomic potentials.

The correction term used in Equations 4.1 and 4.2 is dependent on the surface adsorbates and effectively accounts for the self-energies of the species being adsorbed. The calculation of the correction factors are obtained in a similar fashion as used by de Leeuw *et al.* [145]. For the addition of an associatively adsorbed water molecule E_{corr} (H_2O) is the self-energy of an isolated water molecule, -9.1eV, and the heat of vaporisation, -0.45eV, which makes it relative to aqueous water. The calculation of the adsorption energy, however, is relative to a gaseous molecule, and therefore does not need to include the heat of vaporisation. For the addition of a dissociated water molecule, however, E_{corr} (H-OH) is obtained from the following reaction:

$$M^{2+}_{(g)} + O^{2-}_{(g)} + H_2O_{(l)} \rightarrow M^{2+}_{(g)} + 2OH^{-}_{(g)}$$

This is calculated using the relevant lattice energies and enthalpies of formation from Table 4.3. For CaO this is determined as -6.70eV, and -7.15eV for MgO. The complication of evaluating the self-energy is that the ionic model has to account for the different oxygen charge states (-0.8 in a water molecule, -1.4 in a hydroxide and -2 for a lattice oxygen), therefore effectively accounting for the oxygen electron affinity directly.

The calculation of the energy correction term used for the addition of a carbonate group, E_{corr} (CO_3^{2-}), is calculated in a similar manner, using the data in Table 4.3, where it represents the carbonation from gaseous CO_2 according to:

$$M^{2+}_{(g)} + O^{2-}_{(g)} + CO_{2(g)} \rightarrow M^{2+}_{(g)} + CO^{2-}_{3(g)}$$

This therefore accounts for the energy of the reaction of CO_2 with a surface oxygen atom. The correction term for the carbonation of CaO uses a value of 23.34eV, and 21.66eV is used for MgO.

Table 4.3: Lattice energies and enthalpies of formation [146] used to calculate the energy correction terms for hydroxylation and carbonation.

	Lattice Energy / kJ mol^{-1}	Enthalpy of Formation / kJ mol^{-1}
$MgO_{(s)}$	-3984.80	-601.70
$Mg(OH)_{2(s)}$	-3378.26	-924.50
$MgCO_{3(s)}$	-6175.04	-1095.80
$CaO_{(s)}$	-3468.63	-635.10
$Ca(OH)_{2(s)}$	-2931.15	-986.10
$CaCO_{3(s)}$	-5898.94	-1206.90
$CO_{2(g)}$	-	-393.51
$H^{+}_{(aq)}$	-	0
$H_2O_{(g)}$	-	-241.82

4.4 Water Adsorption

The first molecular species to be considered for surface adsorption is water. The ubiquity of water makes the modelling and understanding of its interactions with mineral surfaces important. Two modes of water adsorption are considered. The first is through associative adsorption, or hydration, shown schematically in Figure 4.5(a). The initial starting configuration of water considered was through placement of the water oxygen above the surface metal atom, as the metal – oxygen interaction is the strongest. The second mode of adsorption is dissociative adsorption, or surface hydroxylation, which involves the splitting of the water molecule into a proton and a hydroxide molecule. These are initially modelled as adsorbing to the surface oxygen and metal atoms, respectively, as shown in Figure 4.5(b). Additionally, surface adsorption of both species was modelled from the adsorption of a single molecule through to monolayer coverage, thus allowing the effect of surface coverage to be

investigated. However, the mixed adsorption of species was not considered due to constraints on the available computational resources. The definition of associatively and dissociatively adsorbed water as hydrated and hydroxylated, respectively, will be used consistently throughout this thesis.

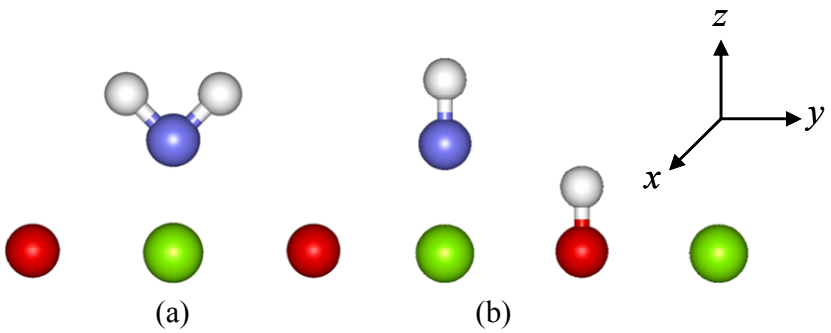

Figure 4.5: Schematic representation of the initial starting configuration for modelling the processes of **(a)** hydration and **(b)** hydroxylation on CaO and MgO surfaces. Hydrogen atoms are shown in white and the oxygen of a water molecule is designated blue.

The definition of surface coverage is essential when discussing the variation of surface energy with adsorbate concentration as there are a number ways of doing this. The definition of surface coverage, for the adsorption of water, is defined as being the percentage of adsorbates above a surface metal atom, up to monolayer coverage. This allows direct comparison between associatively and dissociatively adsorbed water.

Although water adsorption on these simple oxide surfaces has been studied by a number of researchers, as outlined in chapter one, the trialling of such a large number of different surface combinations and the subsequent evaluation of free energies via the configurational entropy has not been. This is only computationally feasible through the use of a high-throughput resource, in this case a CONDOR pool [147].

The variation of surface free energies with water coverage, for both hydration and hydroxylation, are shown in Figure 4.6.

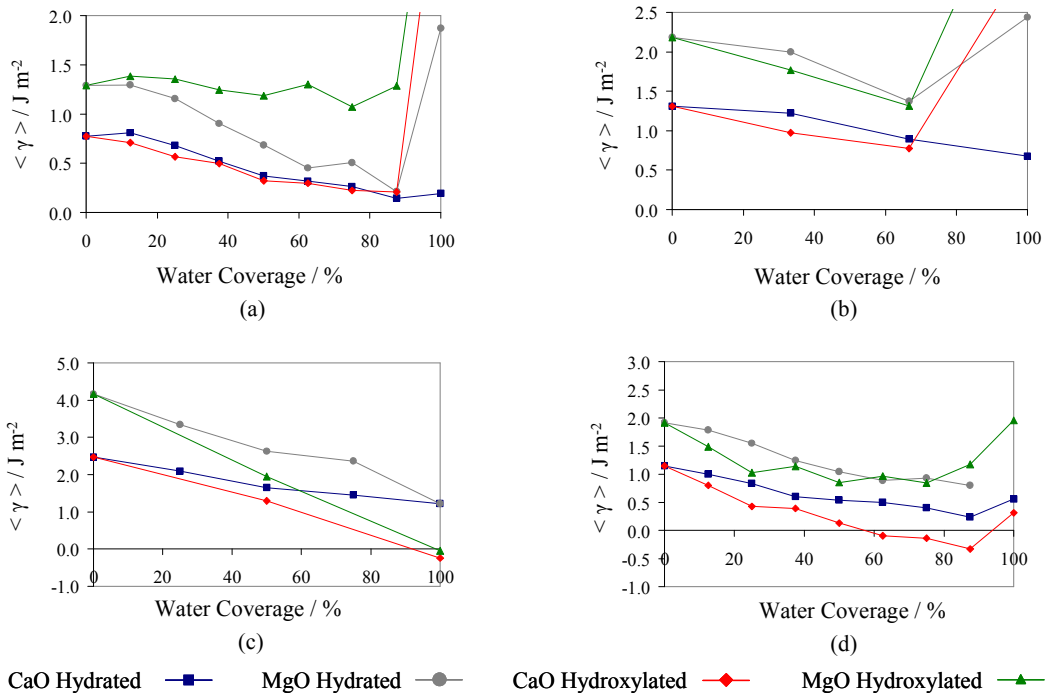

Figure 4.6: Plots of the average surface free energy against water coverage for hydration and hydroxylation of the calcium and magnesium oxide **(a)** {100}, **(b)** {110}, **(c)** {111} and **(d)** {310} surfaces. NOTE: High surface energies at full coverage for some surfaces are not shown for clarity.

Surface hydration and hydroxylation are both seen to reduce the surface energy with increasing coverage, although, for the majority of the surfaces, the minimum surface energies are not at full monolayer coverage. The steric repulsions of the 100% coverage dominate the energy and destabilise the surfaces. This is also reflected by the adsorption energies, which are all exothermic except at these high coverages. The energies of CaO surfaces are also consistently lower than MgO, similar to the dry surface energies. One of the causes of this difference is the lower Madelung potential of CaO, which is a result of the increased lattice constant, effectively destabilising the O^{2-} ion relative to the MgO surface. The {100} surface

Madelung potential for CaO is calculated as 20.2eV, comparing with 23.1eV for MgO.

The {100} surfaces, Figure 4.6(a), show different trends for the two materials. For MgO, hydration offers much more stabilisation than surface hydroxylation. However, for CaO, the two processes offer a similar degree of stabilisation. In fact, at most coverage levels, hydroxylation is the favoured process, although the minimum surface energy is found for hydration. The {110} and {111} surfaces, Figures 4.6(b) and (c), respectively, show similar trends. For these surfaces, hydroxylation produces the lowest surface energies. The {110} surface has closely matched energies but for the {111} surface hydroxylation forms considerably more stable surfaces. This is unsurprising, due to the known stability of the fully hydroxylated {111} surfaces, which effectively forms a layer of the mineral hydroxide [17]. The results of the {310} surface, Figure 4.6(d), also show similar trends for the two materials. Hydroxylation, in general, provides more surface stabilisation, particularly at low coverage where the adsorption occurs at the step. As coverage increases, the stabilisation due to hydroxylation of the calcium oxide {310} surface continues to decrease, as the {100} terraces are hydroxylated. The lower stabilisation of hydroxylation of the {100} surface for MgO results in the surface energy of the {310} levelling out, with similar surface energies to the hydrated surface.

The 100% hydroxylated {111} surfaces and the hydroxylated {310} CaO surface, after approximately 60%, show negative surface energies. This indicates the large surface stabilisation that the reaction to form hydroxide provides. This has been reported before, for example, for the hydroxylation of θ-alumina [148, 149]. According to Tasker *et al*. [150], this also indicates a thermodynamic barrier to sintering, thereby inhibiting crystal growth, indicating the strength of this adsorption. This therefore indicates that although crystal growth would be inhibited the surface would continue to dissociatively adsorb water up to the minimum energy coverage.

As the {100} and {310} surfaces are closely related, the differences between them can be attributed to the presence of the step. A comparison of the hydration and hydroxylation processes on the CaO and MgO surfaces is shown by Figures 4.7(a) and (b), respectively. For both materials, it can be seen that for hydration the variations of surface free energy with coverage mimic each other, with the same order of stability maintained regardless of coverage. However, this is not the case for hydroxylation. After one molecule of water has been added, removing the first of the two steps of the {310} surfaces, the order of stability is maintained. The second molecule of water hydroxylates the other {310} step, causing the surface to have a more regular appearance, similar to the {100} surface. After this, the variation in surface energy is similar to the {100} surface. The CaO surface is seen to increase in stability until steric repulsions become unfavourable, whereas the MgO equivalent levels out in a similar manner to the {100} surface, albeit at a lower energy. Therefore the presence of the step enhances the reactivity of the {100} surface, effectively allowing the surface to become more stable.

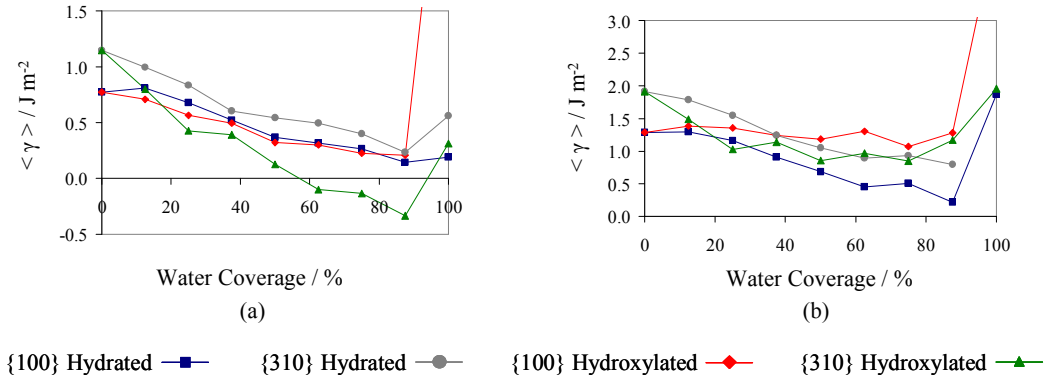

Figure 4.7: Plots of the average surface free energy against water coverage for hydration and hydroxylation of the {100} and {310} surfaces for **(a)** CaO and **(b)** MgO.

Overall, the results show that, for calcium oxide, hydroxylation of the surfaces is more favourable than hydration, providing lower surface energies, particularly for the {111} and {310} surfaces. Whereas, for MgO only the {111} surface shows a large surface stabilisation for hydroxylation over hydration. For the other surfaces

hydration either provides a similar degree of stabilisation or, in the case of the {100}, is considerably more favoured, which is in fact the lowest energy MgO surface. This result is to be expected from the known reactivity of calcium oxide with water being greater than for magnesium oxide. These results are also in broad agreement with previous studies, notably that of de Leeuw [16], where a similar study of hydroxylation was conducted, albeit considering fewer configurations.

4.5 Surface Carbonation

The reaction of carbon dioxide with mineral surfaces is difficult to model using potential-based methods, as the potentials used are only fitted to model a specific chemical species and do not allow for electron transfer. However, as the reaction of carbon dioxide with the surface forms the mineral carbonate we decided to model the post-reacted surface where the carbon species being studied is that of a carbonate ion.

Surface carbonation was modelled in two ways. The first method involved the adsorption *into* the surface, through removal of a surface oxygen atom and replacement with a carbonate ion. The second method was considered as the adsorption *above* the surface of an oxygen deficient surface, where the carbonate was placed over a surface metal atom in a bidentate manner and an oxygen atom was removed to maintain the charge neutrality of the surface. Figures 4.8(a) and (b) shows the first and second methods, respectively, of surface carbonation in a schematic manner. As the carbonate unit is significantly more bulky than the water molecule some surface features may sterically hinder the adsorption of the carbonate on a particular surface site and may be a problem if the carbonate relaxes into a local minimum. Therefore, to overcome this, the carbonate was additionally modelled as having the oxygen atoms in the carbonate aligned with either the *x*- or the *y*-axis, where the *z*-direction is perpendicular to the surface.

The definition of coverage for the purposes of carbonate adsorption follows a similar line to that for the adsorption of water. Carbonate coverage is defined as the number of carbonates added in relation to the number of adsorption sites available, which is the number of surface metal atoms for the first addition method and the number of surface oxygen atoms for the second. As all the modelled surfaces had an equal ratio of magnesium and oxygen atoms, this allows direct comparison between energies for the different methods of carbonate adsorption.

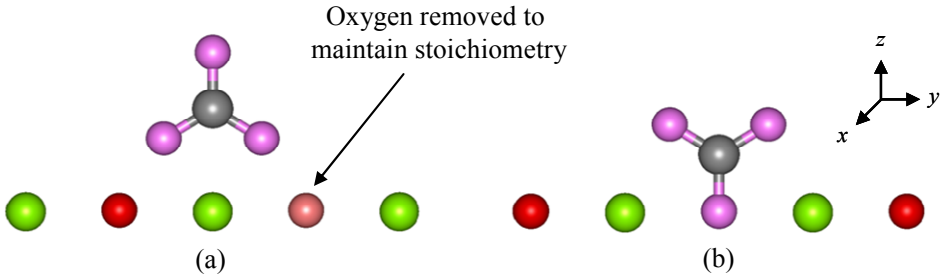

Figure 4.8: Schematic methods of initial carbonate placement on the CaO and MgO surfaces: **(a)** above a metal atom with a surface oxygen atom removed and **(b)** replacement a surface oxygen by a carbonate. The carbon atoms are coloured grey whereas the oxygen of the carbonate is shown in pink.

4.5.1 The Adsorption of a Single Carbonate Unit

Prior to considering the effect of surface coverage, it is useful to study the adsorption of a single carbonate onto these surfaces. To aid in the characterisation and understanding of this adsorption, vibrational frequency analysis can yield information pertaining to the adsorption mode and its strength. The carbonate ion has a number of characteristic vibrational modes which change upon adsorption. These include a Raman-active asymmetric CO stretch, ν_1, an IR-active out-of-plane deformation, ν_2, and a doubly degenerate IR-active symmetric CO stretch, ν_3. Upon adsorption, and the resultant loss of symmetry, ν_1 becomes IR-active and the doubly degenerate ν_3 splits into high and low frequency peaks, ν_{3h} and ν_{3l}, respectively.

These characteristic frequencies of the gaseous carbonate ion were determined using an optimised MP2 Gaussian [151] calculation, using a 6-311+ g (d, p) basis set.

The modes were calculated to be 1012, 854 and 1327cm^{-1} for v_1, v_2, and v_3, respectively. These compare favourably with literature values of 1063, 879 and 1415cm^{-1}, respectively, for the free carbonate ion [152]. However, calculation of using the potential model produced frequencies which were too high in value, although the same trend was observed. This is most likely a result of the enforced rigidity created by the torsional component of the potential. However, as the same model is used throughout this study, all calculated frequencies will be subject to identical constraints. In addition, we are only concerned with the change in force constants rather than their absolute values. Therefore, a scaling factor was defined, as the average scaling factor required to reduce the potential-based frequencies to those seen using the Gaussian calculation. This scaling factor has a value of 0.711 and produced frequencies of 1046, 795 and 1507cm^{-1} for v_1, v_2, and v_3, respectively. This scaling factor was then used for all following potential-based calculations.

A number of reference modes need to be considered to analyse the bonding modes seen for the minimum energy structures of adding a single carbonate. This was done with the {100} surface, using four different bonding configurations, shown schematically in Figure 4.9. The first two modes, Figures 4.9(a) and (b), consist of the insertion of carbonate *into* the surface via direct replacement of a surface oxygen atom with a carbonate group, where the angle between the carbonate is either 90° or 45°, respectively. The other two modes, detailed in Figures 4.9(c) and (d), involve the adsorption of a carbonate ion *above* a surface metal atom in either a bidentate or monodentate manner, respectively. Charge neutrality was ensured for the latter two modes by removing a surface oxygen. The position of this oxygen vacancy was also varied across the surface and the calculated vibrational frequencies summarised as a range. Tables 4.4 and 4.5 detail the calculated vibrational frequencies of the different adsorption modes for the {100} CaO and MgO surfaces, respectively, where the PARAPOCS code [153] was used to minimise the surfaces and calculate the values. These simulations were first minimised, whilst holding the carbon atom fixed, and then the vibrational frequencies were calculated for the resulting structure with the constraint removed.

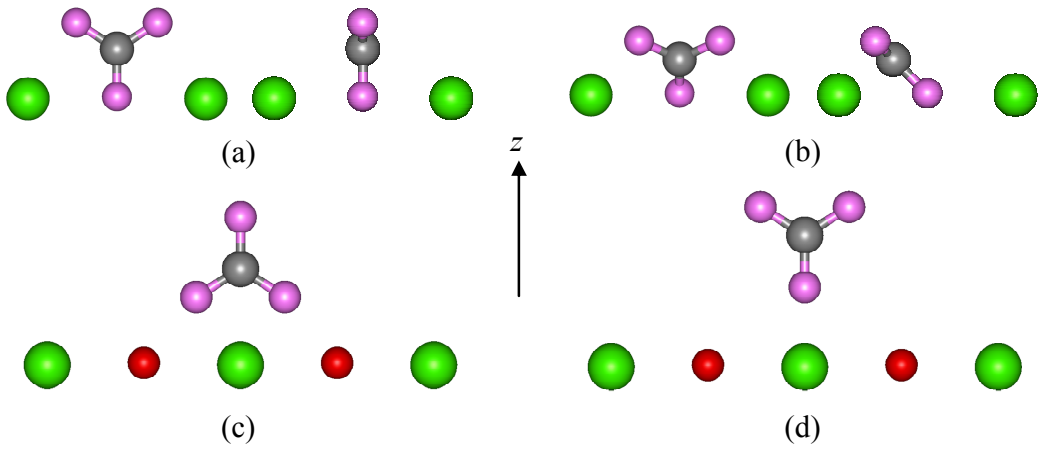

Figure 4.9: Schematics of the different modes of surface carbonation on the {100} CaO and MgO surfaces. These modes comprise of adsorption *into* the surface, with an angle to the surface of **(a)** 90° and **(b)** 45°; and adsorption *above* a surface metal atom in a **(c)** bidentate and **(d)** monodentate manner.

Table 4.4: Calculated vibrational frequencies of surface carbonation of the CaO {100} surface, detailing the results of different reference modes of adsorption.

Carbonate Adsorption	ν_1 / cm^{-1}	ν_2 / cm^{-1}	ν_{3l} / cm^{-1}	ν_{3h} / cm^{-1}
Replacement of O angle 90°	1083	787	1485	1666
Replacement of O angle 45°	1095	791	1531	1652
Monodentate above Ca	1070–1078	774-785	1415-1452	1548-1592
Bidentate above Ca	1052-1070	780-787	1400-1471	1611-1637

Table 4.5: Calculated vibrational frequencies of surface carbonation of the MgO {100} surface, detailing the results of different reference modes of adsorption.

Carbonate Adsorption	ν_1 / cm^{-1}	ν_2 / cm^{-1}	ν_{3l} / cm^{-1}	ν_{3h} / cm^{-1}
Replacement of O angle 90°	1089	785	1468	1703
Replacement of O angle 45°	1101	786	1515	1691
Monodentate above Mg	1080-1087	767-790	1371-1377	1501-1623
Bidentate above Mg	1045-1075	774-776	1350-1447	1622-1677

The results of these reference modes show that the adsorption of carbonate *into* the surface gives rise to higher frequencies than the addition *above* the surface. In addition, the adsorption energies for the incorporation *into* the surface show different results for the two materials. For CaO, both angles of the carbonate to the surface give rise to exothermic energies, with the carbonate placed perpendicular to the surface being the most favoured. However, for the MgO surfaces, only the perpendicular carbonate is seen to be favoured, which is in agreement to the work of Jensen *et al* [29]. Although the vibrational frequencies for the monodentate adsorption are higher, indicating stronger bonding, than the bidentate mode, all adsorption energies for the adsorption of carbonate *above* the surface were found to be unfavourable.

These reference adsorption modes can be compared to the calculated vibrational frequencies for the lowest energy structures of the single carbonate adsorption on the {100} CaO and MgO surfaces. Table 4.6 contains the calculated frequencies, whilst the surface structures are given in Figure 4.10. The results show that for MgO, the lowest energy structure is very similar to the most stable reference mode found, where the carbonate is perpendicular to the surface. However, the results for the equivalent calculations for calcium oxide differ. The vibrational frequencies for this surface reside between the values for the adsorption of a carbonate *into* the surface with the two different angles to the surface. Analysis of the surface structure, Figure 4.10(a), shows that the carbonate on this surface rotates about the *z*-axis, so that the uppermost oxygen can coordinate to two calcium ions, rather than just one. This is achievable for CaO because of the longer *M*-O bond distance compared to MgO.

Table 4.6: Calculated vibrational frequencies for the lowest energy surfaces resulting from the adsorption of one carbonate molecule on the {100} CaO and MgO surfaces.

Surface	ν_1 / cm^{-1}	ν_2 / cm^{-1}	ν_{3l} / cm^{-1}	ν_{3h} / cm^{-1}
CaO	1096	785	1513	1664
MgO	1092	785	1478	1699

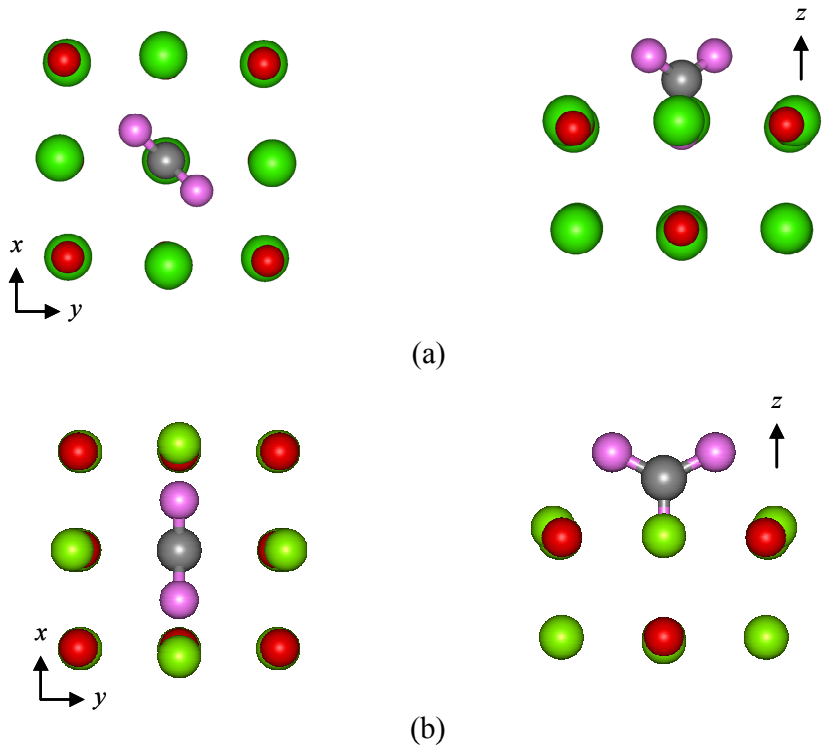

Figure 4.10: Plan and side views showing the lowest energy minimised surface structures of the adsorption of one carbonate ion onto the **(a)** CaO and **(b)** MgO {100} surfaces.

This study of surface adsorption can also be extended to consider the energetic favourability of adding to a single carbonate ion to all the modelled surfaces. The results of this, including the change in surface energy, is given in Table 4.7.

Table 4.7: Change in surface free energies from the pure surface and the associated free adsorption energies upon adsorption of a single carbonate molecule for the surfaces of calcium and magnesium oxide.

Material	CaO				MgO			
Surface	{100}	{110}	{111}	{310}	{100}	{110}	{111}	{310}
Change in γ upon carbonation / J m^{-2}	-0.23	-0.78	-1.21	-0.36	-0.06	-0.13	-2.08	-0.20
E_{ads} (CO_2) / eV	-1.32	-1.62	-3.07	-1.70	-0.29	-0.23	-4.00	-0.74

The results indicate that the adsorption of a single carbonate is favourable for all the modelled surfaces. In addition, adsorption onto the step of the {310} surfaces is calculated to be more energetically favourable than on the flat terrace of the {100}. However, as the pure {100} surface energy is originally lower than the {310} surface, the {100} surface remains the lowest in energy, showing that the step continues to destabilise the surface. Adsorption onto the calcium oxide surfaces again show increased reactivity when compared to the magnesium surfaces, as was seen for the adsorption of water. In accordance with the pure surface, the least stable {111} surface remains the highest in energy, although a decrease in surface energy is seen upon carbonation, with a large adsorption free energy, indicating the instability of this polar surface. Previous work by Jensen *et al*. [29] using cluster-based calculation showed that bonding to the {100} surface occurs in a monodentate manner, which is also seen in this study, monodentate bonding *into* the surface rather than *above* the surface. Comparable adsorption energies are also seen for terrace site. Jensen *et al*. reported adsorption energies of -1.04 and +0.13eV for CaO and MgO terrace sites, respectively. The energetically more favourable energies from this study may be a result of the contribution from van der Waals interactions which are intrinsically present in empirical derived potentials and were not included in the quantum mechanical calculations. Additional differences come from the fact that our simulations use periodic boundary potential-based calculations rather than DFT cluster calculations.

4.5.2 Increasing the Carbonate Coverage

The advantage of using periodic boundary calculations is that the effect of surface coverage can easily be investigated. The effect of surface coverage on both the adsorption mode and surface stability was begun by considering carbonation of a second carbonate group. This was added in a similar manner to the approach described above, with the location of the second carbonate unit trialled across all available surface adsorption sites. The lowest energy structures were found to drop in surface energy from 0.78 and 1.29Jm^{-2} for the pure {100} surfaces to 0.36 and

1.22J m^{-2} for CaO and MgO, respectively. Adsorption energies of -1.19 and -0.15eV were also calculated, indicating that on comparison to the adsorption of a single carbonate, the process of adding two molecules is more favourable. The adsorption energies also indicate that this reaction is far more favourable for the calcium oxide surface than its magnesium equivalent. This adsorption can be further assessed through consideration of the vibrational frequencies, Table 4.8, and the surface structures, Figure 4.11.

Table 4.8: Calculated vibrational frequencies for the lowest energy surfaces resulting from the adsorption of two carbonate molecules on the {100} CaO and MgO surfaces.

Surface	ν_1 / cm^{-1}	ν_2 / cm^{-1}	ν_{3l} / cm^{-1}	ν_{3h} / cm^{-1}
CaO	1094-1095	775-795	1522-1527	1646-1651
MgO	1102-1104	767-798	1517-1522	1680-1682

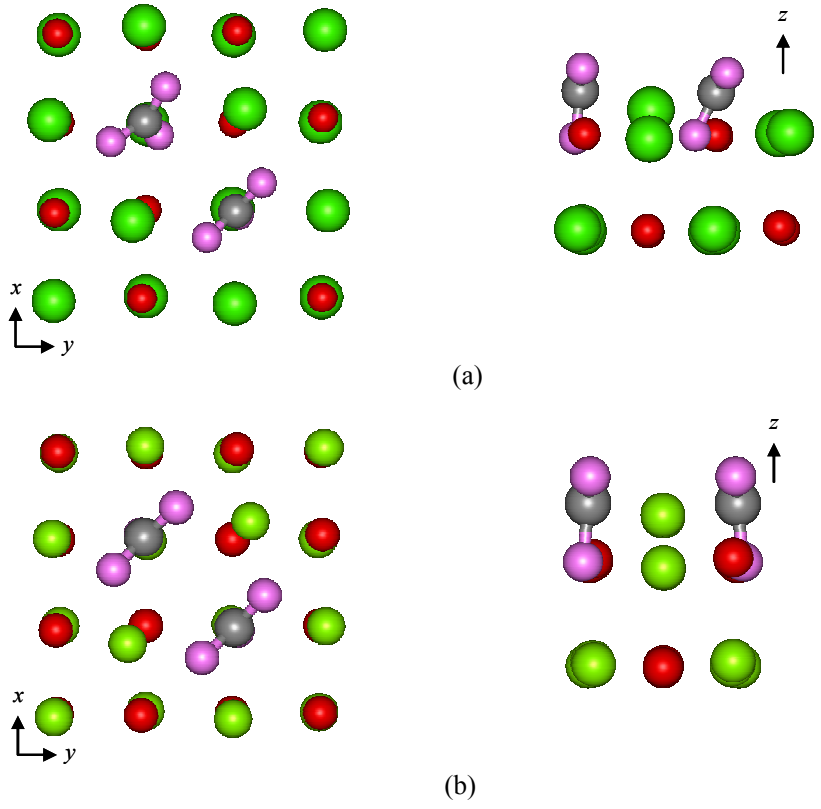

Figure 4.11: Plan and side views showing the lowest energy minimised surface structures of the adsorption of two carbonate ions onto the **(a)** CaO and **(b)** MgO {100} surfaces.

Comparisons to the vibrational frequencies of the single reference modes for CaO and MgO, given Tables 4.4 and 4.5, respectively, show that the adsorption of two carbonate groups are most comparable to the adsorption of a carbonate *into* the surface. Indeed, this is further supported by the surface structures of the relaxed structures. However, the frequencies are slightly higher than the adsorption of a single molecule. This can be rationalised from the surface structure, where both carbonates are clearly adsorbed *into* the surface. It can also be seen that the carbonates prefer to cluster together rather than adsorbing at separated distances. This clustering allows the displacement of the metal atoms, which are sandwiched between the carbonates, out of the surface. The formation of this surface [$M_2(CO_3)_2$] unit enforces further rigidity on the carbonate group, through the formation of bonds from all the oxygen atoms of the carbonate to metal atoms, increasing the vibrational frequencies. The CaO surface additionally shows that one of the carbonate group angles toward the surface, thus creating a bond to a surface calcium atom. This is most likely a result of the relative size of the calcium atoms to magnesium, which is also supported by the carbonates angling toward the central metal atoms on the magnesium oxide surface.

A larger range of coverages can also be analysed to consider the effect this has the average surface free energy and adsorption energy upon carbonation. This was achieved by varying the amount of carbonate up to monolayer coverage for the surfaces. Figure 4.12 shows plots of these results for the two materials.

The results show similar trends to the adsorption of water, with the energies of CaO again lower than the corresponding MgO surfaces and steric interactions causing increased destability at high coverages. The {111} surface, despite showing a large surface stabilisation and associated adsorption energy, remains the highest in energy. The {110} surface, as with the adsorption of a single carbonate has different results for the two different materials. For calcium oxide, carbonation is seen to reduce the surface energy, with the surface energy approaching a similar value to the

{100} surface. However, for MgO, although increased carbonation does reduce the surface energy, it remains less stable than the {100} surface.

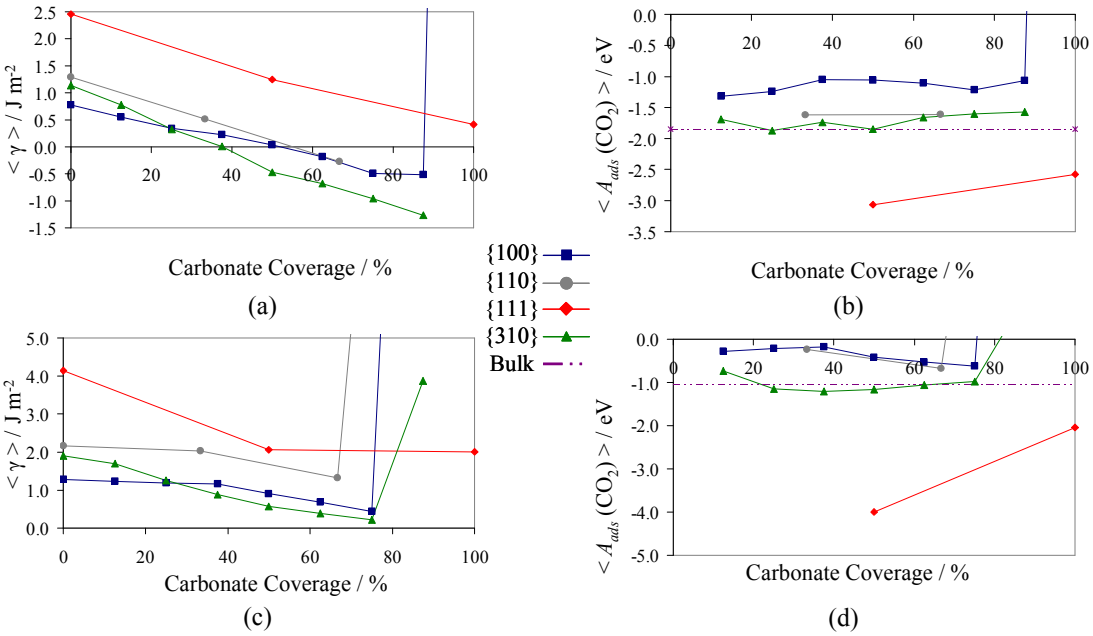

Figure 4.12: Plots of **(a)** average surface free energy and **(b)** average free adsorption energies for CaO as a function of surface coverage, and plots **(c)** and **(d)** show the same respective plots for MgO.

The presence of the step on the {310} surface, when compared to the {100} surface, shows a similar behaviour for carbonation to that seen for surface hydroxylation. Specifically, that after the adsorption of two carbonate groups on the surface the order of stability of the two surfaces switches, with the {310} surface possessing a lower energy. The {310} surface then remains lower in energy with increasing carbonate coverage. Further analysis of the carbonation of the {310} surface shows that carbonation preferentially forms on the step edges prior to carbonation of the {100} terrace. This is highlighted by the minimum energy MgO surfaces at 12.5% and 25% coverage, Figures 4.13(a) and (b), respectively. The adsorption of the first carbonate occurs inside the step at the start of the longer terrace, forming a more regular surface structure. The second molecule then coordinates with the other step, causing the first adsorbed molecule and coordinated

metal atom to rearrange to the top of the step allowing the clustering of the carbonate molecules. This also has the effect of removing the double step motif, creating a single step of double height, which may well be able to be studied using surface sensitive techniques, such as AFM. The CaO {310} surface also shows an identical effect. Despite the surface stabilisation after the removal of one step resulting in a higher surface energy than the {100} surface, the more negative adsorption energy indicates that this process would be more energetically favoured. Additionally as the adsorption energies for the {310} surface remain lower than the {100}, it is more energetically favourable to carbonate the stepped surface regardless of surface coverages. The adsorption energies can also be compared with the energy of the bulk reaction, forming carbonate mineral, labelled as bulk in Figures 4.12(b) and (d) and calculated using values from Table 4.3. It can be seen that this value correlates favourably with the {310} adsorption energies for both calcium and magnesium oxides. In particular, the closest match is with magnesium oxide. The {310} represents the closest to a real surface, thereby indicating that surface carbonation should indeed be favourable for the {310} surface.

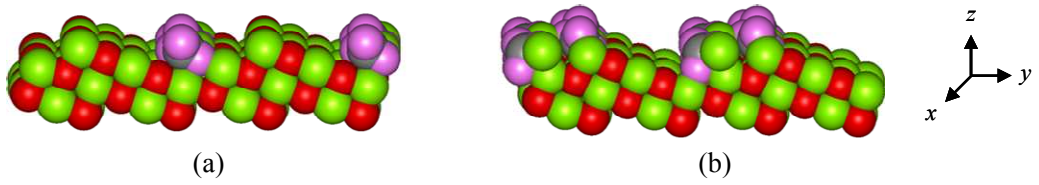

(a) (b)

Figure 4.13: Surface structure of the minimum energy carbonated {310} MgO surfaces with a surface coverage of **(a)** 12.5% and **(b)** 25% coverage.

A further way of distinguishing the surface coverages, and providing predictions for experiment, is by calculating vibrational frequencies of the lowest energy carbonated surfaces for the different surface terminations. As these surfaces will be considerably more complex than the surfaces with a single carbonate it is now not feasible to try to identify individual adsorption modes but we can directly compare these with the relevant carbonate mineral. Thus, a one-layer thick slab of the

relevant metal carbonate, magnesite for $MgCO_3$ and calcite for $CaCO_3$, was analysed and compared directly. The lowest energy surface for these mineral carbonates is the $\{10\bar{1}4\}$ surface and has therefore been used to generate the slabs. Tables 4.9 and 4.10 show the calculated vibrational frequencies of the lowest energy surfaces and the layer of carbonate mineral for CaO and MgO, respectively.

Table 4.9: Calculated vibrational frequencies of the lowest energy carbonated CaO surfaces, form the variation of coverage study, with their associated surface coverage, and a one-layer slab of $\{10\bar{1}4\}$ calcite, $CaCO_3$.

Surface	ν_1 / cm^{-1}	ν_2 / cm^{-1}	ν_{3l} / cm^{-1}	ν_{3h} / cm^{-1}
{100} 87.5% Carbonated Surface	1065-1085	771-795	1516-1548	1558-1591
{110} 66.7% Carbonated Surface	1082-1099	757-784	1542-1568	1594-1617
{111} 100% Carbonated Surface	1064-1076	779-788	1472-1510	1587-1590
{310} 87.5% Carbonated Surface	1087-1087	765-802	1516-1557	1559-1609
One-Layer $\{10\bar{1}4\}$ $CaCO_3$ Slab	1071	794	1540	1549

Table 4.10: Calculated vibrational frequencies of the lowest energy carbonated MgO surfaces, form the variation of coverage study, with their associated surface coverage, and a one-layer slab of $\{10\bar{1}4\}$ magnesite, $MgCO_3$.

Surface	ν_1 / cm^{-1}	ν_2 / cm^{-1}	ν_{3l} / cm^{-1}	ν_{3h} / cm^{-1}
{100} 75.0% Carbonated Surface	1055-1093	732-805	1486-1540	1545-1607
{110} 66.7% Carbonated Surface	1098-1098	746-782	1544-1561	1619-1647
{111} 100% Carbonated Surface	1057-1073	754-807	1440-1459	1572-1631
{310} 75.0% Carbonated Surface	1081-1096	755-797	1520-1564	1588-1638
One-Layer $\{10\bar{1}4\}$ $MgCO_3$ Slab	1078	791	1556	1563

Both materials show a good agreement of the calculated vibrational frequencies between the carbonated surfaces and the layer of mineral carbonate. Thus indicating that the lowest energy surfaces of these carbonated surfaces are indeed in keeping with the formation of the mineral carbonate, which is the ultimate aim of carbon

sequestration. Slight variations in the values can be a cause of either the influence of the underlying oxide material or the difference in structure of the carbonate. The calcite and magnesite slabs have a distinct symmetric ordered structure, which gives rise to a small splitting between v_{3h} and v_{3l}. However, for the more disordered adsorbed carbonate layer, there is a larger splitting as the symmetry of the carbonate is reduced. Indeed, the existence of different carbonate polymorphs means that an alternative structure may be formed or simply an amorphous carbonate layer. Further testing is essential to understand this resultant mineral carbonate.

The comparison of the method used for the initial surface generation of the lowest energy structures also yields differing results to that of the single molecule addition. For the addition of both one and two carbonates on the {100} surfaces the incorporation *into* the surface gives the most stable minimised surface configurations. However, the lowest energy surfaces, with their increased surface coverage, are formed by carbonate addition *above* the surface. Analysis of the surface structures indicates that the reason for this change is the result of the formation of a mineral carbonate layer for high coverage. Further analysis of the surface structure shows that the position of the oxygen vacancy prior to minimisation is adjacent to carbonate units. However, the extensive surface reconstruction around the vacancy position means that it cannot be clearly identified on the relaxed surface structure. Overall, this indicates that surface carbonation on a pure surface would proceed by the incorporation of individual molecules into the surfaces. As the carbonate coverage increases, subsequent molecules will also insert directly into the surface, clustering to form localised regions of carbonate. Continued coverage, approaching a monolayer, will facilitate the formation of a distinct mineral carbonate layer directly on the surface, with the region underneath consisting of the pure mineral oxide.

Overall the results show that the carbonation of the low index surfaces is energetically favourable, with the most reactive surface being the {310} surface, resulting in the lowest energy surfaces with reasonably exothermic adsorption energies. As the {310} was observed to be more stable than the {100}, the presence

of the steps can be inferred as increasing the reactivity of both the calcium and magnesium oxide surfaces. In addition, the CaO surfaces are seen to be more reactive than the MgO equivalents, through the more exothermic adsorption energies. This mimics what is observed for silicate minerals, where wollastonite, $CaSiO_3$, is found to more effective at sequestering carbonate than the magnesium silicate olivine and serpentines [154]. These results do also offer data for the energetics of CO_2 adsorption and reaction under dry conditions as found in high temperature processes. Sequestration at lower temperatures will also involve competition with water for active sites, which we consider next.

4.5.3 The Competition between Carbonate and Water

In reality, a real chemical surface will be in contact with more than one species and the competition between different adsorbates will be key factor in determining the processes which can occur. To help understand the process of surface carbonation in the presence of water we can first compare the surface free energies to evaluate the relative stability provided by the different species. On comparing the results from the individual studies we can consider two separate energies, firstly the adsorption of a single molecule and secondly the lowest energy structure found, regardless of the surface coverage. Table 4.11 compares the first of these energies, for adsorbing a single molecule on each surface.

The results indicate that for CaO there is a preference for surface carbonation over hydration on both the {100} and {110} surfaces. However, for the {111} and {310} surfaces, hydroxylation gives a similar reduction in surface energy, with a larger adsorption energy, indicating its preference to hydroxylation. In contrast, the MgO surfaces, with the exception of the {100} surface, show a stronger preference to hydroxylation. The results also indicate a certain degree of hydrophobicity on the {100} surfaces, as shown by a small positive change in surface energy but a negative value for the adsorption energy. This is due to the adsorption energy being less than

the heat of vaporisation, 0.45eV, indicating that the adsorbed water would be more stable as liquid water than an adsorbed gaseous molecule.

Table 4.11: Adsorption energies and changes in the surface free energy from that of the pure surface following the adsorption of a single carbonate ion, water molecule and hydroxide/proton on the surfaces of CaO and MgO.

Material	CaO				MgO			
Surface	{100}	{110}	{111}	{310}	{100}	{110}	{111}	{310}
$\Delta\langle\gamma\rangle$ / J m^{-2}	**-0.23**	**-0.78**	**-1.21**	**-0.36**	**-0.06**	-0.13	-2.08	-0.20
A_{ads} (CO_2) / eV	-1.32	-1.62	-3.07	-1.70	-0.29	-0.23	-4.00	-0.74
$\Delta\langle\gamma\rangle$ / J m^{-2}	+0.03	-0.09	-0.38	-0.15	+0.01	-0.18	-0.82	-0.13
A_{ads} (H_2O) / eV	-0.26	-0.64	-1.40	-1.14	-0.43	-0.74	-2.01	-0.90
$\Delta\langle\gamma\rangle$ / J m^{-2}	-0.07	-0.34	**-1.18**	**-0.34**	+0.10	**-0.41**	**-2.22**	**-0.43**
A_{ads} (H-OH) / eV	-0.83	-1.14	-3.84	-2.02	-0.03	-1.09	-4.68	-1.94

We can further investigate the competiveness by considering the lowest energy surface, regardless of coverage, shown by Table 4.12, again not allowing mixed adsorption. For the CaO surfaces, similar trends are seen to the single molecule adsorption. The major exception to this is the {111} surface where hydroxylation dominates giving rise to the most stable surface, as expected. In contrast, the MgO surfaces are somewhat different to the results of the single molecule adsorption, with hydroxylation no longer providing the most surface stability, again with the exception of the {111} surface. For the {100} surface, hydration gives considerable stabilisation, however, for the {110}, all three adsorption processes give a similar degree of surface stabilisation and adsorption energy. This thereby indicates that the competition between these surface processes will be important for this surface.

The {310} surfaces for both materials are also qualitatively similar, with carbonation dominating the high coverage surfaces. For the adsorption of a single molecule, hydroxylation was seen to provide either greater or comparable

stabilisation to carbonation. As the most favourable adsorption site on this surface is the step, these results indicate that hydroxylation provides the most stabilisation for this low-coordination site, however, as coverage increases onto the terrace, due to the removal of the step, carbonation will dominate.

Table 4.12: Adsorption energies and changes in the surface free energy from that of the pure surface of the lowest energy carbonated, hydrated, and hydroxylated surfaces of CaO and MgO. Surface coverage is shown as both the percentage of monolayer coverage, θ, and surface concentration.

Material	CaO				MgO			
Surface	{100}	{110}	{111}	{310}	{100}	{110}	{111}	{310}
$\theta_{Carbonation}$ / %	87.5	66.7	100.0	87.5	75.0	66.7	100.0	75.0
$[CO_3^{2-}]$ nm^{-2}	7.6	6.1	5.0	9.6	8.5	8.0	6.5	10.8
$\Delta\langle\gamma\rangle$ / J m^{-2}	**-1.29**	**-1.57**	-2.05	**-2.40**	-0.85	**-0.84**	-2.13	**-1.69**
A_{ads} (CO_2) / eV	-1.06	-1.62	-2.57	-1.57	-0.62	-0.67	-2.05	-0.98
$\theta_{Hydration}$ / %	87.5	100.0	100.0	87.5	87.5	66.7	100.0	87.5
$[H_2O]$ nm^{-2}	7.6	9.1	5.0	9.6	9.9	8.0	13.1	10.8
$\Delta\langle\gamma\rangle$ / J m^{-2}	-0.63	-0.64	-1.26	-0.91	**-1.08**	**-0.81**	-2.94	-1.20
A_{ads} (H_2O) / eV	-0.97	-0.88	-1.24	-1.14	-1.13	-1.09	-1.85	-1.01
$\theta_{Hydroxylation}$ / %	87.5	66.7	100.0	87.5	75.0	66.7	100.0	75.0
[H-OH] nm^{-2}	7.6	6.1	5.0	9.6	8.5	8.0	6.5	10.8
$\Delta\langle\gamma\rangle$ / J m^{-2}	-0.57	-0.54	**-2.71**	-1.48	-0.22	**-0.87**	**-4.21**	-1.07
A_{ads} (H-OH) / eV	-0.92	-1.00	-3.84	-1.42	-0.61	-1.12	-4.46	-1.07

4.6 Mixed Water and Carbonate Adsorption

Although comparing the energies of the individual processes is useful in understanding the relative stability given to the surfaces by the different competing species to adsorption, it does not provide any information any cooperative effects

that mixed adsorption may provide. Thus, we modelled the co-adsorption of both water and carbonate. We did not have sufficient computer resources to consider all possible configurations so for the purposes of this mixed adsorption, and to reduce the total number of individual simulations needed, the lowest energy surface at each coverage level of carbonate was taken as the starting configuration. For each surface, the total number of adsorption sites available was determined and they were then hydrated, from one molecule to monolayer coverage, and then the equivalent operation was performed for hydroxylation. The calculated free energies from these simulations were then used to generate surface phase diagrams as a function of the chemical potentials of gaseous carbon dioxide and water.

The following approach was used for calculating the surface free energies of adsorption. First, the corrected free energy of the surface calculation, A^S_{MO}, was calculated from the previously derived free energies, A_S, using Equation 4.6:

$$A^S_{MO} = A_S - n_{CO_3^{2-}} E_{corr}(CO_3^{2-}) - n_{H_2O} E_{corr}(H_2O) - n_{H\text{-}OH} E_{corr}(H\text{-}OH) \qquad 4.6$$

By correcting the energy of the surface component for the number of adsorbates we can rewrite the expression for surface energy in terms of the number of species in the surface calculation, n, and their change in chemical potential, $\Delta\mu$:

$$\gamma = \frac{1}{S}\left(A^S_{MO} - n_{MO}\mu_{MO} - n_{CO_2}\mu_{CO_2} - n_{H_2O}\mu_{H_2O}\right) \qquad 4.7$$

where *M*O refers to either CaO or MgO. As the surface is in equilibrium with the bulk, its energy, E_{MO}, can be used to calculate the chemical potential of the mineral oxide, assuming that the entropic contribution to bulk free energy, G_{MO}, is negligible:

$$G_{MO} = E_{MO} = m\mu_{MO} \qquad 4.8$$

where m is the number of formula units in the bulk simulation. Additionally, this value is the same as E_B, as defined in Equation 4.1. We can also define the excess, Γ, for both carbon dioxide and water by Equations 4.9 and 4.10, respectively.

$$\Gamma_{CO_2} = \frac{n_{CO_2}}{n_{MO}} = \frac{1}{S} n_{CO_2} \qquad 4.9$$

$$\Gamma_{H_2O} = \frac{n_{H_2O}}{n_{MO}} = \frac{1}{S} n_{H_2O} \qquad 4.10$$

By combining Equations 4.7, 4.8, 4.9 and 4.10, we can now obtain an equation for calculating the surface free energy as a function of the change in chemical potential of carbon dioxide and water:

$$\gamma = \frac{1}{S}\left(A_{MO}^{S} - \frac{n_{MO}}{m} E_{MO} \right) - \Gamma_{CO_2} \Delta\mu_{CO_2} - \Gamma_{H_2O} \Delta\mu_{H_2O} \qquad 4.11$$

Additionally, the change in chemical potential as a result of the temperature can be determined by Equation 4.12:

$$\Delta\mu_{H_2O}(T) = T^{o} \cdot s_{H_2O}(T^{o}) + \Delta h_{H_2O}(T^{o}, T) - T \cdot s_{H_2O}(T) \qquad 4.12$$

where s and h are the entropy and enthalpy, which can be obtained from experimental data [132]. Although Equation 4.12 refers solely to water vapour, an identical expression can be obtained for gaseous carbon dioxide. Additionally, assuming that the water vapour and carbon dioxide act as ideal gases, then the effect of the partial pressure, p, on the change of chemical potential can be calculated using Equation 4.13, where an identical expression can again be written for carbon dioxide.

$$\Delta\mu_{H_2O}(T) = \frac{1}{2} k_B T \log\left(\frac{p_{H_2O}}{p^{o}} \right) \qquad 4.13$$

This technique allows the surface energy to be calculated for any temperature and vapour phase composition, following the procedure described for both alumina and calcite in past studies using *ab-initio* calculation [155, 156]. The use of potential models allows for a computationally cheaper exploration of configurational space. Therefore, if the configurational space is efficiently explored, we can have confidence that all the significant local minima have been found, making the results reliable. The comprehensive study of carbonate and water adsorption in this study therefore allows us to generate similar surface phase diagrams for the {100}, {110}, {111} and {310} surfaces of CaO and MgO respectively, Figures 4.14 to 4.17, respectively. The vertical and horizontal lines represent the chemical potentials of the gases at a pressure of 1 bar and a temperature of 0K (long-dashes), 298K (solid lines) and 1000K (short-dashes). An additional scale is also added to represent the partial pressures of the gases at 298K.

It is immediately apparent from the generated surface phase diagrams that, in accordance with the previous study of surface carbonation, the calcium oxide surfaces are considerably more susceptible to the adsorption of carbon dioxide. The {100} CaO surface, Figure 4.14(a), shows that at atmospheric conditions, 3% CO_2 and a vapour pressure of water of 26.7torr [132], as highlighted by the black circle, the surface will comprise solely as the product of surface carbonation, although below maximum coverage. However, small increases in the water concentration would result in the co-adsorption of water, reducing the amount of surface carbonation significantly. The MgO equivalent, Figure 4.14(b), shows preference to the adsorption of water. At standard conditions this is seen to equate to a 0.62 monolayer coverage of water on this surface, which compares favourably to the experimental work of Xu and Goodman [13] who reported a 0.67 monolayer coverage for this surface. Interestingly, it can be seen that merely reducing the partial pressure of water would not result in carbonation. The surface adsorption of carbon dioxide would also require an increase in concentration of the gaseous carbon dioxide.

The surface phase diagrams for the {110} surface of CaO and MgO, Figures 4.15 (a) and (b), respectively, show similar variations to the {100} surfaces. The calcium oxide surface shows the formation of the maximum coverage carbonated surface at standard conditions, making this appear favourable for carbon dioxide adsorption. The MgO equivalent, however, shows a mixed surface. In a similar manner to the {100} MgO surface, a reduction in water concentration would result in the loss of both adsorbed species, leading to the pure surface. This implies that some cooperation must occur between the species, stabilising the adsorption of carbon dioxide. In contrast, the {111} surfaces, Figure 4.16, show very different behaviour. As expected for these polar surfaces, at atmospheric concentrations there is a strong preference to water adsorption, namely in the formation of a hydroxylated surface. To achieve surface carbonation, significantly larger increases in the partial pressure of CO_2 are required, making this surface unsuitable for carbon sequestration, unless the surface could be dehydrated first.

The {310} surface phase diagrams, as shown in Figure 4.17, also show similarities to the corresponding {100} surfaces. The calcium oxide surface indicates maximum surface carbonation is achieved at standard conditions, indicating that the adsorption is enhanced by this stepped surface. The phase diagram also shows considerably less mixed phases than the {100} equivalent surface. The magnesium oxide surface also shows a greater reactivity towards carbonation than the {100} surface, additionally with a more complex surface phase diagram. At standard conditions, the most stable surface is formed by water adsorption alone. However, carbonation is easily achievable through either a small increase in the carbon dioxide partial pressure or decrease in the concentration of water.

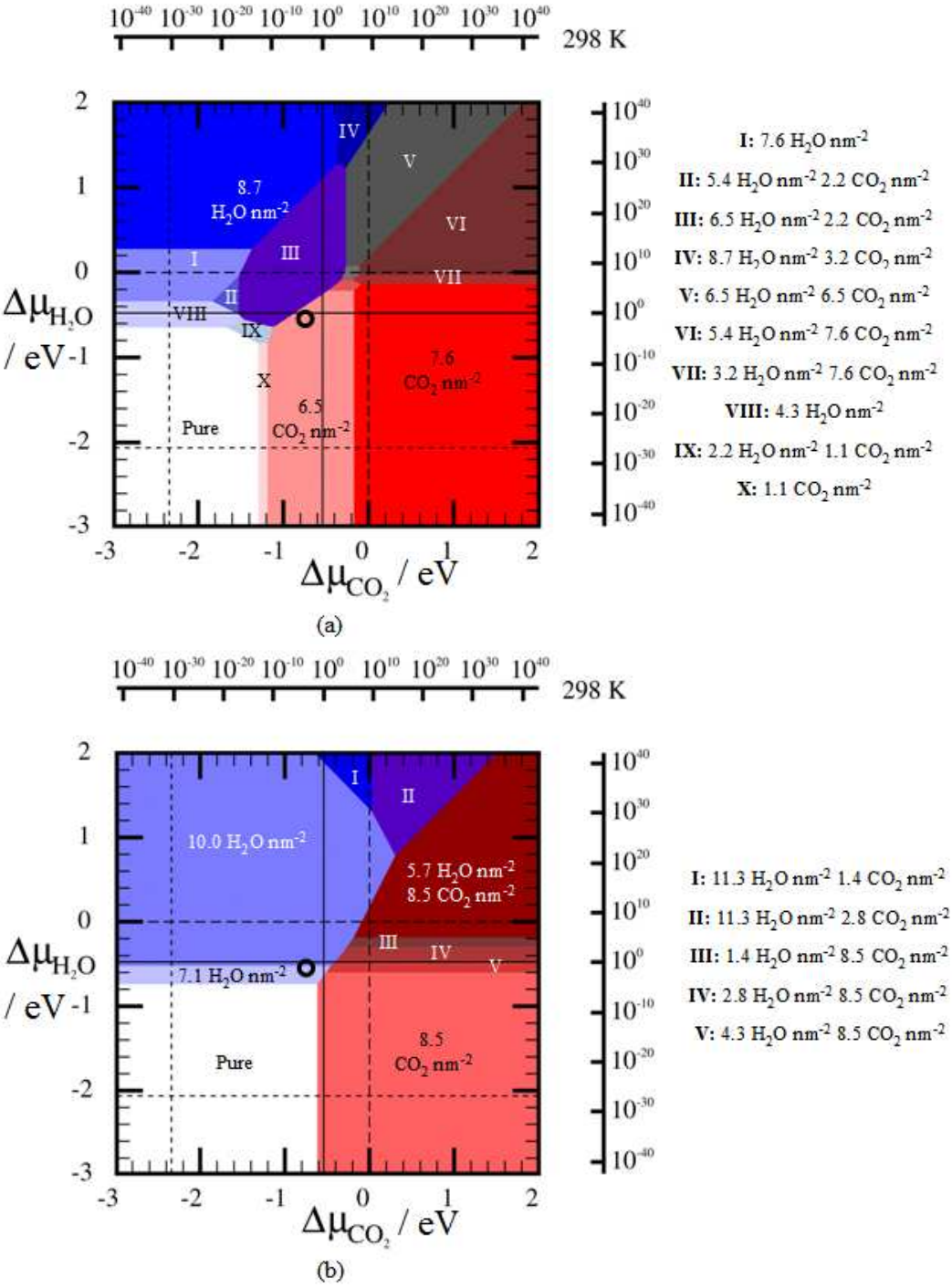

Figure 4.14: Surface phase diagrams of the **(a)** CaO and **(b)** MgO {100} surfaces as a function of the change in chemical potential of gaseous H_2O and CO_2. Right and top axes indicate the pressure of the gas (bars) at 298K and atmospheric conditions are given by the black circle.

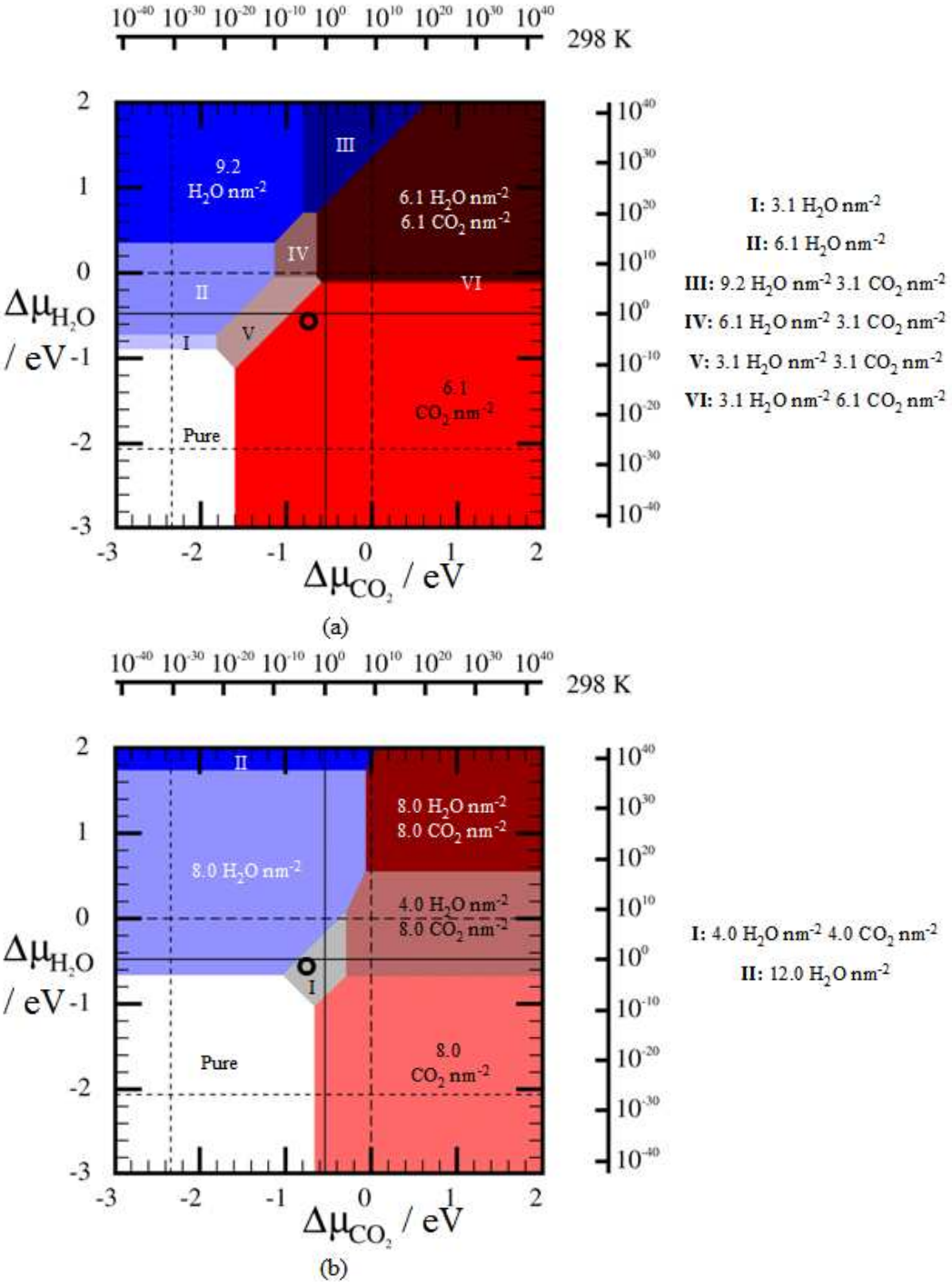

Figure 4.15: Surface phase diagrams of the **(a)** CaO and **(b)** MgO {110} surfaces as a function of the change in chemical potential of gaseous H_2O and CO_2. Right and top axes indicate the pressure of the gas (bars) at 298K and atmospheric conditions are given by the black circle.

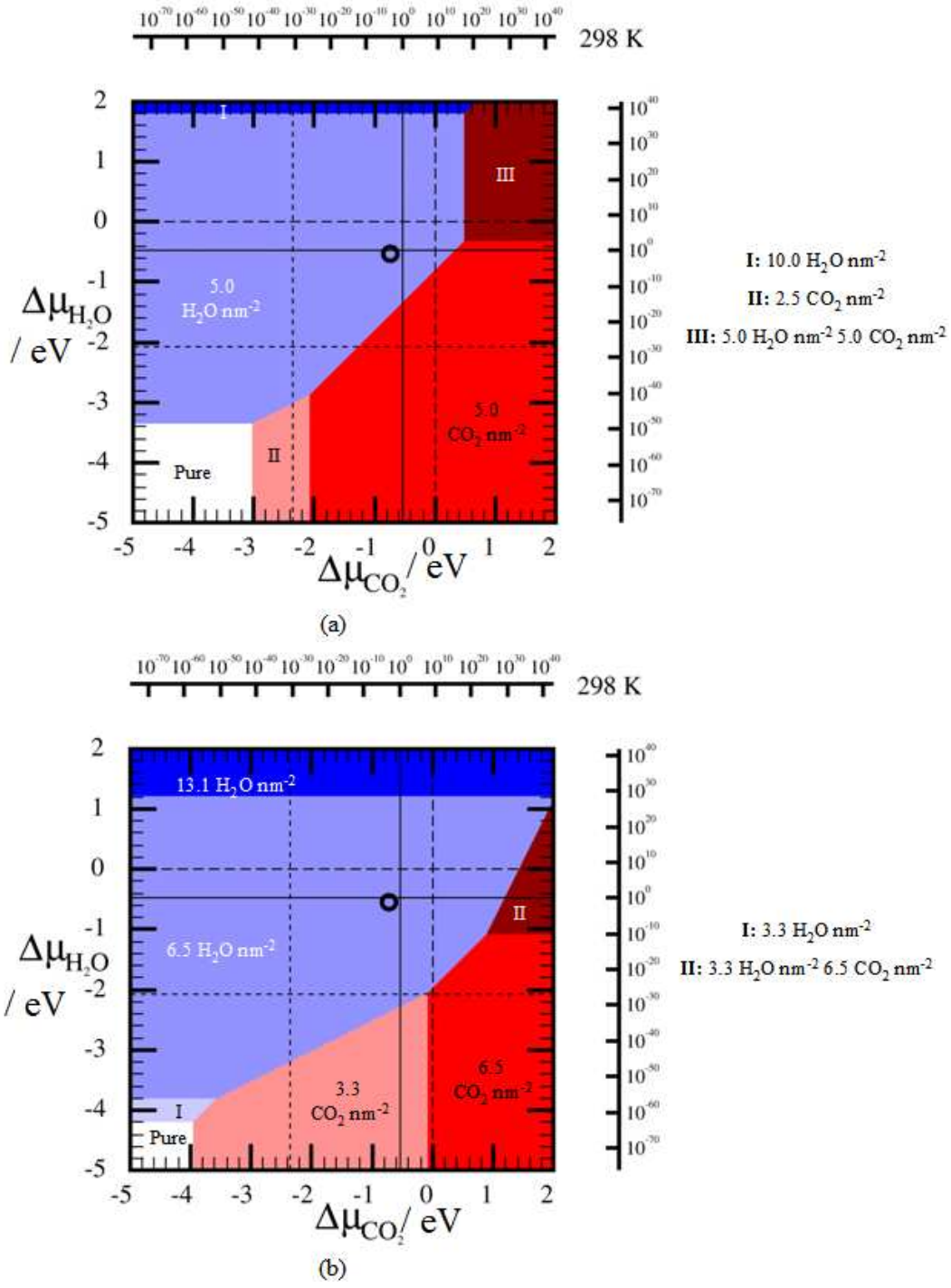

Figure 4.16: Surface phase diagrams of the **(a)** CaO and **(b)** MgO {111} surfaces as a function of the change in chemical potential of gaseous H_2O and CO_2. Right and top axes indicate the pressure of the gas (bars) at 298K and atmospheric conditions are given by the black circle.

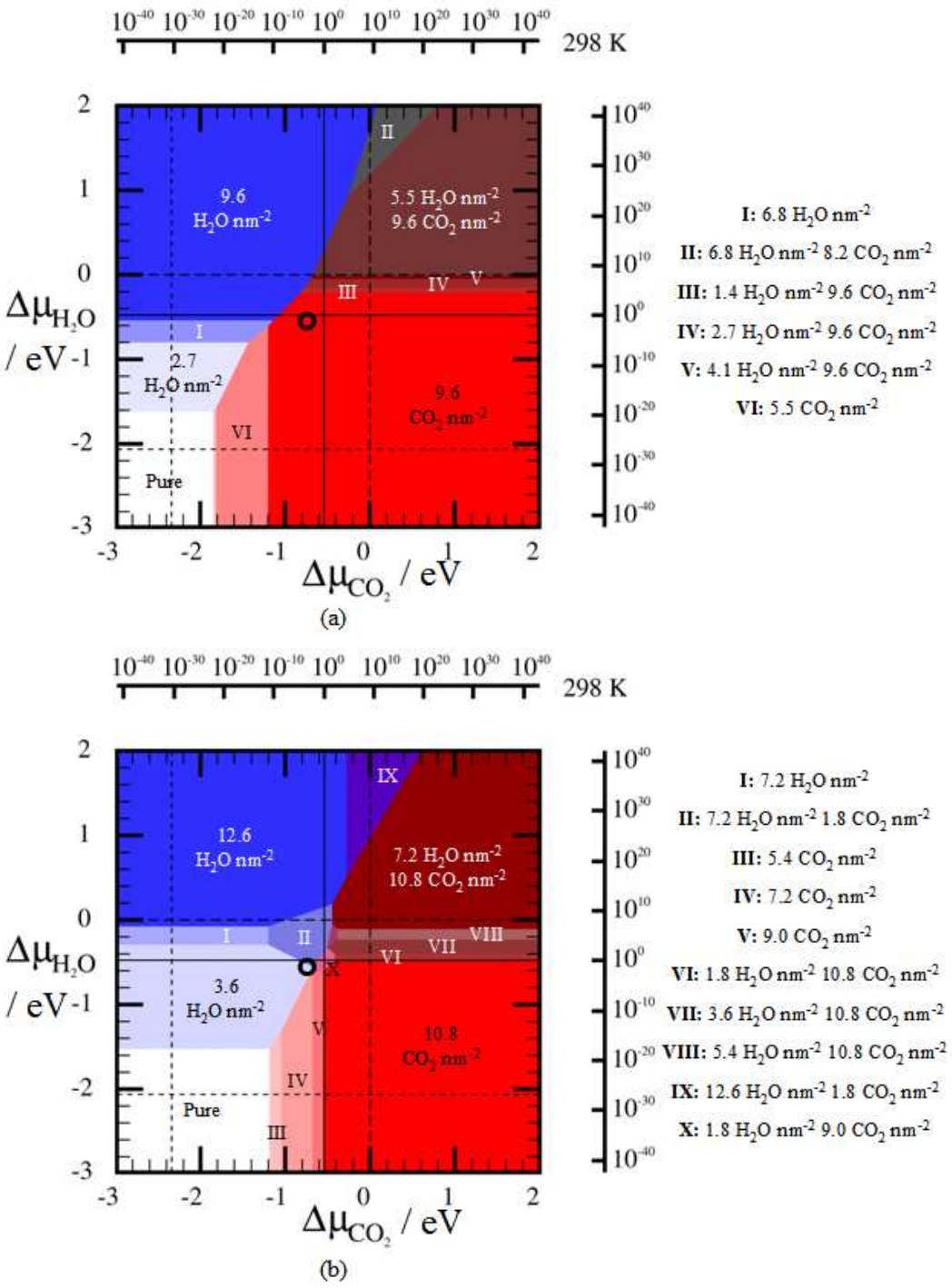

Figure 4.17: Surface phase diagrams of the **(a)** CaO and **(b)** MgO {310} surfaces as a function of the change in chemical potential of gaseous H_2O and CO_2. Right and top axes indicate the pressure of the gas (bars) at 298K and atmospheric conditions are given by the black circle.

In a similar way as for unit activity at 298K, the activity at 1000K can also be plotted to consider the effect of temperature. The small-dashed lines on Figures 4.14 – 4.17 indicate this unit activity. For all surfaces, with the exception of the {111}, at unit activity and 1000K the pure phase dominates, with the absence of any surface adsorbed carbonate or water. However, the {111} surfaces remain dominated by the hydroxylated layer at this high temperature. To consider the variation in partial pressure at 1000K, we can add similar scales to represent this. This is shown for the example of the CaO {100} surface in Figure 4.18. The figure shows that increasing the temperature not only leads to the surface being free of surface adsorbates but also that by increasing the temperature of the system the surface will adsorb less. As with many systems this will consequently lead to a trade off between kinetic and thermodynamic effects to find the most efficient manner of carbonating the surface, although no kinetic data has been calculated in this study.

We can also compare the surface phase diagrams with the results of adding a single molecule and the minimum energy surfaces for the different adsorption processes, Tables 4.11 and 4.12, respectively. The results of the minimum energy surfaces agree with the prediction of the most stable phase at atmospheric conditions. For the surfaces which showed similar surface and adsorption energies for both the addition of water and carbonation, for example, the MgO {110} surface, we find that the surface phase diagram indicates either a mixed phase, in this case, or that the position at atmospheric conditions is very close to a phase boundary. In contrast, agreement of the single molecule adsorption energies with the phase diagrams is not so clear. The only surfaces in which single molecule adsorption leads to the same conclusion are the {100} and {110} surfaces of CaO and the {111} MgO surface. Therefore, by modelling the adsorption of just a single molecule it is not possible, in general, to identify what the most energetically favourable process would be. To clearly identify this, the effect of coverage needs to be considered to identify the minimum energy configuration, which is possible through the use of potential-based approaches.

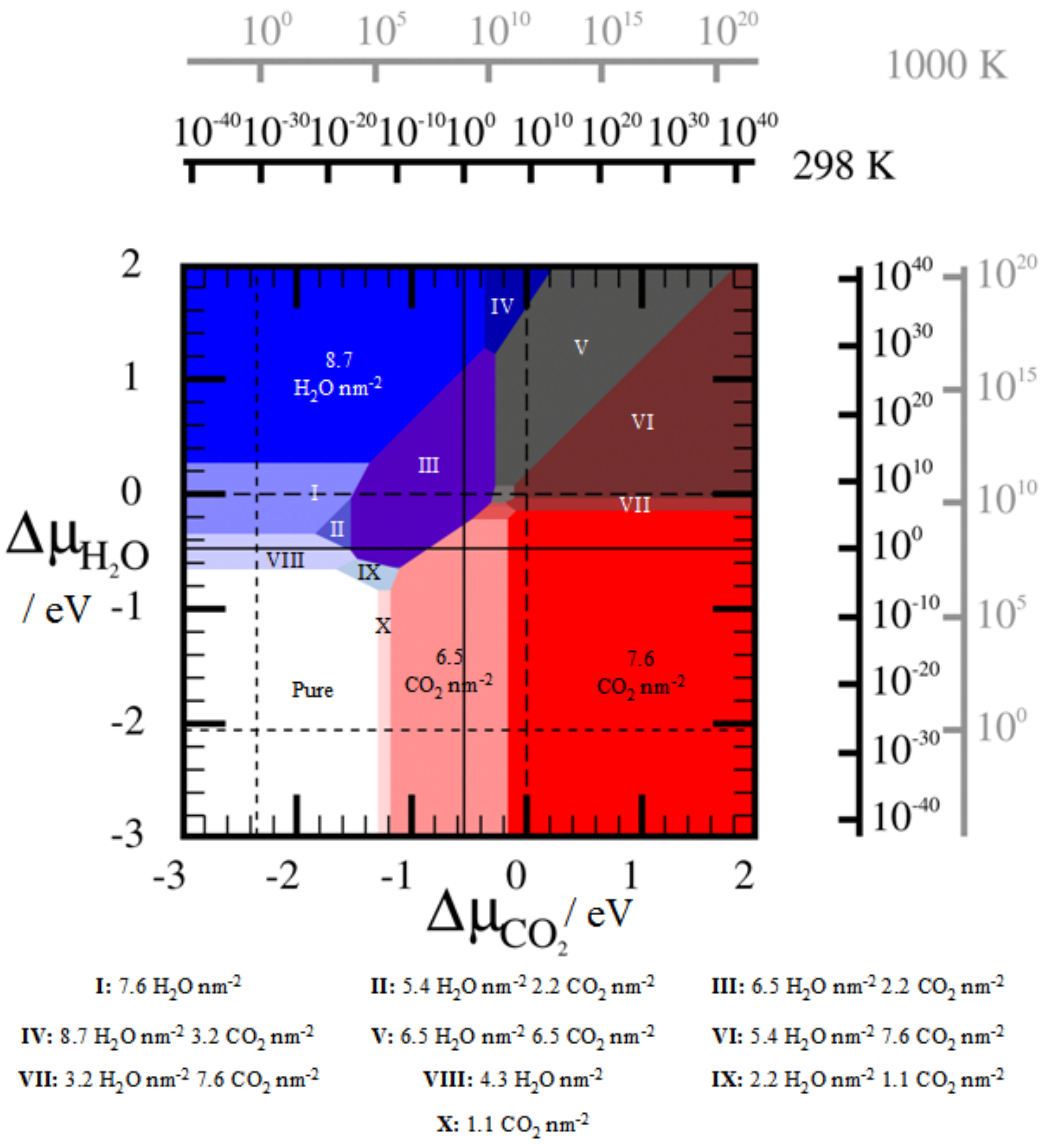

Figure 4.18: Surface phase diagram of the CaO {100} surface as a function of the change in chemical potential of gaseous H_2O and CO_2. Right and top axes refer to the pressure of that gas at 298K (black) and 1000K (grey), with units in bars.

As with all models, the assumptions used must be taken into account. Firstly this model assumes no chemical reactivity between the surface adsorbates. However, reaction between adsorbed water and carbonate species is indeed possible, for example, leading to the formation of bicarbonate ions. Future work could begin to

address this deficiency by modelling the surface adsorption of bicarbonate ions, also considering the effect of surface coverage. The resulting energies from this could then be directly compared with the energies of carbonation and water adsorption to gain insight into the favourability of the different processes. Electronic structure calculations would also be required to consider the surface reactions with carbon dioxide in more detail. Additionally, the adsorption of water is considered as solely consisting of hydration or hydroxylation. However, a mixture of these processes is feasible. Indeed, previous studies of the {100} MgO surface indicates that surface sites of lower coordination will favour hydroxylation, for example, Duński *et al*. [157] allowing the formation of a mixed surface. This will obviously be important for surfaces which are either defective or have a structure that gives rise to a variation in coordination number. The maximum surface coverage in this study was also considered to be the formation of one monolayer. However, increased coverage over this amount could indeed occur and give rise to more stable surfaces. In addition, this model does not allow for any surface reconstructions, other than as a result of the minimisation process.

4.7 Chapter Conclusions

This chapter has used potential-based static lattice minimisation techniques to study the surface carbonation, hydration and hydroxylation processes on the low index surfaces of calcium and magnesium oxides. An understanding of these processes is essential to find an effective agent for use in carbon sequestration. Additionally, these materials can also act as model systems which can give insight for the use of higher oxide materials, such as silicates and serpentines. In this study we have trialled the use of e-science tools for submitting and processing many related datasets on different computers. The use of a potential-based approach also allows for the simulation of a large number of different surface configurations, allowing an evaluation of surface free energies. These free energies have also been used to obtain for the first time free energy surface phase diagrams from potential-based simulations.

The results of this study have shown that carbonation of the low index surfaces of calcium and magnesium oxide are suitable for carbon sequestration. Steps on the surface have also been shown to enhance the surface reactivity, particularly toward surface carbonation and hydroxylation. Carbonation of the surfaces is calculated to occur primarily through adsorption *into* the surface, with clustering seen as coverage increases. As the amount of surface carbonate approaches monolayer coverage, the formation of a layer of mineral carbonate is predicted, as supported by the analysis of vibrational frequencies. Additionally, the presence of steps on the surface is seen to enhance reactivity, allowing for the formation of the most stable surfaces.

Carbonation of the surfaces is also calculated to be considerably more favourable on the calcium oxide surfaces than on the magnesium equivalents, due to the difference in Madelung energy of the surfaces. This also causes carbonate to compete favourably with the adsorption of water for the CaO surfaces, and is supported by examination of the surface phase diagrams. Thus, the carbonated CaO surfaces are predicted to be the most stable surface phase at atmospheric conditions. In contrast, the MgO surfaces are less selective, with many surfaces showing either a mixed carbonate/water surface at atmospheric conditions or dominated by water adsorption. Therefore, the simulations suggest that modification of the MgO surface would be required to enhance its reactivity toward carbon sequestration. However, as the stepped {310} surface is seen to be more reactive than the flat {100} surface, this should indeed be possible. Further to this, increasing the temperature of the system is also seen to make them less reactive toward carbonation, reducing the surface coverage. Therefore, further study is required to consider the kinetics of surface carbonation to help understand the trade off between kinetic and thermodynamic factors.

One of the main deficiencies of static lattice minimisation techniques, despite giving valuable information regarding the surface structure, is that does not provide any dynamical data as temperature is neglected. The next chapter will discuss further extensions to this work which uses molecular dynamics simulation not only to allow

movement of the surface ions over time but by also considering the interactions of the surface with liquid water, moving towards the modelling of more realistic systems. In addition, the adsorption on nanoparticulate surfaces will be considered, as opposed to the effective infinite planar surfaces examined here.

Chapter Five

Dynamic Surface Properties

The aim of this chapter is to use molecular dynamics to investigate the mineral interface with liquid water. Molecular dynamics has the advantage of treating liquids explicitly, therefore giving a better representation of their properties. The effect of the surface adsorption of carbonate on this interface is also considered. A further improvement to earlier studies is that the interaction of water will consider more complex surface configurations, in this case nanoparticles. This work will consider the effects of nanoparticle size and surface hydroxylation on magnesium oxide nanoparticles. The results of the previous chapter showed that calcium oxide is more effective for carbonation and hence the focus here will be the effect of surface carbonation on calcium oxide nanoparticles.

5.1 Modelling the Mineral – Water Interface

The mineral – water interface was initially considered by the addition of water to the pure, uncarbonated slabs of calcium and magnesium oxide. Slabs of these materials were generated with a depth of approximately 20Å, bound on both sides with an identical surface structure. A water layer, approximately 20Å in width, was then added to one side of the slab. A vacuum gap was also added between the water and other surface, approximately 20Å in width, to prevent potential problems which can result from possible residual pressure occurring as a result of using the NVT ensemble. The simulations were also run with the NVE ensemble at 0K for 10ps followed by 1ns at 300K using the NVT ensemble, or until convergence in the configurational energy was seen, with a relaxation constant of 1.0ps.

The structure of the mineral – water interface was examined by considering the average density of the mineral and water components. The density can be viewed in two ways. First, we can consider the relative density between the metal ions and the oxygen of the water molecules. This is calculated by splitting the simulation cell into a series of bins and then measuring the average number of times a particular species enters it. Secondly, the density can be expressed as a function of the z-coordinate, where the z-direction is defined as being perpendicular to the surface. This allows the position of any layered structures or regions of high density to be seen and their relative distance to the surface to be considered. The z-density is defined as the average density of water relative to the density at z_0 and is defined by Equation 5.1 [158]:

$$\rho(z) = \frac{\langle n(z) \rangle}{n(z_0)} \qquad 5.1$$

where $n(z)$ and $n(z_0)$ are the number of water molecules at positions z and z_0, respectively. For the purpose of these calculations, z_0 was taken as being equal to one for the metal component, whereas for the oxygen component of water this was

equal to the bulk density. To allow the hydrogen atom density to be assessed, a value of twice the bulk density was used, therefore shifting the densities relative to the oxygen component.

The relative density and *z*-density plots for the {100}, {110}, {111} and {310} surfaces are shown in Figures 5.1 to 5.4, respectively, for calcium and magnesium oxides. Only the region surrounding the mineral – water interface is shown. For the average density plots, only high regions of density are shown and the slight smearing on the metal sites is caused by vibration about their lattice positions. The *z*-density plots, peak positions are measured in Å relative to the zero position, where the surface metal atoms furthest from a water molecule are considered to have a *z*-coordinate of 0.0Å. Additionally, red represents metal atoms whilst blue and green indicates the oxygen and hydrogen atoms of water, respectively. The *y*-axis is drawn in terms of relative water density; therefore providing a qualitative view of the simulation cell for the oxygen and hydrogen components.

The structure of water in contact with the oxide surface can be examined further by taking a slice of the cell containing only the uppermost layer of metal atoms and the first water layer and viewing down the *z*-axis onto the surface. The water structure above the magnesium oxide surfaces, are shown in Figure 5.5. For the purposes of these diagrams the hydrogen density is also included, although due to the complexity of the {310} surface only a portion of hydrogen atom density is displayed. Although not shown, similar water structures are observed for the equivalent calcium oxide surfaces.

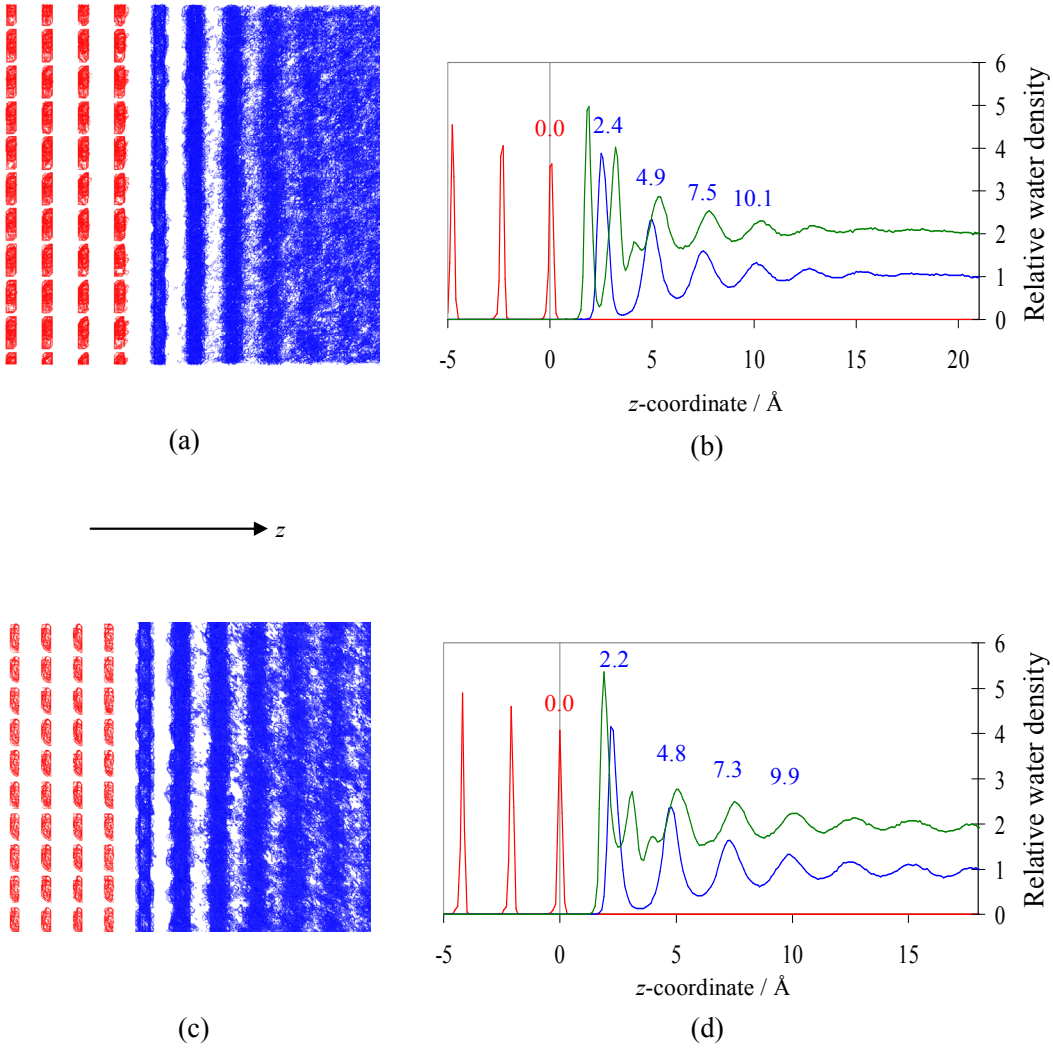

Figure 5.1: Plots showing the **(a)** relative water density and **(b)** *z*-density of the mineral – water interface for the CaO {100} surface. The same respective plots are shown for the MgO {100} surface in **(c)** and **(d)**. Metal density is shown in red and the oxygen and hydrogen of water in blue and green, respectively.

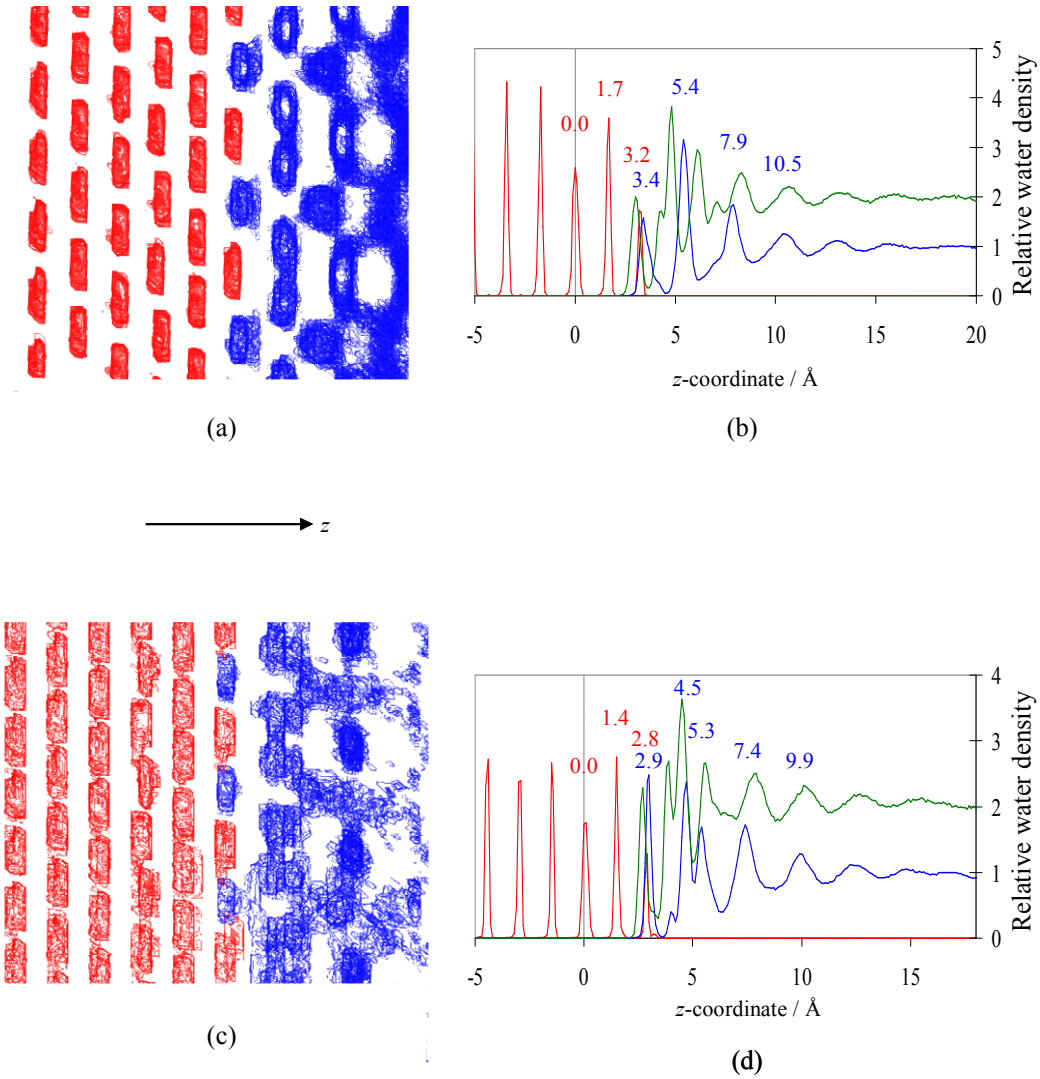

Figure 5.2: Plots showing the **(a)** relative water density and **(b)** *z*-density of the mineral – water interface for the CaO {110} surface. The same respective plots are shown for the MgO {110} surface in **(c)** and **(d)**.

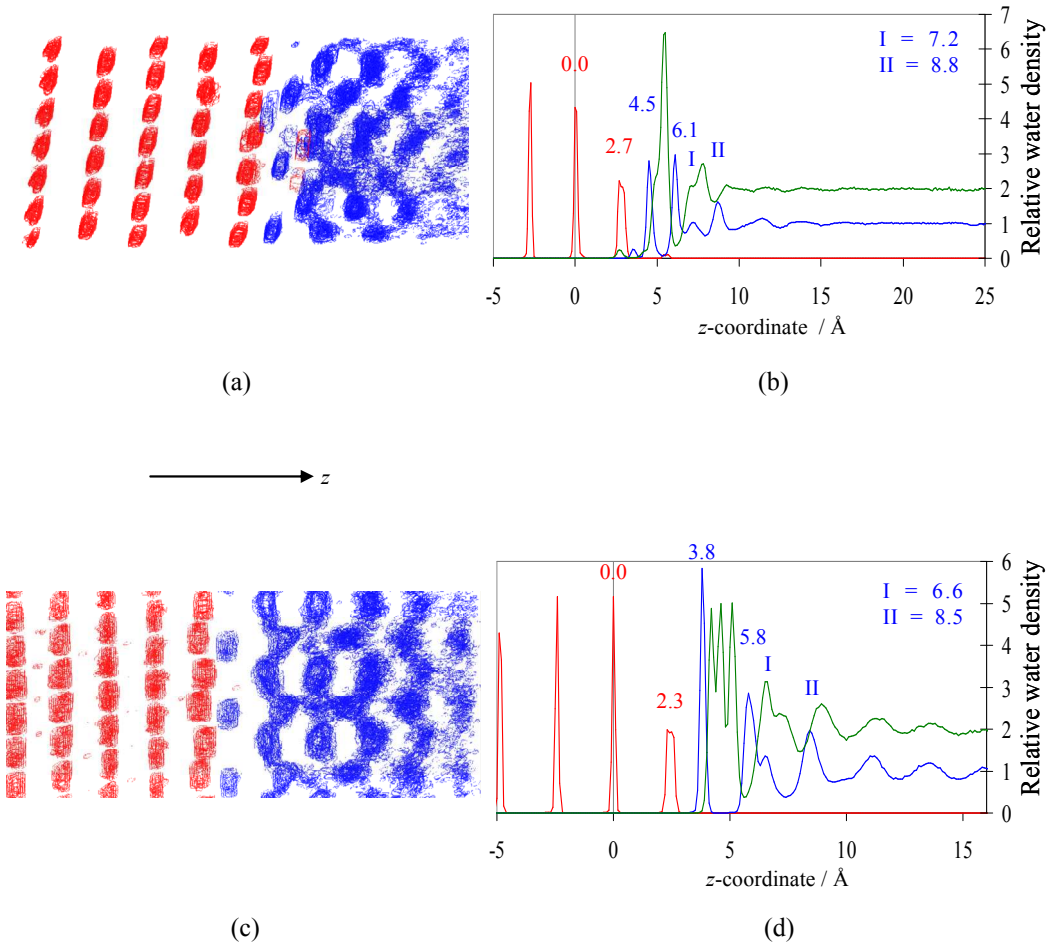

Figure 5.3: Plots showing the **(a)** relative water density and **(b)** *z*-density of the mineral – water interface for the CaO {111} surface. The same respective plots are shown for the MgO {111} surface in **(c)** and **(d)**.

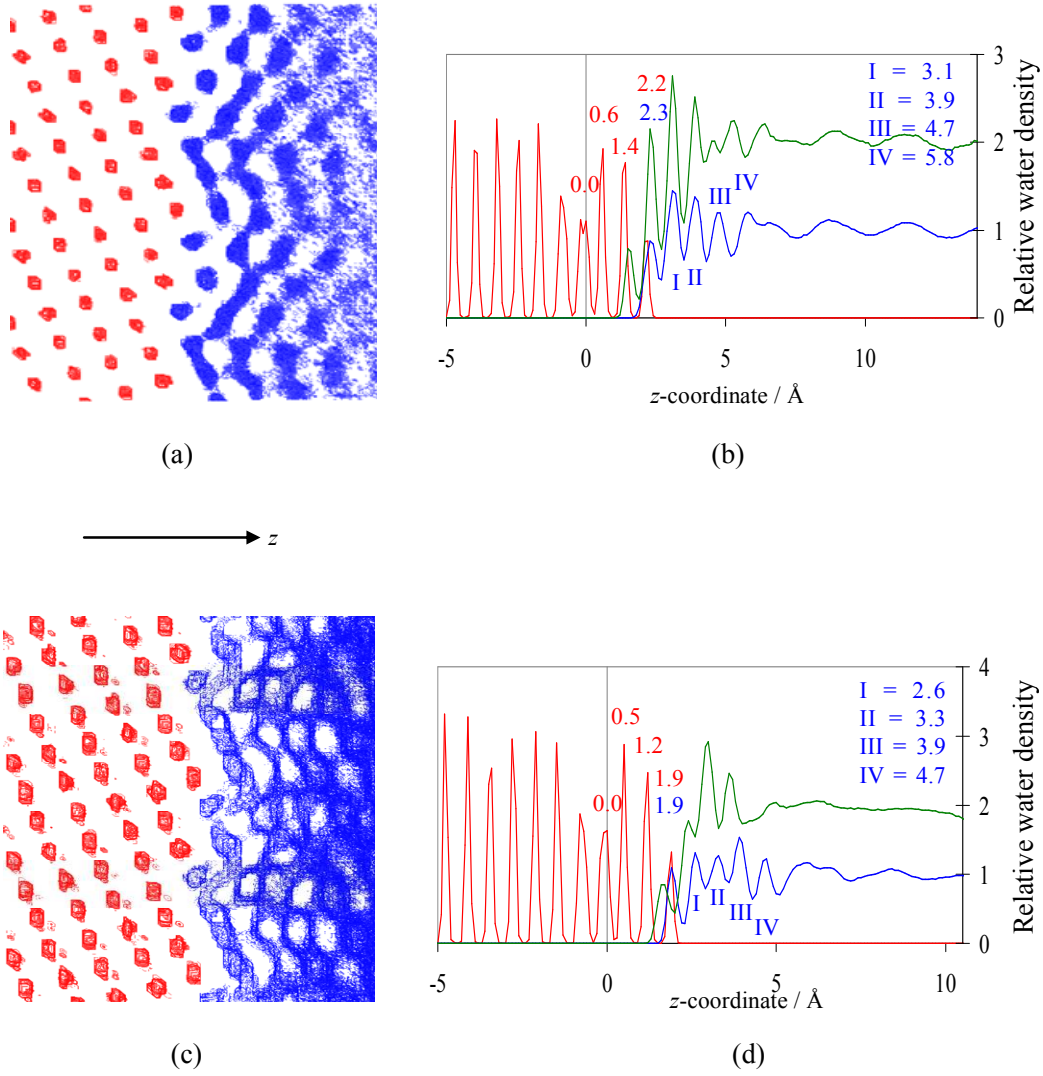

Figure 5.4: Plots showing the **(a)** relative water density and **(b)** *z*-density of the mineral – water interface for the CaO {310} surface. The same respective plots are shown for the MgO {310} surface in **(c)** and **(d)**.

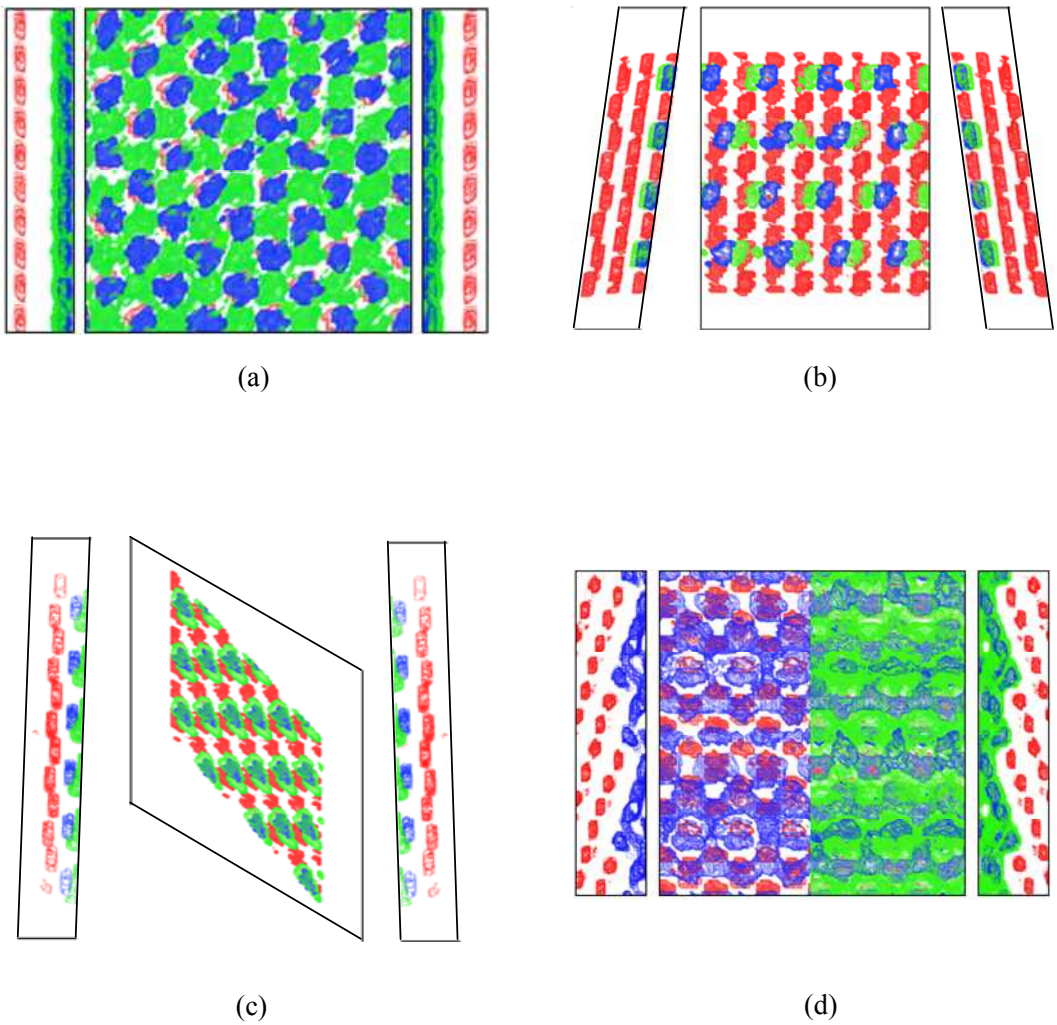

Figure 5.5: Plots showing the average density for the surface oxide layer and first water layer immediately above the surface for the **(a)** {100}, **(b)** {110}, **(c)** {111} and **(d)** {310} MgO surfaces. Plots show the view looking down on the surface along the *z*-axis (central) and the side views (left and right) for each surface. Magnesium density is indicated by red, whereas blue and green are used for the oxygen and hydrogen of water, respectively. NOTE: For clarity, the {310} surface only shows the hydrogen density across half the surface and on only one side.

The {100} surface water densities are given by Figures 5.1 and 5.5(a) and show that the flat surface structure leads to the formation of a two-dimensional array of water molecules bound in crystallographic sites, giving the appearance of flat sheets

of high water density. This water layer is seen to occur with an *M*-O distance of 2.4 and 2.2Å for the CaO and MgO surfaces, respectively. This compares with the bulk *M*-O distance of 2.4 and 2.1Å for calcium and magnesium oxides, respectively. Analysis of this first layer of water indicates the formation of a hydrogen bonded water layer, forming a continuous sheet. Additionally, the relative position of oxygen and hydrogen density indicate that surface coordination is likely to occur to both surface metal and oxygen atoms, respectively, with the hydrogen density seen marginally closer to the surface due to the shorter distance of a hydrogen bond. The formation of subsequent layers continuing toward bulk density is also seen, with the water layers separated by approximately 2.6Å.

The results for micro-faceted {110} surfaces are displayed in Figures 5.2 and 5.5(b) and show that the surface structure directly affects the layering that occurs above the surface. This is different to the {100} surface, again crystallographic water is seen, but the density profiles gives the appearance of continuous rows, rather than flat sheets. The first coordinated layer of water forms within the facets, at a distance of 3.4 and 2.9Å from the bottom, for the CaO and MgO surfaces, respectively. The alignment of the water molecules in these facets is also seen. The water molecules not only form coordinated rows, due to hydrogen bonding, but the direction of the hydrogen bond is also seen to alternate between rows. Subsequent layers then form above this with similar distances between water layers seen as for the {100} surfaces. However, the size difference between Ca and Mg ions affects the water surface. The larger Ca ion at the top of the facet directs the formation of a single second layer above the surface. However, the smaller magnesium ion causes a staggered row, with greater coordination to the water within the facet.

Figures 5.3 and 5.5(c) show the average water density at the {111} CaO and MgO surfaces. They indicate similar patterns to the other surfaces, with water coordinating at distinct sites. Some dissolution of the CaO surface is observed but the MgO surface remains stable throughout the simulation. The first water layer shows that water coordinates at vacant oxygen sites. The CaO surface is calculated

to have a hydrogen density peak marginally closer to the surface, indicating the presence of some hydrogen bonding to the surface oxygen atoms. However, for MgO this coordination occurs via *M*-O bonding as the hydrogen density is at a further distance from the surface. The strongly bound first hydration layer then affects the formation of subsequent layers above it, with clearer, stronger layers seen for the MgO surface.

The stepped {310} surfaces, Figures 5.4 and 5.5(d), give a more complex water structure, as expected. Distinct crystallographic water is identified on the inside of the step and along the short terrace. However, the average density along the longer terrace has a more smeared effect, forming a more diffuse region. The coordination to this surface is clearer for the CaO surface, which is most likely related to the size of the Ca ion giving a larger step height, allowing for a more pronounced structure. The lower step on the MgO surface has a similar but less distinct structure.

The general result from the water density plots is that similar ordering patterns are calculated for the CaO and MgO surfaces, as expected. All surfaces show the first layer of water coordinating in distinct crystallographic sites, predominantly through *M*-O bonds. Layering is then continued into the bulk with spacing between water layers of approximately 2.5Å. The layering into solution extends further from the magnesium oxide surfaces, due to the stronger and shorter Mg-O bond giving rise to stronger coordination of water. Having established that the first water layer is located at crystallographically distinct sites, the question then becomes is the water mobile or forming an ice-like layer?

The mobility of water at the surface can be evaluated by calculating the water residence times. The residence time of a water molecule is defined as the average time a water molecule spends within the first hydration shell of an atom of choice, defined here as being 3.25Å, and can be calculated from the residence time correlation function, Equation 5.2, as suggested by Impey *et al*. [159]. The distance

of 3.25Å was deemed sufficient for both the metal and oxygen atoms from the radial distribution functions, although not shown here.

$$< R(t) >= \left\langle \frac{1}{N_0} \sum_{i=1}^{N_t} \theta_i(0)\, \theta_t(t) \right\rangle \qquad 5.2$$

where N is the number of water molecules in the first hydration shell, $\theta_i(t)$ is the Heaviside function, which is 1 if the i^{th} water molecule is in the first hydration shell at time t and 0 otherwise. A water molecule is only counted as having left the first hydration shell if it has done so for at least 2ps, thus allowing a water to leave the first hydration shell and return, without entering the bulk, for a significant amount of time and still be counted. The residence time, τ, can then be obtained by the integration of $<R(t)>$ using Equation 2.3.

$$\tau = \int_0^\infty < R(t) > dt \qquad 5.3$$

We calculated the residence times of all surface metal and oxygen atoms with the oxygen atoms of water molecules. The residence times were used to construct a contour plot as a function of the atomic coordinates. These plots are shown for the {100}, {110}, {111} and {310} surfaces in Figures 5.6 through to 5.9, respectively, for calcium and magnesium oxide. The residence times are calculated over the last 800ps of the simulation and the values of residence times on all the surfaces are plotted with an identical scale, where light and dark blue indicate short and long residence times, respectively. In addition, the structure of the surfaces at the start of the measurement period is overlaid for reference, assuming that no significant changes in atom position occur during the 800ps time scale.

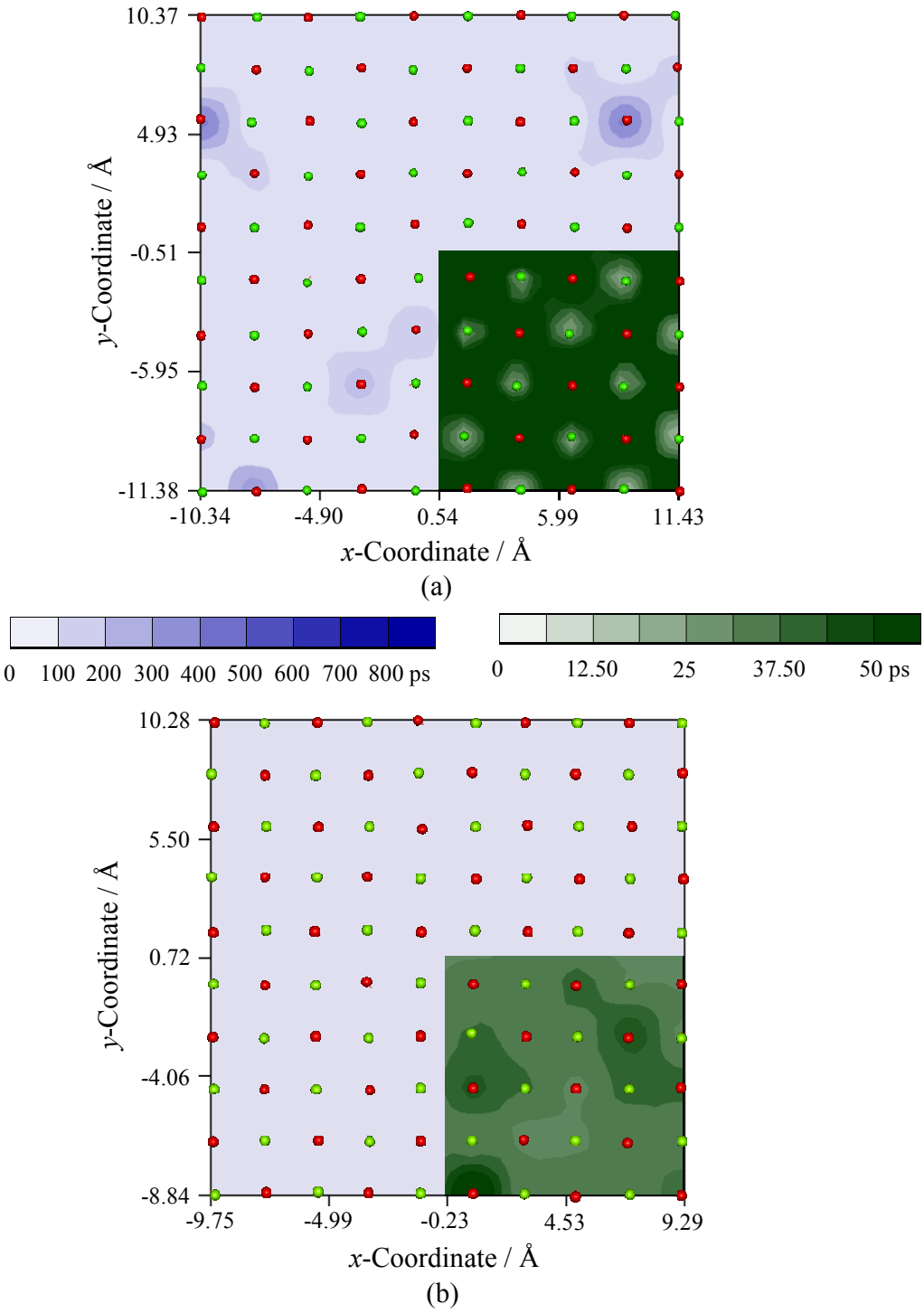

Figure 5.6: Contour plots showing residence times of water as a function of the atomic coordinates for the {100} **(a)** CaO and **(b)** MgO surfaces. The green scaled inset represents a reduced scale from 0-50ps.

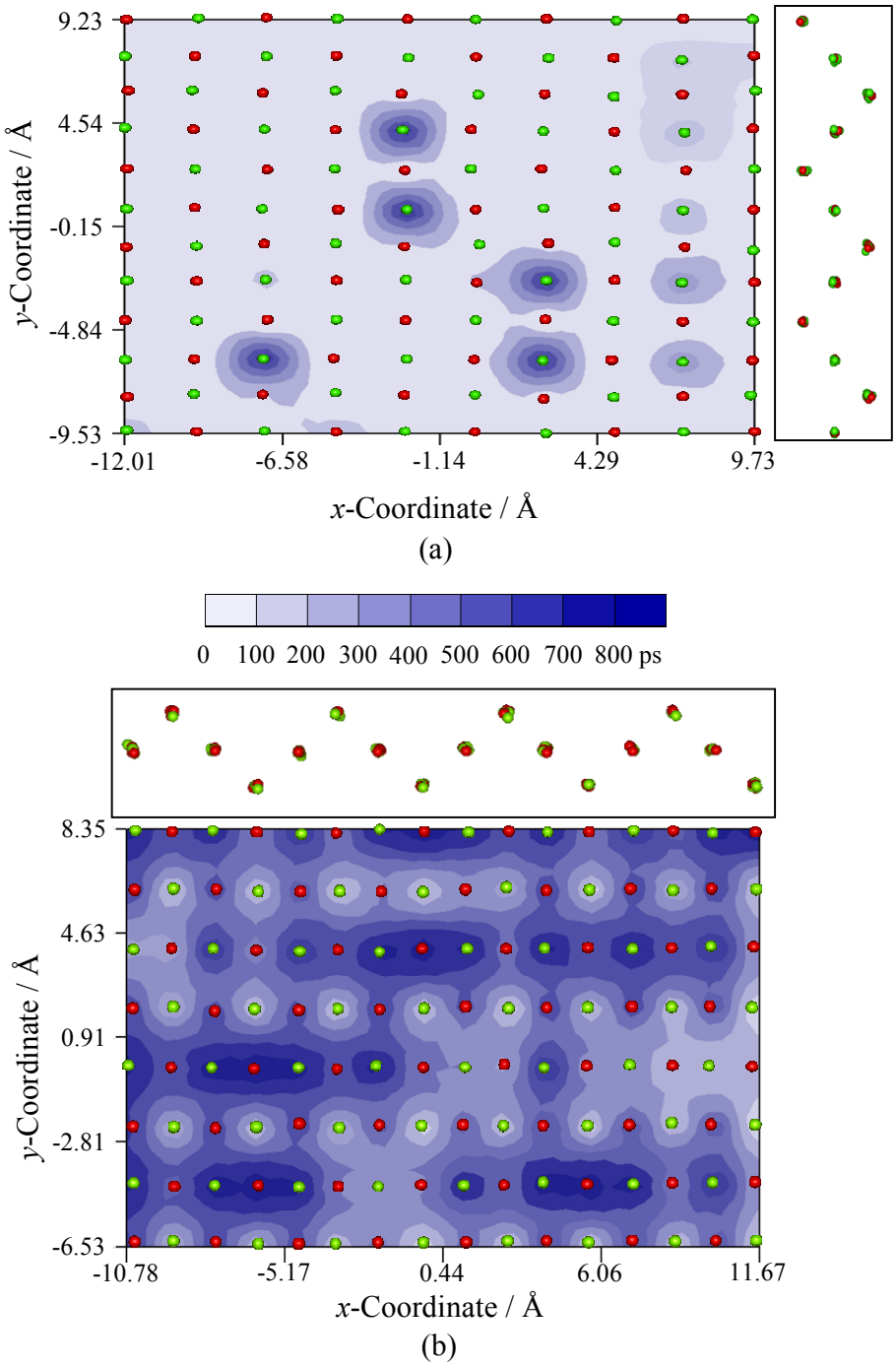

Figure 5.7: Contour plots showing residence times of water as a function of the atomic coordinates for the {110} **(a)** CaO and **(b)** MgO surfaces. NOTE: Due to different surface orientations, surface micro-facets run in different directions as indicated by the side profile.

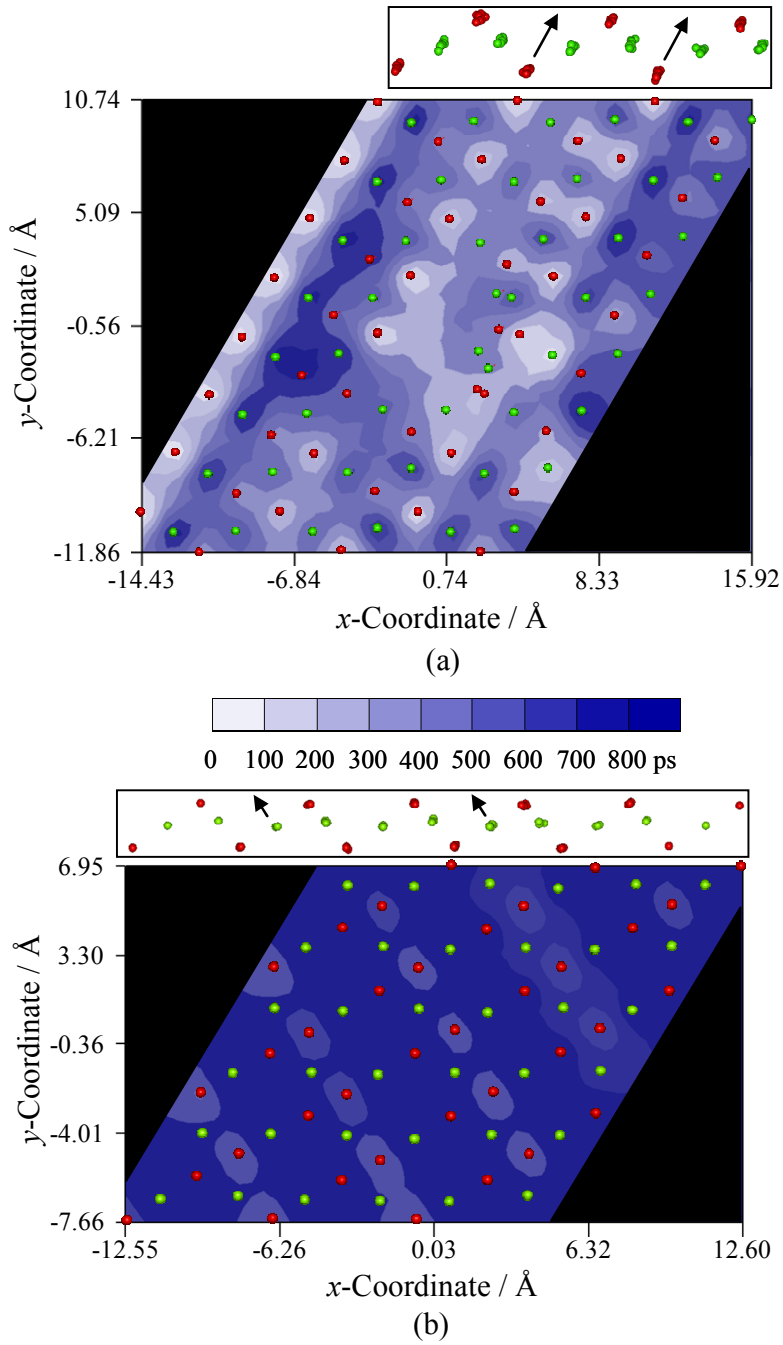

Figure 5.8: Contour plots showing residence times of water as a function of the atomic coordinates for the {111} **(a)** CaO and **(b)** MgO surfaces. NOTE: The two materials have different surface orientations, as indicated by the side profiles above the plot, where the arrows indicate the relative direction of the surface facets.

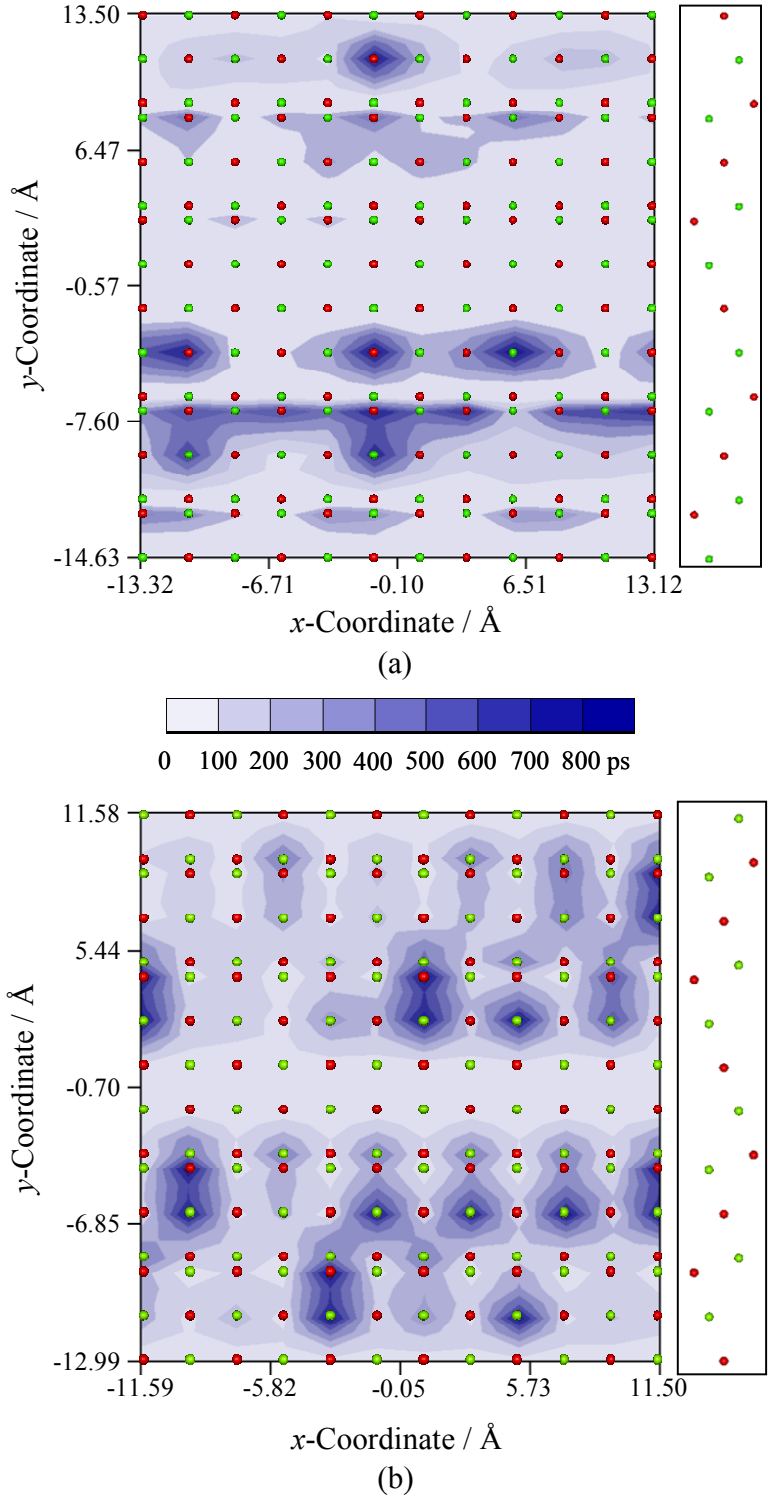

Figure 5.9: Contour plots showing residence times of water as a function of the atomic coordinates for the {310} **(a)** CaO and **(b)** MgO surfaces. Surface topography is shown at the side.

The residence times of water above {100} surfaces, shown in Figure 5.6, indicates that both materials have a highly diffuse water layer above the surface, with residence times mainly below 100ps. Some localised regions of longer times are seen above surface oxygen atoms on the CaO surface. The higher mobility can be examined in a little more detail using a scale from 0-50ps, shown in the inset by light to dark green, respectively, for both materials. For calcium oxide this shows that water spends in excess of 50ps above oxygen atoms and 25ps above calcium. There is no clear pattern for MgO, although predominant coordination of water to surface oxygen atoms is suggested. The results show that water is more tightly bound to CaO than MgO. This is contrary to what is expected, as the Mg-O bond is shorter and stronger than the Ca-O bond, residence times would be expected to be larger for MgO. However, the shorter bond causes a more tightly packed water layer, increasing the steric interactions more than for the CaO surface.

Figure 5.7 gives the plots of residence times for the {110} surfaces. However, due to the difference in surface orientation within the simulation cell, the direction of the surface micro-facets differs for the two materials. The CaO surface, Figure 5.7(a), has micro-facets that run from left to right across the plot, whereas for the MgO surface, Figure 5.7(b), they are orientated from top to bottom. However, similar residence time patterns are seen for the two materials. Unlike the {100} surface, MgO has the lower surface water mobility. The coordination pattern is more clearly visible on the CaO surface, due the high mobility across the majority of the surface. Longer residence times are seen through binding within the micro-facets themselves, mainly through coordination to metal atoms. The result is in agreement with the density profile shown in Figure 5.5(b). The stronger and less diffuse coordination on the MgO surface is most likely contributed to by the shorter *M*-O bond. This also allows for stronger coordination to the oxygen atoms positioned along the bottom of the micro-facets.

The {111} surfaces, Figure 5.8, also differ in the surface orientation for the two materials. The CaO surface in Figure 5.8(a) shows that the direction of the surface

micro-facets runs diagonally from the left to the right of the image. The magnesium oxide surface, Figure 5.8(b), however, shows the micro-facets running diagonally from the right to the left. There is also a distinct difference in the surface water mobility at the two interfaces. The MgO results suggest a much stronger interaction, leading to the layered water remaining coordinated in the same position throughout the majority of the simulation. The only areas of any reduced mobility on this surface are seen along the oxygen atoms at the bottom of the micro-facets. The CaO surface, however, shows more variation in residence time. In addition, some small surface movement of atoms occurred during the initial stages of the simulation, as can be seen in the central region of the plot. However, despite this discontinuous region, coordination structures can be identified. Stronger water coordination, and hence reduced water mobility, is seen to predominantly occur to surface calcium atoms located just inside the facets. Higher water mobility is again seen along the oxygen row at the base of the facet.

The {310} surfaces, Figure 5.9, displays a more distinct mobility pattern specific to the surface structure. Both materials show similar patterns of stronger water coordination across the shorter terrace, predominantly through coordination to the metal atoms. The CaO surface also shows coordination along the sites *above* the step leading to the short step. However, the MgO surface indicates reduced mobility at the positions inside the step *following* the short terrace. In addition, the position of the smeared density above the longer terrace, seen in Figure 5.5(d), is shown here to also be highly diffuse.

The lack of continuous regions of equal residence times also raises the question of the simulation length. Although calculations are checked for convergence of the configurational energy of the system, the initial assumption was that the residence times would be similar for atoms in identical environments. However, the variation seen suggests the possibility that if the simulation length were longer, the regions may move to a more uniform distribution rather than showing localised regions of reduced water mobility. However, further testing is essential to clarify this issue.

In general, the residence time analysis indicates that there are stronger interactions with the MgO surfaces than CaO for all surfaces except the {100} surface. This is likely to be a consequence of the shorter Mg-O bond distance. For the less regular surfaces, this shorter bond distance acts to bind the adsorbed water molecules more tightly, resulting in the higher residence times than for the CaO surfaces. However, for the {100} surface, the regularity of this perfect flat surface causes steric interactions to have an increased effect. The water coordination on the MgO {100} surface gives rise to a more tightly packed water layer than for the CaO equivalent, therefore repulsions between water molecules are more significant above the MgO surface which decreases the residence time more than is calculated for CaO. This also helps rationalise why the {100} surfaces in general show lower residence times than the other surfaces modelled. These results could have important consequences for diffusion properties along, to and from the surface. Regions of highly coordinated water, with reduced mobility, would hinder diffusion as they would be more difficult to displace. For regions of higher mobility, diffusion and transport properties would be facilitated due to the relative ease of displacing more weakly bound molecules. However, electrostatic interactions between regions or high oxygen and hydrogen density would also be expected to influence diffusion to and from the surface.

Analysis of the residence times of water is also useful as they can be used to identify whether the discreet crystallographic positions correspond to ice formation. The continuous arrays of water above {100} surfaces, for example, are highly mobile, despite the distinct coordination pattern, therefore ruling out ice-like formation. However, for the MgO {111} surface, again discreet regions of highly coordinated water are seen in crystallographic sites with high residence times. This could be indicative of ice-like formation, or alternatively, as the {111} surface is most stable when fully hydroxylated; it could be an indicator of particularly strong adsorption sites, which may well be liable to hydroxylation. This is also applicable to the fact that the surface features, such as steps and facets, also show the formation

of more strongly bound coordinated regions of water. The static simulations of the {310} surface, for example, show that the steps have a preference to hydroxylation, whereas the terraces will favour hydration, this therefore rationalises the strongly coordinated water as regions where hydroxylation is favoured. Not only could this therefore be used as a method for identifying possible hydroxylation sites but may also be of use to engineer materials of specific use. For example, flatter and more even surfaces give rise to very mobile regions above them, which could be generated to aid transport to and from the surfaces. However, a more complete understanding of the reactivity of the surface, toward water and other species, as well as the effects this has on the water structure are essential to enable the full exploitation of these surfaces. To begin to address this, we will next consider the effect surface carbonation plays on the interface.

5.1.1 The Effect of Carbonation on the Mineral – Water Interface

The results in chapter four clearly suggest that CaO and MgO can adsorb CO_2 as carbonate, via static calculations. The aim here is to model the adsorption of carbonate on these surfaces in the presence of liquid water and to evaluate the effect this has on the water structure above the {100}, {110}, {111} and {310} surfaces of calcium and magnesium oxide. The approach is described above and involves the use of a slab of mineral, with approximate depth of 20Å. One side of the slab was carbonated, using the lowest energy carbonated structures reported for the surfaces in chapter four. For reference, the coverage used and their associated surface energies are detailed in Table 5.1. The carbonated surface was then put in contact with a slab of water with an equivalent number of molecules as used for the pure surfaces above. A vacuum gap of 20Å was finally placed between the uncarbonated surface and the top of the water layer due to the possible build up of residual pressure resulting from using the NVT ensemble, with a relaxation constant of 1.0ps for the thermostat. The generation of the dipole on the carbonated slab was deemed to be negligible due to; firstly, the size of the cells used in the simulations, and secondly, as the high dielectric constant of the water layer would dampen the effect

of the dipole. Simulations were again simulated at 300K for 1ns, or until convergence was seen, after an initial run of 10ps at 0K in the NVE ensemble.

Table 5.1: Results of static simulations indicating the surface energies and coverage of the lowest energy carbonated {100}, {110}, {111} and {310} surfaces of CaO and MgO used to generate the carbonated slabs.

Material	CaO				MgO			
Surface	{100}	{110}	{111}	{310}	{100}	{110}	{111}	{310}
γ / J m^{-2}	-0.51	0.26	0.42	-1.25	0.44	1.34	2.03	0.22
Carbonate Coverage / %	87.5	66.7	100.0	87.5	75.0	66.7	100.0	75.0

The structures of the interfaces for the carbonated systems were studied using the same techniques described above. The water density and *z*-density plots for the calcium and magnesium oxide {100} and {310} surfaces are shown in Figures 5.10 and 5.11, respectively. The {110} and {111} surfaces are not shown as they show similar disordered structures to the {100} surface with no clear trends apparent. We can also assess the mobility of water on the surface by calculating the residence times at different points on the surface, and the effect surface carbonation has on this. The residence times as a function of the atomic coordinates for the carbonated {100} and {310} surfaces of CaO and MgO are shown in Figures 5.12 to 5.13, respectively. Again, the {110} and {111} surfaces show a disordered structure similar to the {100} surface and hence are not shown but similar conclusions can be drawn to the {100} surface.

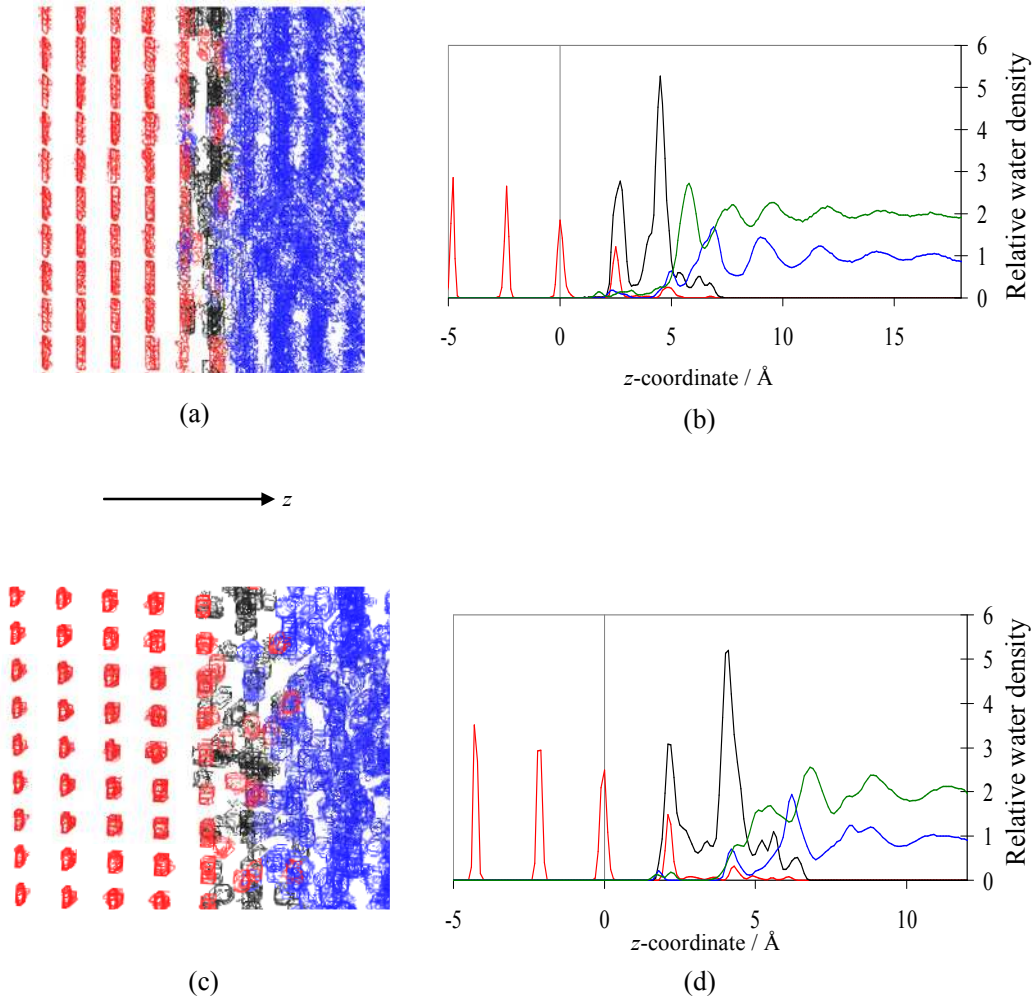

Figure 5.10: Plots showing the **(a)** relative water density and **(b)** *z*-density of the mineral – water interface for the carbonated CaO {100} surface. The same respective plots are shown for the carbonated MgO {100} surface in **(c)** and **(d)**. The density of the metal and carbonate oxygen are shown in red and black, respectively, whereas, the blue and green indicate oxygen and hydrogen density, respectively, from water.

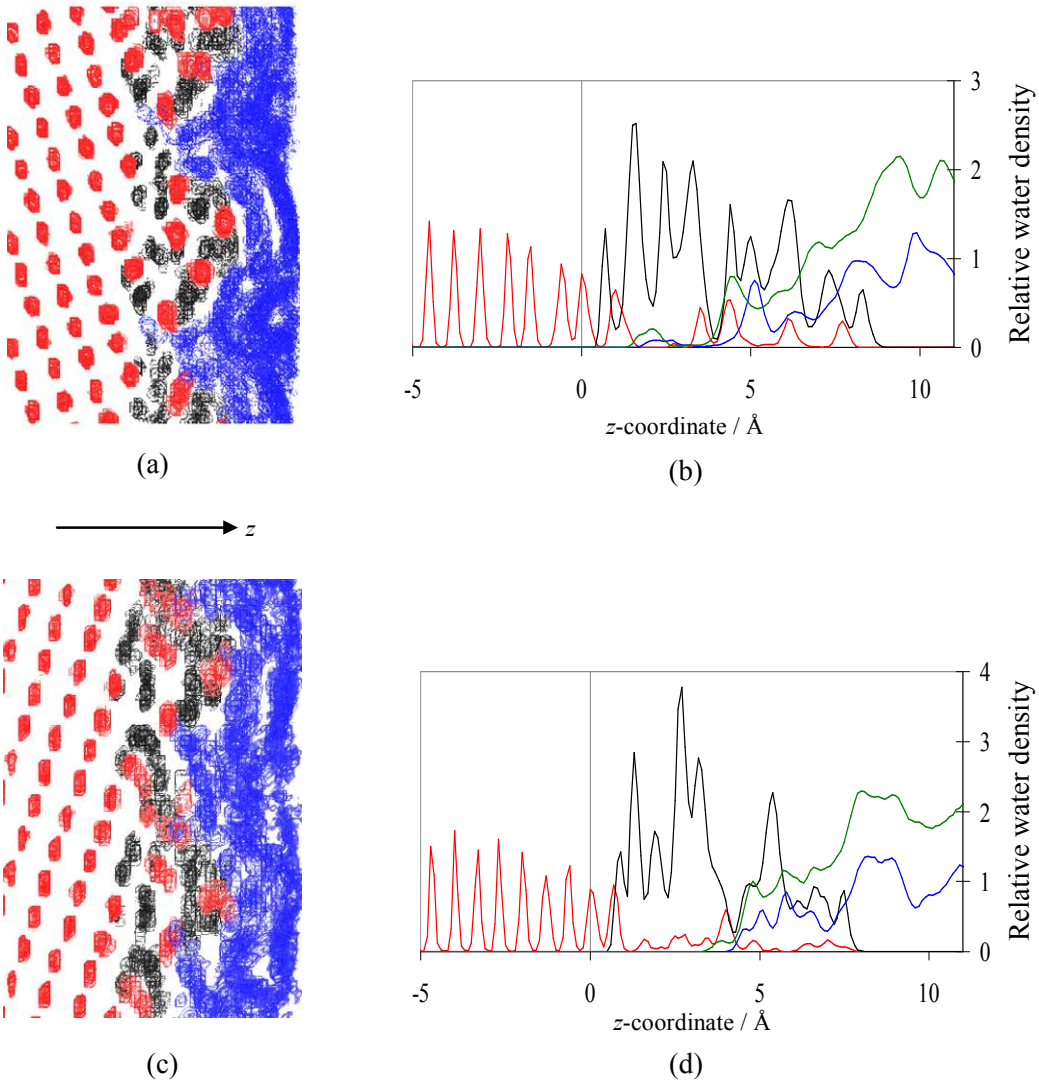

Figure 5.11: Plots showing the **(a)** relative water density and **(b)** *z*-density of the mineral – water interface for the carbonated CaO {310} surface. The same respective plots are shown for the carbonated MgO {310} surface in **(c)** and **(d)**.

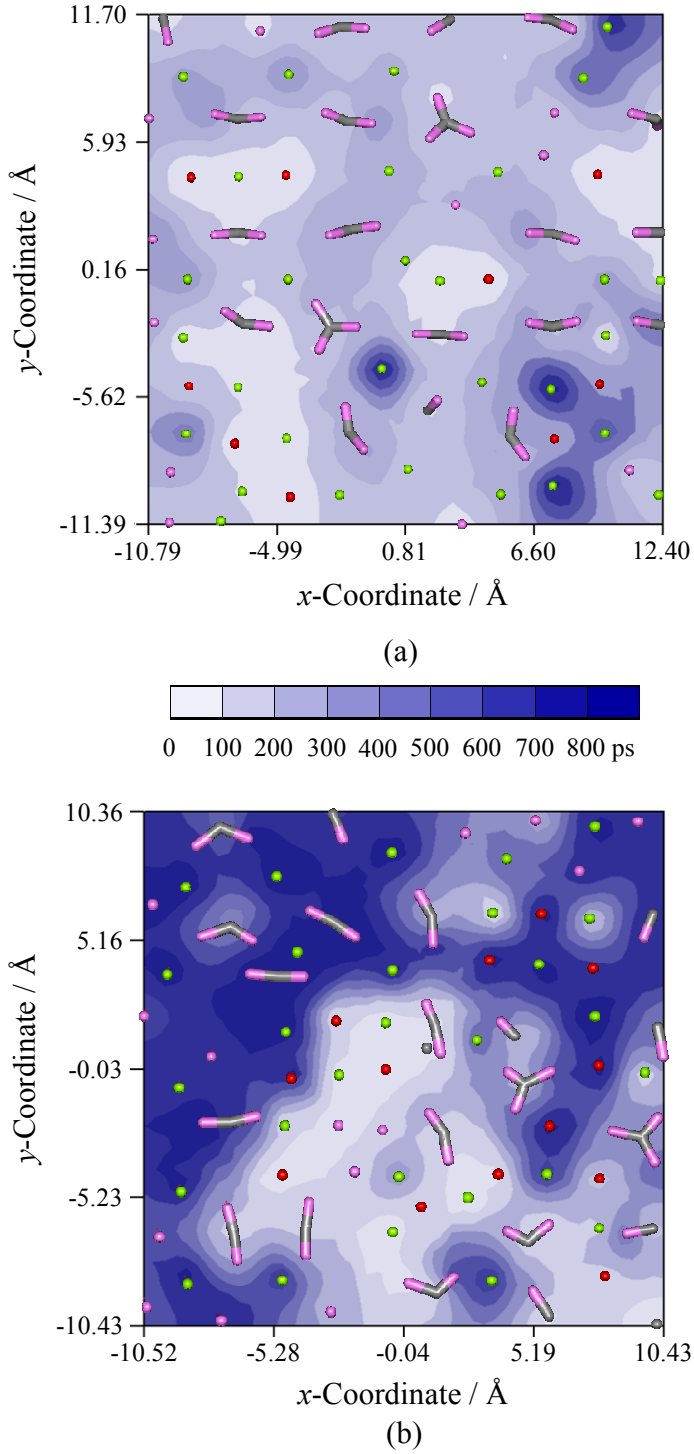

Figure 5.12: Contour plots showing residence times of water as a function of the atomic coordinates for the carbonated {100} **(a)** CaO and **(b)** MgO surfaces. Metal, lattice oxygen, carbon and carbonate oxygen atoms are indicated by green, red, grey and pink, respectively.

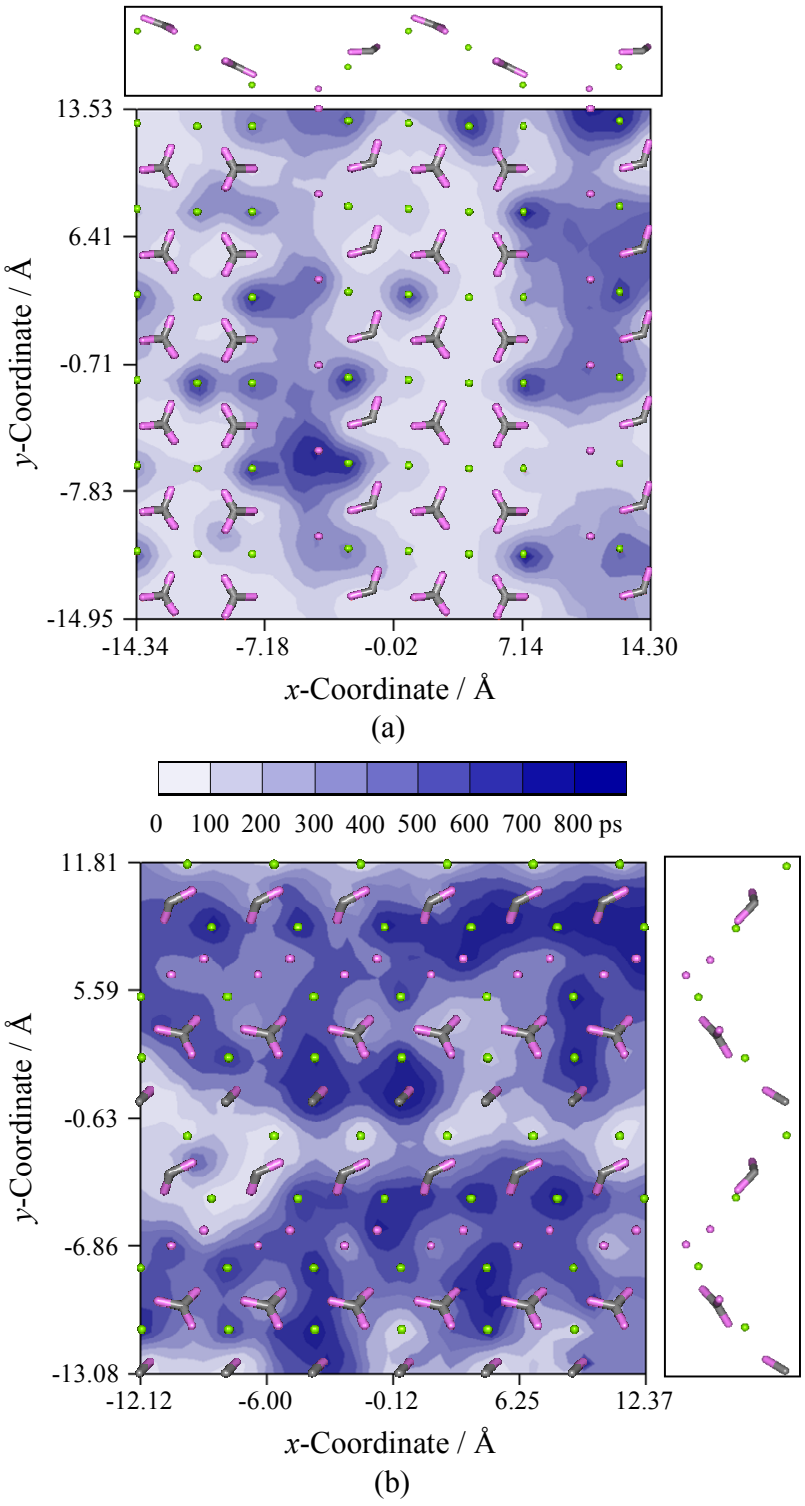

Figure 5.13: Contour plots showing residence times of water as a function of the atomic coordinates for the carbonated {310} **(a)** CaO and **(b)** MgO surfaces. Surface topography is also shown.

The results suggest that the presence of surface carbonation, at least for the {100}, {110} and {111} surfaces, severely disrupts the water layering above the surface. This is most likely a result of the amorphous carbonate layer that is present at these surfaces, which shows local coordination but the lack of regularity impedes the formation of distinct layering. This is more apparent for the MgO surface, which has a greater amount of disruption, possibly indicating a higher degree of ordering in the CaO surface. The residence times for these surfaces also show no clear pattern. In terms of surface water mobility, similar trends are seen to the pure surfaces, where the calcium oxide surface has lower residence times to the magnesium equivalent, even for the {100} surface. However, increased water coordination is seen in comparison to the pure surface, with the carbonation giving rise to rougher surfaces, thus providing more adsorption sites, despite the loss in water structure. Although not clearly visible from the above plots, the regions of higher water coordination correspond mainly to depressions in the surface structure, caused by the irregularity of the surface. Therefore the higher water mobility on the CaO surface may also indicate a higher degree of ordering on this carbonated surface, giving rise to a more regular, and flatter, surface structure.

The carbonated {310} surface represents a more ordered structure, with the carbonation of the steps resulting in a facet-like appearance which has consequences for the water adsorption above it. Although the density plots also indicate a disruption, and hence a more disordered water structure immediately above the surface compared to the pure material. However, some structure remains, it can be seen that, as with the pure stepped surface, water binds predominantly along the centre and sides of the surface trenches, with the lower coordinated sites at the top of the trench being considerably more susceptible to displacement of water, resulting in a high mobility.

Further analysis of the final structures of these surfaces indicates the presence of water molecules within the carbonate layer, thus forming an amorphous carbonate hydrate layer. This is seen for the majority of different surfaces, and is illustrated in

Figure 5.14 using the carbonated CaO {100} surface as an example. Analysis of the residence times for the nearest calcium atoms reveals that once the water becomes trapped in the carbonate it remains there for the rest of the simulation. This suggests the formation of an amorphous hydrate; it could also suggest sites where bicarbonate formation would occur. However, further calculation would be required to assess the energetics, concentration of trapped water and the consequences this has for the carbonate layer.

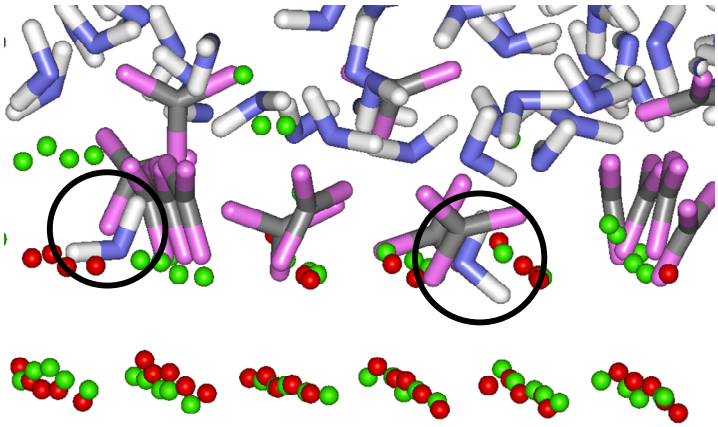

Figure 5.14: A section of the final configuration of the carbonated CaO {100} surface following simulation at 300K for 1ns. Trapped water molecules within the carbonate layer are highlighted by the black circles.

The use of dynamical models has allowed us to consider periodic mineral oxide surfaces and their interactions with water. The remainder of this chapter will focus on nanoparticulate systems, where the effect of low-coordinate, high energy surface sites can be probed.

5.2 Nanoparticles

Nanoparticles represent an important system to study because the available surface area is increased as well as the presence of high energy sites which may not inherently be present on regular two-dimensional surfaces, such as corners and edge sites. In addition, the formation and growth of nanoparticles may be carried out in a

manner which leads to the expression of higher energy surfaces which are likely to be more reactive. Thus the remaining sections of this chapter will detail initial work of adsorption and interactions with CaO and MgO nanoparticles. Namely, the interaction of liquid water with pure and fully hydroxylated MgO nanoparticles and the interaction of carbonate with a {100} dominated CaO nanoparticle.

5.2.1 The Effect of Nanoparticle Size and Surface Hydroxylation

We elected to consider a range of different MgO nanoparticles to understand the effect that size and shape have on nanoparticle stability. We modelled nanoparticles bound by three different surfaces, namely the {100}, {110} and {111} to allow for the effects of different surface configurations. These were generated by initially calculating the morphology that these surfaces would generate, using the calculated surface energies detailed in chapter four to produce Wulff constructions. For this system, a {100} bound nanoparticle gives rise to a cubic construction, whereas the {110} and {111} surfaces generate rhombic dodecahedral and octahedral shapes. This morphology is then used as a 'template' to cut a nanoparticle of a certain diameter from the bulk MgO structure. These idealised crystal morphologies are shown in Figure 5.15.

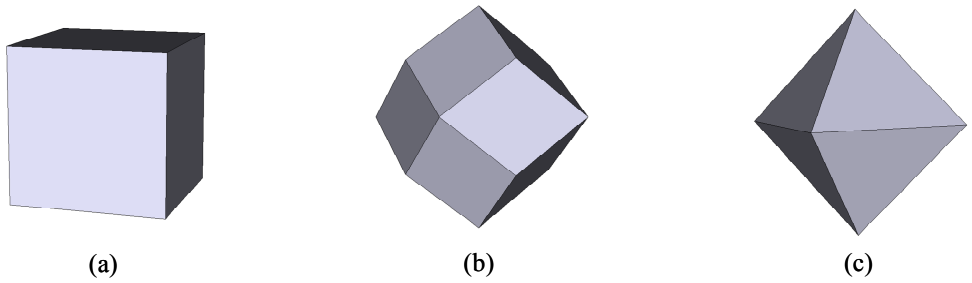

Figure 5.15: Idealised morphologies for a **(a)** {100}, **(b)** {110} and **(c)** {111} dominated MgO nanoparticle.

Three diameters were used to consider the effect of nanoparticle size, using diameters of 20, 30 and 40Å. These nanoparticles were then simulated in two ways.

Firstly, they were simulated for 1ns in the NVT ensemble at a temperature of 300K with a relaxation constant of 0.5ps. However, to allow the nanoparticles to undergo surface rearrangement to form the most stable surface, simulated annealing was also used, via a similar approach to that used by Sayle *et al*. [140]. This process involves taking the initial surface structure and simulating it in the NVT ensemble for 500ps at a temperature of 2500K, allowing the surface atoms to have sufficient kinetic energy to rearrange to find the optimum positions. The temperature was then reduced in steps of 500K until the temperature of the system reached 300K. Each temperature was run for 500ps, with the 300K simulation having a simulated real time of 1ns. However, to reduce the number of calculations required, only the 30 and 40Å sized nanoparticles were simulated in this manner.

The initial structures of the nanoparticles, as well as the final structures from both simulation methods are shown in Figure 5.16 for the 40Å nanoparticles. The results show that the different simulation processes give rise to differing shapes. For the nanoparticles simulated at 300K, the {100} nanoparticle does not undergo surface rearrangement. The {110} nanoparticle also retains its shape and surface structure. However, there is some rearrangement of corner sites, with atoms clustering at these sites to remove the low-coordinated magnesium sites. The {111} nanoparticle, however, undergoes a more dramatic rearrangement. The high energy {111} surface can be seen to rearrange giving a multi faceted structure, with the appearance of the more stable {100} surface structure, containing flat sheets of magnesium and oxygen atoms. The shape of the nanoparticles follow the same trend in stability to those seen for the surface simulations in chapter four, where the {100} surface is the most stable.

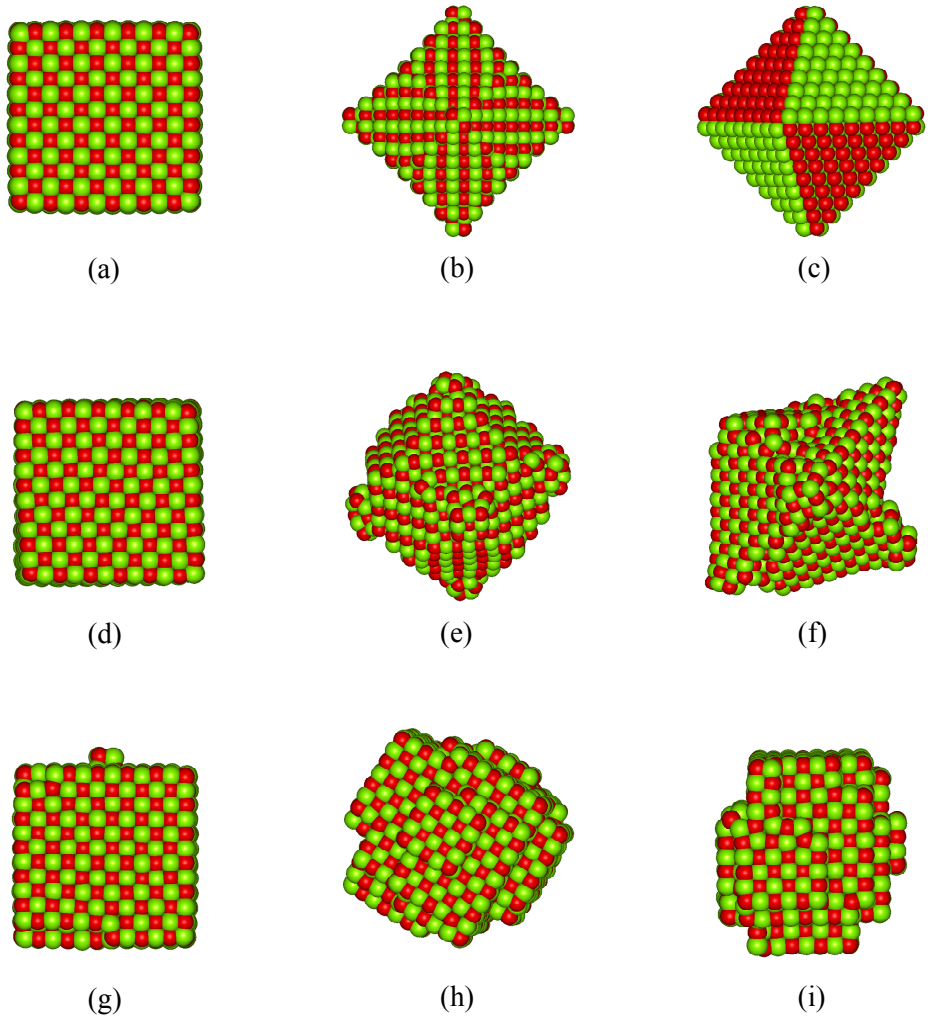

Figure 5.16: Initial structures for the 40Å MgO nanoparticles bound by the **(a)** {100}, **(b)** {110} and **(c)** {111} surfaces. The final structures following simulation at 300K are shown in **(d)**, **(e)** and **(f)**, respectively. The final structures following a method of simulated annealing are shown in **(g)**, **(h)** and **(i**), respectively.

On simulated annealing, a greater rearrangement is observed. The stability of the {100} is underlined by retention of the cubic shape, with only minor surface faceting. However, the {110} and {111} both show the formation of a multi-faceted nanoparticles, comprising principally of {100} surfaces. Hence, we can infer that in the absence of other species the nanoparticles will possess a more ordered cubic morphology. These simulations highlight the strengths of the simulated annealing process, allowing for the formation of more complex rearrangements, which are

either not seen in the simulations at 300K, due to insufficient kinetic energies, or would take a considerably longer simulation time to form.

We can further assess the effect of surface structure and size by considering the energies of the nanoparticles. These are shown, per MgO unit, for the nanoparticles using both methods in Table 5.2. The stability of the {100} nanoparticle is again demonstrated by the result that both processes give rise to similar energies, which are lower than the energies from the {110} and {111} nanoparticles for each size. This is in agreement with experimental studies considering MgO nanoparticles formed from smokes, which show a cubic morphology [27]. In addition, the surface faceting of the {110} and {111} nanoparticles is seen to lead to significant stabilisation, with the differences in energies due to the different number of atoms in the nanoparticles. In terms of size, as expected, it can be seen that the larger the nanoparticle, the more stable it is as it contains more bulk material. This can also be compared with the calculated bulk energy of MgO, detailed in chapter four, of -41.30eV.

Table 5.2: Table detailing energies, per MgO unit, for the different sized unannealed and annealed {100}, {110} and {111} dominated MgO nanoparticles.

Surface	Diameter / Å	Average configurational energy per MgO unit / eV	
		300K	Annealed from 2500K
{100}	20	-40.45	-
	30	-40.67	-40.67
	40	-40.87	-40.85
{110}	20	-39.90	-
	30	-40.46	-40.63
	40	-40.58	-40.74
{111}	20	-39.92	-
	30	-40.25	-40.49
	40	-40.57	-40.69

The results in chapter four suggest that surface hydroxylation is an important process and that surface interactions with water will give rise to a certain degree of hydroxylation. To begin to address this, we have studied the full surface hydroxylation of these nanoparticles. The approach was to replace surface oxygen atoms with hydroxide groups with a corresponding addition of a hydroxide group above surface magnesium atoms. These were then simulated at 300K for 1ns with the NVT ensemble and a relaxation constant of 0.5ps. The initial and final configurations of the 40Å nanoparticles are shown in Figure 5.17. However, due to instabilities in high energy sites, mainly those on corners, the nanoparticles failed to converge with the annealing methodology used for the pure nanoparticles. Therefore only the energies of the nanoparticles which were simulated at 300K have been computed, as shown in Table 5.3.

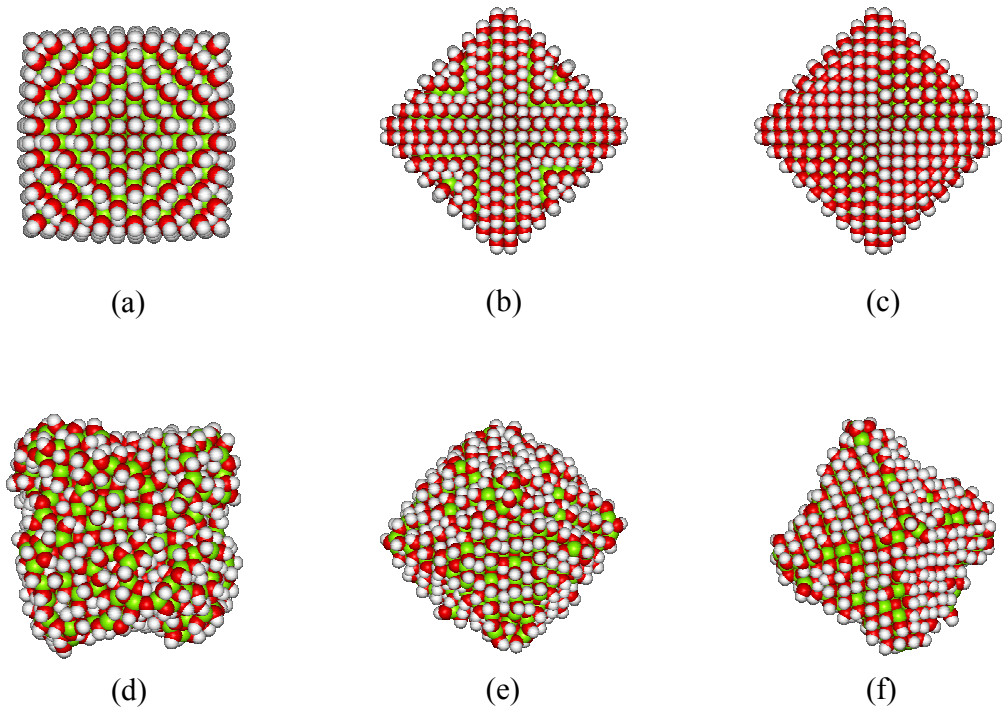

Figure 5.17: Initial structures for the fully hydroxylated 40Å MgO nanoparticles bound by the **(a)** {100}, **(b)** {110} and **(c)** {111} surfaces. The final structures following simulation at 300K are shown in **(d)**, **(e)** and **(f)**, respectively.

Table 5.3: Table detailing corrected energies, per MgO unit, for the different sized unannealed fully hydroxylated {100}, {110} and {111} dominated MgO nanoparticles.

Surface	Diameter / Å	Average configurational energy per MgO unit / eV
{100}	20	-41.15
	30	-41.16
	40	-41.17
{110}	20	-41.09
	30	-41.18
	40	-41.17
{111}	20	-41.16
	30	-41.21
	40	-41.21

The energies for the hydroxylated nanoparticles have also been corrected to account for the self-energy of water, in a similar way to the hydroxylated slabs described in chapter four. The approach was to subtract the energy of the pure nanoparticle from the hydroxylated one and then add the correction term for each OH/H pair in the system, which was -7.15eV. The energies of the fully hydroxylated nanoparticles show that in general, surface hydroxylation stabilises the nanoparticles, making them more stable than the dry forms. The {111} stabilisation is particularly apparent as the dry {111} dominated nanoparticle is the least stable of the three, whilst hydroxylation causes sufficient stabilisation of the surfaces to make it the most stable. This is similar to hydroxylation of the {111} surface, shown in chapter four. The stabilisation gives rise to octahedral shaped nanoparticles, again in agreement with experimental results [27], showing that when left in water, hydroxylated (111) surfaces dominate giving a stabilised octahedral morphology. The stability of the crystals starting with {100} and {110} habits approaches similar values, which is also seen to an extent for the surfaces. In addition, in comparison to the calculated bulk energy of MgO, -41.30eV, it can be seen that the surface hydroxylation dramatically stabilises these nanoparticles, with the energies being closer to the bulk value. Consideration of the initial and final structures shows that

there is significantly more rearrangement of the cubic {100} nanoparticle than is calculated for the other nanoparticles, with distinct roughening of the surface. The {111} nanoparticle remains roughly in an octahedral shape, with a small amount of faceting seen on the higher energy corner sites, whereas the {110} nanoparticle appears to become slightly more rounded whilst still retaining a similar shape to the initial configuration.

Overall this study shows that the trend in the surface stability of nanoparticles is similar to the lowest energy surfaces. This result holds for both the pure and hydroxylated systems, namely that the {100} surface is the most stable for the pure surface, whilst following hydroxylation, the minimum energy surface becomes the {111} surface. In addition, nanoparticulate systems appear to be much more susceptible to surface reconstruction, in an effort to reduce their energy. The use of dynamical methods, however, also allows for us to consider the interaction with liquid water, in a similar way to the surfaces described previously. This will therefore be the subject of the following section.

5.2.2 Interactions with Water

The study of water adsorption discussed in chapter four, as well as the hydroxylated nanoparticles above, makes it clear that hydroxylation of the {111} termination produces the most stable surfaces for MgO. This is particularly apparent in the calculated surface phase diagram in Figure 4.16 where this hydroxylated surface dominates. We have therefore elected to further study the fully hydroxylated nanoparticle, with a size of 40Å, by placing it in a box containing 9179 water molecules. The particle was simulated for 900ps in the NPT ensemble, with relaxation constants of 1.0ps for both the Hoover thermostat and barostat, with a temperature of 300K; ensuring convergence in the configurational energy was achieved.

The average water density profile surrounding the nanoparticle can be determined in an identical manner to that used above and is shown in Figure 5.18. The spots of water density which appear to be inside the hydroxide layer are due to the nanoparticle not being aligned to the cell edge. However, the water structuring is evident around the nanoparticle itself, with water layering extending three to four layers into the bulk regions. This water layering primarily appears above the faces of the nanoparticle. The water density around the corner sites appears to show considerably less ordering however, with distinct regions of coordinated water immediately above the sites but with no long range ordering seen. The lack of long range order is also true for edge sites, although coordination to the innermost layer of water still remains; it is simply the extended layering which is lost. The difference in ordering is simply caused by the coordination number of the sites. Sites with a higher surface coordination will restrict the number of sites a water molecule can reside in. For a regular surface structure, such as this one, this is even more restricted, giving rise to the coordinated sheets. For sites with lower coordination, the greater degrees of freedom allow the water density to ether smear around the site or, in the case of the corners, reside at discrete crystallographic positions.

The water structuring around this nanoparticle can also be compared to that of a flat hydroxylated {111} surface. Thus a 22Å fully hydroxylated {111} MgO slab was generated; with 878 water molecules spanning the 57Å between the two surfaces. The slab was then simulated in the NPT ensemble for 1ns, with the same relaxation constants as for the nanoparticle. The equivalent water density profile is shown in Figure 5.19. Again water layering clearly forms above the surface, reminiscent of the pure MgO {100} surface, extending into the bulk by 3-4 layers. This gives a similar appearance to the flat faces of the hydroxylated nanoparticle above, with possibly slightly longer range ordering seen.

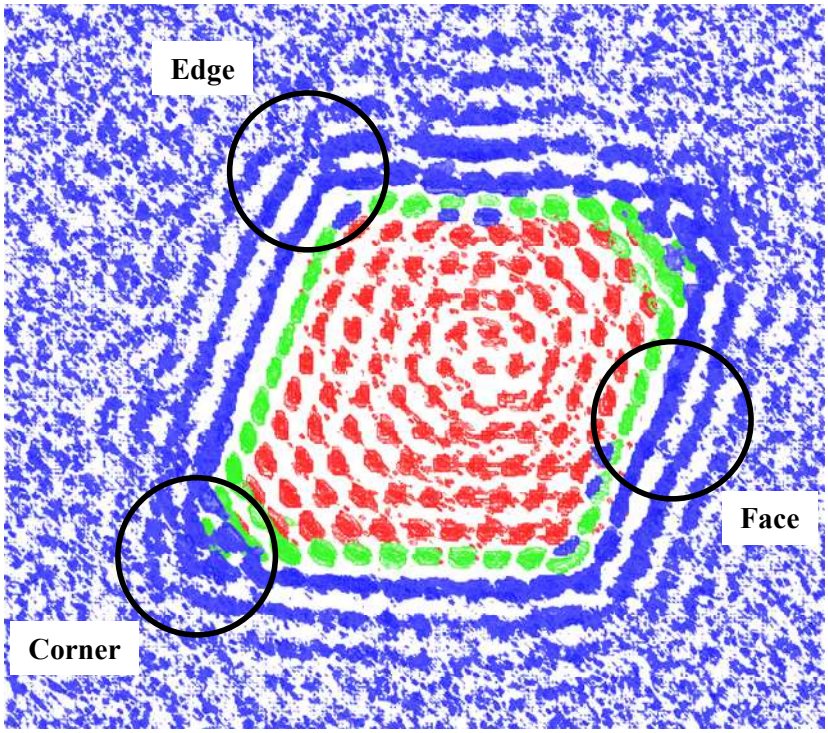

Figure 5.18: Average water density of a fully hydroxylated {111} dominated MgO nanoparticle. Magnesium, hydroxide hydrogen and water oxygen density is represented by red, green and blue respectively. Black circles indicate corner, edge and face sites.

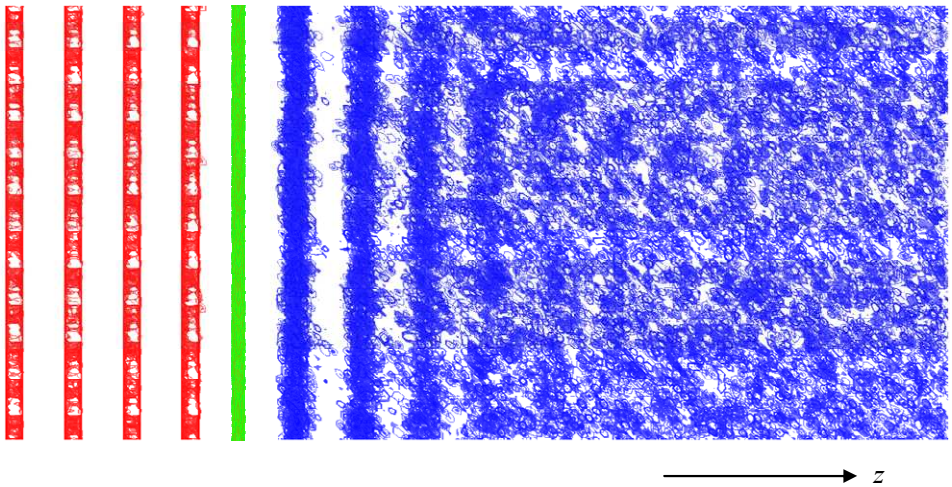

Figure 5.19: Average water density above one surface of a fully hydroxylated {111} MgO slab. The average density of magnesium, the hydrogen atoms of the hydroxide groups and the oxygen atoms of water molecules are indicated by red, green and blue, respectively. NOTE: smearing is due to vibrations about the atomic positions.

As in section 5.1, we can calculate the variation of water mobility for the nanoparticle and surface via the water residence times. Analysis of the residence times of surface hydrogen atoms with water oxygen atoms indicated a uniform pattern across the surface, with a residence time varying between 6-8ps. Thus there is high water mobility in the first layer of coordinated water, allowing more favourable displacement of coordinated water molecules. Comparison to the residence time for the nanoparticle, however, is more complex as the residence time will vary depending on the surface site and its coordination. Therefore, we calculated the variation of the residence times for all surface hydrogen atoms of the nanoparticle, projected onto an isosurface across these atoms and coloured according to the residence times. This approach was also applied to the calculated average number of water molecules coordinated to the surface atoms. It is also informative to compare these plots to those for a pure surface. To allow this, similar plots have been constructed for a {100} nanoparticle, with residence time and number of coordinated water molecules determined for surface magnesium atoms. The {100} nanoparticle, constructed and simulated by Spagnoli [160], has a diameter of 17.5Å and was surrounded by 2613 water molecules. The simulation was run for 600ps using the NPT ensemble, with relaxation parameters of 0.5ps for both the thermostat and barostat, at a temperature of 300K. Previous analysis by Spagnoli also showed a distinct layering of water around the surfaces of the nanoparticle, similar to that shown in Figure 5.18 for the hydroxylated nanoparticle. The contour plots showing residence times and coordination number for both the pure {100} and fully hydroxylated {111} nanoparticles are given in Figure 5.20.

The first observation that is apparent for the {111} hydroxylated nanoparticle, is the movement of hydroxide groups on the faces. Opposing faces on the nanoparticle show holes in the hydroxide arrangement, leading to exposure of surface magnesium atoms. Although not clear from the image, these hydroxides appear to move toward corner sites, increasing the hydroxide concentration at the higher energy sites, with a flattening or rounding occurring on some corners. The nanoparticle also shows a

large degree of symmetry with a similar movement seen on the bottom face of the nanoparticle, indicating that this stabilisation of corner sites is not a random process. Analysis of the residence times for the hydroxylated nanoparticle show that there is no clear pattern of residence time varying with corner, edge and face sites. However, strong coordination around the exposed magnesium atoms is seen. The length of residence time is also in agreement with that of the pure {100} nanoparticle, which shows an approximately continuous residence time across the particle surface. In addition, comparison to the residence times on the {111} hydroxylated slab, shows agreement with low residence times across the regular, fully hydroxylated regions of the nanoparticle. The strong coordination above exposed surface magnesium ions may also be indicative of further hydroxylation sites, as seen for the surfaces detailed previously. The relative length of residence time above surface hydrogen and magnesium is unsurprising due to the comparative weakness of hydrogen bonding to the Mg-O_W bonding.

The variation of average number of coordinated water molecules, however, does vary depending on the position of the surface atom. Corner sites show the highest number of coordinated water, followed by edge and the face sites. This is also seen, to a lesser extent, for the {100} nanoparticle, although if the nanoparticle were of a larger size, a variation pattern more similar to the hydroxylated nanoparticle would be expected. The regions of exposed magnesium on the {111} nanoparticle also give rise to increased numbers of coordinated water, due to both the roughening of the surface as well as increased hydrogen bonding.

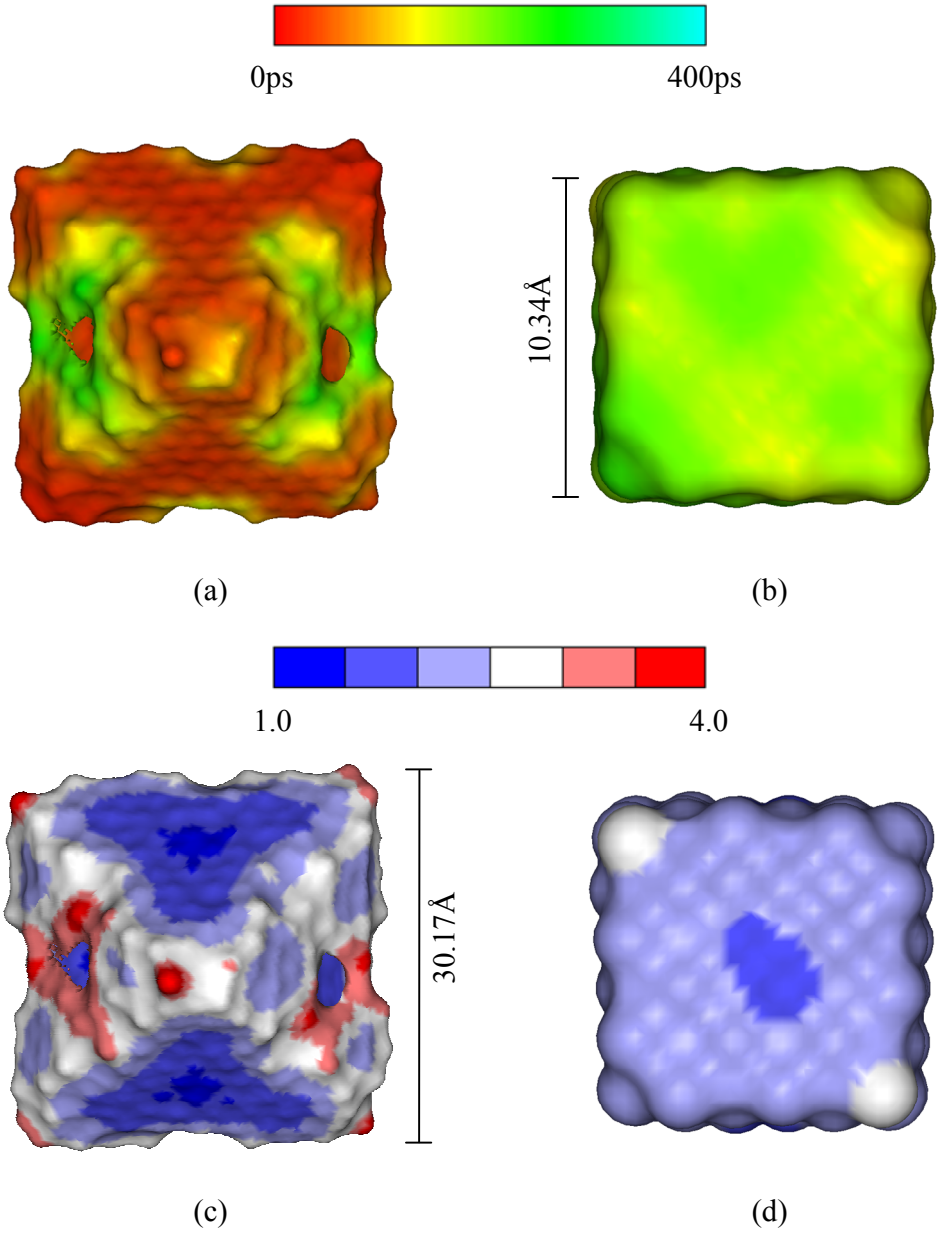

Figure 5.20: Contour plots showing the water residence times on **(a)** a fully hydroxylated {111} and **(b)** a pure {100} MgO nanoparticle, where the colour varies from red to turquoise indicating low to high residence time. The average number of coordinated water molecules on the **(c)** fully hydroxylated {111} and **(d)** pure {100} MgO nanoparticles vary in colour from blue to red, showing low to high numbers of coordinated water molecules.

Overall this study shows that trends seen for a surface can be translated to a nanoparticle comprised of the same surface structure. Hydroxylation of the surfaces gives rise to the formation of highly mobile but structured water layers. For the nanoparticle, the variation in atom coordination number of the nanoparticle has a strong influence on the number of water molecules which can surround it, which in turn affects the water structuring pattern. Above flat regular portions, water layers have the appearance of continuous sheets; however, at the lower coordinated edge and corner sites, this changes to form more distinct crystallographic coordination, with the number of coordinated water molecules increasing with the lowering of the coordination number of the surface site. However, the residence times do not show this variation, and are dependent on the surface composition, with stronger surface bonding giving rise to increased residence times. In addition, rearrangement of the hydroxide groups are seen for the nanoparticle, in an ordered manner to ensure no net dipole is formed, giving rise to more rounded corner sites. This results in exposed surface magnesium atoms, which could undergo dissociative water adsorption, indicated by increased water coordination at these sites.

The next section will investigate the reactivity of the surface sites by considering surface carbonation of corner, edge and face sites.

5.2.3 Carbonation of Nanoparticles

The previous study in chapter four revealed that CaO was more reactive toward carbon dioxide than MgO, thus we elected to study carbonate adsorption on a CaO nanoparticle. As with MgO, the calculated surface energies give rise to a cubic morphology, due to the {100} surface stability. Carbon dioxide adsorption was then modelled as before through the addition of a carbonate group, whilst ensuring charge neutrality is maintained. Surface adsorption was considered on three sites on the nanoparticle, namely a corner, the middle of an edge and in the centre of a face. The initial placement of the carbonate unit was also varied, as with the surfaces, considering both the placement of the carbonate *into* and *above* the surface. When

the carbonates were added *above* the surface, an adjacent oxygen atom was removed. Following this initial addition, the nanoparticles were energy minimised to evaluate the relative stability of the different sites and their associated adsorption energies, as detailed in Table 5.4. The procedure for calculating adsorption energies is the same as that given in chapter four. The minimised structures are also shown in Figure 5.21.

Table 5.4: Energies of adsorption for a single carbonate on different surface sites of a {100} dominated CaO nanoparticle following structure minimisation. The energy for the different CaO surfaces, as detailed in chapter four, is included for comparison.

Adsorption Site		Adsorption energy / eV
Above	Corner	-2.16
	Edge	-2.20
	Face	-1.20
Into	Corner	-2.36
	Edge	-2.20
	Face	-1.20
{100} Surface Site		-1.32
{110} / {310} Surface Sites		-1.62 / -1.70
{111} Surface Site		-3.07

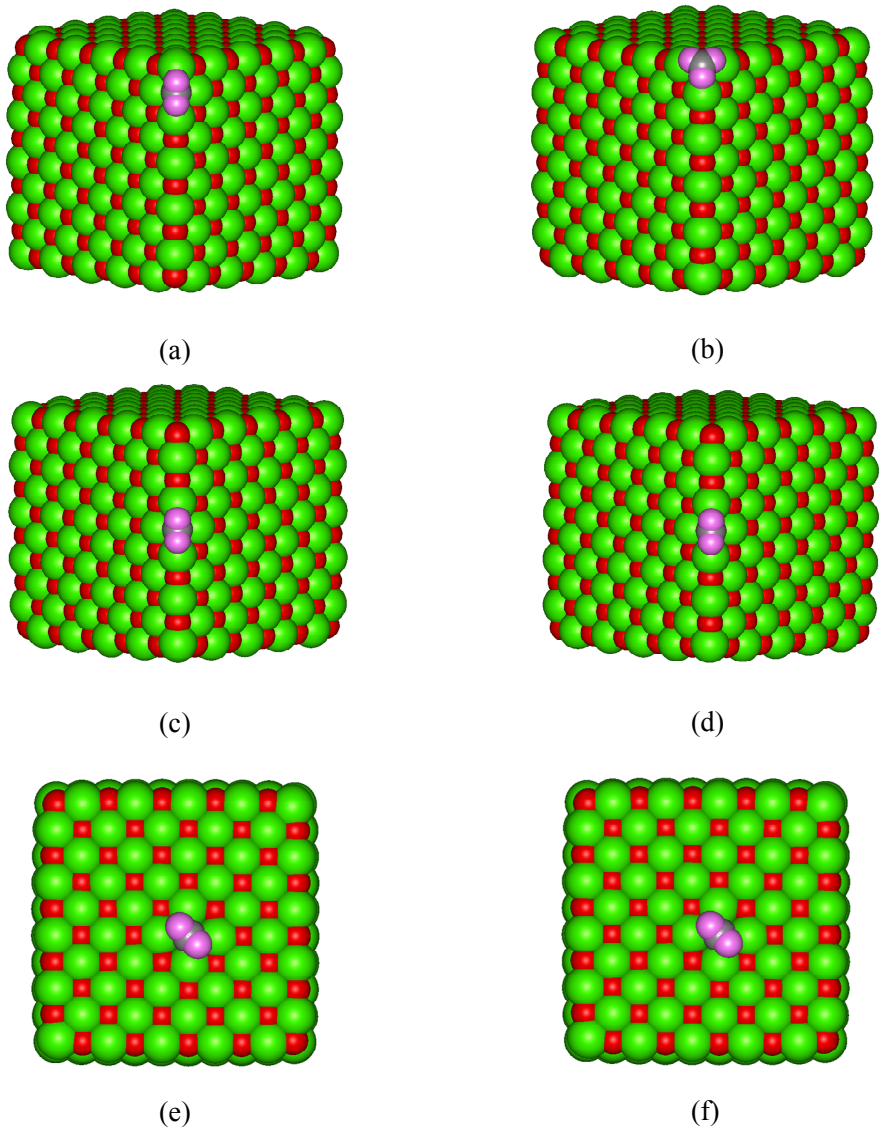

Figure 5.21: Structures of the minimised {100} CaO nanoparticles following adsorption of a single carbonate **(a)** *above* and **(b)** *into* a corner site; **(c)** *above* and **(d)** *into* an edge site, and **(e)** *above* and *into* a face site.

The results clearly indicate carbonation of CaO nanoparticles is indeed a favourable process with the adsorption onto face sites being the least favourable process. Moreover, both the addition *above* and *into* the site minimise to identical structures, with the carbonate becoming integrated into the surface, with the same adsorption energies. A similar case is seen for the addition to an edge site, with both

initial carbonate placement methods giving rise to the same minimised structure and adsorption energies, with the carbonate inserting into the edge rather than above it. Adsorption at an edge site is also calculated to be more favourable than at a face site. However, the different adsorption methods for corner sites do not give identical structures, see Figures 5.21(a) and (b). Firstly, the addition of a carbonate group *above* a corner site gives rise to an adsorption energy of slightly less that the edge sites. The resulting structure shows that the carbonate group, placed initially above an edge calcium atom with an adjacent oxygen vacancy, relaxed into the vacant site. This gives rise to a structure similar to that in the centre of the nanoparticle edge, however, it is destabilised more by proximity to the high energy corner site. Secondly, carbonate addition *into* the corner allows relaxation of the carbonate to adjust itself to form three calcium – oxygen interactions, stabilising this mode. This also gives rise to the most favourable adsorption mode. Overall this shows that the trend in adsorption site, from most to least favourable, being corner > edge > face.

The adsorption onto the different nanoparticle adsorption sites can also be compared to the adsorption onto flat surfaces, as detailed previously in chapter four. For the {100} surface, good agreement is seen with that of the faces, with both adsorption energies being similar in the energy. Edge sites can be compared to {110} and {310} surfaces, which are similar due to their respective micro-facets and steps. Adsorption on the nanoparticle is seen to be more stable by approximately 0.50eV. This is unsurprising as the high energy surface sites will gain additional stability from the rest of the surface, whereas this is not possible for a nanoparticle, making adsorption more energetically favourable. The high energy corner sites can also be compared to the {111} surface. In this case, however, surface adsorption is seen to be more stable. This is a result of the instabilities of this surface being greater than an isolated corner site. The adsorption of a carbonate on the {111} surface will add stability to more than one low-coordinated surface ion, therefore producing increased reactivity.

The results show that there is more than one local minimum for the corner site. Therefore, following this, the nanoparticles were simulated at 300K in the NVT ensemble for 1ns, using a relaxation constant of 0.5ps, with the carbonate group unconstrained, thus allowing it to potentially move to a more stable adsorption site. The final configurations of these nanoparticles are shown in Figure 5.22. However, as the two simulations of the edge sites minimised to the same structure, as well as the face sites, only one of these nanoparticles was simulated further.

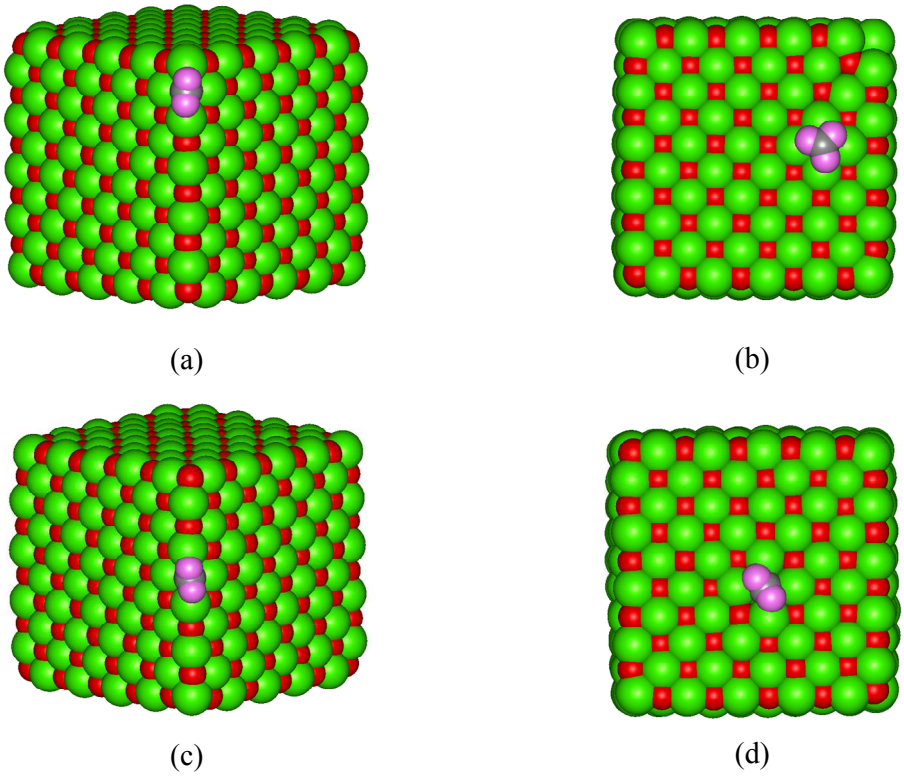

Figure 5.22: Final structures of the {100} CaO nanoparticles following simulation at 300K for 1ns after the adsorption of a single carbonate **(a)** *above* and **(b)** *into* a corner site, as well as at **(c)** an edge site and **(d)** a face site.

The results suggest that the majority of modelled adsorption sites are stable, with location of the carbonate group remaining the same. The exception to this is the nanoparticle with carbonate adsorption *into* the corner. To elucidate the reason for

this movement, the adsorption energy resulting from this structure was calculated and found to be -2.24eV. This is similar, although slightly less favourable, than the original mode, therefore indicating that the energy barrier for the movement of the ion is low. Interestingly, this mode is also more stable than found for the adsorption *into* the face. In addition, the larger number of adsorption sites identical to this are much greater than the corner site, therefore having an additional entropic driving force. This result also indicates that the oxygen vacancy is more stabilised on the corner than in an edge or face site. The other adsorption modes have a sufficiently higher barrier to the carbonate migration so that it is not seen. This is most likely due to the increased binding energy to the carbonate in other sites, coupled with the instability of oxygen vacancies at edge and face sites.

In conclusion this study shows that carbonation of the {100} CaO nanoparticulate system is indeed more favourable than the surface carbonation of the surface structure, at least for the adsorption of a single carbon dioxide. In addition, based on the results of the surface calculations, increased carbonation would be expected to further stabilise the system, although more detailed simulation would be required to assess this. It is also seen that carbonation will preferentially occur on high energy sites comprising of under coordinated calcium atoms.

5.3 Chapter Conclusions

This chapter has used dynamical models to consider the effect both surfaces and nanoparticles have on the structure of liquid water and developed a robust approach for evaluating the residence times for surface species across the whole surface. In addition, the effect that adsorbed carbonates and, in the case of nanoparticles, dissociatively adsorbed water has on this structure has also been considered.

The molecular dynamics simulations indicate that the surface topography has a direct influence on the structure of the water. Water structure forms through coordination of the water molecules closest to the mineral surface, which in turn

causes the formation of further layers, with interlayer spacing of approximately 2.5Å. The first water layer is seen to form about 2.4 and 2.2Å away from the surfaces for CaO and MgO, respectively, with coordination seen both through *M*-O interactions as well as hydrogen bonding to surface oxygen atoms. Flat surfaces, such as the {100} surface, are seen to give rise to highly mobile layers of coordinated water with a sheet-like appearance, which is also seen above the terraces of the {310} surface. The presence of surface features, such as steps and facets, act to localise water, therefore reducing its mobility. Density plots revealed that water coordination around these features form rows of high water density following the surface structure, with reduced water mobility indicating the strength of this coordination. A general feature is that the water molecules tend to be more strongly adsorbed to the surface metal atoms, rather than through hydrogen bonding to surface oxygen atoms. Upon carbonation, this water structuring is seen to be disrupted and water mobility is seen to increase due to the formation of an amorphous carbonate layer on the mineral surface.

The simulations of magnesium oxide nanoparticles confirm the stability of the {100} surface by giving rise to cubic morphologies. Simulation of nanoparticles with different shapes show higher energies and, with simulated annealing, the {110} and {111} bound nanoparticles undergo surface faceting to form a multi-faceted cubic arrangement thereby reducing the nanoparticle energy. In addition, the effect of nanoparticle size, ranging from 20-40Å, does not appear to alter the relative stabilities. However, increasing the size does reduce the energy of the nanoparticle, though the greater amount of bulk material. Surface hydroxylation, as expected, is seen to destabilise the {100} surface, whilst dramatically stabilising the high energy {111} nanoparticle, in accordance with the study of hydroxylation of the surfaces. In addition, the surface hydroxylation of the nanoparticles was seen to reduce the energy for all morphologies, making them more stable than their pure counterparts. The addition of water to the hydroxylated nanoparticle system was also modelled, with results showing water structuring similar to the surfaces, with lower coordinated sites giving rise to a more isolated coordination pattern. The effect of

carbonation has also been studied on the {100} bound CaO nanoparticle, with key results being the energetic favourability of carbonation of low-coordination sites over the flat surfaces. This implies that carbonation efficiency can be increased through the use of nanoparticulate systems.

The results discussed in this thesis thus far have focussed on adsorption processes on alkaline earth metal oxide surfaces. However, the same techniques and methodologies can also be applied to more complex materials, such as the actinide oxides. However, modelling actinide oxide materials is more complex than the simple alkaline earth metal oxides, due to the unpaired *f*-electrons giving rise to difficulties in simulating the electronic and magnetic structure of the bulk material and their surfaces. Therefore, prior to considering the adsorption of water of uranium dioxide surfaces, the simulation of this material using electronic structure techniques will be discussed and their use in modelling non-stoichiometric thin film structures.

Chapter Six

Bulk Uranium Dioxide & Thin Film Structures

The previous chapters have shown that potential models are not only robust but that they can also calculate both static and dynamic properties of oxide systems accurately and reliably. The disadvantage of these models, however, is the lack of description of the electronic and magnetic structure of the materials, which require the use of electronic structure techniques to determine. It is likely that for a material like uranium dioxide the magnetic properties may play a significant role in surface structure, stability and reactivity. This chapter aims to not only further understand the electronic and magnetic properties of uranium dioxide but to also investigate the

value of DFT+U modelling. Initially, the focus will be on bulk UO_2 but will be followed by an investigation of thin film structures. The understanding of defects in bulk UO_2 and the variation in stoichiometry of the thin films will then be used to elucidate the oxygen segregation behaviour in this material.

Chapter two outlined how density functional theory techniques can be used to simulate the forces between atoms in the system of study, leading to the use of energy minimisation to find the lowest energy structures. However, the practical use of DFT requires the selection of a number of important parameters in order to simulate the material of interest accurately. Therefore, the first section of this chapter will consider the parameter selections and DFT methodologies for simulating bulk UO_2.

6.1 Modelling Uranium Dioxide with DFT

Uranium dioxide is naturally found as the mineral uraninite and is structurally analogous to the cubic fluorite structure, where the uranium atoms form a face-centred cubic array with oxygen atoms residing in the tetrahedral holes. The structure of the unit cell of UO_2 is shown below in Figure 6.1.

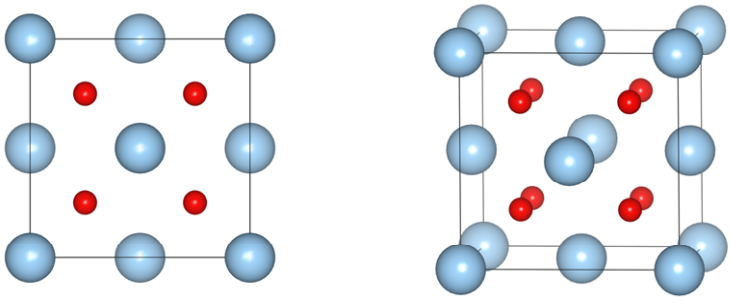

Figure 6.1: Top and side view of the structure of the unit cell of UO_2. Uranium atoms are coloured light blue and red represents oxygen atoms.

Initially, a standard DFT methodology was considered. Bulk UO_2 was modelled in the $Fm\bar{3}m$ space group, with parameter selection conducted from the modelling of AFM (antiferromagnetic) UO_2 with PW91 GGA pseudopotentials. The first requirement was the selection of the plane wave cutoff, the energy convergence parameters and the selection of a k point grid. The plane wave cutoff was selected as 500eV, which is suitably large as to ensure energy convergence. Two sets of convergence criteria for the ionic and electronic relaxation steps were considered, allowing for efficient use of computational resources. These are defined as 'high' and 'low' accuracy and consider convergence as being when the energy of the system varies less than $1x10^{-5}$ and $1x10^{-4}$eV, respectively. In addition, k point convergence was found through the simulation of bulk UO_2 using the 'high accuracy' parameters and four different k point grids, namely the 3x3x3, 4x4x4, 5x5x5 and 6x6x6. Suitable convergence was seen for a 5x5x5 grid, giving a bulk energy of -30.91eV per UO_2 unit. As with the majority of previous studies, discussed in chapter one, the magnetic structure is modelled using a collinear model, with spin-coupling neglected.

We next considered the selection of approaches to approximate the exchange-correlation energy. LDA and GGA methods were considered, with both PW91 and PBE pseudopotentials used for the GGA approach. In addition the PW91 simulations were also carried out using the 'low accuracy' convergence parameters. The magnetic structure was also modelled using AFM and FM (ferromagnetic) distributions. In addition to analysing the lattice energies per U atom, it is also informative to consider the electronic. Therefore comparison is also made to the relative energy difference between AFM and FM structures and the electronic band gap. These results are tabulated in Table 6.1, with comparisons also made to experimental data. One point of interest in the results is that of the lattice parameters. All methodologies show that the FM material retains its cubic structure; however, a distortion away from this is seen for AFM UO_2. The distortion is most likely the result of the different electronic spin distributions in the bulk cell and will be discussed in more detail later in this section.

Table 6.1: Comparison of bulk UO_2 structural and electronic properties for different DFT methodologies, including experimental results where *a* is [161] and *b* is [63].

Methodology	Energy per UO_2 / eV			Lattice Constants / Å (Volume / Å^3)		Band Gap / eV	
	AFM	FM	E_{FM}-E_{AFM}	AFM	FM	AFM	FM
GGA PW91 High accuracy	-30.91	-31.06	0.15	*a* = 5.405 *b* = 5.415 *c* = 5.405 (158.194)	*a* = *b* = *c* 5.425 (159.661)	0	0
GGA PW91 Low accuracy	-30.91	-31.06	0.15	*a* = 5.402 *b* = 5.413 *c* = 5.402 (157.960)	*a* = *b* = *c* 5.425 (159.661)	0	0
LDA	-33.82	-33.87	-0.05	*a* = 5.278 *b* = 5.277 *c* = 5.278 (147.003)	*a* = *b* = *c* 5.277 (146.947)	0	0
GGA PBE	-30.96	-31.14	-0.18	*a* = 5.410 *b* = 5.421 *c* = 5.410 (158.662)	*a* = *b* = *c* 5.424 (159.573)	0	0
Experiment	-		>0[a]	5.470[a] (163.667)		2.1[b]	

Results clearly show the failure of the LDA approach to predict the structure and band gap of this material accurately. This is also shown by its failure to predict the AFM structure as the most stable phase. In comparison with GGA, the PBE functional also fails to predict the AFM structure as the most stable phase. The PW91 pseudopotentials, however, give a more stable AFM phase whilst giving reasonable lattice parameters. In addition, varying the accuracy of the minimisation

appears to have little effect on these energies or lattice parameters, indicating that it can appropriately be used to find minimum energy structures.

The electronic band gap is determined from the total energy density of states (DOS) of the material. The DOS is a representation of the number of available electronic states in the system under study, and is characterised by the number of bands. The Fermi energy is the energy of the highest occupied band at 0K and the band gap is a measure of the difference in energy between the highest energy occupied and lowest energy unoccupied energy levels. Figure 6.2 shows the DOS for both AFM and FM UO_2 structures using the GGA method with high accuracy convergence parameters and PW91 pseudopotentials, where the energy scale is adjusted so that 0eV represents the Fermi level. Although not shown, similar DOS are predicted for the other DFT methodologies. As can be seen neither the AFM or FM structures have a band gap, with the Fermi level in the middle of a band. In comparison to the known DOS, as outlined in chapter one, the DOS appears to show correct prediction of the O 2*s* and U 6*p* bands, present between approximately -15 to -13eV. The O 2*p* band is also present, located between approximately -8 to -4eV. The major failure is that the 5*f* band is predicted to be a continuous band, whereas the previous experimental study shows that localisation occurs and the occupied and unoccupied states are split to give a band gap [51].

Overall, it can be seen that standard DFT approaches fail to accurately model both AFM and FM bulk UO_2. Hence to improve the electronic structure we need to move to an alternative scheme, such as the DFT+U methodology, which has been shown to give the necessary localisation of the 5*f* band. The majority of previous studies, for example, [49, 57], have used a value of U of 4.0eV, fitted to the experimental XPS/BIS studies of Baer and Schoenes [51]. However, this totally neglects the effect of U on the lattice parameter, which is likely to affect the defect properties nearly as much. Hence, we elected to compromise by using U=3eV but also include U=5eV for comparison.

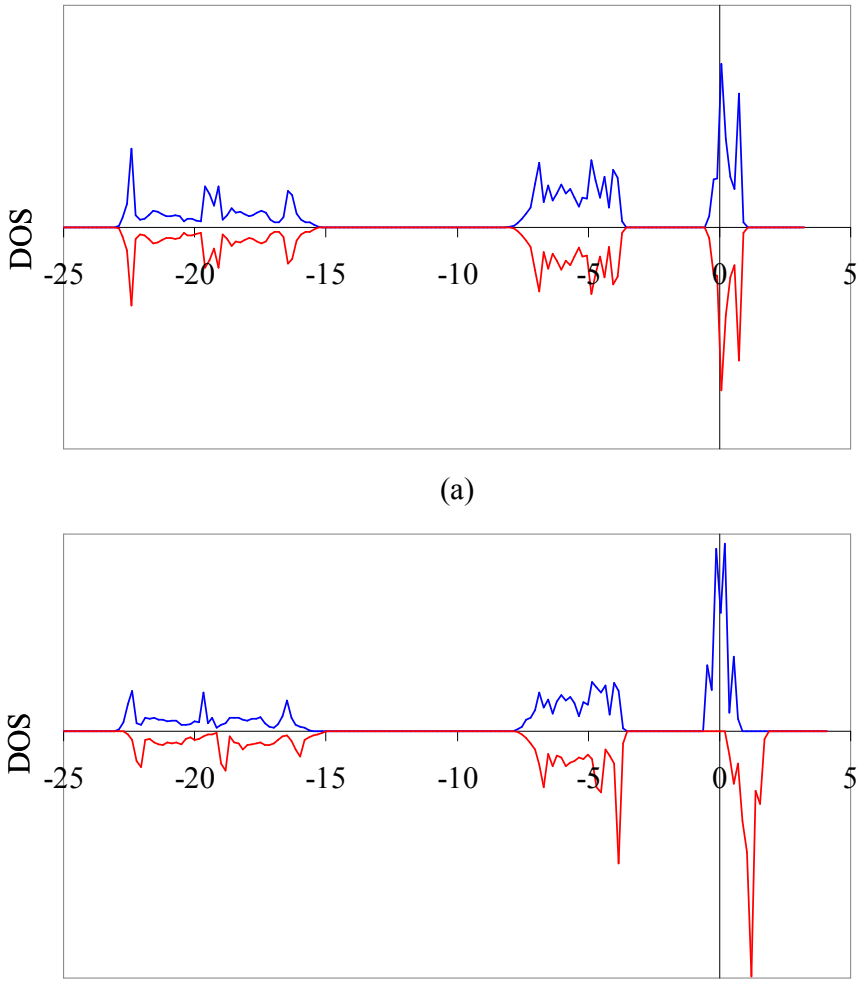

Figure 6.2: Total energy density of states (DOS) for **(a)** AFM and **(b)** FM bulk UO_2 structures using a GGA PW91 approach with high accuracy convergence parameters, where the energy scale is adjusted so that 0eV represents the Fermi energy. Blue and red lines represent spin up and spin down states, respectively.

The effect of the different U values is shown in Table 6.2. The results not only indicate an underprediction of the band gap using a U value of 3eV but also that the increased value of 5eV more correctly predicts the band gap whilst overestimating the lattice parameter. Therefore, when constraints in available computational resources occurred only one series of calculations was run, using a value of 3eV, as

this gives rise to a greater degree in accuracy for the lattice parameters, and hence the structural features. The comparison of 'high' and 'low accuracy' methods again show little variation, thereby indicating that these 'low accuracy' parameters can be used successfully to predict low energy structures.

Table 6.2: Comparison of bulk UO_2 structural and electronic properties for different DFT+U methodologies, including experimental results.

Methodology	Energy per UO_2 / eV			Lattice Constants / Å (Volume / Å^3)		Band Gap / eV	
	AFM	FM	E_{FM}-E_{AFM}	AFM	FM	AFM	FM
GGA+U PW91 (U=3eV) High accuracy	-29.13	-28.65	0.48	a = 5.549 b = 5.529 c = 5.549 (170.246)	$a = b = c$ 5.517 (167.923)	1.15	0
GGA+U PW91 (U=3eV) Low accuracy	-29.14	-28.65	0.49	a = 5.560 b = 5.510 c = 5.560 (170.334)	$a = b = c$ 5.517 (167.923)	1.32	0
GGA+U PW91 (U=5eV) High accuracy	-28.50	-27.17	1.33	a = 5.592 b = 5.550 c = 5.592 (173.551)	$a = b = c$ 5.571 (172.902)	2.55	0
GGA+U PW91 (U=5eV) Low accuracy	-28.50	-27.17	1.33	a = 5.581 b = 5.565 c = 5.581 (173.336)	$a = b = c$ 5.569 (172.716)	2.55	0
Experiment	-		>0	5.470 (163.667)		2.1	

We have calculated the DOS generated using the DFT+U methodology, shown by Figure 6.3 for AFM and FM UO_2. In comparison to the DOS generated using the

standard DFT approach, Figure 6.2, it can be seen that the effect of the on-site correction term is to increase the splitting of the filled and unoccupied *f* bands, for both the AFM and FM materials. This is due to the increased localisation of *f*-electrons causing repulsion with the unoccupied *f* states. Although the FM material is still predicted as being conducting, the DOS has been improved through the inclusion of the U term. Increasing the U parameter from 3 to 5eV can be seen to increase the splitting in *f* bands whilst moving the occupied *f* band closer in energy to the occupied O 2*p* band.

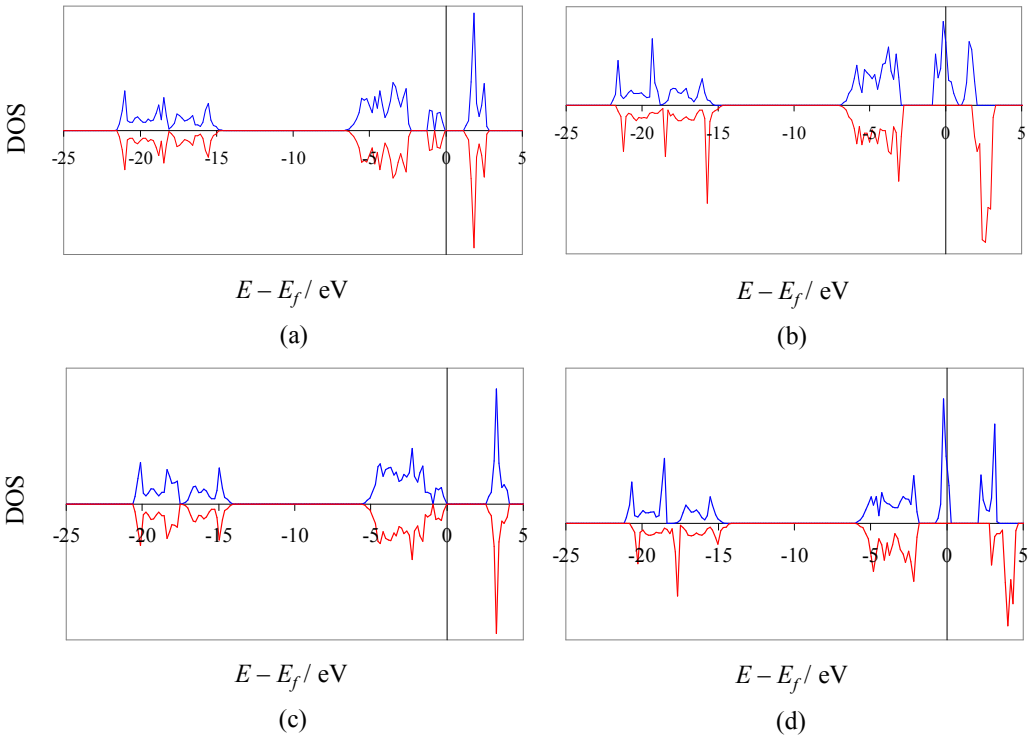

Figure 6.3: DOS for the **(a)** AFM and **(b)** FM bulk UO_2 structures using a DFT+U methodology, where U=3eV. The same respective DOS for a U value of 5eV are shown in **(c)** and **(d)**. NOTE: the energy scale is adjusted so that 0eV represents the Fermi energy.

The band structure can be considered in more detail through the analysis of the partial DOS (PDOS). The PDOS decomposes the DOS into contributions as a result of different angular momentum components, i.e. whether the levels are *s*-like or *p*-like, etc, thus allowing the contribution of different orbitals to be evaluated. The

PDOS for bulk AFM and FM UO_2, calculated using U=3eV, is shown in Figure 6.4. This clearly supports that it is the *f* bands which are separating from the inclusion of the U term, with the band gap appearing between occupied and unoccupied states.

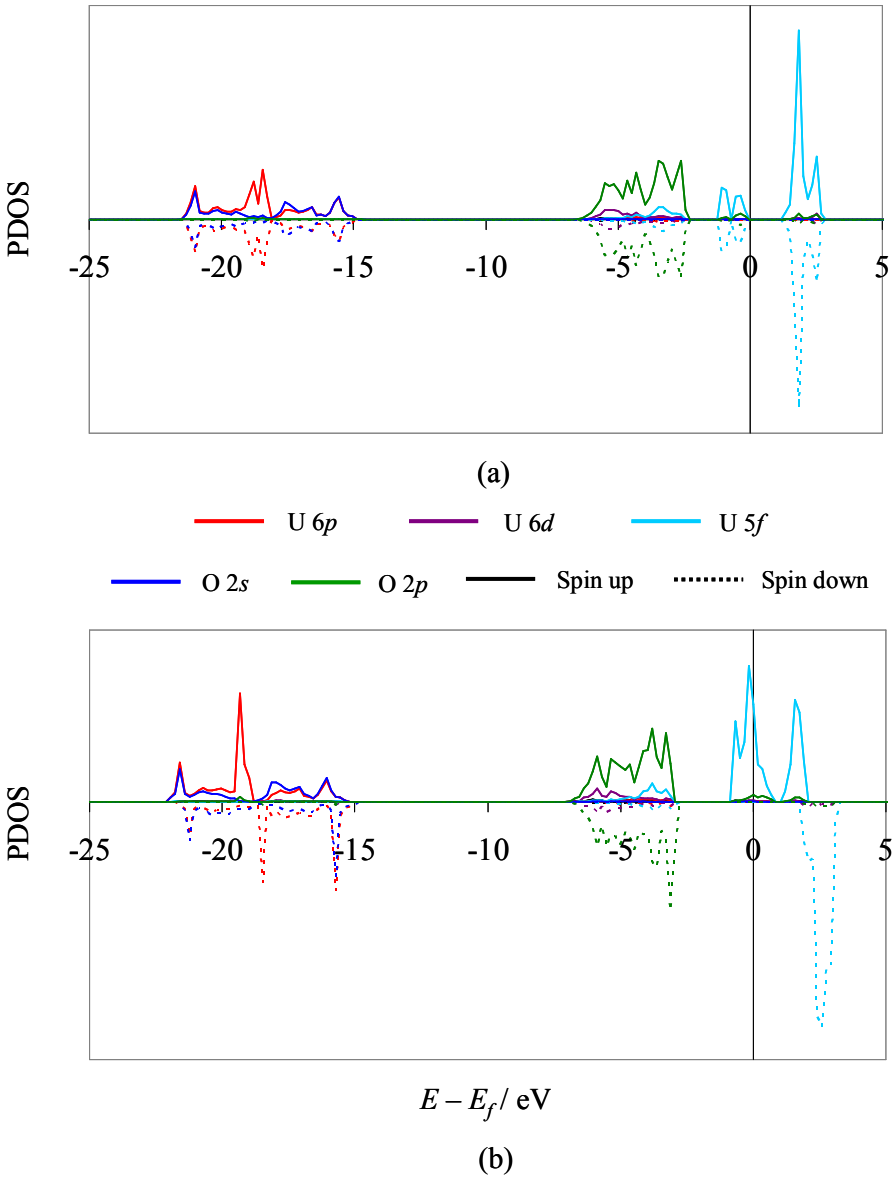

Figure 6.4: Partial energy DOS (PDOS) for the **(a)** AFM and **(b)** FM bulk UO_2 structures using a GGA+U methodology, where U=3eV. NOTE: the energy scale is adjusted so that 0eV represents the Fermi energy.

The implications of increasing the value of U can be further considered through its effect of the PDOS. Figure 6.5 shows the PDOS for AFM UO_2, calculated using a GGA+U method where U=5eV. It can be seen that whilst increasing the on-site correction provides a more precise value for the band gap in AFM UO_2, the PDOS shows that the band structure differs more from experimental observations [53]. Although orbital hybridisation occurs between the O 2*p* and U 6*d*/5*f* orbitals, a distinct peak is seen in XPS data at the top of the band gap, which is primarily attributed to the 5*f* electrons. However, Figure 6.5 shows that the peak at the top of the valence band when using a U value of 5eV contains a much greater contribution from the O 2*p* than expected.

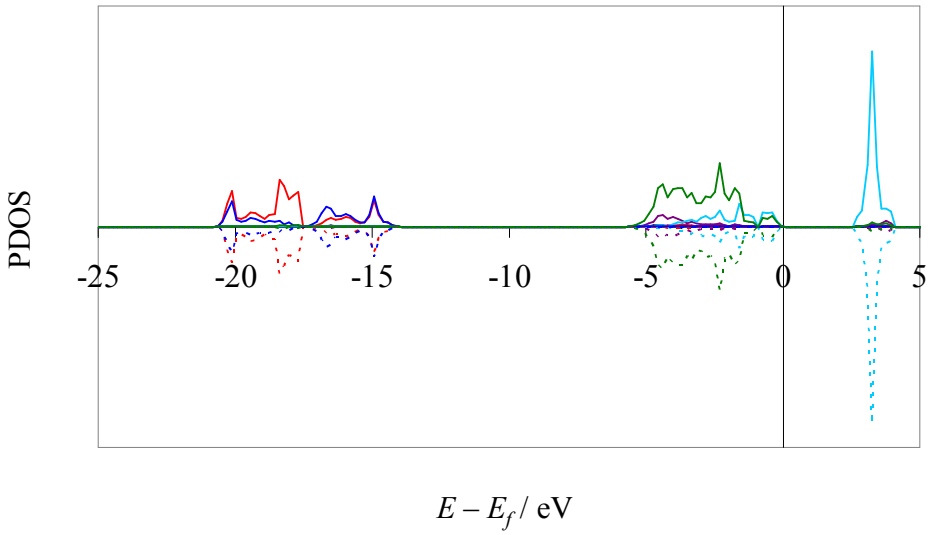

Figure 6.5: Partial energy DOS (PDOS) for the AFM bulk UO_2 structure, calculated using a GGA+U methodology, where U=5eV. NOTE: the energy scale is adjusted so that 0eV represents the Fermi energy and the colour scheme for different orbital bands is identical to that used in Figure 6.4.

The electronic structure of UO_2 can be further probed through consideration of the charge distribution in the cell. Bader charge analysis can be used to determine the effective charges on the uranium and oxygen atoms in the cell, indicating the degree of covalency, with the results detailed in Table 6.3. Bader charge analysis is a method to determine the effective charge on an atom based on its electron density.

To do this, the minimum in electron density between all bonds is used to define a volume around each atom, which can then be integrated to determine the total number of electrons. By subtracting this from the number of electrons initially used, the effective charge is calculated. It can be seen that varying the DFT methodology does not appear to give rise to a large difference in the Bader charge on either the uranium or oxygen atoms. However, as the value of the on-site correction term is increased the difference in charges between the AFM and FM systems is also seen to increase. The uranium and oxygen atoms are significantly different to their formal charges of +4 and -2, respectively, thus indicating that there is covalency in the U – O bond.

Table 6.3: Comparison of Bader charge analysis on uranium and oxygen atoms in bulk UO_2 using different DFT methodologies. NOTE: All data refer to high accuracy calculations.

Methodology	AFM		FM	
	U Charge	O Charge	U Charge	O Charge
GGA PW91	+2.49	-1.24	+2.48	-1.24
GGA+U PW91 U=3eV	+2.49	-1.24	+2.45	-1.23
GGA+U PW91 U=5eV	+2.52	-1.26	+2.46	-1.23

The charge distribution can further be considered through the spin density. The spin density is determining by subtracting the spin down charge density from the spin up charge density, thereby indicating regions of excess up and down spin. The calculated spin density for bulk AFM UO_2, with the on-site correction varying from 0 to 3 to 5eV, is shown in Figure 6.6. The most apparent feature of these plots is the spin density surrounding the uranium atoms. Firstly, the AFM distribution is clearly seen by the alternating layers of spin up and down density. Secondly, the shape of the spin distribution is seen to significantly change as the value of U is increased. In the absence of an on-site correction, the spin distribution has a roughly oval shape around the uranium atoms, whereas when U is increased, a more defined shape is

seen, with an appearance more in line with the *f*-orbital shape, caused as a result of increased electron localisation. Although, due to complex hybridisation between uranium orbitals, designation of orbital occupancies is unfeasible.

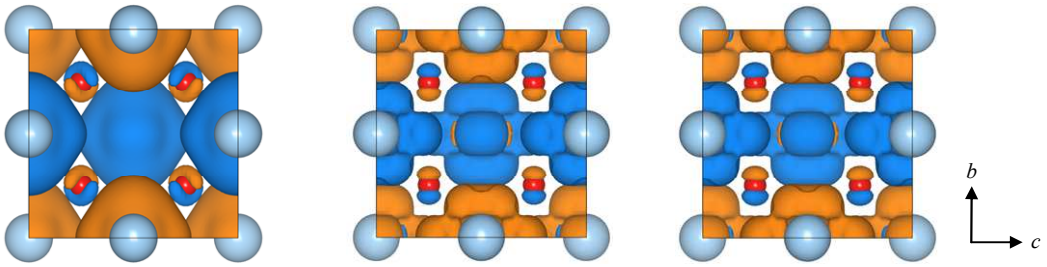

Figure 6.6: Spin density plots for bulk AFM UO_2 using an on-site correction term of **(a)** 0, **(b)** 3 and **(c)** 5eV. Cells are viewed along *a* axis, with 50% of the cell removed in this direction for clarity. Regions of excess spin up and down density are coloured orange and blue, respectively with an isosurface of 0.01 electrons $Å^{-3}$.

The other noticeable feature is the effect on the spin density of the oxygen atoms. This is a result of the hybridisation and mixing between the uranium and oxygen atoms. The minimum energy will occur when interactions between electrons of opposing spin between uranium and oxygen are minimised. This also correlates with the distortion seen in the *b* lattice parameter for the AFM configuration. The more spherical distributions in the absence of U cause a larger smearing of charge across the oxygen atoms. The consequence of this is that there is also a larger degree of repulsion between electrons of the same spin, giving rise to an elongation of the *b* lattice parameter. When the on-site correction term is included, the spin density on oxygen becomes confined to the *b* direction. As this dramatically reduces interactions of electrons with identical spins, a reduction in the *b* parameter is seen due to attraction in this direction. It has been suggested though that due to the noncollinear magnetism in UO_2, with magnetic moments pointing along the <111> directions, with an equivalent distortion of the oxygen cage, a cubic cell would still be seen experimentally [162].

In summary, this study has shown the failure of standard DFT methodologies to simulate bulk uranium dioxide. Inclusion of an on-site correction term improves this significantly, correctly predicting a band gap for AFM UO_2. Increasing the value of the U term gives rise to increased localisation of the *f*-electrons, causing the band gap to be widened, although a corresponding increase in the lattice parameter is also seen, away from the experimental value.

Overall, this comparison of DFT methodologies has enabled the selection of parameters for use in later calculations. Namely with a DFT+U method using GGA PW91 pseudopotentials and a 5x5x5 k point grid. Results of the 'high' and 'low accuracy' suggest that whilst energy prediction is consistent between the two approaches, band gap predication is not. Therefore, due to these calculations being computationally expensive, the 'low accuracy' approach will be used to identify the most stable configurations. These will then be minimised in 'high accuracy'. As noted above, a U value for the DFT+U methodology of 3eV has been selected for primary use, although a U value of 5eV will also be used for comparative reasons where feasible.

Following the selection of simulation parameters, we can next consider the non-stoichiometry in both the bulk material and thin film structures.

6.2 Non-Stoichiometric Uranium Dioxide

As discussed in chapter one, the fluorite structure of uranium dioxide allows the formation of hyperstoichiometric structures, by accommodating oxygen interstitial defects in the octahedral sites in the structure allowing for the formation of a range of different oxides. The formation energies for both anion and cation defects, have been considered using both a potential-based approach, for example, Catlow [46], and DFT+U, for example, Nerikar *et al*. [49], as well as Frenkel energies, and will be detailed in the next section.

However, there has been little simulation work on the non-stoichiometry of thin film structures or surfaces, which is important for understanding the processes which occur for this material. This is also important as oxide layers will form on uranium metal in storage. Although the interactions between the oxide layer and the underlying metal will also be of importance, in this preliminary study only the structure and stability of the oxide thin films will be considered.

The next sections in this chapter will therefore begin to consider the non-stoichiometry of both bulk material, in the form of point defects, and thin film structures. Firstly, we will use the aforementioned DFT+U methodology to consider anion defect formation energies in AFM bulk UO_2. The simulation of non-stoichiometric thin films will then be detailed and utilised to generate thin film phase diagrams as a function of the change in chemical potential of oxygen. Finally, both sets of simulations will be used to consider oxygen segregation.

6.2.1 Point Defects

Previous studies have shown than uranium defects are highly unfavourable in bulk UO_2, with DFT+U vacancy and interstitial formation energies of 6.0 and 8.2eV, respectively, [48]. We have elected to perform some preliminary calculations to provide some rough estimates of point defect energies, both to investigate the approaches described in the literature for DFT simulations and to provide a comparison with our thin film structures. Therefore, for this study of point defects, we have solely considered oxygen vacancy and interstitial defects in the bulk AFM UO_2 cell. These have been calculated using a DFT+U approach, with values of both 3 and 5eV used for the on-site correction. In addition, defects have been simulated using a standard cubic unit cell, as well as a supercell generated using the rhombohedral reduced unit cell, which can be represented as having a volume of $8V_r$, where V_r is the reduced unit cell volume and is equal to $40.39Å^3$. The effective volume of the cubic cell is $4V_r$.

Initially, neutral defects were calculated, where an oxygen atom was either added or removed. These defects can also be represented using Kröger-Vink notation, which is routinely used to describe defect states, by Equations 6.1 and 6.2, for the neutral oxygen vacancy and interstitial formation, respectively.

$$O_O^X \rightarrow \tfrac{1}{2} O_{2(g)} + V_O^{\bullet\bullet} + 2e' \qquad 6.1$$

$$\tfrac{1}{2} O_{2(g)} \rightarrow O_i'' + 2h^{\bullet} \qquad 6.2$$

The formation energies of a neutral vacancy, $G_O^{\text{neutral, vacancy}}$, and a neutral interstitial, $G_O^{\text{neutral, interstitial}}$, are calculated using Equations 6.3 and 6.4, respectively. These neutral vacancy and interstitial formation energies are also equivalent to the heats of reduction and oxidation, respectively. For the following discussion of these energies they are referred to as neutral vacancy and interstitial formation energies.

$$G_O^{\text{neutral, vacancy}} = E_{UO_2}^{\text{defective}} + \mu_{O,298K} - E_{UO_2}^{\text{pure}} \qquad 6.3$$

$$G_O^{\text{neutral, interstitial}} = E_{UO_2}^{\text{defective}} - E_{UO_2}^{\text{pure}} - \mu_{O,298K} \qquad 6.4$$

where $\mu_{O,298K}$ is the chemical potential of oxygen at 298K. The underlying assumption is that the free energies of the solid phases of uranium metal and uranium dioxide do not vary with temperature, i.e. the vibrational entropy contributions are small, allowing for the simple calculation of $\mu_{O,298K}$, and hence the calculation of defect formation energies at this temperature. This is evaluated via Equation 6.5.

$$\mu_{O,298K} = \tfrac{1}{2}\left[\left(E_{UO_2}^{\text{pure}} - \mu_{U_{\text{metal}}}\right) - \Delta G_{formation}^{\text{experimental}}\right] \qquad 6.5$$

where $\mu_{O,298K}$ is determined from two terms. The first refers to the self-energy of O_2 at 0K, calculated from the difference in simulated bulk UO_2 and the chemical

potential of uranium metal. The second term, $\Delta G_{formation}^{experimental}$, is the change in free energy of formation of UO_2 at 298K which represents the change in μ_O at 298K, and is taken from data tables [132]. The half comes from considering the chemical potential of oxygen from oxygen gas. The bulk energy of uranium metal, used for the chemical potential of uranium metal, $\mu_{U_{metal}}$, was calculated using high accuracy convergence parameters, and an increased 13x13x13 k point mesh with a U value of 3eV, to ensure consistency with the UO_2 simulations.

The method also allows for the calculation of μ_O at different temperatures. Therefore we have also determined its value at 1000K. This has been done using a similar approach as mentioned in chapter four. In summary, the chemical potential at 1000K can be determined from the entropy, s_{1000K}, and the change in enthalpy at 1000K, $\Delta h_{1000K\text{-}0K}$, again taken from data tables. This is shown by Equation 6.6.

$$\mu_{O,1000K} = \tfrac{1}{2}\left[\mu_{O_2,0K} + \Delta h_{1000K-0K} - 1000 \cdot s_{1000K}\right] \qquad 6.6$$

where $\mu_{O_2,0K}$ is the chemical potential of oxygen gas at 0K and can be calculated from $\mu_{O,298K}$ using Equation 6.7.

$$\mu_{O_2,0K} = 2\mu_{O,298K} - \Delta h_{298K-0K} - 298 \cdot s_{298K} \qquad 6.7$$

In this approach, we have also assumed that the chemical potential of oxygen in bulk UO_2 is constant between the different sized unit cells, thus only using the value calculated for the $4V_r$ cell for all neutral formation energies. The formation energies for the neutral oxygen vacancies are given in Table 6.4, whilst Table 6.5 details the formation energies for neutral oxygen interstitial, with comparison made to the DFT+U energies, where U=4eV, of Nerikar *et al*.

Table 6.4: Calculated formation energies (eV) for a neutral oxygen vacancy in AFM bulk UO_2 at 298 and 1000K.

Temperature	Cell	U=3eV	U=5eV	Nerikar *et al.*
298K	$4V_r$	5.89	5.52	5.29
	$8V_r$	5.97	6.21	
1000K	$4V_r$	5.06	4.69	
	$8V_r$	5.15	5.38	

Table 6.5: Calculated formation energies (eV) for a neutral oxygen interstitial in AFM bulk UO_2 at 298 and 1000K.

Temperature	Cell	U=3eV	U=5eV	Nerikar *et al.*
298K	$4V_r$	0.91	1.88	-1.34
	$8V_r$	-0.70	1.48	
1000K	$4V_r$	1.74	2.71	
	$8V_r$	0.13	2.31	

The results show that neutral oxygen vacancy formation at 298K is considerably unfavourable in bulk UO_2, although, as expected, a slight reduction in energy is seen as the cell size is increased. In comparison, neutral interstitial oxygen defects are also shown to be generally unfavourable, with the only the grown cell at 298K simulated with a U value of 3eV providing a negative defect formation energy. The increase of temperature is seen to make vacancy formation more favourable, whilst oxygen interstitial formation becomes unfavoured, due to the shift in equilibrium toward the formation of oxygen gas.

The effect of increasing the on-site correction term is seen to have different effects on the two processes. For neutral oxygen interstitial defects, increasing the U value is seen to destabilise their formation, as the insertion of a neutral oxygen atom will give rise to a shift in charge from the uranium atoms to stabilise the excess oxygen. The increased electron localisation, with a U value of 5eV, would therefore penalise this electron density shift more than for the reduced U value of 3eV, giving rise to

increased formation energies. For oxygen vacancy formation, different trends are seen for the different sized cells. For the $4V_r$ cell, increasing U decreases the energy to remove a neutral oxygen atom. This is again due to the increased localisation of electrons, allowing the two electrons available from the removal of a neutral oxygen atom to be further stabilised with the increased U value. However, for the cells grown from the reduced unit cell this is not the case, with increasing the U value making the neutral vacancy formation less favourable. This is most likely a result of symmetry constraints on the non-cubic cell, where the charge imbalance in the cell caused by the increase in electron density on uranium atoms surrounding the vacancy destabilises the cell relative to the less localised electrons when U is equal to 3eV.

The relative energies of the oxygen vacancy and interstitial formation are also in agreement with the values reported by Nerikar *et al*., with interstitial formation being favoured. This also concurs with the known hyperstoichiometry of uranium oxides. However, differences in the actual values for the energies are seen. These differences can be attributed to a number of causes. Firstly, the simulation cells used by Nerikar *et al.* were larger, using an effective $32V_r$ unit cell grown from the cubic $4V_r$ cell. The larger cell would therefore be expected to give reduced energies due to the smaller concentration of defects. In addition, the formation energies were calculated from the simulation of charged unit cells, therefore containing both a different number and distribution of electrons to this study.

These defects can be analysed further by considering the change in charge density, as shown in Figure 6.7. These are constructed by subtracting the charge density of the pure bulk material from that of the defective cell. The change in charge density can then be considered through the positive and negative regions. For the cell containing a neutral vacancy, not only is the position of the vacancy clear, from the large reduction in charge density, but the location of charge density on the uranium atoms where the original uranium – oxygen bonds also changes. This also results in redistribution of charge over the uranium atoms. Analysis of the Bader charges

shows that this results in a reduction in charge on the uranium atoms, to approximately +2.2, from the pure bulk value of +2.5.

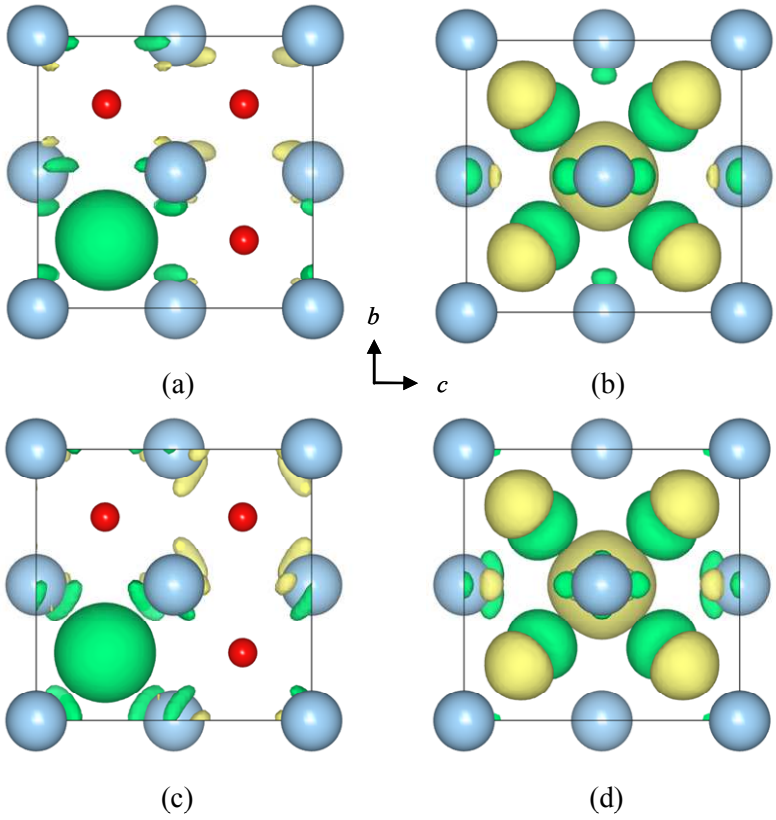

Figure 6.7: Changes in charge density from the pure $4V_r$ unit cell as a result of an oxygen atom **(a)** vacancy and **(b)** interstitial using a U value of 3eV. The same is shown for a U value of 5eV by **(c)** and **(d)**, respectively. Positive and negative changes in charge density are coloured yellow and green, respectively, with an isosurface of 0.2 electrons $Å^{-3}$.

For the neutral oxygen interstitial defects, the insertion of an oxygen atom causes repulsion to the regular lattice oxygen atoms. Although the oxygen positions remain the same, due to the constant volume minimisation, this repulsion causes a shift in the oxygen electron density toward the uranium atoms on the corners of the unit cell. This results in increased bonding to these atoms. Changes in the charge density are also seen in the uranium atoms closest to the interstitial, with charge density shifted as to minimise the energy. Analysis of the Bader charges shows an increased charge on all uranium atoms, to approximately +2.6, due to the increased bonding with the

interstitial oxygen. Although, due to the greater number of uranium – oxygen bonds the interstitial oxygen needs to accommodate, it does show a reduced charge from that seen for the regular oxygen atoms. In addition, an increase in charge is seen for the corner uranium atoms, increasing to a charge of +2.8, due to the increase in bonding to the regular lattice oxygen atoms.

We can compare to experiment by considering the Frenkel oxygen defect energy for the $4V_r$ cells. The oxygen Frenkel defect is defined as a defect where an atom or ion leaves it lattice position and becomes an interstitial on a nearby location not normally occupied in the perfect lattice. It can be represented using Kröger-Vink notation by Equation 6.8.

$$O_O^X \rightarrow V_O^{\bullet\bullet} + O_i'' \qquad 6.8$$

The Frenkel energy can therefore be calculated from the sum of formation energies for the oxygen vacancy and interstitial. We have calculated the Frenkel energies for two sets of oxygen defect simulations. The first set considers neutral cells, as described above. The second set are determined from the simulation of charged cells, where the defect and interstitial can be represented in Kröger-Vink notation by Equations 6.9 and 6.10, respectively.

$$O_O^X \rightarrow O_{(g)}^{2-} + V_O^{\bullet\bullet} \qquad 6.9$$

$$O_{(g)}^{2-} \rightarrow O_i'' \qquad 6.10$$

The calculation of individual defect formation energies from charged cells is made difficult through the need to account for the change in electronic potential in the cell, represented by the Fermi energy, relative to the change in charge. However, as the Frenkel energy is calculated from the sum of vacancy and interstitial energies, these terms will cancel, representing the same process as the neutral defects in Equation

6.8. This method of using charged defects corresponds to that used in the recent work by Nerikar *et al*. allowing for comparison to be made.

The calculated Frenkel defect energies should also be corrected to account for the change in Fermi energy from the perfect cell as a result of the defect formation. As both the requirement and value of this correction term are unclear, both uncorrected and corrected oxygen Frenkel defect energies are presented in Table 6.6 for the 1x1x1 unit cell simulations. The corrected energies are calculated using Equation 6.11, where the Frenkel energy, G_{Frenkel}, is adjusted to account for the change in Fermi energy, E_f, from the perfect bulk value as a result of the addition of a vacancy and interstitial. This correction arises for the need to cancel out the resultant charge imbalance with the surrounding infinite lattice created by the defects.

$$G_{\text{Frenkel}}^{\text{corrected}} = G_{\text{Frenkel}} - \left(E_f^{\text{vacancy}} - E_f^{\text{pure}}\right) - \left(E_f^{\text{interstitial}} - E_f^{\text{pure}}\right) \qquad 6.11$$

Table 6.6: Calculated oxygen Frenkel pair energies (eV) of neutral and charged defects for bulk AFM UO_2. Energies are also corrected according to the difference in Fermi energy between the perfect and defective bulk materials.

	Neutral	Neutral (Corrected)	Charged	Charged (Corrected)	Nerikar *et al*.	Expt.
U=3eV	6.80	5.89	6.66	6.06	3.95	3.0 - 4.6
U=5eV	7.40	5.54	7.43	6.28		

The results show that for the uncorrected Frenkel energies, the energies for the charged systems are roughly the same, with a slightly reduced energy for the charge defects with a U value of 3eV. The corrected energies do show more differences though. These energies show that the Frenkel energy is lower for the neutral cells than for the charged cells. The implication of this is that the neutral clusters are the most stable. This prediction is also supported by the experimentally observed Willis 2:2:2 defect structure, which shows the clustering of vacancy defects with half the interstitials. The clustering of these defects would confine the charge imbalance to a

localised region, whilst allowing the formation of neutral defects to still occur. Although, further simulation, particularly with larger simulation cells is required to explore this postulate and ensure fully converged defect energies.

The higher defect energies quoted here are not surprising as the $4V_r$ simulation cell gives an unrealistic population of defects. The calculated values are qualitatively similar to the calculated Frenkel energy of Catlow [46] of 5.47eV. Equivalent calculation using the potential outlined in chapter two by Parker [163] using a two region Mott-Littleton approach, with constant volume minimisation, gives a comparable value of 6.12eV. This relatively good agreement of the potential-based simulations with our DFT+U calculated values may be fortuitous and needs to be compared with larger supercells before full confidence can be gained.

Despite these caveats we next detail the simulation of non-stoichiometric thin film structures and compare the defect formation energies found at the surfaces.

6.2.2 Thin Film Structures and Oxygen Segregation

Prior to calculating the variation in stoichiometry of thin film structures, the stoichiometric form needs to be considered first. These simulations are computationally expensive, hence only the {100} and {111} bound thin films were considered. As noted in chapter one, these are the surfaces seen in the morphology and thus are the most significant. The thin films were generated using the METADISE code from the DFT+U minimised bulk AFM structure. An arbitrary AFM ordering pattern was assumed and was then minimised using the VASP code with U=3eV and high accuracy convergence parameters. However, as the slabs are bound by a vacuum gap, this allows the reduction of the k point folding parameter in that direction to 1. In addition, convergence tests showed that a 4x4x1 k point grid was sufficient for the desired accuracy of these thin films. The AFM ordering pattern, along with the minimised structure is detailed in Figure 6.8. The details of the

surface structure will be discussed in chapter seven, where the surface configuration is more important for studying the adsorption of water.

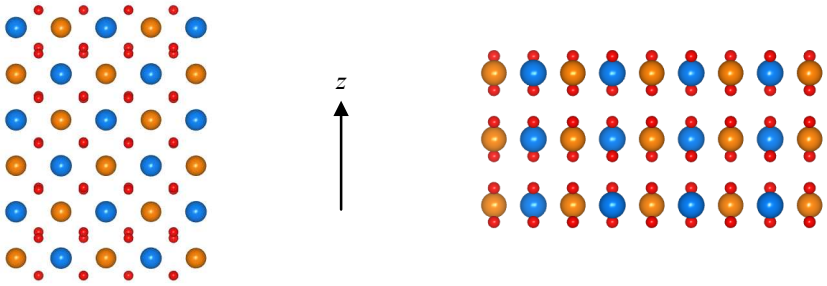

(a) (b)

Figure 6.8: Initial magnetic ordering and minimised structure for the **(a)** {100} and **(b)** {111} UO_2 thin films. Uranium atoms are coloured orange and blue for net spin up and spin down states.

We calculated the surface energies, via Equation 6.12. The surface energy, γ, is defined as the difference in energy of the slab, E_{slab}, and the bulk E_{bulk}, divided by twice the surface area, S, due to the use of a slab model. The calculated surface energies for these thin films, which are compared to the surface energies calculated by Skomurski *et al*. [65] using DFT, are given in Table 6.7. Comparison between the energies is favourable, with differences attributed to the DFT methodology used, where Skomurski *et al* use a standard GGA approach with no on-site corrections.

$$\gamma = \frac{E_{slab} - E_{bulk}}{2S} \qquad 6.12$$

Table 6.7: Calculated surface energies for the {100} and {111} UO_2 thin films, with comparison to surface energies predicted by Skomurski *et al*.

Surface	Skomurski *et al*.	This work
{100}	1.21 J m^{-2}	1.49 J m^{-2}
{111}	0.51 J m^{-2}	0.55 J m^{-2}

The variation in thin film stoichiometry then was considered, using these {100} and {111} thin film structures. The stoichiometry was varied through the sequential removal of surface oxygen and uranium atoms, from both the upper and lower surfaces to ensure that there were no net dipole moments. These structures were then minimised using an on-site correction of U=3eV using AFM magnetic ordering. The energies of these surfaces were then used to generate thin film phase diagrams, as a function of the changing chemical potential of oxygen. This can be calculated using a similar approach to that used to generate the surface phase diagrams in chapter four, adapting Equation 4.11 to become Equation 6.13, where 2*S* is required due to the use of a slab model. In addition *E* is used due to the neglect of entropic contributions.

$$\gamma = \frac{1}{2S}\left(E_{UO_2}^{thin\ film} - n_U E_{UO_2}^{bulk}\right) - \Gamma_O \mu_O \qquad 6.13$$

where the oxygen excess, Γ_O, is calculated from Equation 6.14.

$$\Gamma_O = \frac{1}{2S}\left[n_O - 2n_U\right] \qquad 6.14$$

Rather than display the surface energy as a function of the chemical potential of oxygen, it is more meaningful to use the change in chemical potential relative to oxygen gas at 0K. The chemical potential of oxygen gas is calculated in the same manner as shown previously in Equations 6.5 to 6.7, although a factor of 2 is introduced to give the value for oxygen gas rather than an oxygen atom.

For reference, we can also deduce the partial pressure, p_{O_2}, assuming it is an ideal gas, from the change in chemical potential at different temperatures, such as 298 and 1000K, by using Equation 6.15.

$$\Delta\mu_{O_2}(T) = k_B T \log\left(\frac{p_{O_2}}{p^{o}}\right) \qquad 6.15$$

The thin films were initially simulated at low accuracy. This allowed the key phases to be identified and further simulated to high accuracy. These diagrams for the {100} and {111} thin films are shown in Figure 6.9, where the thin films simulated to high accuracy are shown by the solid lines, other low accuracy thin films are represented by dashed grey lines. For reference, the change in chemical potential representing an oxygen partial pressure of 1bar are indicated for 298 and 1000K by the vertical black lines, solid and dashed, respectively.

Both thin film phase diagrams show the dominance of the stoichiometric phase at standard pressures for both 0 and 298K. However, for a p_{O_2} of 1bar at 1000K, substoichiometric phases are seen to be more favoured. For the {100} thin film this is $UO_{1.7}$ whereas for the {111} thin film $UO_{1.5}$ is predicted. The formation of hyperstoichiometric phases is also seen, although the partial pressures of oxygen required, at both 298 and 1000K, would make them inaccessible. For the {100} thin film this is seen as a change to $UO_{2.5}$, through $UO_{2.2}$. However, the $UO_{2.2}$ thin film is not seen to be expressed for the {111}, with a transition directly to $UO_{2.5}$. The transition to hyperstoichiometry is also seen to occur at different regions of the phase diagram, indicating the relative stabilities of the thin films to hyperstoichiometry. For the {100} thin film, this occurs at lower concentration than for the {111} thin film, indicating reduced reactivity of the {111} thin film to oxygen adsorption.

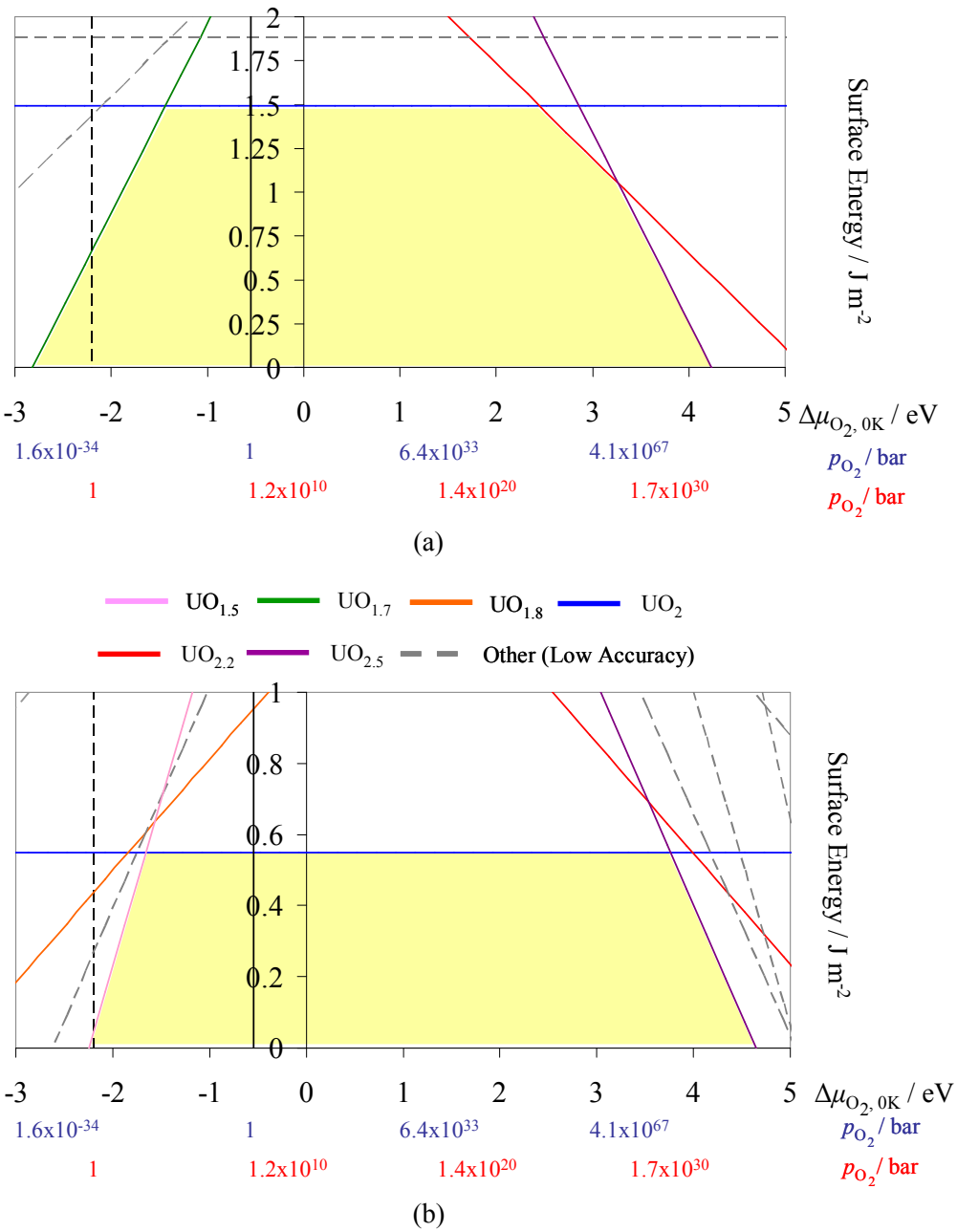

Figure 6.9: Thin film phase diagrams for the **(a)** {100} and **(b)** {111} thin film structures as a function of the change in chemical potential relative to oxygen gas at 0K. The partial pressures of oxygen, p_{O_2}, at 298 and 1000K are given in blue and red, respectively. The yellow region represents the region of stability.

To assess the effect of varying the DFT methodology, the main phases in the {100} and {111} thin film phase diagrams were also modelled with low and high accuracy convergence parameters, as well as simulating the thin films with U=5eV at high accuracy. Figure 6.10 shows the results of these different methods. It can be seen that for U=3eV, varying the accuracy of convergence parameters has only a minor effect on both the calculated energies and the thin film phase diagram itself. This therefore suggests, that the approach used above, where all surfaces were minimised using low accuracy parameters, followed by further minimisation of the important surfaces with increased accuracy is appropriate. However, the comparison between the different values of on-site correction produces more variation, despite the same qualitative features remaining. The increase of U is seen to destabilise the surface. This is due to there being a greater binding energy for the surface relative to the bulk for the U=3eV than U=5eV.

We can then use the information from the point defects and thin film structures to determine oxygen segregation behaviour. The oxygen segregation energy, $E_{seg,}$ can be calculated from the difference in defect energies between the thin films and the bulk, as shown in Equation 6.16.

$$E_{seg} = \Delta E_{def}^{thin\ flim} - \Delta E_{def}^{bulk} \qquad 6.16$$

where $\Delta E_{def}^{thin\ flim}$ is the difference in energy between the defective and stoichiometric thin films, per oxygen defect, and ΔE_{def}^{bulk} is the difference in energy between the defective and pure bulk structure, using the neutral defect energies. A positive energy indicates segregation of defects into the bulk, whereas a negative value shows segregation to the surface. The calculated segregation energies are given in Table 6.8.

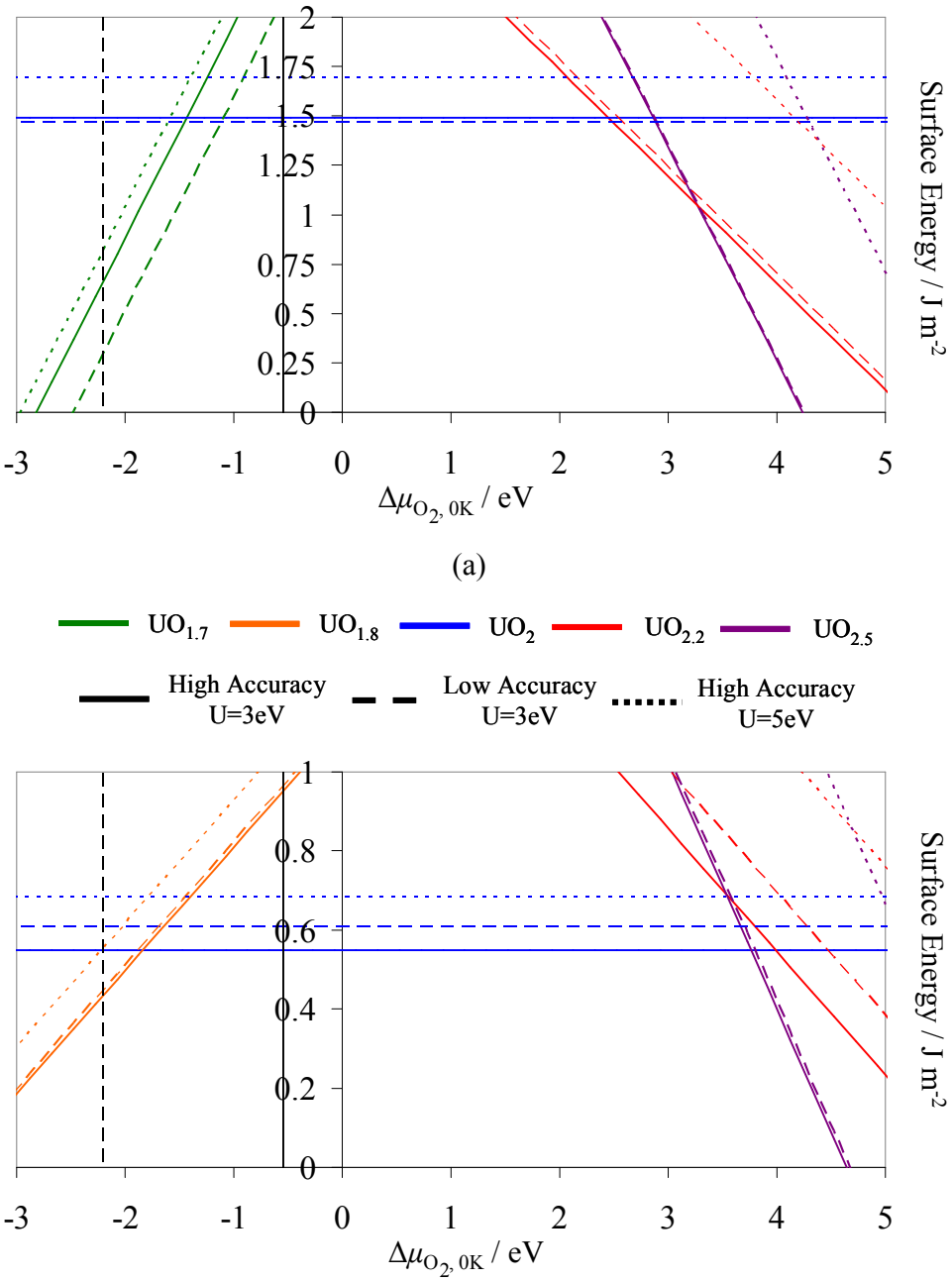

Figure 6.10: Thin film phase diagram for the **(a)** {100} and **(b)** {111} thin film structures as a function of the changing chemical potential of oxygen, showing the effect of different DFT methodologies.

Table 6.8: Table showing oxygen atom segregation energies, in eV, for thin film structures of varying stoichiometry.

Stoichiometry	{100}	{111}
$UO_{1.7}$	-0.06	-
$UO_{1.8}$	-	0.34
$UO_{2.2}$	-2.86	-1.32
$UO_{2.5}$	-2.36	-1.54

The results suggest that interstitial defects are stabilised at both the {100} and {111} surface. This implies that there is a barrier to diffusion of oxygen atom interstitials into the bulk. In addition, the segregation energies for interstitials are higher for the {100} surface than for the {111} implying that oxygen excess on this surface is more probable, which is also in agreement with the thin film phase diagrams. Both surfaces show oxygen vacancy segregation energies are energetically unfavourable. Indeed, if as we suspect, the small bulk simulations underestimate the defect stability, then both surfaces show a marked preference for oxygen vacancies to migrate to the bulk. Potential-based calculations by Parker [163] using the potential detailed in this thesis, shows a segregation energy of 0.12eV for charged defects, concurring with our results. This is in agreement with the thin film surface phase diagram showing the stability of the stoichiometric phase, with no appearance of a substoichiometric thin film structure at 0K.

One of the constraints of these computationally expensive simulations is that it is not feasible to consider a large range of magnetic configurations in the thin film structures, which could feasibly result in the lowering of energies. Therefore the next section will consider the magnetic ordering in more detail in an effort to develop a predictive tool and to gauge the sensitivity of surface stability to magnetic ordering.

6.3 Predicting the Magnetism in Bulk and Thin Film Structures

The previous work, highlighted in chapter one, has demonstrated that, for bulk UO_2, AFM ordering is more stable than FM. However, for thin film structures the magnetic ordering patterns are not known. At the present time, these simulations are computationally expensive and hence it is not feasible to model all spin configurations. Therefore a tool that could predict the relative stabilities of different spin configurations would be of great benefit for modelling these systems. An additional benefit would be that by knowing the relative stability of spin configurations, an energy correction could be formulated and applied to potential-based simulations, which effectively neglect spin polarisation. This aim of this section is to detail preliminary work on using a simple mathematical model, based on bulk interactions, to model the relative energies of different magnetic orderings in thin film structures. Even if unsuccessful, the consideration of different spin configurations and relative complexity of modelling the interactions will give insight into the nature of magnetic ordering in thin film structures.

The simple Ising model is an effective Hamiltonian model used to model phenomena which occur in pairs to produce a collective result. For studying collinear magnetism, where spin states can exist as either 'up' or 'down', we can use it to model the relative stability of the AFM structure versus FM. The Ising model states that the energy of the spin interactions, E_{int}, is the sum of all interactions between two spins s_i and s_j, which can have a value of +1 or -1, multiplied by a coupling constant J_{ij}, as shown by Equation 6.17.

$$E_{\text{int}} = -\sum_{ij} J_{ij} s_i s_j \qquad 6.17$$

For computational ease, all interactions of same spin are set as zero, so that the coupling constant, and hence interaction energy, is purely a result of the coupling constant multiplied by the number of different spin interactions. In addition, we can

assume that only nearest neighbour interactions will contribute to this energy. The value of this coupling constant can then be fitted to the relative difference in energy between FM and AFM bulk UO_2. For a U value of 3eV, the difference is equal to -1.93eV, with 16 different spin interactions with nearest neighbours in the standard 1x1x1 unit cell, giving rise to a coupling constant equal to -0.12eV.

To trial this model, we can attempt to predict the relative energy of the bulk system with a ratio of spin up to spin down of 1:3. The Ising model predicts a relative stability to FM UO_2 of -1.45eV, which compares to a relative DFT+U energy of -1.67eV. This difference in energy therefore suggests that further complexity is required to calculate the absolute energy difference. The inclusion of further interactions such as next and next next nearest neighbours gave rise to a linear increase in the number of different interactions, therefore meaning a series of coupling constants could not be fitted to both the 1:1 and 1:3 spin up to down ratio systems.

Despite the failure of the model to predict the quantitative difference, we tested the model to investigate whether it could calculate the relative stability of AFM thin film structures relative to the FM configuration qualitatively. The {100} and {111} structures described above were tested. Further more, a thin film structure was also generated for the {110} bound thin film and minimised, as shown in Figure 6.11(a), where the arbitrary AFM ordering assigned consists of the alternating FM planes aligned diagonally with the surface. Following this, the surface energy was determined as being equal to 1.87J m^{-2}. This compares with the value calculated by Skomurski *et al.* of 1.01J m^{-2}. Clearly, there is disagreement here, not only in the actual value, but also in the trend of stability. To examine this further, the AFM ordering was changed so that the alternating FM planes were perpendicular to the surface, shown in Figure 6.11(b). Following minimisation, a surface energy of 1.18J m^{-2} was calculated, which agrees both in terms of the relative trend in surface energies, as well as comparing more favourably to the value obtained by Skomurski *et al*.

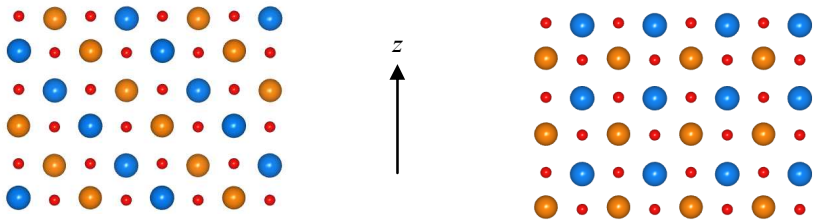

(a) (b)

Figure 6.11: Initial magnetic ordering and minimised structures of the {110} thin film AFM UO_2 structures with the planes of alternating FM sheets running **(a)** diagonal and **(b)** perpendicular to the surface. Uranium atoms are coloured orange and blue for net spin up and spin down states.

The calculated energy differences of these thin film structures were compared to the relative differences in energy as predicted using the simple Ising model. The results of this are given in Table 6.9, where {110} (a) and (b) refer to the AFM ordering of FM sheets running diagonal and perpendicular, respectively, to the surface.

Table 6.9: Calculated energies (eV) of AFM ordered thin films relative to the FM structure of calculated DFT+U energies and predicted via an Ising model. For the {110} surface alignment of alternating FM sheets is (a) diagonally and (b) perpendicular to the surface. * {100} FM calculation was simulated at low accuracy only.

Surface	{100}	{110} (a)	{110} (b)	{111}
DFT+U	-0.54*	+3.53	-1.17	-1.65
Ising	-5.44	-4.92	-4.92	-4.92

The Ising model clearly fails to predict the variations in energy in either a qualitative or quantitative manner. Therefore, this suggests that the trends and relative energies resulting from magnetic ordering are too complex for the Ising model to predict. There are a number of reasons for this. Firstly, as mentioned above, further interactions beyond nearest neighbour could be important in ordering,

highlighted by the observation that the Ising model predicts the same relative stabilisation for the {110} and {111} structures. This is due to the ordering patterns possessing the same number of nearest neighbour different spin interactions. Secondly, magnetic interactions on the surfaces could differ to those within the bulk material.

The magnetic ordering was investigated in more detail by evaluating the spin density of the different surfaces, as shown in Figure 6.12. The bulk AFM spin density is also shown for reference. The central regions of the {100} and {111} thin film structures show similar spin density on the uranium atoms to that in the bulk structure. However, different spin densities are seen for the surface regions, with the {100} surface termination causing a marked depth effect on the spin density. The different AFM spin configurations of the {110} surface also show differences in their spin density arrangements. The thin film which gave rise to the incorrectly predicted surface energy, Figure 6.12(c), shows a marked difference with both the {100} and {111} surfaces, as well as with the bulk structure. However, the configuration comprised of aligned planes perpendicular to the surface shows a more regular form, Figure 6.12(d). For this structure, the central region of the thin film is similar to the bulk density, with the two uppermost uranium layers showing a large difference due the surface. This implies that different surface orientations and configurations give rise to different arrangements of spin density. Therefore not only may surface interactions be different to the bulk state, but also different spin density arrangements may also affect the interactions between atoms of different spin, or even the same spin.

Although this shows the difficulty in predicting magnetic structure for different surface terminations, it only begins to consider different spin configurations for identical surfaces. This can be considered in more detail through the simulation of six different {111} bound thin films, with varying spin ordering. The spin density and calculated raw energies are given in Figure 6.13.

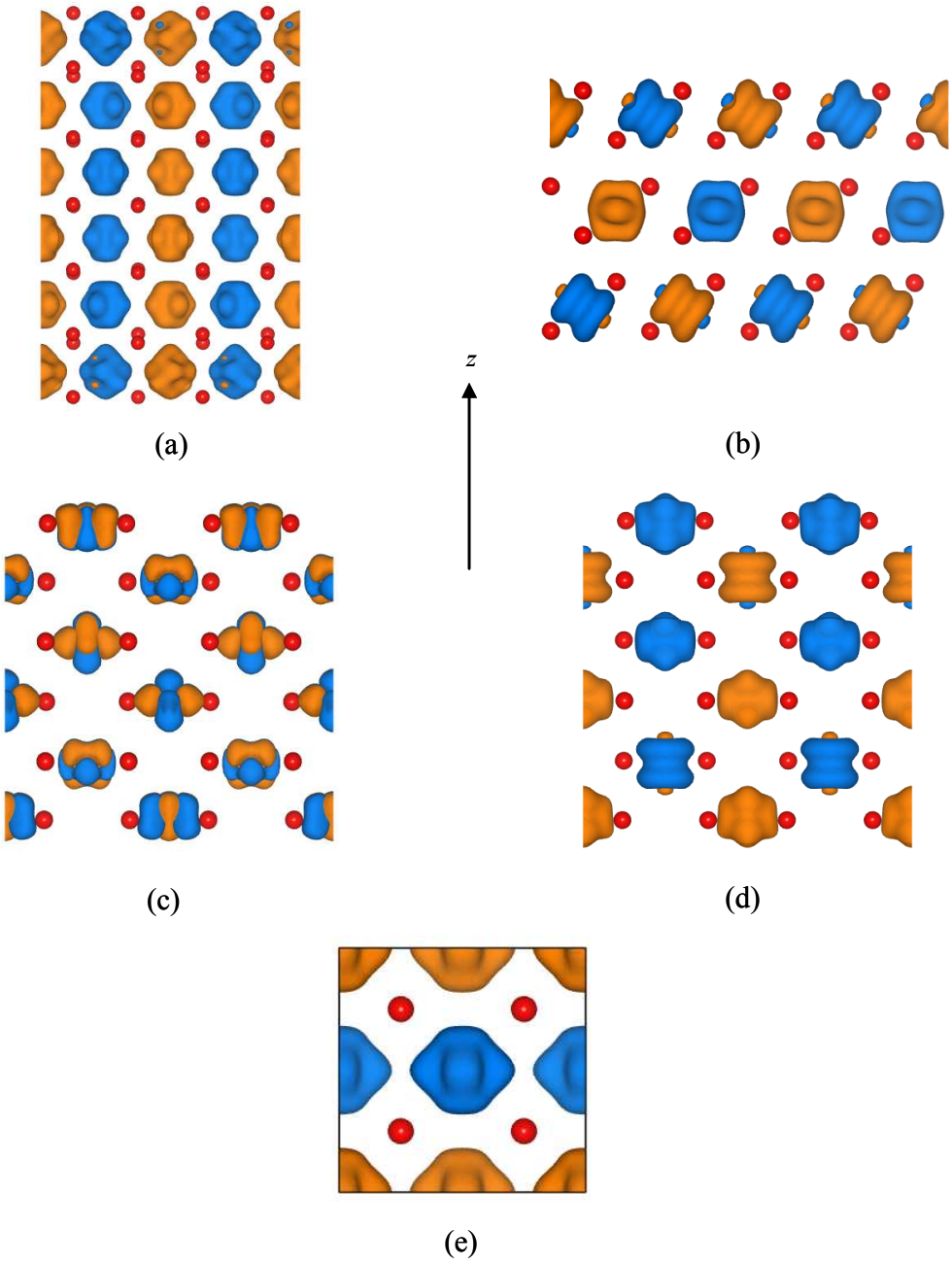

Figure 6.12: Spin density plots for UO_2 **(a)** {100} and **(b)** {111} thin film structures. Parts **(c)** and **(d)** show {110} thin films, with initial AFM ordering of FM sheets positioned diagonal and perpendicular to the surface, respectively. The AFM bulk spin density is shown in **(e)** for reference. Excess spin up and down density are coloured orange and blue, respectively, with an isosurface of 0.1 electrons $Å^{-3}$. Uranium atoms are omitted for clarity.

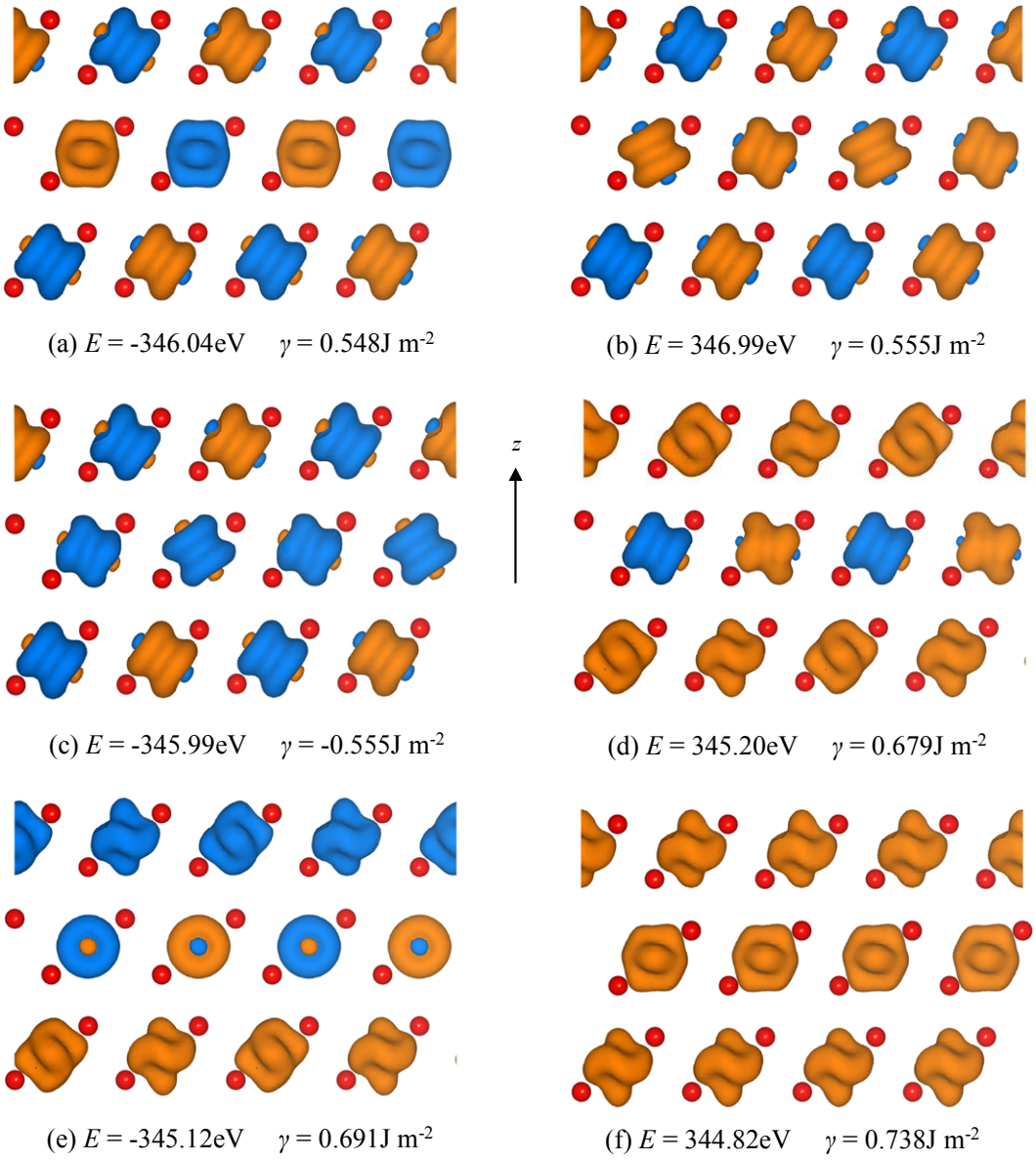

(a) E = -346.04eV γ = 0.548J m^{-2} (b) E = 346.99eV γ = 0.555J m^{-2}

(c) E = -345.99eV γ = -0.555J m^{-2} (d) E = 345.20eV γ = 0.679J m^{-2}

(e) E = -345.12eV γ = 0.691J m^{-2} (f) E = 344.82eV γ = 0.738J m^{-2}

Figure 6.13: Spin density plots for different spin configurations of the {111} UO_2 thin films with an isosurface of 0.1 electrons Å^{-3}. Configurations **(a)** to **(f)** are ordered in terms of decreasing stability and surface energy, γ. Uranium atoms have been omitted for clarity.

The spin densities of the {111} surfaces not only show variation in the spin arrangements between surfaces, but also in their orientations. Three basic types of spin density arrangements can be identified from these density plots. These are identifiable from Figures 6.13(a) and (f), the standard AFM and FM arrangements,

respectively. For the AFM arrangements, as shown earlier, the central row shows bulk-like spin density, with a different distribution at the surfaces, most likely formed through an effort to maximise interactions of opposing spin. For the FM arrangement, again bulk-like spin density is seen in the central row of uranium atoms, however, the surface configurations show a different spin density distribution to that seen for the AFM ordered structure. These differences highlight the complex nature of spin density in uranium dioxide and suggest that an Ising-like model using a complex interaction energy scheme needs to be employed. This could be achieved through the fitting of a range of coupling constants to interactions for different spin distributions, although this would have potential implications for the transferability of such a model. Therefore significant further calculation and testing is required to enable the formation of a method of correcting potential-based calculations for different spin arrangements.

Overall, despite this simple approach failing to both predict both qualitative and quantitative differences, it does highlight not only the complexity of spin interactions for surfaces and thin films but also important considerations which need to be taken into account for the future modelling of spin ordering. AFM spin ordering patterns should therefore not be assigned arbitrarily as this can lead to inaccuracies in calculated orders of stability, as demonstrated for the {110} thin film.

6.4 Chapter Conclusions

The aim of this chapter has been to consider the electronic structure of bulk and thin film UO_2 structures. The choice of DFT methodology has also been examined along with the implications of the DFT+U method, through the consideration of the bounds of the U correction term, compared to that which has been previously used. The first result was that we found the presence of the *f*-electrons caused the simulations to be poorly convergent and any simulation beyond the stoichiometric bulk took a vast amount of CPU time.

The simulation of the perfect bulk material showed that the omission of the U correction term failed to predict the correct electronic structure of UO_2, by predicting a delocalisation of electrons over the *f* orbitals of the uranium atoms which was in disagreement with experiment. Inclusion of the on-site correction term causes an increased localisation, resulting in the splitting of the *f* bands in the DOS to generate a band gap for AFM UO_2. Increasing the value of the U term, was seen to result in an increased localisation effect, causing an improved band gap whilst also increasing the lattice constants and the extent of hybridisation between the oxygen 2*p* and uranium 5*f* orbitals.

A preliminary investigation of the variation in stoichiometry was then undertaken on the bulk material and on non-stoichiometric thin films. Point defect calculations, despite using a small simulation cell, showed a general agreement with previous work in this area. Calculation of Frenkel energies showed that the formation of defects, with localised regions of reduced or oxidised electron density, may be more stable than charge neutral defects formed from the addition and removal of an O^{2-} ion. This may also suggest why the clustering of interstitial and vacancy defects is seen experimentally. Simulations of thin film structures showed that the stoichiometric forms of the {100} and {111} bound thin films are the most stable at ambient conditions. At reduced partial pressure, and increased temperature, substoichiometric forms were seen to be stabilised. However, very large increases in oxygen partial pressure were seen to be required for the formation of hyperstoichiometric thin films. Segregation studies at the {100} and {111} thin film surfaces suggest that interstitial defects are stabilised at the surface, relative to the bulk. However, vacancy formation is particularly unfavoured at the {111} surface, which would result in movement into the bulk material. For the {100} surface, the segregation energy was sufficiently small that a distribution of vacancies would be observed throughout its surface and in the bulk material.

Finally, different arrangements of magnetic ordering and spin density were considered for bulk and thin film structures based on a simple Ising model fitted to

nearest neighbour interactions. The aim of this was to generate a model which could predict energy differences between different magnetic ordering, allowing a correction which could be applied to potential-based simulations. However, the analysis of spin density arrangements revealed that different distributions of spin density are observed for different ordering patterns and different surface configurations. Therefore, generation of a model, based on the simple Ising approach, was unfeasible in both a quantitative and qualitative manner. However, ordering patterns for different ordering configurations for the {111} thin film suggest that some correlations may be apparent for same surface configurations, although if and how this could be fitted to a model requires extensive further work.

Following the simulation of the bulk UO_2 phases and thin film structures, we can now continue to consider the surfaces and the adsorption of water. However, due to the computational extensiveness of the DFT+U calculations this is not feasible with electronic structure techniques. This study has established that the surface stoichiometry is dominated by stoichiometric UO_2 surfaces at all sensible oxygen partial pressures; therefore we can be confident that potential-based simulations using these surfaces will be reliable.

Chapter Seven

Water Adsorption on UO_2 Surfaces

Modelling the interactions of uranium oxide with water is important for understanding the processes which may occur during the long-term storage of both this and other related nuclear materials. The aim of this study will be to consider the surface adsorption of H, in the form of associatively and dissociatively adsorbed water. The previous chapter focussed on the use of DFT calculation to model the electronic and physical properties of UO_2. However, to explore the interactions of water with the surfaces of UO_2 fully, it was not feasible for us to use electronic structure methodologies as they are too expensive in terms of CPU time. Therefore, this study will primarily employ potential-based calculations, as was shown for CaO and MgO in chapters four and five, again taking advantage of their ability to scan large numbers of different surface configurations. Furthermore, the DFT simulations

did confirm the stoichiometric surfaces are the most stable and hence the system is well suited to potential-based simulation. The interaction of the UO_2 surfaces with liquid water can also be studied using dynamical models, allowing the water structure immediately above the surface to be characterised, which will have importance for considering the diffusion of materials to and from the surface. However, prior to simulating the interaction with water it is essential to ensure that our potential can accurately reproduce the structure of both bulk UO_2 and its surfaces.

7.1 Bulk UO_2

The potential model used in this thesis is described in chapter two. The reliability of this potential can be assessed through comparison with data for the bulk material. The other potential models used for comparison are the original Busker model [70], the Catlow2 model [46], which was derived to fit Hartree-Fock calculations, and the quantum mechanically derived potential of Skomurski *et al*. [65]. The model used in this study uses the same uranium potential as the Busker model and should therefore give similar results. The compromise we are applying is that we wanted to employ the same oxygen – oxygen potential used in our previous studies of oxides so that it would form part of a set of transferable parameters. The comparison is detailed in Table 7.1.

Clearly, our potential model is not as accurate as the other models. However, as the major focus of this study using potential models is to simulate structural properties and to consider the surface adsorption of water, the potential was deemed to simulate the system to a sufficiently high degree to allow this. In particular, close agreement is seen on comparison with both the lattice parameter and average bond distances, with these quantities all being within 1% difference to experiment. In addition, the lattice energy is predicted within 2% of experiment. Therefore this model will be used for all subsequent potential-based models of UO_2.

Table 7.1: Bulk physical properties of UO_2 as calculated using the potential model used in this study, with comparison values from other potential models and experiment. Experimental values are referenced by Catlow [46], * are given by Abramowski *et al*. [70] and bond lengths were calculated from the lattice constant by Skomurski *et al*. [65].

Potential Used	Catlow2	Busker	Skomurski	This Work	Experiment
Lattice Constant / Å	5.521	5.468	5.526	5.446	5.468
Lattice Energy / eV	-94.5	-104.47	-	-104.6	-106.7
Static Dielectric Constant, ε_0	20.83	18.53	24	17.32	24
High-Frequency Dielectric Constant, ε_∞	5.37	6.20	6.73	3.88	5.3
Bulk Modulus / 10^{11} dyn cm^{-2}	22.30	25.85	-	25.47	17.89*
Shear Modulus, C_S / 10^{11} dyn cm^{-2}	14.80	20.49	-	18.60	9.01*
Shear Modulus, C_{44} / 10^{11} dyn cm^{-2}	6.52	11.84	-	12.89	5.97*
O – U / Å	2.391	2.370	2.393	2.360	2.368
O – O / Å	2.761	2.730	2.793	2.720	2.734
U – U / Å	3.904	3.870	3.907	3.850	3.866

7.2 Surface Structures

The low index surfaces chosen were the {100}, {110} and {111} surfaces. The {100} surface termination of UO_2 forms a polar Type III surface. The simplest reconstruction to neutralise the dipole perpendicular to the surface is to micro-facet the surface. The simplest facet involves moving 50% of the surface oxygen atoms to the bottom of the block. There are a number of different arrangements to achieve this, however, the lowest in energy was found to have the surface structure seen in Figure 7.1(a), where complete rows of oxygen atoms have been removed, giving rise

to a surface energy of 2.92J m^{-2}. A recent STM study of the (001) UO_2 surface by Muggelberg [66] suggests the possibility of larger micro-faceting occurring on this surface, working to stabilise the surface by increasing the amount of {111} surface present. Figure 7.1(b) shows the micro-faceted surface on the √2 x √2 R45° {100} surface. Surface stability is gained through increasing the depth of the facet, resulting in lower surface energies, as detailed in Table 7.2. In addition, these facets were also modelled using a rigid ion approach, the results of which are given in Table 7.2. The same potential models described above are used; however, the shells of the uranium and oxygen atoms are removed. The variation in energy using a rigid ion approach predicts the change in surface energy to increase with increasing facet depth, which is in contrast to experimental evidence. This clearly both validates and highlights the importance of using shells for considering the surfaces of UO_2. However, despite the reduction in energy, the size of the larger micro-faceted surfaces makes the study of water adsorption beyond our resources due to the large number of surface adsorption sites, therefore all studies on the {100} surface will consist solely of the 1x1 surface with the movement of 50% of surface oxygen atoms.

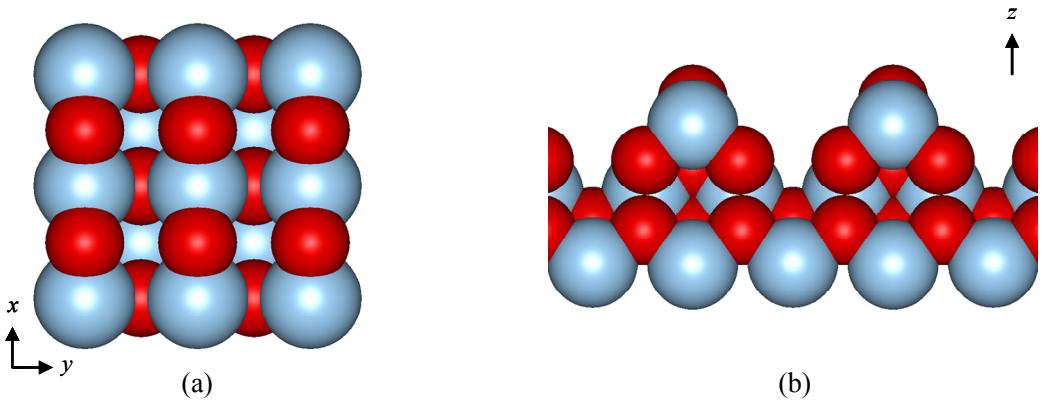

Figure 7.1: Surface structure of the minimum energy **(a)** (plan view) {100} with 50% movement of surface oxygen atoms and **(b)** faceted √2 x √2 R45° {100} (side view) UO_2 surfaces. Uranium atoms are coloured light blue, whereas oxygen atoms are coloured red. Axis indicators are arbitrary and reflect the relative view of structure.

Table 7.2: Table detailing the {100} UO_2 surface energy variation as a result of surface facet depth for both shell and rigid ion models.

Surface Reconstruction	Facet Depth / Å	γ_{shell} / J m^{-2}	$\gamma_{rigid\text{-}ion}$ / J m^{-2}
1 x 1	1.97	2.91	1.70
2 x 2	4.74	2.38	1.77
√2 x √2 R45°	4.74	2.38	1.77
2√2 x 2√2 R45°	7.67	2.21	1.83

The {110} and {111} surfaces, however, are non-polar, and therefore do not require the rearrangement seen for the {100}. The {110} surface, shown in Figure 7.2(a), possesses a structure which is terminated by complete UO_2 stoichiometric units, giving rise to the presence of a grooved, or faceted, surface structure. Whereas the most stable surface, namely the {111}, Figure 7.2(b), is oxygen terminated. The surface energies for the {110} and {111} surfaces are calculated as being 2.14 and 1.27J m^{-2}, respectively.

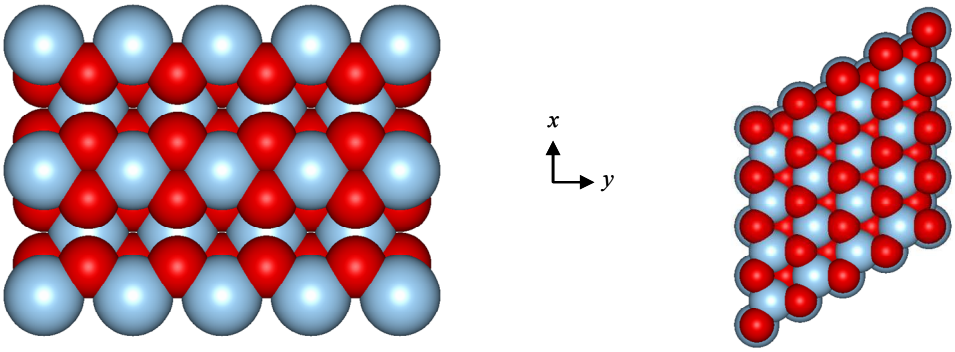

(a) (b)

Figure 7.2: Plan views of the minimum energy **(a)** {110} and **(b)** {111} UO_2 surface structures. Axis indicators are arbitrary and reflect the relative view of structure.

The relaxed surface energies, Table 7.3, along with the structure, can be compared with those predicted using previously derived potentials to further validate the potential used. The results show a large variation in the values of surface energy for

the three surfaces, however, all four models show the same trend in stability with the {111} surface being the most stable and the {100} surface being the least. It is clear that for the Catlow2 and Skomurski potentials the ratio of {111} to {110} surface energies is different to the Busker model. The significance of this can be assessed by using them to generate a Wulff construction of the equilibrium morphology, as shown in Figure 7.3, for the four potential models.

Table 7.3: Relaxed surface energies of the low index {100}, {110} and {111} UO_2 surfaces, including comparison with other potential models.

	$\gamma_{\{100\}}$ / J m^{-2}	$\gamma_{\{110\}}$ / J m^{-2}	$\gamma_{\{111\}}$ / J m^{-2}
This work	2.92	2.14	1.27
Busker	2.81	2.19	1.30
Catlow2	1.53	1.28	0.92
Skomurski QM Derived	1.95	0.97	0.87

The predicted morphologies show identical octahedral structures for the model used in this study and the Busker model. However, the models of Catlow2 and Skomurski both show faceting of the structure. This comprises of {100} facets for the Catlow2 model and {110} facets for the Skomurski morphology. Experimental work by Castell [69] suggests that the morphology of UO_2 crystals, following the characterisation of voids in UO_2 crystals, comprises of a truncated octahedron with corner faceting a result of the {100} surface. All morphologies show the dominance of the {111} surface, however, only the Catlow2 model predicts the {100} expression in the resultant crystal. The failure of the models to correctly predict this morphology is thought to be related to complexity associated with the {100} surface structure. Although studies have modelled various different methods of removing the dipole on this surface, experimental work by Muggelberg [66] suggests a maze-like structure comprising of {111} facets, which may be formed during an annealing process. Tan *et al*. [68] further considered different {100} terminations, revealing that the formation a {111} trench on a 3 x 3 supercell did indeed give a more stable surface energy, however, this does not afford any change in the predicted

morphology using their surface energies from that shown in Figure 7.3(b). The next step is to consider the surface adsorption of water on these surfaces, to understand the effect this has on surface stability and trends.

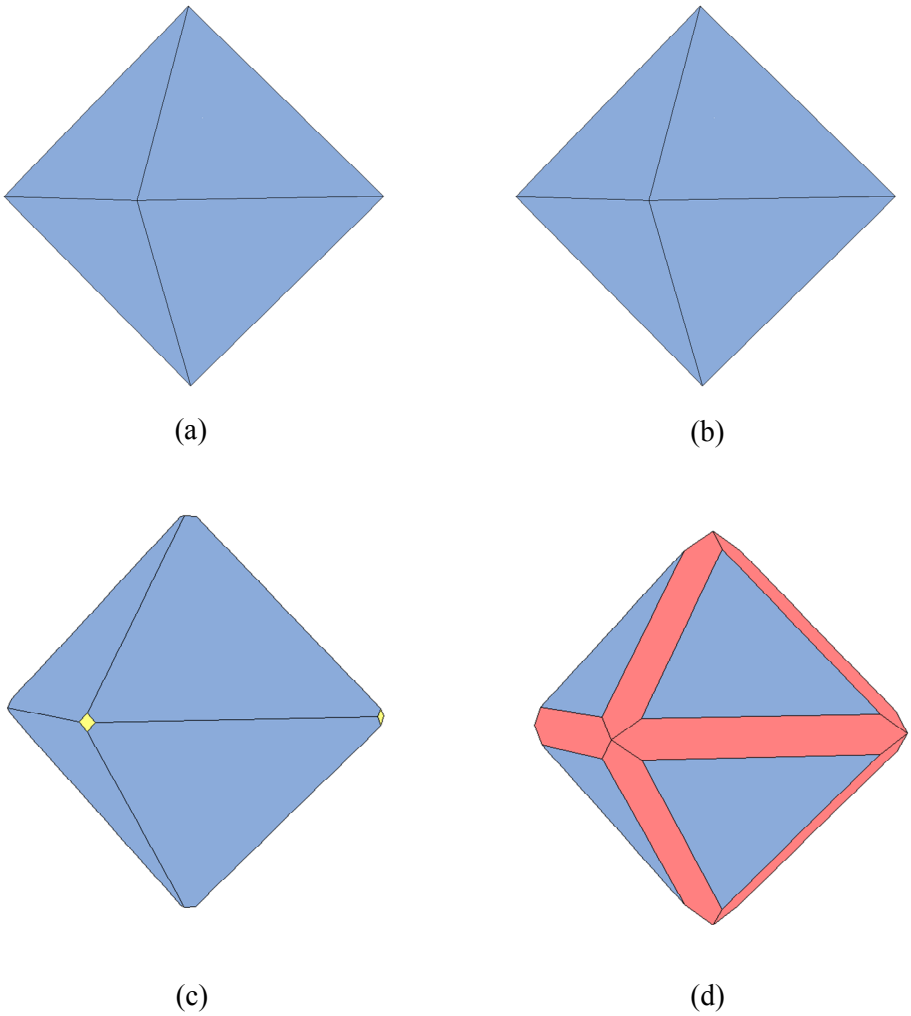

Figure 7.3: Equilibrium morphologies predicted using surface energies calculated from **(a)** our potential, **(b)** the Busker, **(c)** Catlow2 and **(d)** Skomurski *et al*. models. The {100}, {110} and {111} surfaces are represented by the colours yellow, red and blue, respectively.

7.3 Modelling Water Adsorption

The approach used for modelling water adsorption on the surfaces of UO_2 was similar to that described for the surfaces of CaO and MgO in chapter four, shown schematically in Figure 7.4(a) and (b). The first method is where the water was placed above a surface uranium atom, bonding through the oxygen of the water molecule. The second adsorption mode is via a hydrogen-bonding interaction between the water and the lattice oxygen present on the surface. Finally, dissociative water adsorption was also considered, Figure 7.4(c). In addition, an extra site was included for the {100} surface. The vacant oxygen rows on the surface, generated to remove the dipole perpendicular to the surface, was also used to initially position the addition of a hydroxide group, centring on the vacancy itself. As with the earlier studies of water adsorption in chapter four, associatively and dissociatively adsorbed water will be termed as hydrated and hydroxylated, respectively, for brevity.

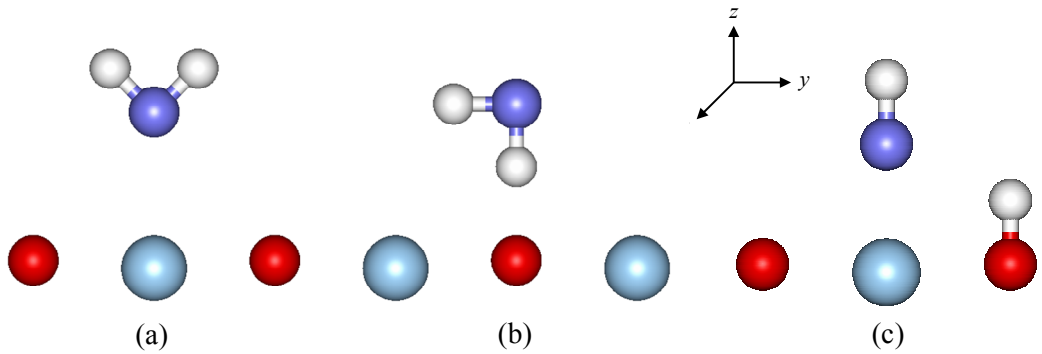

Figure 7.4: Schematic representation of the starting configuration for the addition of water **(a)** above a surface uranium atom, **(b)** above a surface oxygen atom and **(c)** in a hydroxylated manner.

As no potential was available for modelling the U – O interactions with water and hydroxide a potential needed to be derived which would be compatible for modelling adsorption processes at different surfaces with both low and high Miller indices. Thus the model should be capable of modelling the extreme coordination differences. The initial distances between the oxygen of water and hydroxide with

the surface uranium atoms, as well as the potential parameters themselves, were determined by adjusting the U – O parameters to reproduce the structure of the uranium clusters $U(OH)_4$, and $U(OH)_4(H_2O)_2$, as shown in Figure 7.5. These clusters were minimised using a GGA+U approach via the VASP code. The value of U used was 3eV, as discussed in chapter six.

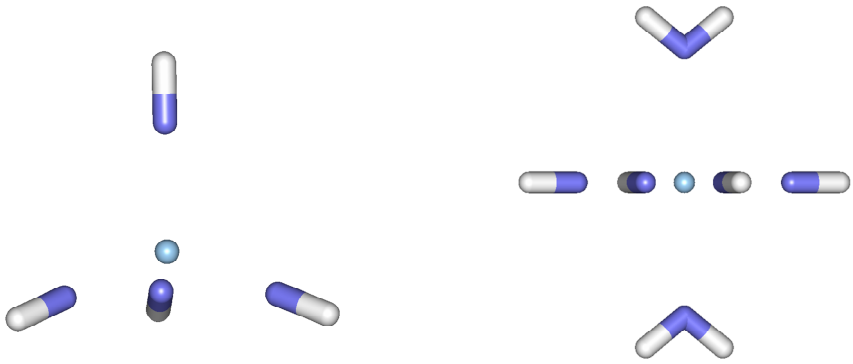

(a) (b)

Figure 7.5: Relaxed structures of the hypothetical uranium clusters **(a)** $U(OH)_4$, and **(b)** $U(OH)_4(H_2O)_2$.

The fitting of the potential parameters for the interactions of uranium with the oxygen atoms in water and hydroxide molecules was completed by firstly using the simplified variation of the Schröder *et al.* approach to modify the *A* parameter by the fractional charge of the oxygen component, *q*, shown by equation 7.1 below using the hydroxide oxygen as an example:

$$A_{U-O_H} = A_{U-O} \times \frac{q_{O_H}}{q_O} \qquad 7.1$$

These were then adjusted to reproduce the structure of the relevant cluster models. The average DFT and potential bond distances in these molecules are detailed in Table 7.4. As can be seen, the fitted potential parameters accurately reproduce the DFT predicted clusters, with variation between the DFT and potential-based distances being less than 1% difference.

Table 7.4: Table detailing the U – O bond distances, as predicted using DFT and potential-based approaches, for the $U(OH)_4$ and $U(OH)_4(H_2O)_2$.

Cluster	Average U – O_H / Å		Average U – O_W / Å	
	DFT	Potential	DFT	Potential
$U(OH)_4$	2.11	2.13	-	-
$U(OH)_4(H_2O)_2$	2.17	2.16	2.56	2.56

7.3.1 Calculating Surface Free Energies

The calculation of surface free energies for the hydration and hydroxylation of UO_2 surfaces were conducted in an identical manner to CaO and MgO, using Equations 4.1 to 4.5 to allow the generation of surface free energies and free adsorption energies. However, determining the value of the correction term for the hydroxylation, E_{corr} (H-OH), was not as simple. The lattice energy and structure of a $U(OH)_4$ solid phase was not available as the hydroxide of uranium exists as the uranyl dihydroxide, $UO_2(OH)_2$, with the uranium in a +6 oxidation state. An alternative approach, used by Redfern *et al*. [164] for studying the hydroxylation of zirconia surfaces, is to use thermodynamic data via a Born-Haber cycle to calculate the second electron affinity directly and then to use this to determine the correction term from the formation of the hydroxide species. However, this approach does not include any component of the uranium – hydroxide interaction and hence the uncertainty may be large. Therefore, the approach we took was to calculate a correction factor specific to the dissociation of water on a UO_2 surface using DFT calculations. This is also susceptible to error, but by using an energy difference we expect the error to be smaller.

The approach used was to generate a {111} UO_2 slab, followed by addition of either associatively or dissociatively adsorbed water on both the top and the bottom of the slab. These slabs were then modelled using a GGA+U approach, again with a U value of 3eV and a 4x4x1 k point grid. The magnetic structure of the material was also modelled as AFM, with alternating spins. The minimised structures of the

hydrated and hydroxylated UO_2 {111} surfaces are shown in Figure 7.6. Additionally, the energies of an isolated water molecule and the slab in the absence of adsorbed water were also determined using DFT.

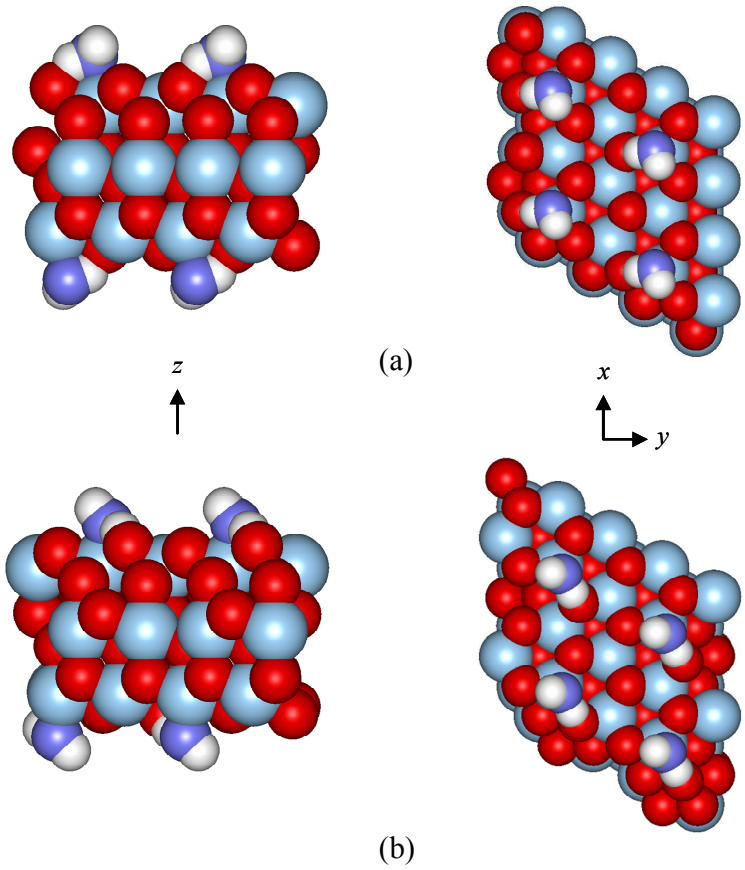

Figure 7.6: Structures of the DFT-minimised {111} UO_2 slabs with the adsorption of a single **(a)** hydrated and **(b)** hydroxylated water molecule per side. Both a side view and plan view of the top surface are shown, with the slabs grown 2x2 for clarity.

Following the calculation of DFT-predicted energies, the minimised structure was then simulated with the potential model. The energies from these simulations are given in Table 7.5.

Table 7.5: Table showing the calculated energies of the UO_2 slab, E_{UO_2}, an isolated water molecule, E_{H_2O}, and a UO_2 slab hydrated and hydroxylated with one water molecule per side, $E_{UO_2+H_2O}$ and $E_{UO_2+H\text{-}OH}$, respectively, using DFT and potential-based approaches.

	DFT	Potential-based
$E_{UO_2+H_2O}$ / eV	-375.30	-1266.86
$E_{UO_2+H\text{-}OH}$ / eV	-375.10	-1231.48
E_{UO_2} / eV	-346.03	-1247.61
E_{H_2O} / eV	-14.02	-9.10

Additionally, the energies of reaction, per water molecule, for both the hydration, $E_{reaction}$ (UO_2 + H_2O), and hydroxylation, $E_{reaction}$ (UO_2 + H-OH), can be defined and calculated using Equations 7.2 and 7.3, respectively.

$$E_{reaction}(UO_2 + H_2O) = \frac{E_{UO_2+H_2O} - [E_{UO_2} + 2E_{H_2O}]}{2} \quad 7.2$$

$$E_{reaction}(UO_2 + H\text{-}OH) = \frac{E_{UO_2+H\text{-}OH} - [E_{UO_2} + 2E_{H_2O}]}{2} \quad 7.3$$

where the energy of water, for calculating the energy of reaction for hydroxylation using potentials, is set as zero as this is the correction term. Therefore, the correction term for hydroxylation, E_{corr} (H-OH), on the UO_2 surface can be calculated using Equation 7.4, where the correction term is simply the difference between the potential and DFT-predicted hydroxylation calculations with the addition of the DFT-calculated energy of dissociation.

$$\begin{aligned} E_{corr}(H\text{-}OH) = {} & E^{Potential}_{reaction}(UO_2 + H\text{-}OH) - E^{DFT}_{reaction}(UO_2 + H\text{-}OH) \\ & + [E^{DFT}_{reaction}(UO_2 + H_2O) - E^{DFT}_{reaction}(UO_2 + H\text{-}OH)] \end{aligned} \quad 7.4$$

This gives rise to a calculated correction term of 8.47eV per water molecule.

To confirm correct prediction of the correction term, we can apply it to calculating the energy of dissociation, $E_{dissociation}$ (H_2O), of a water molecule on the UO_2 surface. This can be done using both DFT and potential-based calculated energies according to Equations 7.5 and 7.6, respectively.

$$E_{dissociation}(H_2O) = E^{DFT}_{reaction}(UO_2 + H_2O) - E^{DFT}_{reaction}(UO_2 + H - OH) \quad 7.5$$

$$E_{dissociation}(H_2O) = E^{Potential}_{reaction}(UO_2 + H_2O) - [E^{Potential}_{reaction}(UO_2 + H - OH) + E_{corr}(H - OH)] \quad 7.6$$

This gives calculated dissociation energies of -0.104 and -0.118eV for the DFT and potential-based approaches, respectively. The difference in these values is less than 2% and can therefore be considered as accurate. Following the derivation of potentials and the associated correction factor for determining surface energies, we can now continue to consider the adsorption of water of the surfaces of UO_2. This was studied as three processes: surface hydration, surface hydroxylation and a mixture of the two. Additionally, the effect of coverage was also considered, from the adsorption of a single water molecule through to monolayer coverage.

7.3.2 The Adsorption of a Single Water Molecule

The adsorption of water can initially be considered as the adsorption of a single water molecule, highlighting the energetics of the individual processes. For each UO_2 surface, a single water molecule was added as either associatively or dissociatively adsorbed and relaxed via energy minimisation at all possible surface adsorption sites. Table 7.6 contains the surface and adsorption energies for the minimum energy hydrated and hydroxylated surfaces, along with comparison to the DFT-simulated surfaces used to calculate the correction term.

Table 7.6: Table showing the change in surface free energy, from the dry surface, adsorption energies and bond distances for the minimum energy {100}, {110} and {111} UO_2 surfaces following the adsorption of a single water molecule, using a potential-based approach. Comparison is also made to the DFT-calculated results.

Associative Adsorption of Water					
UO_2 Surface	$\Delta\gamma$ / J m^{-2}	E_{ads} (H_2O) / eV		U – O_W / Å	
		Potential	DFT	Potential	DFT
{100}	-0.24	-1.34	-	2.68	-
{110}	-0.21	-1.00	-	2.70	-
{111}	-0.02	-0.52	-0.62	2.76	2.59
Dissociative Adsorption of Water					
UO_2 Surface	$\Delta\gamma$ / J m^{-2}	E_{ads} (H-OH) / eV		U – O_H / Å	
		Potential	DFT	Potential	DFT
{100}	-0.53	-2.42	-	2.21	-
{110}	-0.58	-1.97	-	2.23	-
{111}	-0.01	-0.42	-0.51	2.27	2.30

Differences can be seen between the surfaces for the adsorption of a single water molecule. The change in surface energy from that of the pure surface shows that there is a preference for hydroxylation of both the {100} and {110} surfaces, each surface also showing similar changes in surface energies for both hydration and hydroxylation. However, there is a difference in adsorption energy, with the {100} having larger energies for both processes than the {110} surface. A negligible change in surface energy is seen for the {111} surface, with no strong preference for either process. Indeed, the calculated adsorption energies are similar to the energy of the vaporisation of water, -0.45eV, thereby indicating that the surface adsorption of a single water molecule is unlikely to be favoured.

On comparison with our DFT-calculated adsorption energies, the potential-based simulations show the same order of stability as the DFT-simulated surfaces, albeit being approximately 0.1eV lower. Comparison of bond lengths show good

agreement for the dissociatively adsorbed water but an extended associatively adsorbed water – uranium distance for the potential-based approach.

Comparison can be also made to the results of Skomurski *et al*. [74] and Hay [73] where the surfaces were simulated using a standard DFT methodology and are given in Table 7.7. A greater difference to the results of this study is expected for those of Hay due to the lower plane wave cutoff of 400eV and his assuming of a FM structure. Additionally, the surfaces in the Hay study were smaller, with the adsorption of a single water molecule representing a 50% surface coverage.

Table 7.7: Table detailing the adsorption energies and bond distances for {110} and {111} UO_2 surfaces following the adsorption of a single water molecule as reported by Skomurski *et al*. [74] and Hay [73] using standard DFT methodologies.

Associative Adsorption of Water				
UO_2	E_{ads} (H_2O) / eV		U – O_W / Å	
Surface	Hay	Skomurski	Hay	Skomurski
{110}	-0.46	-	2.67	-
{111}	-0.52	-0.69	2.74	2.63
Dissociative Adsorption of Water				
UO_2	E_{ads} (H-OH) / eV		U – O_H / Å	
Surface	Hay	Skomurski	Hay	Skomurski
{110}	-1.13	-	2.13	-
{111}	-0.68	-0.43	2.22	2.18

The results of Skomurski *et al*. and the DFT-calculated values of this study for the {111} surface are in agreement. The trend in stability remains, namely that associative adsorption of water has a more favourable adsorption energy than hydroxylation. One noticeable difference is seen in the bond lengths, although this is likely to be a cause of differences in simulation methodologies, as the work of Skomurski *et al*. does not use a U on-site correction term. As detailed in chapter one, the results of Skomurski *et al*. and Hay differ in terms of the trend in adsorption

energies for surface hydration and hydroxylation. Our results show these same differences with the results of Hay. This is again attributed to differences in simulation methodology, where the simulations of Hay modelled water adsorption on only one side of the slab, with the bottom layers held fixed to mimic the underlying bulk. Therefore, the differences between the work of Hay with our DFT results may be a result of magnetic interactions, or indeed through formation of a dipole leading to dipole – dipole interactions between slabs.

A larger discrepancy is seen between our potential-based adsorption energies for the {110} surface with those reported by Hay. This difference is most likely related to the size of the simulation cell used. To assess this further, we modelled the adsorption of a single water molecule on a smaller {110} surface, generated from the reduced unit cell, finding energies of -0.78 and -1.14eV for hydration and hydroxylation, respectively. These values are in much better agreement with those of Hay, particularly for the dissociatively adsorbed water.

These comparisons confirm that the results of the single water molecule results are sensible, therefore we can next consider the effect that increasing the amount of water present on the surface has on calculated surface energies and adsorption energies. This was achieved initially by considering surface hydration and hydroxylation as being separate processes.

7.3.3 The Effect of Coverage

Prior to discussing the results of the simulations of varying water coverage it is important to define coverage for the adsorption of water. It is defined in as in the previous chapters, as the percentage of surface adsorption sites filled. However, we consider two types of adsorption site, either above a surface uranium or above a surface oxygen atom. Therefore, the associative adsorption of a single water molecule will occupy one adsorption site, whereas dissociative adsorption will occupy two sites per water molecule, an OH^- above a surface uranium and an H^+ above a surface oxygen atom. The number of surface uranium and oxygen atoms in the simulation cells for the three surfaces are given in Table 7.8.

Table 7.8: Number of surface uranium and oxygen atoms on the modelled {100}, {110} and {111} surfaces.

Surface	Number of Surface U	Number of Surface O	Total Adsorption Sites
{100}	4	4	8
{110}	2	4	6
{111}	4	4	8

The effect of coverage on the surface adsorption of both hydrated and hydroxylated water was studied by increasing the number of surface adsorbed water molecules in a stepwise manner up to monolayer coverage. The trialling of all possible surface combinations for each coverage level allows the evaluation of surface free energies and adsorption energies. Figure 7.7 shows plots of the surface free energies and adsorption energies for these surfaces as a function of surface coverage. The surface structures of the lowest energy hydrated and hydroxylated surfaces are also shown in Figures 7.8 and 7.9, respectively.

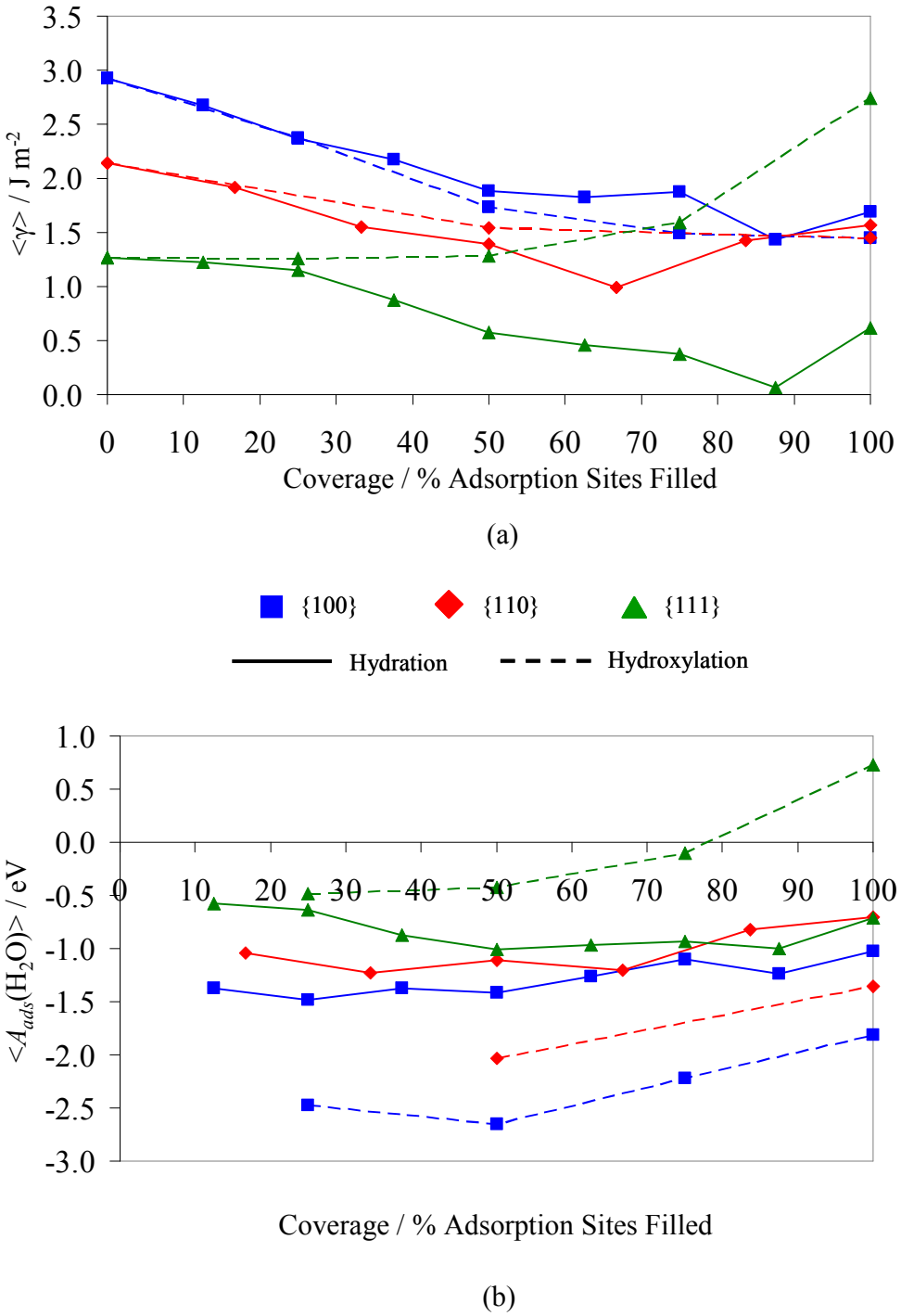

Figure 7.7: Plots showing the **(a)** surface free energies and **(b)** free adsorption energies for the hydration and hydroxylation of the low index UO_2 surfaces.

The results show that for all three surfaces hydration tends to reduce the surface free energy with increasing coverage, leading to a lower energy surface than when hydroxylated. This is particularly true for the {111} UO_2 surface, where hydroxylation destabilises the surface and the surface free energy increases with increasing coverage. The disruption of the stable surface as a result of hydroxylation gives rise to unfavourable energies at high coverage. Surface hydration can stabilise the surface through a hydrogen bonding arrangement, without necessarily altering the surface configuration, as seen in Figure 7.8(c). Hydroxylation, however, will inherently have a direct influence on the surface structure, through addition of a proton to a surface oxygen atom, Figure 7.9(c), which can destabilise the surface from its stoichiometric structure. In addition, there will also be a larger degree of repulsion between the oxygen atoms of hydroxide groups on this oxygen terminated surface.

The {100} surface energies also show that increasing amounts of surface hydration works to reduce the surface free energy, with the minimum energy surface showing an ordered water structure with apparent hydrogen bonding, Figure 7.8(a). However, surface hydroxylation shows a similar trend but with lower surface energies than hydration. The strong preference for hydroxylation is a result of the formation of a regular, flat surface as shown by the lowest energy hydroxylated surface, Figure 7.9(a), which contains monolayer coverage of surface hydroxylation.

The {110} surface has a lowest energy hydrated structure consisting of hydrogen bonded layers running along the grooves, or facets, on the surface, Figure 7.8(b), at a coverage of 66.7% water. The most stable hydroxylated surface however is that found at monolayer coverage, Figure 7.9(b). Consideration of the free adsorption energies also suggests that, for this surface, hydroxylation would be the preferred processes.

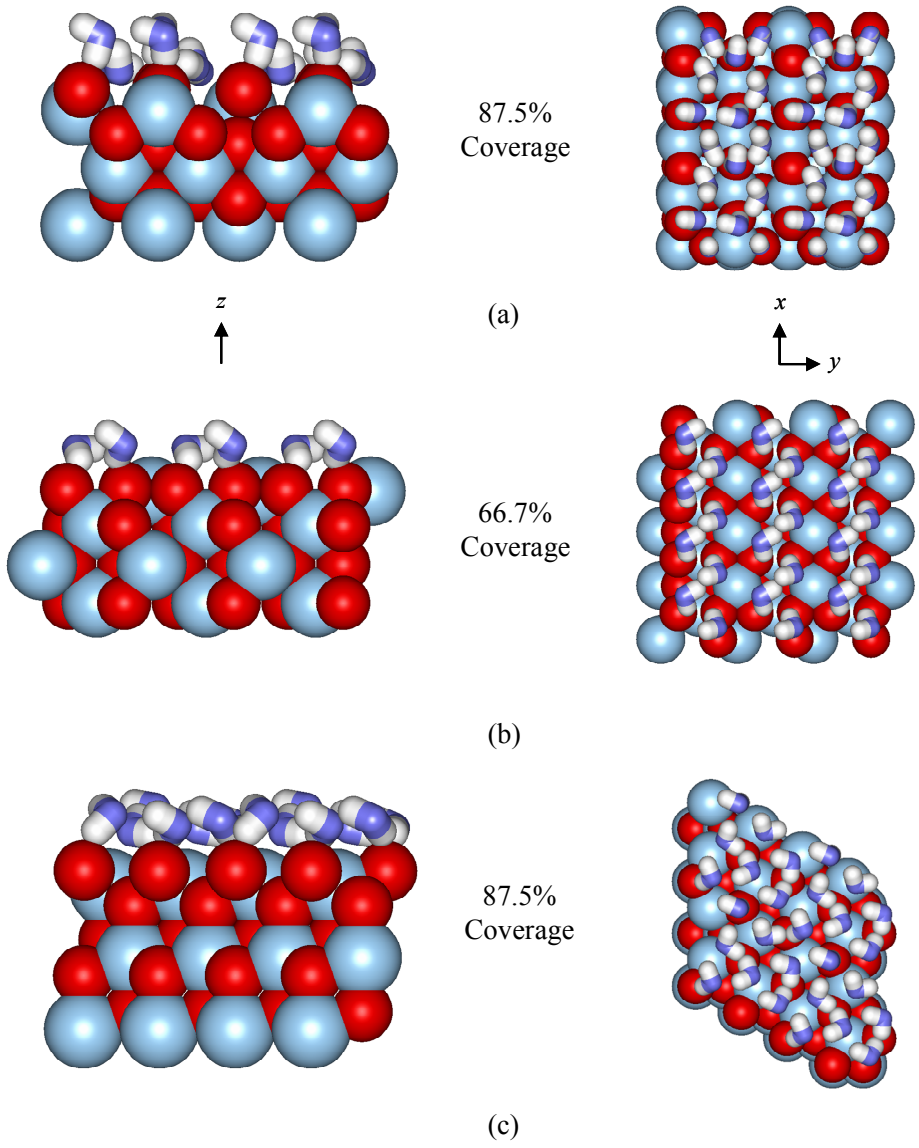

Figure 7.8: Surface structures of the minimum energy hydrated **(a)** {100}, **(b)** {110} and **(c)** {111} UO_2 surfaces. The water coverage of each surface is also indicated. Axis indicators are arbitrary and reflect the relative view of structure.

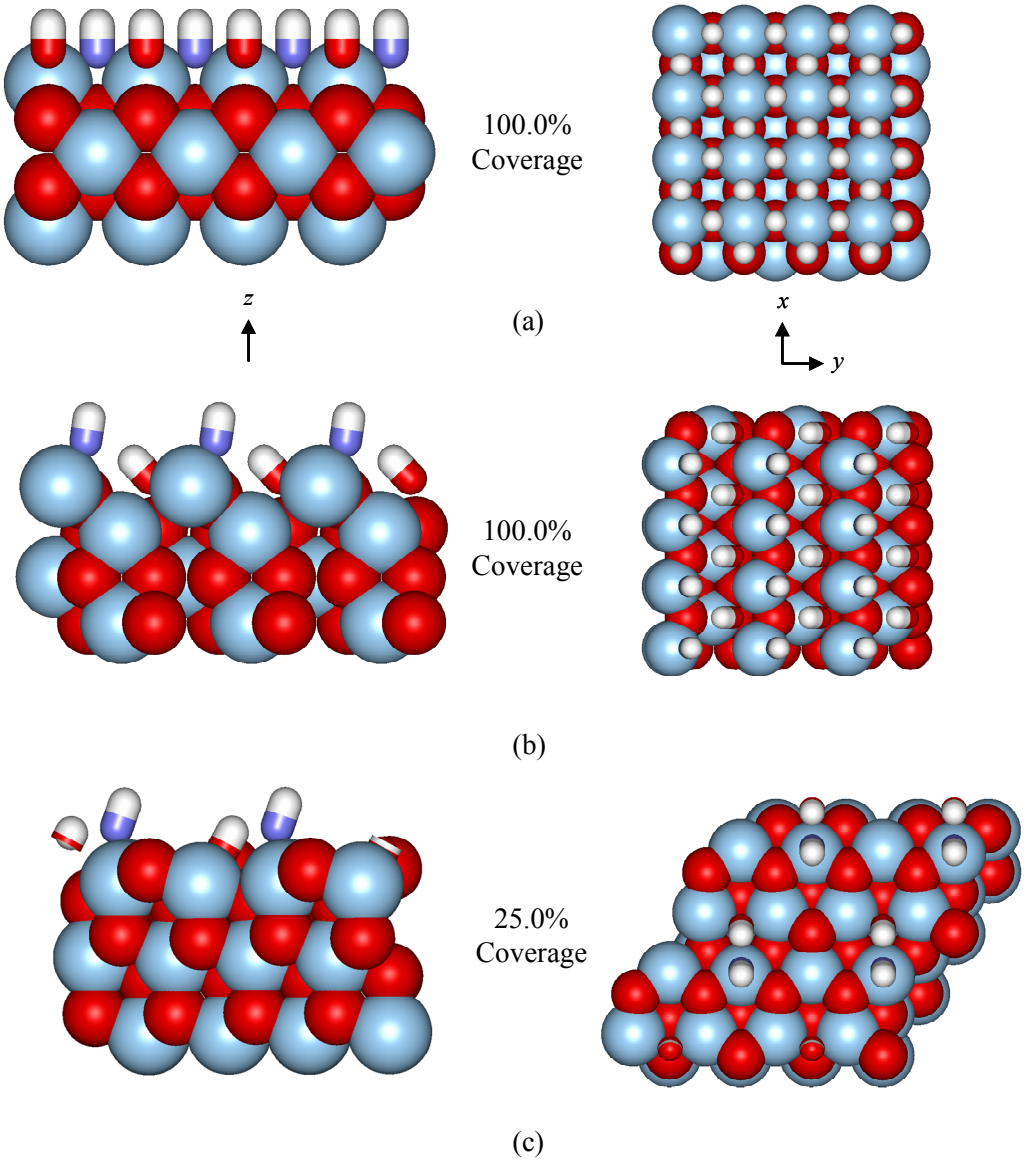

Figure 7.9: Surface structures of the minimum energy hydroxylated **(a)** {100}, **(b)** {110} and **(c)** {111} UO_2 surfaces. The water coverage of each surface is also indicated. Axis indicators are arbitrary and reflect the relative view of structure.

The results of the surface hydroxylation are also in relatively good agreement in comparison to the work of Abramowksi *et al.* [75] and Tan *et al.* [76]. Figure 7.10 shows a comparison of our results with their published data for the hydroxylation of

the {100} and {111} surfaces. The main differences between the data are a result of the correction factors used. Both Abramowski *et al*. and Tan *et al*. use a correction factor determined from a Born-Haber cycle, which will be subject to the problems previously discussed. This correction factor will have a larger effect as the number of added species increases, giving rise to a greater difference in results as coverage increases, which is indeed seen. The main consequence of this for those surfaces shown is that the stabilisation from hydroxylation is over estimated, leading to lower surface energies. This results in the surface energies of the {100} being lower than they should be but more importantly, in the case of Abramowski *et al*., incorrectly predicts the trend in {111} surface energy with increasing coverage.

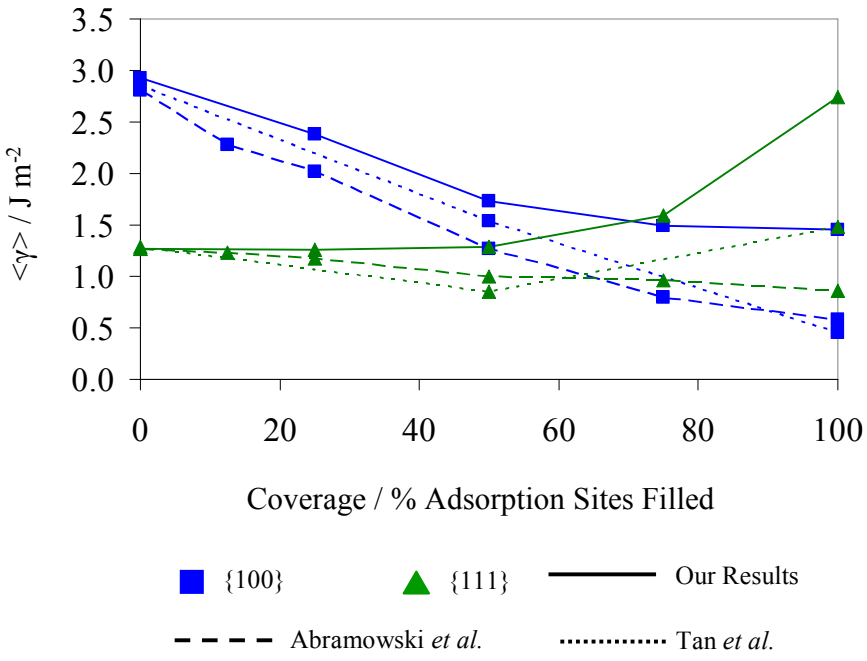

Figure 7.10: Plot showing comparison of the surface energies of the {100} and {111} UO_2 surfaces as calculated using our potential with the published results of Abramowski *et al.* and Tan *et al*.

7.3.4 Mixed Hydroxylation/Hydration

In real systems, however, water adsorption does not always consist of solely hydration or hydroxylation. Both of these processes are able to occur simultaneously, giving rise to mixed surfaces. Therefore, the modelling of the products of mixing the processes is imperative to fully characterise and model the process of water adsorption. The approach was similar to that used for the individual processes, with all surface combinations trialled allowing the determination of free energies. The variation of surface free energy with the water coverage is shown in Figure 7.11(a).

The results, in general, show that as the amount of adsorbed water is increased the surface energy decreases down to the minimum. For the {100} and {110} surfaces this exists at full coverage, however, for the {111} surface this is present just before monolayer coverage. However, at all levels of coverage the same trend, in terms of the order of stability, remains constant, with the {100} being the least stable and the {111} surface being the most. This also provides no change in the predicted equilibrium morphologies from being solely dominated by the {111} surface. In addition to considering the variation of energy, it is also informative to consider the extent of hydration and hydroxylation present in the lowest energy structures at each coverage level, shown in Figure 7.11(b). However, as surface coverage is defined here relative to the number of filled adsorption sites, it should be noted that the adsorption on a single adsorption site is always a result of purely hydration as hydroxylation requires two surface adsorption sites. These results show similar results as the individual adsorption processes. The hydrated {111} surface remains the most stable indicating that the surfaces are dominated by hydration. The {100} and {110} surfaces, however, show an almost constant level of surface hydroxylation, independent of total coverage.

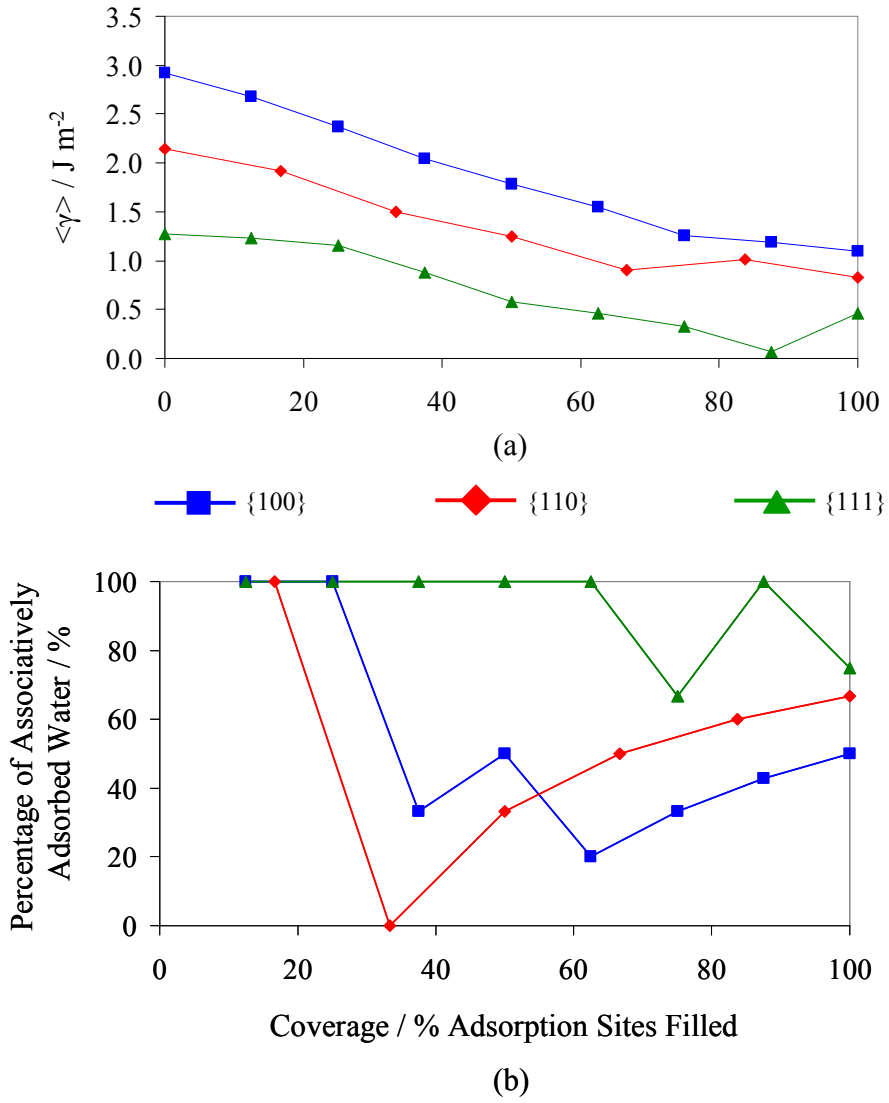

Figure 7.11: Plots showing **(a)** the variation of surface free energies with surface coverage following mixed surface hydration/hydroxylation on the low index UO_2 surfaces, and **(b)** the percentage of associatively adsorbed water on the lowest energy structures at each coverage.

The structures of the lowest energy surfaces as a result of mixed surface hydration and hydroxylation can also yield important information on the nature of how these processes occur at the surface, as shown by Figure 7.12.

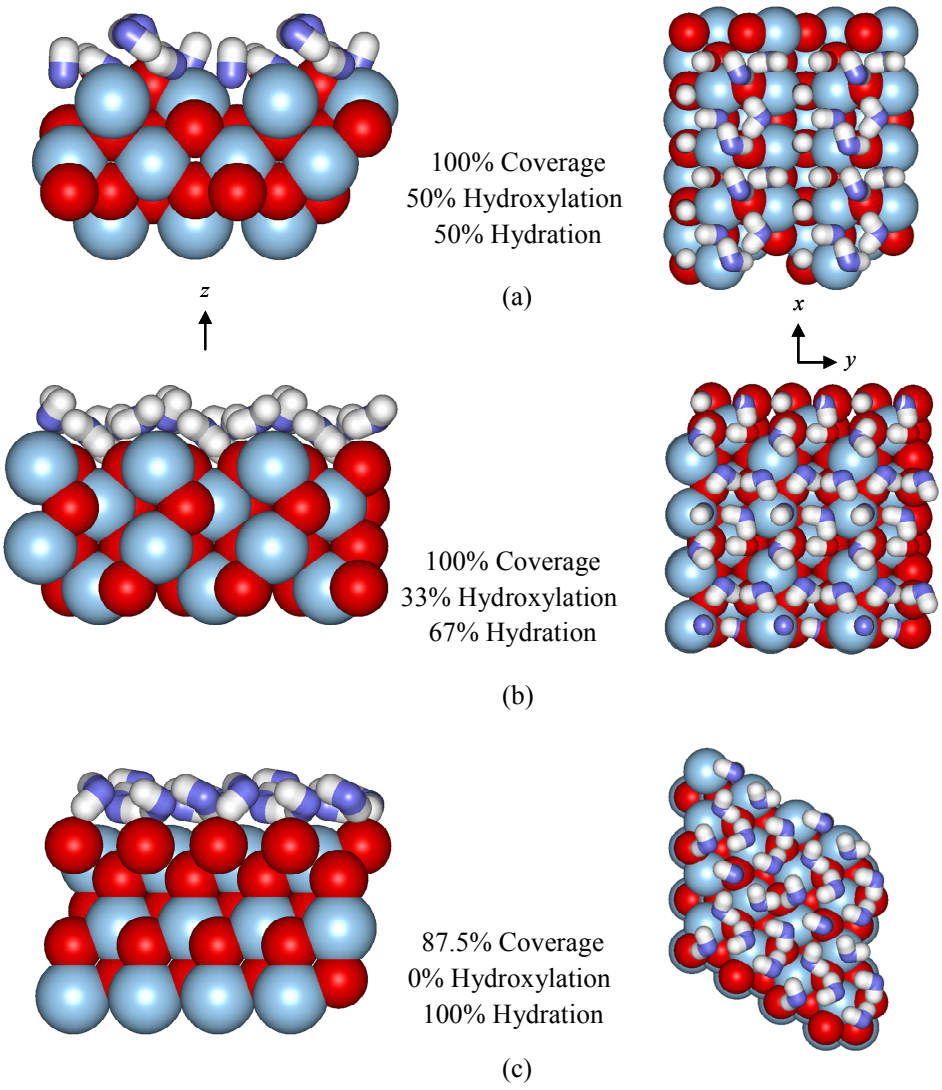

Figure 7.12: Side and plan views showing the structure of the lowest energy surfaces following mixed hydration and hydroxylation on the UO_2 **(a)** {100}, **(b)** {110} and **(c)** {111} surfaces. The water coverage of each surface is also indicated. Axis indicators are arbitrary and reflect the relative view of structure.

The structural consequence of hydrating hydroxylated {100} surfaces is to fill the missing oxygen rows with hydrated water spanning the gap between hydroxide ions, as seen in Figure 7.12(a). This is in partial agreement with the experimental work of Hedhili *et al*. [43] who suggest that water is completely dissociated, rather than hydroxide formation, on this surface. Their results of $D_2{}^{18}O$ adsorption show no

evidence of OD formation but ^{18}O incorporation into the surface, with the suggestion of subsequent diffusion into the bulk. Therefore the differences with the results of this study could arise from the fact that we do not account for any oxygen diffusion from the surface and do not allow for the hydroxide to dissociate. Figure 7.12(b) shows the {110} surface where the structure differs with the {100} surface. This surface shows that the hydroxylation only occurs on half of the surface groove, with hydrated water stabilising the remaining surface. The study of the mixed hydration and hydroxylation also highlights the importance of studying mixed adsorption rather than solely relying on the results following similar trends to the individual processes. By modelling the single process alone, any cooperative effects between different adsorption will be lost and thus the results will be incomplete.

The calculation of a large range of surface energies at different coverages of surface hydration and hydroxylation allows us to predict the surface composition as a function of the change in water chemical potential. The approach is similar to that described for the surface phase diagrams for CaO and MgO, and uses Equation 7.7 to calculate the surface energy as a function of the chemical potential of water.

$$\gamma = \gamma_{p=0} - \frac{n_{H_2O}}{S}\Delta\mu_{H_2O} \qquad 7.7$$

The variation in surface energy with changing chemical potential can then be plotted, with the lowest energy surface at each value of chemical potential representing the most stable surface configuration. The plots showing the surface composition at different chemical potentials are shown in Figure 7.13.

The plots all show dominance of a single phase, comprising of the minimum energy surface found for the mixed adsorption. However, the dominant {110} surface changes composition at a chemical potential of -1.4. This leads to the 67% coverage surface, with a hydroxylation/hydration ratio of 50%/50%. This is caused only as a result of the changing number of hydrated water molecules adsorbed on the

surface, indicating the strength of the hydroxylation in 50% of the surface grooves. The absence of the dry surface in the surface phase diagrams indicates the strength and favourability of water adsorption on these surfaces. The minimum in chemical potential at a value of -3.0 is comparable with a water partial pressure of 10^{-40}bar at 300K, therefore the continued presence of these water coated surface structures indicates the strength of the adsorption.

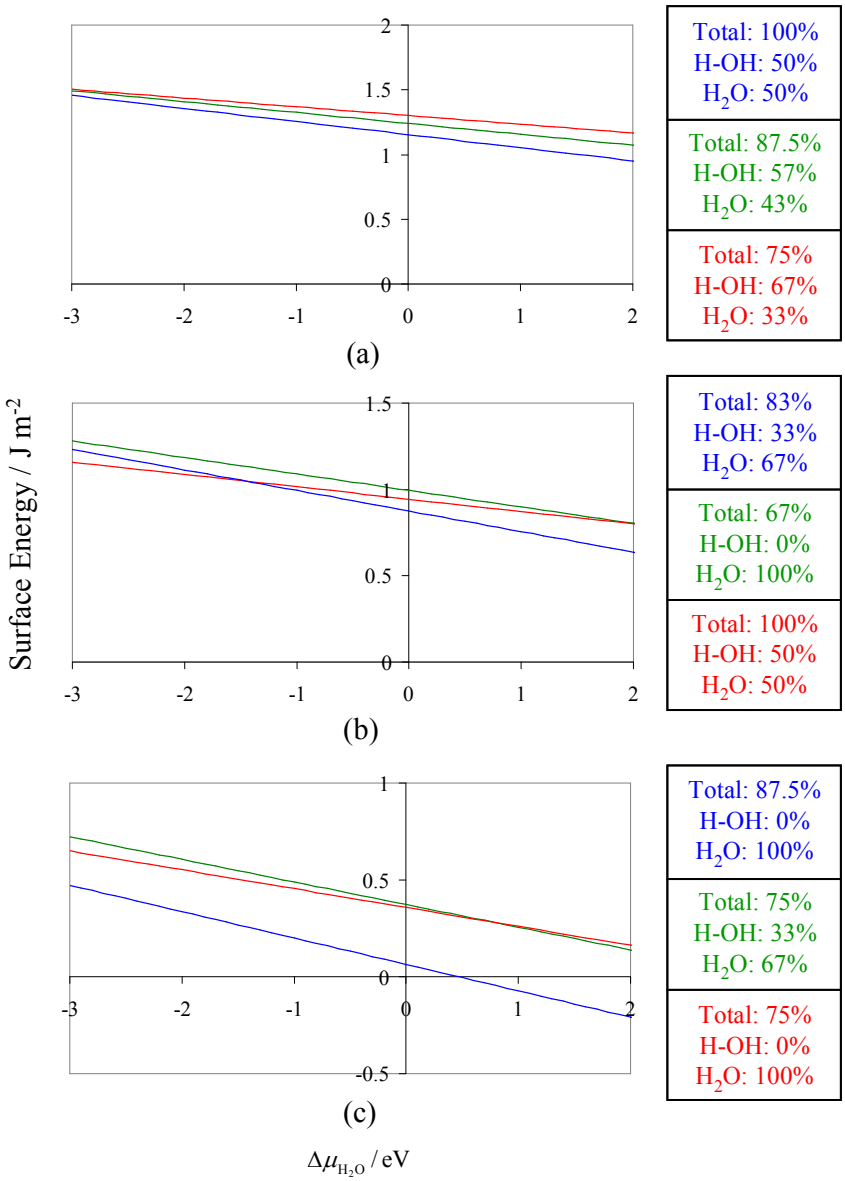

Figure 7.13: Surface phase diagrams showing the change in surface composition as a function of the chemical potential of water for the **(a)** {100}, **(b)** {110} and **(c)** {111} UO_2 surfaces. NOTE: Only the lowest energy surface compositions are shown.

We next considered the effect of multiple water layers, and as noted earlier, when there is an excess of liquid water present it is more appropriate to used molecular dynamics.

7.4 The UO_2 – Water Interface

The interaction with liquid water required the generation of UO_2 slabs to be generated, with an approximate thickness of 20Å. These were then put in contact with a 20Å layer of water on one side and an equivalent vacuum gap on the other. These calculations were then run using the NVT ensemble at 300K for 1ns, following a 10ps run at NVE to stabilise the system, with a relaxation parameter of 1ps. The structuring of water can again be considered using relative density plots, both in the *z*-direction and throughout the cell. Figure 7.14 shows these plots for the three surfaces studied. We can also consider the first layer of water above the surface to further understand the effect the surface plays on water structuring, Figure 7.15 shows water density plots for the uppermost layer of uranium atoms and the first layer of oxygen from the water molecules.

The {100} surface, Figures 7.14(a) and 7.15(a), shows four water layers extending from the surface, the first two being clear and the second two being less distinct before moving to a bulk-like density. The first layer can be seen to coordinate along the rows of missing oxygen on the surface, predominantly through a U – O interaction. The second oxygen layer is then seen 2.6Å above the surface oxygen atoms, with a hydrogen layer in between. The presence of this hydrogen layer, 1.7Å above the lattice oxygen atoms indicates that this second layer is formed through hydrogen-bonded interactions. This compares favourably with the lowest energy structure seen from the energy minimisation study above, Figure 7.12(a), where the hydroxylation is seen to be preferred along these rows of missing oxygen atoms. The adsorbed hydrated water then coordinates in between these forming another row. Although, hydroxylation is not explicitly modelled in this molecular dynamics study, water would be expected to be strongly coordinating, with a low mobility, in

preferred hydroxylation sites. As this is seen here it can be concluded that the results concur.

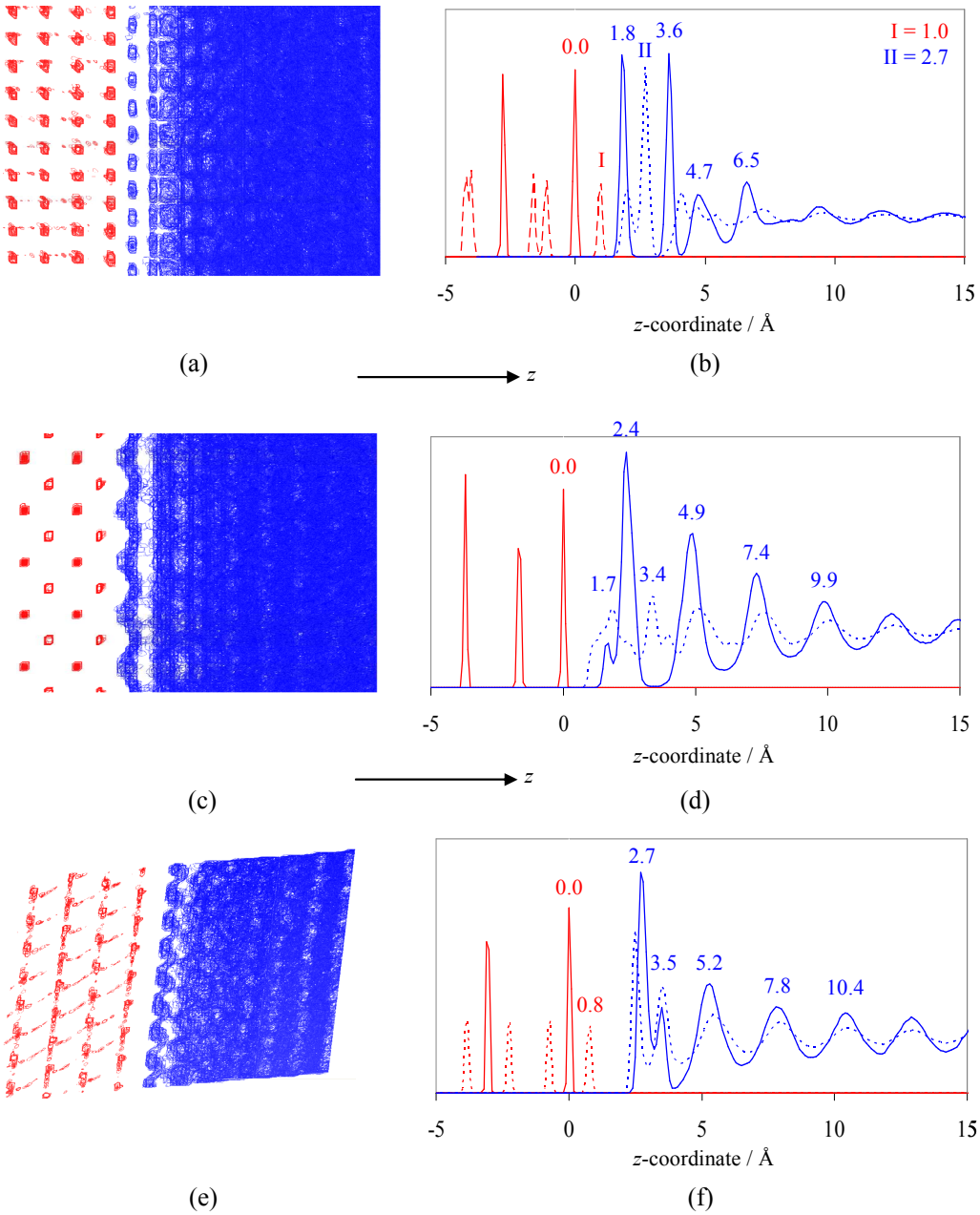

Figure 7.14: Plots showing the **(a)** relative water density and **(b)** *z*-density of the UO_2 – water interface on the {100} surface. The same respective plots are shown for the {110} surface in **(c)** and **(d)**, and for the {111} surface in **(e)** and **(f)**. Uranium density is shown in red and the oxygen of water in blue, dashed blue lines refer to hydrogen density and the density of lattice oxygen is shown in **(b)** and **(f)** by the dashed red line.

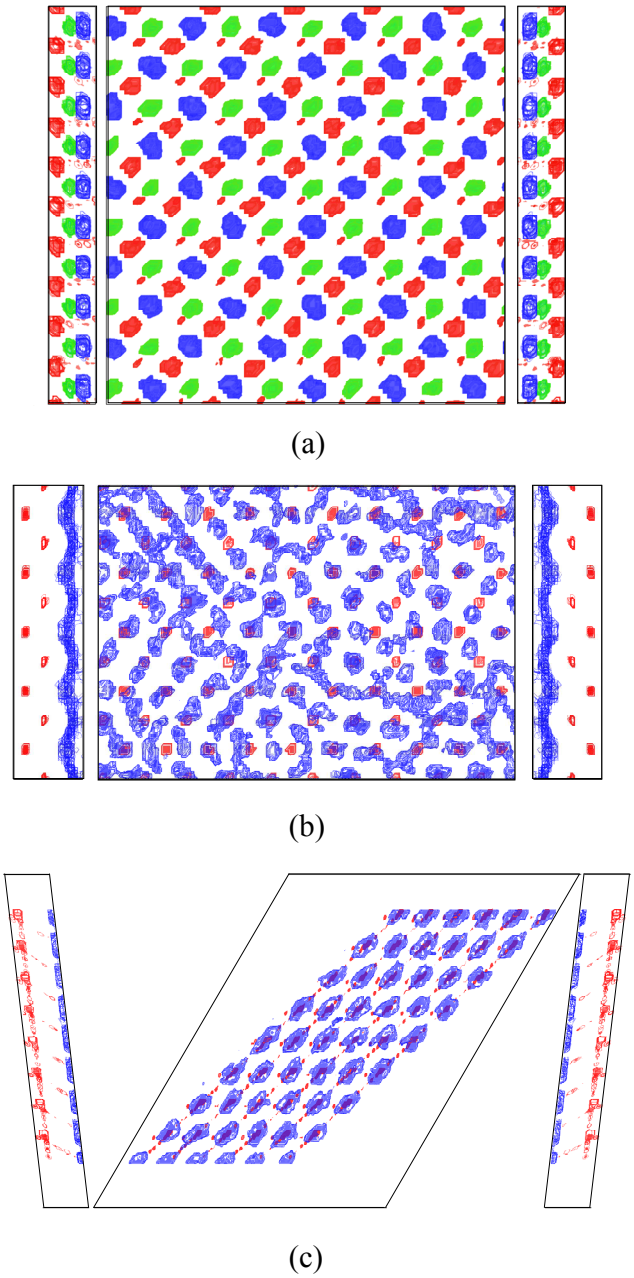

Figure 7.15: Plots showing the average density for the surface oxide layer and first water layer immediately above the surface for the **(a)** {100}, **(b)** {110} and **(c)** {111} UO_2 surfaces. Plots show the view looking down on the surface (central) and the side views (left and right) for each surface. Red and blue indicate uranium and water oxygen density. The green in **(a)** represents the density of the uppermost layer of lattice oxygen atoms.

The {110} surface, shown in Figures 7.14(b) and 7.15(b), has a similar ordering profile, with four clear layers extending away from the surface. However, further analysis of the structure of the first coordinated layer indicates a more disordered structure. This layer appears to vary between some water coordinating above the surface trenches and other molecules 2.4Å above the surface uranium atoms, which compares with the U-O bulk distance of 2.37Å, however, no apparent structure is visible.

The structuring of water also extends into the bulk for the {111} UO_2 surface, Figures 7.14(c) and 7.15(c). This surface additionally appears to have a greater effect on the water, with the density oscillating in a layered-like manner to a greater distance from the surface than for the {100} and {110} surfaces. The first coordinated layer appears to be mainly comprised of water coordinated above surface uranium atoms, followed by possibly some indistinct coordination to surface oxygen atoms. Consideration of the hydrogen density, which is seen to approximately overlap with the water oxygen density, indicates that molecules are predominantly orientated parallel with the surface.

The strength of interaction can also be assessed using the water residence time. Figure 7.16 gives the residence time plots as a function of the atomic coordinates for the {110} and {111} UO_2 surfaces. The residence times for the {100} surface showed the formation of a strongly bound layer, with residence times across the surface being approximately 800ps, the measured time, for all surface atoms, thereby indicating the strength of adsorption and low water mobility in the first adsorbed water layer. The results for the {110} surface, in Figure 7.16(a), show a similar pattern to the average density plot, with no clear ordered structure occurring, simply regions of mobile and coordinated water across the surface. The plot of water residence time on the {111} surface, Figure 7.16(b), shows a similar pattern. However, mobility on this surface is seen to be greater, indicated by the lower residence times. In addition, regions of reduced mobility are seen over some surface uranium atoms, indicating that surface coordination is likely to occur in this manner.

However, as with the CaO and MgO surfaces, these discontinuous residence time plots do suggest that longer simulation times are required to obtain quantitative results.

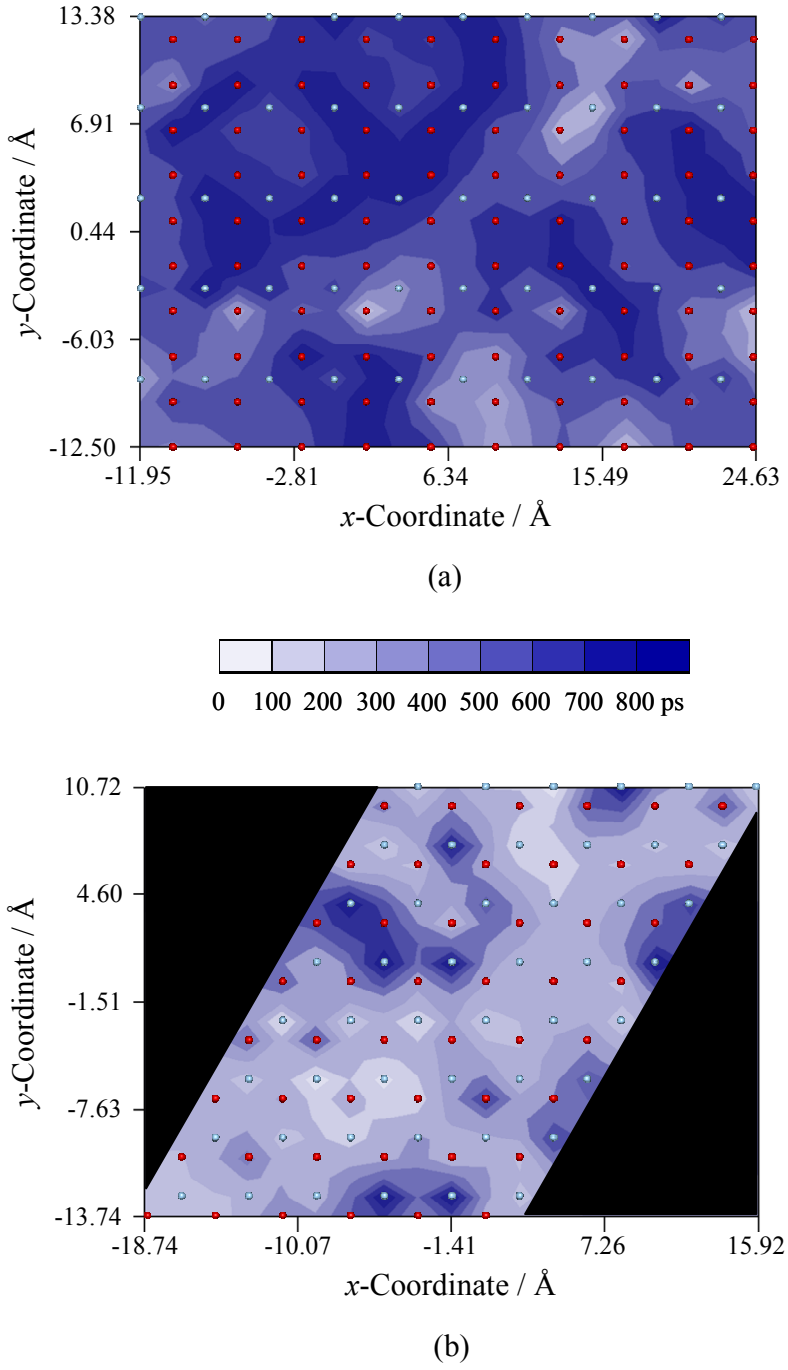

Figure 7.16: Contour plots of water residence time as a function of the atomic coordinates for the **(a)** {110} and **(b)** {111} surfaces of UO_2.

7.5 Chapter Conclusions

This chapter has described a study of water on the low index surfaces of UO_2. These surfaces have been modelled using a potential modified from the previously used Busker potential, with the Catlow oxygen – oxygen interactions to allow the transferability to our water, hydroxide and oxide models. Further testing of this showed the accurate prediction of bond distances in the bulk structure as well as the low index surface structure and relative energies. DFT calculations were employed in the study of uranium cluster molecules and water adsorption on the {111} surface, allowing the fitting of a potential to model the interaction of water with the uranium ion.

The resulting potential has enabled the study of the adsorption of water, in both associatively and dissociatively adsorbed forms, as a function of surface coverage on the {100}, {110} and {111} surfaces. The evaluation of surface free energies and adsorption free energies was made possible by performing a large number of different surface energy minimisations. Both hydration and hydroxylation were initially considered as separate processes, followed by the simulation of mixed adsorption. Results suggest that hydroxylation is the dominant process for both the {100} and {110} surface. This occurs primarily along the rows of vacant sites on these surfaces, with associatively adsorbed water providing additional stability between the hydroxide ions. The {111} surface, however, is predicted to be unstable towards hydroxylation, with associative adsorption of water dominating. In addition, the results of surface composition with varying water chemical potential show that the minimum energy configurations were seen to dominate. Another interesting result of this study suggests that the single molecule adsorption energies are sufficient to give insight into the relative binding energies.

The interaction of UO_2 with water was further explored by considering the mineral – water interface using molecular dynamics. Although surface hydroxylation was not explicitly modelled in this study, highly coordinated water throughout the

simulation appears to be indicative of hydroxylation sites on the surface. This was particularly true for the {100} surface, which showed that first layer of adsorbed water is present along the vacant oxygen rows on the surface and has an extremely low mobility. This suggests that molecular dynamics simulations of associated water molecules could be used as a simple probe for identifying hydroxylation sites. Overall it was seen that, as with the modelled surfaces of CaO and MgO detailed in chapter five, the nature of the surface distinctly affects the structuring of water in the vicinity immediately above it, but does not extend into the bulk water to the same extent as for CaO and MgO surfaces. The {110} surface shows a varied pattern, with distinctly coordinated water on the surface, but with no strong presence over coordination to surface uranium or oxygen atoms. The {111} surface, however, shows a more mobile water structure, with coordination of the first water layer concentrated above the uppermost uranium atoms.

Chapter Eight

Conclusions & Future Work

The work detailed in this thesis has considered two broadly connected research areas. Both of which ultimately aim at improving our understanding of hydrogen, oxygen and carbon at oxide surfaces. The first section of this work was concerned with the process of carbon sequestration, with simulations focussing on the interaction of water and carbon dioxide with calcium and magnesium oxide surfaces. The second section was aimed at developing the description of the more complex actinide oxides by considering uranium dioxide, through the simulation of thin film structures and the interaction of water with UO_2 surfaces. As the future work which can continue from these broad sections is vast, it is informative to consider them separately. Therefore the following sections will draw the main conclusions from

these studies and from this suggest possible routes for future study in these areas. Finally, some general conclusions and achievements of this thesis will be given.

8.1 Adsorption Processes on Alkaline Earth Metal Oxide Surfaces

Chapter four described the results of the surface adsorption of gaseous water and carbon dioxide, in the form of a carbonate, on the low index surfaces of calcium and magnesium oxide, with CaO showing increased reactivity as expected. One of the simulation issues is ensuring that there is sufficient statistics covering the different possible configurations. Thus we investigated a 'grid' strategy for sampling the structures to give the free energies of adsorption. The majority of surfaces were predicted to be amenable to carbonation, with the exception of the {111} surface with its preference for the formation of hydroxide compared to the carbonate. Surface phase diagrams illustrate that most CaO surfaces will take up CO_2 at atmospheric conditions, whereas most MgO surfaces will primarily consist of adsorbed water. However, relatively modest increases in the concentrations of CO_2 will result in carbonation for the {100} and {310} MgO surfaces. In addition, surface features, are seen to increase reactivity, particularly to carbonation and hydroxylation. The formation of a mineral carbonate layer is also seen to occur via the adsorption of carbonate into the surface, followed by clustering of carbonates with increasing coverage, until an amorphous monolayer is formed.

One possible extension of this study would be to consider the mixed adsorption of molecular and dissociated water on both pure surfaces and with the co-adsorption of carbon dioxide using the atomistic methods used in this study. The modelling of bicarbonate species would also be of value for carbon dioxide and water adsorption, due to its occurrence in solutions. This could also be easily incorporated in the generated surface phase diagrams. Furthermore, electronic structure methods could also be employed to consider the reaction of carbon dioxide itself to form the surface-bound carbonate species, both in the absence and presence of water. The simulation of defective surfaces would also be informative, moving the simulations

closer to real surfaces. Finally, the transferability of these methodologies could be used to probe carbonation of other materials, such as the hydroxides, silicates and hydroxysilicates, in an effort to improve the carbon sequestration process.

The interactions of surfaces with liquid water were then investigated in chapter five. The main results showed that the structuring and ordering of water is directly influenced by the surface structure and composition. The first hydration layer was seen to be primarily composed of coordinated water in distinct crystallographic positions, with specific orientations to the surface. As the distance to the surface was increased, the layers became more diffuse, showing less structure until they became bulk-like in appearance. Increased water mobility was also seen for CaO surfaces due to the weaker coordination. Surface carbonation was seen to cause a distinct disruption of the water structuring, with water mobility varying across the surface with no clear pattern.

Possible further calculations would be to determine other properties for these systems. For example, the evaluation of water diffusion coefficients at the surface, although most likely giving similar information to the residence times analysis, could be used in conjunction with adsorption profiles. The adsorption profiles of different species, for example, carbonate and bicarbonate, to the surface could be determined through the use of potential of mean force calculations. The principle of these simulations is to calculate the free energy of the adsorbing species at different distances from the surface, until adsorption occurs. This allows for the generation of a free energy profile, which, when combined with diffusion and the relative density profile could reveal information on the process of carbon sequestration in aqueous solution. The incorporation of hydroxide ions into the simulations would also be instructive as it was seen to be a favourable process for a number of surfaces, in particular for high energy surface sites.

The nanoparticle study showed that the water structuring on the particle faces was similar to that seen above surfaces, with reduced structure at higher energy corner

and edge sites. In addition, although the number of coordinated water molecules was seen to vary with atom position across the nanoparticle surface, residence times were predicted to be sensitive to surface composition only. Finally, adsorption of carbonate was calculated to be more favourable at corner sites, than higher coordinated edge and face sites. Therefore, this suggests that multi-faceted nanoparticles may improve adsorption behaviour.

Further simulations of the stability as a function of varying hydroxide coverage would allow for a clearer understanding of the effect hydroxylation has on these nanoparticle surfaces. In addition, the inclusion of liquid water in all nanoparticle simulations is an obvious next step. Following this the processes of nanoparticle growth, rearrangement, aggregation and dissolution could be considered using the computational techniques detailed in this thesis. The carbonation of a {100} CaO nanoparticle could be extended to both further consider different surface terminations, as well as increased carbonation to gain a more complete understanding of this process. In addition, the inclusion of liquid water and bicarbonate ions would also aid further characterisation of this system. A more advanced study could also be employed to consider mixed systems containing promoters, such as Al_2O_3, to assist in the improvement of these systems for use in carbon sequestration.

8.2 Uranium Dioxide and its Interaction with Water

The second part of this thesis detailed simulations of uranium dioxide structures and the adsorption of water at its surfaces. The electronic structure of bulk and thin film UO_2 structures was the focus of chapter six. The application of a DFT+U methodology was seen to improve the simulation of AFM UO_2, through the increased localisation of the *f*-electrons. Following this, preliminary work was described on defective UO_2. Oxygen defect formation energies for a 1x1x1 cell indicate that vacancy formation is considerably less favourable than interstitial defects. Following the simulation of defective thin film structures, the oxygen

segregation behaviour was also considered. Oxygen interstitials were shown to segregate to the surfaces, whereas vacancies would migrate into the bulk. The calculation of thin film phase diagrams showing the effect of oxygen chemical potential highlights the stability of the stoichiometric surfaces, which is seen to degrade slightly to form a substoichiometric phase at an elevated temperature of 1000K. Formation of hyperstoichiometric thin films was seen to require large oxygen partial pressures to form. Finally, the magnetic structure was considered in more detail in an effort to generate a simple model which could predict the stabilities of different configurations relative to the FM phase. However, complex ordering was seen, causing the simple models to fail. Although increased parameterisation, or increases in the complexity of the model could improve this.

This study could easily be extended in a number of ways. Firstly, the simulation using different hybrid-DFT methods would be instructive, in terms of both structure prediction and an increased understanding on how it improves the electronic structure and spin density prediction in comparison to the DFT+U approach. The simulations could also be further advanced with the inclusion of spin-coupling effects and noncollinear magnetism. The defect work could be extended using a supercell approach, allowing the effect of defect concentration to be investigated. Moreover, the simulation of uranium defects to allow the calculation of Schottky defect energies. Molecular dynamics could also be employed to consider oxygen and uranium diffusion in both bulk and thin film structures to understand the segregation of defects in more detail. The depth of thin film structures can also be varied more to consider its effect. In addition, the trialling of a larger range of different magnetic ordering in thin film structures would be of benefit in the generation of a model to predict difference stabilities resulting from magnetic ordering.

Following this work, the interaction of UO_2 surfaces with gaseous water was considered in chapter seven using potential-based modelling techniques, with DFT employed to enable the construction of a model for the interaction between water and the surfaces. The results of this showed that hydroxylation of the {100} and

{110} surfaces is highly favoured, with the presence of hydrogen-bonded water molecules improving surface stability. The {111} surface, however, was seen to be relatively unstable to hydroxylation, with hydration providing the most surface stabilisation. In addition, contrary to previous simulations, the adsorption of water was not seen to change the relative stabilities of the three low index surfaces, with the {111} remaining the most stable at all surface coverages. Simulations of the mineral – water interface showed similar structuring effects to the CaO and MgO surfaces, although to a diminished extent. In addition, strongly coordinated water was seen to form above the hydroxylation sites predicted from the gas phase adsorption.

The adsorption of water continues to be an interesting topic and could be studied using DFT simulation, the dissociation of the hydroxide and oxygen diffusion into the bulk material could usefully be investigated. The processes of hydrogen adsorption and hydroxide transport through the surface and bulk material could also be explored. The effect water adsorption has on the transport of other species to the surface and how this alters surface reactivity could also be of use to understanding how water affects this material in its long-term storage. The adsorption of other chemical important species could also be considered, such as carbon dioxide. Finally, the techniques used here could be applied to other actinide oxide materials.

8.3 Overall Conclusions

In summary, the work contained in this thesis has demonstrated the use of computational modelling techniques to study adsorption processes on oxide surfaces. In addition to the detailed conclusions drawn above, a number of general observations and achievements can be noted.

Firstly, the study of surface carbonation and water adsorption on the mineral oxide surfaces showed that when coverage was increased, the relative trends in stability for the majority of surfaces were seen to differ. Although, this differs from that seen for

UO_2 surfaces, where increased coverage followed the same trends as individual molecule adsorption, this suggests that analysis of single molecule adsorption processes alone is insufficient to predict the relative stabilities of different adsorbates on these surfaces and that at least some study of increased coverage is required.

In addition, the study of the mineral – water interface also shows an effective way for determining surface adsorption sites. This was shown on not only the alkaline earth metal oxide surfaces but also on the UO_2 surfaces, where sites of strongly coordinated water, with associated large residence times, corresponded with favoured hydroxylation sites from static calculations. One of the deficiencies with molecular dynamics is that the lengthy simulation times do not allow for the trialling of a large number of different surface configurations. Therefore, by running a material, in contact with liquid water, would allow a suitable estimate of hydroxylation sites to be used in further calculation.

The calculation of residence times on various surfaces has generated different results as to what was previously expected. A uniform pattern was expected for atoms in identical chemical environments. However, this was not seen, which queries the required simulation length for convergence of these parameters. Although simulation for 1ns is sufficient for energy convergence, further testing is crucial to understanding the variation in water mobility prediction.

The importance of magnetic structure was shown in chapter six for uranium dioxide, although the implications of this study are important for all simulations concerning unpaired electrons. The results show how the energy of the system, regardless of whether it is bulk or surface structures, can vary significantly with different magnetic ordering. This suggests that suitable testing of lowest energy magnetic structure is required to ensure simulation accuracy.

Finally, one of the main achievements of this thesis has been the formation of surface phase diagrams through the use of potential-based methods. Previous studies have relied on lengthy electronic structure calculation. This not only allows for a reduction in the time required to generate these plots, but also allows for a larger trialling of surface configurations which provide a better estimation of the free energy.

Acknowledgments

The completion of this thesis and the work contained within would not have been possible without the various sources of help and support I have had over the time spent studying for my PhD. Therefore I would like to acknowledge a number of people.

Firstly, my family for all the support they have given, both mentally and financially, throughout my university career. I would also like to thank my friends, who have both listened patiently while I have talked about computational chemistry or provided various necessary breaks from the work. Although by no means exhaustive, my special thanks goes to fellow chemists Iwan, Sam and Tom, and also to past and present WHSmith colleagues Richard, Jon, James, Emma, Katie and Lucy for helping me balance working a part-time job whilst studying, as well as forming the successful quiz team 'Team Girlie ❁'! My additional thanks also goes for Tina, not only for help with 'basic' maths but also for the care and support she has given me throughout my PhD and for putting up with me during the stressful time of writing this thesis.

I also wish to thank the past and present members of the Parker group at Bath who have given me an incredible amount support and provided me with a fantastic, if somewhat noisy at times, office group. In particular to David Cooke, Sebastien Kerisit, Dino Spagnoli, Paul Martin, Arnaud Marmier, Corinne Arrouvel, Wojtek Greń, Marco Molinari and Veluz Maria Hart Prieto.

Funding acknowledgements must be made to EPSRC and the University of Bath, with funding through a DTA grant, as well as AWE for additional funding. In particular, my thanks also go to Dr. David Price and Dr. Mark Read of AWE for both being my industrial supervisors and providing me with endless support whenever I needed it.

The simulations detailed here would also not have been achievable without the various computer resources, of which I have relied heavily upon. Firstly, to the Materials Consortium and NERC for the granting of time on the HPCx and HECToR high performance computers. HPCx is provided by EPCC at the University of Edinburgh and by STFC Daresbury Laboratory, and funded by the Department for Innovation, Universities and Skills through EPSRC's High End Computing Programme. HECToR is provided by UoE HPCx Ltd at the University of Edinburgh, Cray Inc and NAG Ltd, and funded by the Office of Science and Technology through EPSRC's High End Computing Programme. Second, to the use of the UCL CONDOR pool and Clovis Chapman for help whenever it went down. Finally, the Mott2 facility (EPSRC Grant GR/S84415/01), run by the STFC e-Science Centre, which has been extensively used to generate my results, with particular thanks to Jonathan Churchill for his support and running of the machine.

Lastly, and by no means least, I must thank Prof. Steve Parker for guiding me from the start of my MChem project through to now, and for whom this project would not have even been possible without! Steve’s knowledge, patience and experience knows no limits and is always happy to help and support regardless of how basic the question!

[163]

References

1. Prutton, M., *Surface physics*. 2nd Edition. Burge, E.J., Ingram, D.J.E. and Matthew, J.A.D., Editors. 1983, Oxford University Press: Oxford, UK.
2. Atkins, P. and de Paula, J., *Atkins' physical chemistry*. 7th Edition, Oxford University Press, Oxford, UK, 2002.
3. Seifritz, W., *CO_2 disposal by means of silicates.* Nature, 1990. **345**, 486-486.
4. Palandri, J.L., Rosenbauer, R.J. and Kharaka, Y.K., *Ferric iron in sediments as a novel CO_2 mineral trap: CO_2-SO_2 reaction with hematite.* Applied Geochemistry, 2005. **20**, 2038-2048.
5. Maroto-Valer, M.M., Tang, Z. and Zhang, Y., *CO_2 capture by activated and impregnated anthracites.* Fuel Processing Technology, 2005. **86**, 1487-1502.
6. Haywood, H.M., Eyre, J.M. and Scholes, H., *Carbon dioxide sequestration as stable carbonate minerals - environmental barriers.* Environmental Geology, 2001. **41**, 11-16.
7. Teir, S., Kuusik, R., Fogelhohn, C.J. and Zevenhoven, R., *Production of magnesium carbonates from serpentinite for long-term storage of CO_2.* International Journal of Mineral Processing, 2007. **85**, 1-15.
8. Stolaroff, J.K., Lowry, G.V. and Keith, D.W., *Using CaO- and MgO-rich industrial waste streams for carbon sequestration.* Energy Conversion and Management, 2005. **46**, 687-699.
9. Alexander, G., Maroto-Valer, M.M. and Gafarova-Aksoy, P., *Evaluation of reaction variables in the dissolution of serpentine for mineral carbonation.* Fuel, 2007. **86**, 273-281.
10. Maroto-Valer, M.M., Fauth, D.J., Kuchta, M.E., Zhang, Y. and Andresen, J.M., *Activation of magnesium rich minerals as carbonation feedstock materials for CO_2 sequestration.* Fuel Processing Technology, 2005. **86**, 1627-1645.
11. Huijgen, W.J.J., Comans, R.N.J. and Witkamp, G.J., *Cost evaluation of CO_2 sequestration by aqueous mineral carbonation.* Energy Conversion and Management, 2007. **48**, 1923-1935.

12. Watson, G.W., Kelsey, E.T., de Leeuw, N.H., Harris, D.J. and Parker, S.C., *Atomistic simulation of dislocations, surfaces and interfaces in MgO.* Journal of the Chemical Society-Faraday Transactions, 1996. **92**, 433-438.
13. Xu, C. and Goodman, D.W., *Structure and geometry of water adsorbed on the MgO(100) surface.* Chemical Physics Letters, 1997. **265**, 341-346.
14. Johnson, M.A., Stefanovich, E.V., Truong, T.N., Gunster, J. and Goodman, D.W., *Dissociation of water at the MgO(100)-water interface: Comparison of theory with experiment.* Journal of Physical Chemistry B, 1999. **103**, 3391-3398.
15. Abriou, D. and Jupille, J., *Self-inhibition of water dissociation on magnesium oxide surfaces.* Surface Science, 1999. **430**, L527-L532.
16. de Leeuw, N.H., Watson, G.W. and Parker, S.C., *Atomistic simulation of the effect of dissociative adsorption of water on the surface structure and stability of calcium and magnesium oxide.* Journal of Physical Chemistry, 1995. **99**, 17219-17225.
17. Refson, K., Wogelius, R.A., Eraser, D.G., Payne, M.C., Lee, M.H. and Milman, V., *Water chemisorption and reconstruction of the MgO surface.* Physical Review B, 1995. **52**, 10823-10826.
18. Vermilyea, D.A., *The dissolution of MgO and $Mg(OH)_2$ in aqueous solution.* Journal of the Electrochemical Society, 1969. **116**, 1179-1183.
19. de Leeuw, N.H., Purton, J.A., Parker, S.C., Watson, G.W. and Kresse, G., *Density functional theory calculations of adsorption of water at calcium oxide and calcium fluoride surfaces.* Surface Science, 2000. **452**, 9-19.
20. de Leeuw, N.H., Watson, G.W. and Parker, S.C., *Atomistic simulation of adsorption of water on three-, four- and five-coordinated surface sites of magnesium oxide.* Journal of the Chemical Society-Faraday Transactions, 1996. **92**, 2081-2091.
21. de Leeuw, N.H. and Parker, S.C., *Computer simulation of dissociative adsorption of water on CaO and MgO surfaces and the relation to dissolution.* Research on Chemical Intermediates, 1999. **25**, 195-211.

22. de Leeuw, N.H. and Parker, S.C., *Molecular dynamics simulation of MgO surfaces in liquid water using a shell-model potential for water.* Physical Review B, 1998. **58**, 13901-13908.
23. Kerisit, S., Parker, S.C. and Harding, J.H., *Atomistic simulation of the dissociative adsorption of water on calcite surfaces.* Journal of Physical Chemistry B, 2003. **107**, 7676-7682.
24. Spagnoli, D., Cooke, D.J., Kerisit, S. and Parker, S.C., *Molecular dynamics simulations of the interaction between the surfaces of polar solids and aqueous solutions.* Journal of Materials Chemistry, 2006. **16**, 1997-2006.
25. Kerisit, S. and Parker, S.C., *Free energy of adsorption of water and metal ions on the {10.4} calcite surface.* Journal of the American Chemical Society, 2004. **126**, 10152-10161.
26. Altman, I.S., Agranovski, I.E. and Choi, M., *On nanoparticle surface growth: MgO nanoparticle formation during a Mg particle combustion.* Applied Physics Letters, 2004. **84**, 5130-5132.
27. Hacquart, R. and Jupille, J., *Hydrated MgO smoke crystals from cubes to octahedra.* Chemical Physics Letters, 2007. **439**, 91-94.
28. Geysermans, P., Finocchi, F., Goniakowski, J., Hacquart, R. and Jupille, J., *Combination of (100), (110) and (111) facets in MgO crystals shapes from dry to wet environment.* Physical Chemistry Chemical Physics, 2009. **11**, 2228-2233.
29. Jensen, M.B., Pettersson, L.G.M., Swang, O. and Olsbye, U., *CO_2 sorption on MgO and CaO surfaces: A comparative quantum chemical cluster study.* Journal of Physical Chemistry B, 2005. **109**, 16774-16781.
30. Fukuda, Y. and Tanabe, K., *Infrared study of carbon dioxide adsorbed on magnesium and calcium oxides.* Bulletin of the Chemical Society of Japan, 1973. **46**, 1616-1619.
31. Shen, J.Y., Kobe, J.M., Chen, Y. and Dumesic, J.A., *Synthesis and surface acid/base properties of magnesium aluminium mixed oxides obtained from hydrotalcites.* Langmuir, 1994. **10**, 3902-3908.

32. Yanagisawa, Y., Takaoka, K., Yamabe, S. and Ito, T., *Interaction of CO_2 with magnesium oxide surfaces: a TPD, FTIR and cluster-model calculation study.* Journal of Physical Chemistry, 1995. **99**, 3704-3710.

33. Pacchioni, G., Ricart, J.M. and Illas, F., *Ab-initio cluster model calculations on the chemisorption of CO_2 and SO_2 probe molecules on MgO and CaO (100) surfaces. A theoretical measure of oxide basicity.* Journal of the American Chemical Society, 1994. **116**, 10152-10158.

34. Krischok, S., Höfft, O. and Kempter, V., *Adsorption on metal oxides: Studies with the metastable impact electron spectroscopy.* Nuclear Instruments & Methods in Physics Research Section B-Beam Interactions with Materials and Atoms, 2002. **193**, 466-473.

35. Voigts, F., Bebensee, F., Dahle, S., Volgmann, K. and Maus-Friedrichs, W., *The adsorption of CO_2 and CO on Ca and CaO films studied with MIES, UPS and XPS.* Surface Science, 2009. **603**, 40-49.

36. Kadossov, E. and Burghaus, U., *Adsorption kinetics and dynamics of CO, NO, and CO_2 on reduced CaO(100).* Journal of Physical Chemistry C, 2008. **112**, 7390-7400.

37. Masini, P. and Bernasconi, M., *Ab initio simulations of hydroxylation and dehydroxylation reactions at surfaces: amorphous silica and brucite.* Journal of Physics-Condensed Matter, 2002. **14**, 4133-4144.

38. Yoshida, T., Tanaka, T., Yoshida, H., Funabiki, T., Yoshida, S. and Murata, T., *Study of dehydration of magnesium hydroxide.* Journal of Physical Chemistry, 1995. **99**, 10890-10896.

39. Béarat, H., McKelvy, M.J., Chizmeshya, A.V.G., Sharma, R. and Carpenter, R.W., *Magnesium hydroxide dehydroxylation/carbonation reaction processes: Implications for carbon dioxide mineral sequestration.* Journal of the American Ceramic Society, 2002. **85**, 742-748.

40. Churakov, S.V., Iannuzzi, M. and Parrinello, M., *Ab initio study of dehydroxylation-carbonation reaction on brucite surface.* Journal of Physical Chemistry B, 2004. **108**, 11567-11574.

41. Wu, S.F., Li, Q.H., Kim, J.N. and Yi, K.B., *Properties of a nano CaO/Al_2O_3 CO_2 sorbent.* Industrial & Engineering Chemistry Research, 2008. **47**, 180-184.

42. Lee, S.C., Chae, H.J., Lee, S.J., Choi, B.Y., Yi, C.K., Lee, J.B., Ryu, C.K. and Kim, J.C., *Development of regenerable MgO-based sorbent promoted with K_2CO_3 for CO_2 capture at low temperatures.* Environmental Science & Technology, 2008. **42**, 2736-2741.

43. Hedhili, M.N., Yakshinskiy, B.V. and Madey, T.E., *Interaction of water vapor with $UO_2(001)$.* Surface Science, 2000. **445**, 512-525.

44. Burns, J.H., in *The Chemistry of the Actinide Elements Vol. 2*, Katz, J.J., Seaborg, G.T. and Morss, L.R., Editors., Chapman and Hall, New York, USA, 1986.

45. Willis, B.T.M., *Defect structure of hyper-stoichiometric uranium dioxide.* Acta Crystallographica Section A, 1978. **34**, 88-90.

46. Catlow, C.R.A., *Point defect and electronic properties of uranium dioxide.* Proceedings of the Royal Society of London Series A-Mathematical Physical and Engineering Sciences, 1977. **353**, 533-561.

47. Jackson, R.A., Catlow, C.R.A. and Murray, A.D., *Point defect calculations on UO_2.* Journal of the Chemical Society-Faraday Transactions II, 1987. **83**, 1171-1176.

48. Gupta, F., Brillant, G. and Pasturel, A., *Correlation effects and energetics of point defects in uranium dioxide: a first principle investigation.* Philosophical Magazine, 2007. **87**, 2561-2569.

49. Nerikar, P., Watanabe, T., Tulenko, J.S., Phillpot, S.R. and Sinnott, S.B., *Energetics of intrinsic point defects in uranium dioxide from electronic-structure calculations.* Journal of Nuclear Materials, 2009. **384**, 61-69.

50. Veal, B.W., Lam, D.J., Diamond, H. and Hoekstra, H.R., *X-ray photoelectron spectroscopy study of oxides of transuranium elements Np, Pu, Am, Cm, Bk and Cf.* Physical Review B, 1977. **15**, 2929-2942.

51. Baer, Y. and Schoenes, J., *Electronic structure and coulomb correction energy in UO_2 single crystal.* Solid State Communications, 1980. **33**, 885-888.
52. Naegele, J.R., Ghijsen, J. and Manes, L., *Localization and hybridization of 5f states in the metallic and ionic bond as investigated by photoelectron spectroscopy.* Structure and Bonding, 1985. **59-0**, 197-262.
53. Wu, Z.Y., Jollet, F., Gota, S., Thromat, N., Gautier-Soyer, M. and Petit, T., *X-ray absorption at the oxygen K edge in cubic f oxides examined using a full multiple-scattering approach.* Journal of Physics-Condensed Matter, 1999. **11**, 7185-7194.
54. Kelly, P.J. and Brooks, M.S.S., *Electronic structure and ground state properties of the actinide oxides.* Journal of the Chemical Society-Faraday Transactions II, 1987. **83**, 1189-1203.
55. Boettger, J.C. and Ray, A.K., *All-electron LCGTO calculations for uranium dioxide.* International Journal of Quantum Chemistry, 2000. **80**, 824-830.
56. Kudin, K.N., Scuseria, G.E. and Martin, R.L., *Hybrid density-functional theory and the insulating gap of UO_2.* Physical Review Letters, 2002. **89**, 266402.
57. Dudarev, S.L., Manh, D.N. and Sutton, A.P., *Effect of Mott-Hubbard correlations on the electronic structure and structural stability of uranium dioxide.* Philosophical Magazine B-Physics of Condensed Matter Statistical Mechanics Electronic Optical and Magnetic Properties, 1997. **75**, 613-628.
58. Laskowski, R., Madsen, G.K.H., Blaha, P. and Schwarz, K., *Magnetic structure and electric-field gradients of uranium dioxide: An ab initio study.* Physical Review B, 2004. **69**.
59. Prodan, I.D., Scuseria, G.E. and Martin, R.L., *Assessment of metageneralized gradient approximation and screened Coulomb hybrid density functionals on bulk actinide oxides.* Physical Review B, 2006. **73**.
60. Roy, L.E., Durakiewicz, T., Martin, R.L., Peralta, J.E., Scuseria, G.E., Olson, C.G., Joyce, J.J. and Guziewicz, E., *Dispersion in the Mott insulator UO_2: A*

comparison of photoemission spectroscopy and screened hybrid density functional theory. Journal of Computational Chemistry, 2008. **29**, 2288-2294.

61. Ryzhkov, M.V. and Kupryazhkin, A.Y., *First-principles study of electronic structure and insulating properties of uranium and plutonium dioxides.* Journal of Nuclear Materials, 2009. **384**, 226-230.
62. Kelly, P.J., Brooks, M.S.S. and Allen, R., *Electronic structure and ionicity of actinide dioxides.* Journal de Physique, 1979. **40**, 184-186.
63. Frazer, B.C., Shirane, G., Cox, D.E. and Olsen, C.E., *Neutron-diffraction study of antiferromagnetism in UO_2.* Physical Review, 1965. **140**, A1448-A1452.
64. Faber, J. and Lander, G.H., *Neutron diffraction study of UO_2: antiferromagnetic state.* Physical Review B, 1976. **14**, 1151-1164.
65. Skomurski, F.N., Ewing, R.C., Rohl, A.L., Gale, J.D. and Becker, U., *Quantum mechanical vs. empirical potential modeling of uranium dioxide (UO_2) surfaces: (111), (110), and (100).* American Mineralogist, 2006. **91**, 1761-1772.
66. Muggelberg, C., Castell, M.R., Briggs, G.A.D. and Goddard, D.T., *An STM study of the UO_2(001) surface.* Applied Surface Science, 1999. **142**, 124-128.
67. Muggelberg, C., Castell, M.R., Briggs, G.A.D. and Goddard, D.T., *The atomic structure of the UO_{2+x}(110) surface and the effects of interstitial oxygen: an elevated-temperature STM study.* Surface Science, 1998. **402**, 673-677.
68. Tan, A.H.H., Abramowski, M., Grimes, R.W. and Owens, S., *Surface defect configurations on the (100) dipolar surface of UO_2.* Physical Review B, 2005. **72**.
69. Castell, M.R., *Wulff shape of microscopic voids in UO_2 crystals.* Physical Review B, 2003. **68**.
70. Abramowski, M., Grimes, R.W. and Owens, S., *Morphology of UO_2.* Journal of Nuclear Materials, 1999. **275**, 12-18.

71. Stultz, J., Paffett, M.T. and Joyce, S.A., *Thermal evolution of hydrogen following water adsorption on defective $UO_2(100)$.* Journal of Physical Chemistry B, 2004. **108**, 2362-2364.

72. Senanayake, S.D. and Idriss, H., *Water reactions over stoichiometric and reduced $UO_2(111)$ single crystal surfaces.* Surface Science, 2004. **563**, 135-144.

73. Hay, P.J., *Theoretical studies of hydrogen and water adsorption on actinide oxide surfaces.* Materials Research Society Symposia Proceedings, 2006. **893**, 0893-JJ0808-0804.

74. Skomurski, F.N., Shuller, L.C., Ewing, R.C. and Becker, U., *Corrosion of UO_2 and ThO_2: A quantum-mechanical investigation.* Journal of Nuclear Materials, 2008. **375**, 290-310.

75. Abramowski, M., Redfern, S.E., Grimes, R.W. and Owens, S., *Modification of UO_2 crystal morphologies through hydroxylation.* Surface Science, 2001. **490**, 415-420.

76. Tan, A.H.H., Grimes, R.W. and Owens, S., *Structures of UO_2 and PuO_2 surfaces with hydroxide coverage.* Journal of Nuclear Materials, 2005. **344**, 13-16.

77. Hohenberg, P. and Kohn, W., *Inhomogeneous electron gas.* Physical Review, 1964. **136**, B864-B871.

78. Parr, R.G. and Yang, W., *Density-functional theory of atoms and molecules*. 1st Edition, Oxford University Press, Oxford, UK, 1994.

79. Kohn, W. and Sham, L.J., *Self-consistent equations including exchange and correlation effects.* Physical Review, 1965. **140**, A1133-A1138.

80. Perdew, J.P., in *Electronic Structure of Solids '91*, Ziesche, P. and Eschrig, H., Editors., Akademie Verlag, Berlin, Germany, 1991.

81. Perdew, J.P., Burke, K. and Ernzerhof, M., *Generalized gradient approximation made simple.* Physical Review Letters, 1996. **77**, 3865-3868.

82. Perdew, J.P., Burke, K. and Wang, Y., *Generalized gradient approximation for the exchange-correlation hole of a many-electron system.* Physical Review B, 1996. **54**, 16533-16539.

83. Dudarev, S.L., Botton, G.A., Savrasov, S.Y., Humphreys, C.J. and Sutton, A.P., *Electron-energy-loss spectra and the structural stability of nickel oxide: An LSDA+U study.* Physical Review B, 1998. **57**, 1505-1509.
84. Blöchl, P.E., *Projector augmented-wave method.* Physical Review B, 1994. **50**, 17953-17979.
85. Kresse, G. and Joubert, D., *From ultrasoft pseudopotentials to the projector augmented-wave method.* Physical Review B, 1999. **59**, 1758-1775.
86. Monkhorst, H.J. and Pack, J.D., *Special points for Brillouin zone integrations.* Physical Review B, 1976. **13**, 5188-5192.
87. Born, M. and Huang, K., *Dynamical theory of crystal lattices*. Oxford University Press, Oxford, UK, 1954.
88. Ewald, P.P., *Die berechnung optischer und elektrostatischer gitterpotentiale.* Annalen der Physik, 1921. **64**, 253-287.
89. Parry, D.E., *Electrostatic potential in the surface region of an ionic crystal.* Surface Science, 1975. **49**, 433-440.
90. Parry, D.E., *Erratum.* Surface Science, 1976. **54**, 195-195.
91. Kittel, C., *Introduction to solid state physics*. 2nd Edition, John Wiley & Sons, New York, USA, 1963.
92. Heyes, D.M., Barber, M. and Clarke, J.H.R., *Molecular dynamics computer simulation of surface properties of crystalline potassium chloride.* Journal of the Chemical Society-Faraday Transactions II, 1977. **73**, 1485-1496.
93. Allan, N.L., Rohl, A.L., Gay, D.H., Catlow, C.R.A., Davey, R.J. and Mackrodt, W.C., *Calculated bulk and surface properties of sulfates.* Faraday Discussions, 1993. **95**, 273-280.
94. Watson, G.W., Parker, S.C. and Wall, A., *Molecular dynamics simulation of fluoride-perovskites.* Journal of Physics-Condensed Matter, 1992. **4**, 2097-2108.
95. Dick Jr., B.G. and Overhauser, A.W., *Theory of dielectric constants of alkali halide crystals.* Physical Review, 1958. **112**, 90-103.
96. Cooke, D.J., *Atomistic simulation of segregation to the surfaces of hematite and goethite*. PhD, University of Bath, 2003

97. Lewis, G.V. and Catlow, C.R.A., *Potential models for ionic oxides.* Journal of Physics C-Solid State Physics, 1985. **18**, 1149-1161.

98. Kresse, G. and Furthmuller, J., *Efficiency of ab-initio total energy calculations for metals and semiconductors using a plane-wave basis set.* Computational Materials Science, 1996. **6**, 15-50.

99. Kresse, G. and Furthmuller, J., *Efficient iterative schemes for ab-initio total energy calculations using a plane-wave basis set.* Physical Review B, 1996. **54**, 11169-11186.

100. Kresse, G. and Hafner, J., *Ab-initio molecular dynamics for liquid-metals.* Physical Review B, 1993. **47**, 558-561.

101. Kresse, G. and Hafner, J., *Ab-initio molecular dynamics simulation of the liquid-metal amorphous semiconductor transition in germanium.* Physical Review B, 1994. **49**, 14251-14269.

102. Gale, J.D. and Rohl, A.L., *The General Utility Lattice Program (GULP).* Molecular Simulation, 2003. **29**, 291-341.

103. Catlow, C.R.A., *Defect structures in fluorite crystals*. PhD, University of Oxford, 1974

104. Catlow, C.R.A., James, R., Mackrodt, W.C. and Stewart, R.F., *Defect energetics in α-Al_2O_3 and rutile TiO_2.* Physical Review B, 1982. **25**, 1006-1026.

105. Saul, P., Catlow, C.R.A. and Kendrick, J., *Theoretical studies of protons in sodium hydroxide.* Philosophical Magazine B-Physics of Condensed Matter Statistical Mechanics Electronic Optical and Magnetic Properties, 1985. **51**, 107-117.

106. Wright, K., Freer, R. and Catlow, C.R.A., *The energetics and structure of the hydrogarnet defect in grossular - a computer simulation study.* Physics and Chemistry of Minerals, 1994. **20**, 500-503.

107. Baram, P.S. and Parker, S.C., *Atomistic simulation of hydroxide ions in inorganic solids.* Philosophical Magazine B-Physics of Condensed Matter Statistical Mechanics Electronic Optical and Magnetic Properties, 1996. **73**, 49-58.

108. Kerisit, S., Cooke, D.J., Marmier, A. and Parker, S.C., *Atomistic simulation of charged iron oxyhydroxide surfaces in contact with aqueous solution.* Chemical Communications, 2005, 3027-3029.

109. Kerisit, S., *Atomistic simulation of calcite surfaces*. PhD, University of Bath, 2004

110. Schröder, K.P., Sauer, J., Leslie, M., Catlow, C.R.A. and Thomas, J.M., *Bridging hydroxyl groups in zeolitic catalysts: a computer simulation of their structure, vibrational properties and acidity in protonated faujasites (H-Y zeolites).* Chemical Physics Letters, 1992. **188**, 320-325.

111. de Leeuw, N.H. and Parker, S.C., *Atomistic simulation of the effect of molecular adsorption of water on the surface structure and energies of calcite surfaces.* Journal of the Chemical Society-Faraday Transactions, 1997. **93**, 467-475.

112. Pavese, A., Catti, M., Price, G.D. and Jackson, R.A., *Interatomic potentials for $CaCO_3$ polymorphs (calcite and aragonite), fitted to elastic and vibrational data.* Physics and Chemistry of Minerals, 1992. **19**, 80-87.

113. Pavese, A., Catti, M., Parker, S.C. and Wall, A., *Modelling of the thermal dependence of structural and elastic properties of calcite, $CaCO_3$.* Physics and Chemistry of Minerals, 1996. **23**, 89-93.

114. de Leeuw, N.H. and Parker, S.C., *Modeling absorption and segregation of magnesium and cadmium ions to calcite surfaces: Introducing $MgCO_3$ and $CdCO_3$ potential models.* Journal of Chemical Physics, 2000. **112**, 4326-4333.

115. Smith, W. and Forester, T.R., *DL_POLY_2.0: A general-purpose parallel molecular dynamics simulation package.* Journal of Molecular Graphics, 1996. **14**, 136-141.

116. Parker, S.C., Catlow, C.R.A. and Cormack, A.N., *Prediction of mineral structure by energy minimisation techniques.* Journal of the Chemical Society, Chemical Communications, 1983. **17**, 936-938.

117. Fletcher, R. and Reeves, C.M., *Function minimization by conjugate gradients.* The Computer Journal, 1964. **7**, 149-154.

118. Norgett, M.J. and Fletcher, R., *Fast matrix methods for calculating relaxation about defects in crystals.* Journal of Physics Part C Solid State Physics, 1970. **3**, L190-L192.

119. Fletcher, R. and Powell, M.J.D., *A rapidly convergent descent method for minimization.* Computer Journal, 1963. **6**, 163-168.

120. Broyden, C.G., *The convergence of a class of double-rank minimization algorithms.* Journal of the Institute of Mathematics and its Applications, 1970. **6**, 76-90.

121. Fletcher, R., *A new approach to variable metric algorithms.* Computer Journal, 1970. **13**, 317-322.

122. Goldfarb, D., *A family of variable-metric methods derived by variational means.* Mathematics of Computation, 1970. **24**, 23-26.

123. Shanno, D.F., *Conditioning of quasi-Newton methods for function minimization.* Mathematics of Computation, 1970. **24**, 647-656.

124. Polak, E., *Computational methods in optimization*. Academic Press, New York, USA, 1971.

125. Leach, A.R., *Molecular modelling - principles and applications*. 2nd Edition, Pearson Education Limited, Harlow, UK, 2001.

126. Verlet, L., *Computer "Experiments" on Classical Fluids. I. Thermodynamical Properties of Lennard-Jones Molecules.* Physical Review, 1967. **159**, 98.

127. Hockney, R.W. and Eastwood, J.W., *Computer simulations using particles*. McGraw-Hill, New York, USA, 1981.

128. Swope, W.C., Andersen, H.C., Berens, P.H. and Wilson, K.R., *A computer simulation method for the calculation of equilibrium constants for the formation of physical clusters of molecules: Application to small water clusters.* Journal of Chemical Physics, 1982. **76**, 637-649.

129. Lindan, P.J.D. and Gillan, M.J., *Shell model molecular dynamics simulation of superionic conduction in CaF_2.* Journal of Physics-Condensed Matter, 1993. **5**, 1019-1030.

130. Ferneyhough, R., Fincham, D., Price, G.D. and Gillan, M.J., *The melting of MgO studied by molecular dynamics simulation.* Modelling and Simulation in Materials Science and Engineering, 1994. **2**, 1101-1110.
131. Mitchell, P.J. and Fincham, D., *Shell-model simulations by adiabatic dynamics.* Journal of Physics-Condensed Matter, 1993. **5**, 1031-1038.
132. *CRC handbook of chemistry and physics*. 61st Edition, CRC Press Inc., Florida, USA, 1981.
133. Nose, S., *A unified formulation of the constant formulation of the constant temperature molecular dynamics methods.* Journal of Chemical Physics, 1984. **81**, 511-519.
134. Bertaut, F., *Le terme électrostatique de l'énergie de surface.* Compte Rendus Hebdomadaire des Séances de l'Académie des Sciences, 1958. **246**, 3447-3450.
135. Tasker, P.W., *Stability of ionic crystal surfaces.* Journal of Physics C-Solid State Physics, 1979. **12**, 4977-4984.
136. Oliver, P.M., Parker, S.C. and Mackrodt, W.C., *Computer simulation of the crystal morphology of NiO.* Modelling and Simulation in Materials Science and Engineering, 1993. **1**, 755-760.
137. Gibbs, J.W., *Collected Works*. Longmans, Green and Co., New York, USA, 1928.
138. Wulff, G., *Zur frage der geschwindigkeit des wachstums und der auflösung der krystallflagen.* Zeitschrift fur Krystallographie und Mineralogie, 1901. **34**, 449-530.
139. Watson, G.W., Oliver, P.M. and Parker, S.C., *Computer simulation of the structure and stability of forsterite surfaces.* Physics and Chemistry of Minerals, 1997. **25**, 70-78.
140. Sayle, T.X.T., Parker, S.C. and Sayle, D.C., *Shape of CeO_2 nanoparticles using simulated amorphisation and recrystallisation.* Chemical Communications, 2004, 2438-2439.

141. Catlow, C.R.A., Faux, I.D. and Norgett, M.J., *Shell and breathing shell model calculations for defect formation energies and volumes in magnesium oxide.* Journal of Physics C-Solid State Physics, 1976. **9**, 419-429.

142. Landolt-Börnstein, *Numerical data and functional relationships in science and technology*. Springer Berlin Heidelberg, 1980.

143. Henrich, V.E., *Thermal faceting of (110) and (111) surfaces of MgO.* Surface Science, 1976. **57**, 385-392.

144. Onishi, H., Egawa, C., Aruga, T. and Iwasawa, Y., *Adsorption of Na atoms and oxygen containing molecules on MgO (100) and (111) surfaces.* Surface Science, 1987. **191**, 479-491.

145. de Leeuw, N.H., Higgins, F.M. and Parker, S.C., *Modeling the surface structure and stability of α-quartz.* Journal of Physical Chemistry B, 1999. **103**, 1270-1277.

146. Johnson, D.A., *Some thermodynamic aspects of inorganic chemistry*. 2nd Edition, Cambridge University Press, 1982.

147. Dove, M.T., Calleja, M., Bruin, R., Wakelin, J., Tucker, M.G., Lewais, G.J., Hasan, S.M., Alexandrov, V.N., Keegan, M., Ballard, S., Tyer, R.P., Todorov, I., Wilson, P.B., Alfredsson, M., Price, G.D., Chapman, C., Emmerich, W., Wells, S.A., Marmier, A., Parker, S.C. and Du, Z., *The eMinerals collaboratory: tools and experience.* Molecular Simulation, 2005. **31**, 329-337.

148. Lodziana, Z., Topsoe, N.-Y. and Norskov, J.K., *A negative surface energy for alumina.* Nature Materials, 2004. **3**, 289-293.

149. Mathur, A., Sharma, P. and Cammarata, R.C., *From our readers: Negative surface energy - clearing up confusion.* Nature Materials, 2005. **4**, 186-186.

150. Tasker, P.W., Colbourn, E.A. and Mackrodt, W.C., *Segregation of isovalent impurity cations at the surfaces of MgO and CaO.* Journal of the American Ceramic Society, 1985. **68**, 74-80.

151. Frisch, M.J., Trucks, G.W., Schlegel, H.B., Scuseria, M.A., Robb, M.A., Cheeseman, J.R., Montgomery, J.A., Vreven, T., Kudin, K.N., Burant, J.C., Milia, S., Millam, J.M., Iyengar, S.S., Tomasi, J., Barone, V., Mennucci, B.,

Cossi, M., Saclmani, G., Rega, N., Petterson, G.A., Nakatsuji, H., Hada, M., Ehara, M., Toyota, K., Fukada, R., Hasegawa, J., Ishida, M., Nakajima, T., Honda, Y., Kitao, O., Nakai, H., Klene, M., Li, X., Knox, E., Hratchian, H.P., Cross, J.B., Adamo, C., Jaramillo, J., Gomperts, R., Stratmann, R.E., Yazyev, O., Austin, A.J., Cammi, R., Pomelli, C., Ochterski, J.W., Ayala, P.Y., Morokuma, K., Voth, G.A., Salvador, P., Dannenberg, J.J., Zakrzewski, V.G., Dapprich, S., Daniels, A.D., Strain, M.C., Farkas, O., Malick, D.K., Rabuck, A.D., Ragahavachari, K., Foresman, J.B., Ortiz, J.V., Cui, Q., Baboul, A.G., Clifford, S., Cioslowski, J., Stefanov, B.B., Liu, G., Liashenko, A., Piskorz, P., Komaromi, I., Martin, R.L., Fox, D.J., Keith, T., Al-Laham, M.A., Peng, C.Y., Nanayakkara, A., Challacombe, M., Gill, P.M.W., Johnson, B., Chen, W., Wong, M.W., Gonzalez, C. and Pople, J.A., *Gaussian03 (Revision B.04)*; Gaussian, Inc.; Pittsburgh, PA, 2003

152. Herzberg, G., *Infrared and Raman spectra of polyatomic molecules*. Van Nostrand, New York, USA, 1945.

153. Parker, S.C. and Price, G.D., *Computer modelling of phase transitions in minerals.* Advances in Solid State Chemistry, 1989. **1**, 295-327.

154. Huijgen, W.J.J., Witkamp, G.J. and Comans, R.N.J., *Mechanisms of aqueous wollastonite carbonation as a possible CO_2 sequestration process.* Chemical Engineering Science, 2006. **61**, 4242-4251.

155. Kerisit, S., Marmier, A. and Parker, S.C., *Ab-initio surface phase diagram of the {10-14} calcite surface.* Journal of Physical Chemistry B, 2005. **109**, 18211-18213.

156. Marmier, A. and Parker, S.C., *Ab-initio morphology and surface thermodynamics of α-Al_2O_3.* Physical Review B, 2004. **69**, 115409.

157. Duński, H., Jozwiak, W.K. and Sugier, H., *Dehydroxylation of the surface of magnesium oxide by temperature programmed desorption.* Journal of Catalysis, 1994. **146**, 166-172.

158. Stockelmann, E. and Hentschke, R., *A molecular-dynamics simulation study of water on NaCl(100) using a polarizable water model.* Journal of Chemical Physics, 1999. **110**, 12097-12107.

159. Impey, R.W., Madden, P.A. and McDonald, I.R., *Hydration and mobility of ions in solution.* Journal of Physical Chemistry, 1983. **87**, 5071-5083.

160. Spagnoli, D., *Atomistic simulations of the mineral water interface*. PhD, University of Bath, 2006

161. Schoenes, J., *Optical properties and electronic structure of UO_2.* Journal of Applied Physics, 1978. **49**, 1463-1465.

162. Caciuffo, R., Amoretti, G., Santini, P., Lander, G.H., Kulda, J. and Du Plessis, P.D., *Magnetic excitations and dynamical Jahn-Teller distortions in UO_2.* Physical Review B, 1999. **59**, 13892-13900.

163. Parker, S.C., *Personal communication*.

164. Redfern, S.E., Grimes, R.W. and Rawlings, R.D., *The hydroxylation of t-ZrO_2 surfaces.* Journal of Materials Chemistry, 2001. **11**, 449-455.

Copyright Information for Images

Please note that certain images from the results in this thesis are already published in the chemical literature and therefore the publishers who hold the copyright for these images must be acknowledged.

Figures 4.8, 4.9, 4.10, 4.11 and 4.13 are reproduced from:

Allen, J.P., Parker, S.C. and Price, D.W. *Atomistic simulation of the surface carbonation of calcium and magnesium oxide surfaces*. Journal of Physical Chemistry C, 2009. **113**, 8320-8328.

DOI: 10.1021/jp810885m

As published by the American Chemical Society, http://pubs.acs.org.

Figures 5.1(a), 5.3(a), 5.4(a), 5.10(a) and 5.11(a) are reproduced, in part, from:

Allen, J.P., Greń, W., Molinari, M., Arrouvel, C., Maglia, F. and Parker, S.C. *Atomistic modelling of adsorption and segregation at inorganic solid surfaces*. Molecular Simulation, 2009. **35**, 584-608.

DOI: 10.1080/08927020902774570

As published by the Taylor and Francis Group, http://www.informaworld.com.